THE WORK IS COMPLETED AT

HCM CITY UNIVERSITY OF TECHNOLOGY AND EDUCATION

Supervisor 1: Assoc. Prof. Dr NGUYEN XUAN HUNG

Supervisor 2: Assoc. Prof. Dr DANG THIEN NGON

PhD thesis is protected in front of

EXAMINATION COMMITTEE FOR PROTECTION OF DOCTORAL THESIS

HCM CITY UNIVERSITY OF TECHNOLOGY AND EDUCATION,

Date .... month .... year .....

ORIGINALITY STATEMENT

I, Nguyen Thi Bich Lieu, hereby assure that this dissertation is my own work, done under the guidance of Assoc. Prof. Dr. Nguyen Xuan Hung and Assoc. Prof. Dr. Dang Thien Ngon with the best of my knowledge.

The data and results stated in the dissertation are honest and were not been published by any works.

Ho Chi Minh City, October 2019

Nguyen Thi Bich Lieu

ACKNOWLEDGEMENTS

This dissertation has been carried out in the Faculty of Civil Engineering, HCM City University of Technology and Education, Viet Nam. The process of conducting this thesis brings excitement but has quite a few challenges and difficulties. And I can say without hesitation that it has been finished thanks to the encouragement, support and help of my professors and colleagues.

First of all, I would like to express my deepest gratitude to Assoc. Prof. Dr. Nguyen Xuan Hung and Assoc. Prof. Dr. Dang Thien Ngon, especially Assoc. Prof. Dr. Nguyen Xuan Hung from CIRTech Institute, Ho Chi Minh City University of Technology (HUTECH), Vietnam for having accepted me as their PhD student and for the enthusiastic guidance and mobilization during my research. Also, I would like to sincerely thank Dr. Thai Hoang Chien, a close brother, for his helpful guidance at first step of doing research and his support for my overcoming of the hardest time.

Secondly, I would like also to acknowledge Msc. Nguyen Van Nam, Faculty of Mechanical Technology, Industrial University of Ho Chi Minh City, Vietnam for their troubleshooting and the cooperation in my study. Furthermore, I am grateful to Chau Nguyen Khanh and the staffs at CIRTech Institute, HUTECH, Vietnam for their professional knowledge, interactive discussion, and immediate support.

Thirdly, I take this chance to thank all my nice colleagues at the Faculty of Civil Engineering, Ho Chi Minh City University of Technology and Education, for their professional advice and friendly support.

Finally, this dissertation is dedicated to my family, especially my beloved husband, who has always given me valuable encouragement and assistance.

Nguyen Thi Bich Lieu

ABSTRACT

Isogeometric analysis (IGA) was introduced in 2005 by Hughes et al. [5] as a breakthrough in numerical simulation. The main advantage of the IGA is to use the same basis function to describe the geometry and to approximate the problem unknowns. It integrates Computer Aided Design (CAD) and Computer Aided Engineering (CAE) and so far the effectively numerical tool for the analysis of a variety of practical problems. The computational cost is decreased significantly as the meshes are generated within the CAD. IGA produces the results with higher accuracy because of the smoothness and the higher-order continuity between elements. For the last decade of development, isogeometric analysis has surpassed the standard finite elements in terms of effectiveness and reliability for various problems, especially for the ones with complex geometry.

Owing to its important role in many engineering structures and modern industries, laminated plate structures are widely used in a diverse array of structures in many areas such as aviation, shipbuilding and civil engineering. Laminated plates have excellent mechanical properties, including high strength to weight and stiffness to weight ratios, wear resistance, light weight and so on. Besides possessing the superior material properties, the laminated composites also supply the advantageous design through the arrangement of the stacking sequence and layer thickness to obtain the desired characteristics, that's why they have received considerable attention of many researchers worldwide.

In this dissertation, an isogeometric finite element formulation is developed based on Bézier extraction to solve various plate problems, using a seven-dof higher-order shear deformation theory for both analysis and control the responses of plate structures. One key point in this dissertation is to exploit the distinctive advantage of Bézier extraction in analysis of plate structures. In the conventional isogeometric analysis, the B-spline or Non-uniform Rational B-spline (NURBS) basis functions span over the entire domain of structures not just a local domain as Lagrangian shape

functions in FEM. The global structure induces the complex implementation in a traditional finite element context. In addition, in order to compute the shape functions, the Gaussian integration points force to transform to parametric space. By choosing Bernstein polynomials as the basis functions, IGA will be performed easily similar to the way of implementation in FE framework. The B-spline/NURBS basis can be rewritten in form of the combination of Bernstein polynomials and Bézier extraction operator. That is called Bézier extraction for B-spline/NURBS/T-spline.

Although IGA is suitable for the problems which have the higher-order continuity, the findings of using a higher-order shear deformation theory with the C^0-continuity show the convieniences for plate analysis.

Furthermore, both linear and nonlinear responses for four material models including laminated composite plates, piezoelectric laminated composite plates, piezoelectric functionally graded porous plates with graphene platelets reinforcement and functionally graded piezoelectric material porous plates are investigated. The control algorithms based on the constant displacement and velocity feedbacks are applied to control linear and geometrically nonlinear static and dynamic responses of the plates, where the effect of the structural damping is considered, based on a closed-loop control with piezoelectric sensors and actuators. The predictions of the proposed approach agree well with analytical solutions and several other available approaches. Through the analysis, numerical results indicated that the proposed method achieves high reliability as compared with other published solutions. Besides, some numerical solutions for PFGPM plates and FG porous reinforced by GPLs may be considered as reference solutions for future work because there have not yet been analytical solutions so far.

TÓM TẮT

Phân tích đẳng hình học (IGA) được giới thiệu năm 2005 bởi Hughes và các cộng sự [5] như là một sự đột phá trong tính toán mô phỏng số. Ưu điểm chính của IGA là sử dụng cùng một hàm cơ sở để mô tả cho cả hình học và xấp xỉ nghiệm số. Nó tích hợp việc thiết kế dựa trên máy tính cũng như công nghệ liên quan đến việc sử dụng hệ thống máy tính để phân tích đối tượng hình học CAD (CAE) và những công cụ số hiệu quả khác nhằm giải quyết nhiều lớp bài toán kỹ thuật khác nhau. Chi phí tính toán giảm đáng kể vì hình học chính xác được tạo ra trong CAD, sau đó đưa vào tính toán mà không bị sai số hình học. Hơn nữa, IGA cho kết quả nghiệm số với độ chính xác cao hơn vì tính trơn và tính liên tục bậc cao hơn giữa các phần tử. Trong một thập kỷ phát triển gần đây, phân tích đẳng hình học đã vượt qua phân tích phần tử hữu hạn (FEM) về tính hiệu quả và độ tin cậy đối với các bài toán khác nhau, đặc biệt đối với các bài toán có hình học phức tạp.

Bởi vì đóng vai trò quan trọng trong nhiều kết cấu kỹ thuật và công nghiệp hiện đại, kết cấu tấm nhiều lớp được sử dụng rộng rãi trong nhiều lĩnh vực khác nhau chẳng hạn như hàng không, đóng tàu, kỹ thuật dân dụng, vv. Kết cấu tấm nhiều lớp có các tính chất cơ học tuyệt vời, bao gồm độ bền và độ cứng cao, khả năng chống mài mòn cao, trọng lượng nhẹ và nhiều đặc tính khác ưu việt khác. Bên cạnh việc sở hữu các đặc tính tốt đó, vật liệu tổng hợp nhiều lớp còn cung cấp những thiết kế thuận lợi thông qua việc sắp xếp trình tự xếp chồng và độ dày các lớp để có được các đặc tính cơ học mong muốn, đó là lý do tại sao chúng nhận được sự quan tâm nghiên cứu đáng kể của nhiều nhà nghiên cứu trên toàn thế giới.

Trong luận án này, một công thức phần tử hữu hạn đẳng hình học được phát triển dựa trên trích xuất Bézier để giải quyết các bài toán tấm khác nhau, sử dụng lý thuyết biến dạng cắt bậc cao liên tục C^0 cho cả phân tích và điều khiển đáp ứng của các cấu trúc tấm. Một trong những điểm mới của luận án này là khai thác lợi ích vượt trội của trích xuất Bézier trong phân tích kết cấu tấm. Trong phân tích đẳng hình học truyền thống thông thường, các hàm cơ sở B-spline hoặc hàm NURBS phân bố trên toàn bộ miền của các cấu trúc chứ không chỉ là một miền cục bộ như các hàm dạng

Lagrangian trong FEM. Việc hàm dạng phân bố toàn cục như vậy làm cho việc thực hiện tính toán phức tạp. Ngoài ra, để tính toán các hàm dạng, các điểm tích phân Gauss buộc phải chuyển đổi sang không gian tham số. Bằng cách chọn đa thức Bernstein làm hàm cơ sở, IGA sẽ được thực hiện dễ dàng tương tự như cách triển khai trong phương pháp phần tử hữ hạn. Các hàm cơ sở B-spline / NURBS có thể được viết lại dưới dạng kết hợp các đa thức Bernstein và toán tử trích xuất Bézier. Đó được gọi là trích xuất Bézier cho B-spline / NURBS / T-spline.

Lý thuyết biến dạng cắt bậc cao với bậc liên tục C^0 được sử dụng thống nhất cho tất cả các chương. Hơn nữa, cả đáp ứng tuyến tính và phi tuyến cho bốn loại vật liệu tấm bao gồm tấm composite nhiều lớp, tấm composite nhiều lớp có dán lớp áp điện, tấm vật liệu chức năng dán lớp áp điện có lỗ rỗng được gia cường bằng các tấm graphene và tấm vật liệu áp điện chức năng có lỗ rỗng được nghiên cứu. Các thuật toán điều khiển dựa trên các tín hiệu phản hồi chuyển vị và vận tốc không đổi được áp dụng để điều khiển đáp ứng tĩnh và động của tấm cho cả đáp ứng tuyến tính và phi tuyến hình học, trong đó hiệu ứng của giảm chấn cấu trúc được xem xét, dựa trên điều khiển kín với các cảm biến và bộ truyền động áp điện. Thông qua phân tích phần ví dụ số, các kết quả đạt được chỉ ra rằng phương pháp đề xuất đạt được độ tin cậy cao khi so với các giải pháp khác đã được công bố trên các tạp chí uy tín. Ngoài ra, một số lời giải số cho các tấm vật liệu chức năng dán lớp áp điện có lỗ rỗng được gia cường bằng các tấm graphene và tấm vật liệu áp điện chức năng có lỗ rỗng có thể được coi là nguồn tài liệu tham khảo cho những nghiên cứu khác trong tương lai vì cho đến nay vẫn chưa có lời giải giải tích nào đưa ra.

CONTENTS

NOMENCLATURE

Latin Symbols

$\mathbf{C}$	Global damping matrix
$\mathbf{D}$	Matrix of material
$\mathbf{K}$	Global stiffness matrix
$\mathbf{M}$	Global mass matrix
$\mathbf{N}_{i,p}$	B-splines basis functions
$\mathbf{J}$	Jacobian matrix
$\mathbf{P}$	Control points
$\mathbf{R}$	Rational basic function
$\mathbf{u}$	Displacement field
$\dot{\mathbf{u}}$	Velocity
$\ddot{\mathbf{u}}$	Acceleration
$\mathbf{f}$	Global force vector
$\mathbf{k}$	Dielectric constant matrix
$\mathbf{e}$	Piezoelectric constant matrix
$\mathbf{q}_s$	The surface charges
$\mathbf{Q}_p$	The point charges
$\mathbf{E}$	The gradient of the electric potential
E	Young's modulus
h	The thickness
w	Weights
G_d	The constant displacement feedback control gain
G_v	The constant velocity feedback control gain
t	Time
V_m	The volume fraction of the metal

V_c	The volume fraction of the ceramic
V_0	Electric voltage

Greek Symbols

ν	Poisson's ratio
ω	Natural frequency
ρ	Mass density
$\boldsymbol{\sigma}$	Stress field
σ_{xx}	Normal stress in *x* direction
σ_{yy}	Normal stress in *y* direction
γ_{xy}	Shear stress in *xy* direction
γ_{yz}	Shear stress in *yz* direction
γ_{xz}	Shear stress in *xz* direction
$\boldsymbol{\varepsilon}$	Strain field
ε_{xx}	Normal strain in *x* direction
ε_{yy}	Normal strain in *y* direction
ε_{xy}	Shear strain in *xy* direction
ε_{yz}	Shear strain in *yz* direction
ε_{xz}	Shear strain in *xz* direction
$\xi;\eta$	Parametric coordinates
ϕ	The electric potential field

Abbreviations

2D	Two dimensional
3D	Three dimensional
CAD	Computer Aided Design

CAE	Computer Aided Engineering
CFS	Closed form solution
CLPT	Classical laminate plate theory
CPT	Classical plate theory
DQM	Differential quadrature method
EFG	Element-free Galerkin
ESDT	Exponential shear deformation theory
ESL	Equivalent single layer
FEA	Finite Element Analysis
FEM	Finite Element Method
IGA	Isogeometric Analysis
FGM	Functionally graded material
FSDT	First-order shear deformation theory
FSM	Finite strip method
GLHOT	Global-local higher-order theory
GSDT	Generalized shear deformation theory
HSDT	Higher-order shear deformation theory
ITSDT	Inverse tangent shear deformation theory
LHOT	Local higher-order theory
LWT	Layer-wise theory
NURBS	Non-Uniform Rational B-splines
RBF	Radial Basis Function
RPIM	Radial point interpolation method
RPT	Refined plate theory
SCFs	Shear correction factors
SSDT	Sinusoidal shear deformation theory
TrSDT	Trigonometric shear deformation theory
TSDT	Third-order shear deformation theory
UTSDT	Unconstrained third-order shear deformation theory

UISDT	Unconstrained inverse trigonometric shear deformation theory
USSDT	Unconstrained sinousoidal shear deformation theory
DOF	Degree of Freedom
C, S, F	Clamped, simply supported, and free boundary conditions
FGPM	Functionally graded piezoelectric material
FGPMP	Functionally graded piezoelectric material with porosity
ES-DSG3	Edge-based smoothed and discrete shear gap plate element
GDQ	Generalized differential quadrature
GPLs	Graphene platelets
CNTs	Carbon nanotubes
PFGP	Piezoelectric functionally graded porous plate
NL	Nonlinear
DKQ	Discrete Kirchhoff quadrilateral

LIST OF TABLES

LIST OF FIGURES

Chapter 1
LITERATURE REVIEW

1.1 Introduction

The main objective of this dissertation is to develop an isogeometric finite element method to analyze and control the responses of the laminated plate structures. This chapter introduces an overview of isogeometric analysis and state of the art development of some laminated plate structures which are used in this dissertation. The key drivers and novelty points of the dissertation are also provided to give readers better outline of the dissertation's content.

1.2 An overview of isogeometric analysis

Over the time, benefits of the numerical procedures have been recognized. As a matter of fact, they have been extensively developed to compute, analyze and simulate the response as well as dynamic characteristics of laminated plate. Some of the popular numerical procedures used are boundary element method (BEM), finite element method (FEM), finite difference method (FDM), mesh-free method, finite volume method (FVM) and so on. Generally speaking, the numerical methods can be divided into two groups:

- Group 1: methods that require meshing; e.g. FEM, FDM, BEM and FVM.
- Group 2: methods that do not require meshing; e.g. mesh-free methods.

In group 1, FEM is most well-known for solving many various technical problems and has become the universally applicable technique for solving boundary and initial value problems. This method has been widely exploited in all engineering and science research domains. Although FEM is an extremely versatile and powerful technique, it has certain disadvantages, such as overvalued stiffness, inaccuracy in stress results of linear elements and meshing problems. In order to address these shortcomings, three solutions are suggested, as follows

- Improve the variational method.

- Improve the finite element spaces.
- Improve both the variational method and the finite element spaces.

Therefore, the isogeometric analysis (IGA) is proposed in order to implement the aforementioned solutions. At first, it is necessary to know a brief history of IGA and what it is.

Since its first introduction in the early 1940s, computer has been extensively utilized for mathematical computation, and to solve practical engineering problems. This leads to the rise of the so-called Computer-Aided Engineering (CAE) which is being developed and applied ubiquitously. Since the 1960s [1], along with the developments and improvements of computer's hardware and algorithms, a new technique called FEM has been devised. FEM has become the most common numerical tool for solving (partial) differential equations that describe physical problems. As a result, it has been studied worldwide, and a great number of articles and books on the method have been written accordingly. Today, FEM is a well-established method that is applied in every field of the industry.

With the rapid developments of modern technology, more sophisticated structures have arisen. For instance, a typical personal automobile has roughly 3.000 parts, while a Boeing 777 has 100.000 parts or so [2]. These large numbers of study subjects lead to a more complex process of modeling, analysis and construction which is currently a severe bottleneck of the conventional FEM.

Later on, in 1966, two French automotive engineers Pierre Bézier of Renault and Paul de Faget de Casteljau of Citröen initiated the development of geometry modeling. Bézier employed the Bernstein polynomials to produce curves and surfaces. The contemporary was invented by Riesenfield in 1972 [3] and its generalization to NURBS was conducted by Versprille in 1975 [4]. These seminal works have contributed to a system of so-called Computer Aided Design (CAD) which becomes a standard industrial tool for geometry representation nowadays. However, for several decades, the CAD system has developed independently with the development of CAE. There are several reasons for this trend, but the main reason is

the different target of each field. While designers concentrated on systems that easily manipulate for visualization purpose, the analyst concentrated on systems that are as simple as possible for fast computation due to the limits of computing power during that time. With the advancement of computer power and high-tech constructions, the need for analyzing more and more complicated structure is in demand. The problem is that due to the discrepancy in geometry description between CAD and CAE, any CAD model created by designers need to be simplified and converted to a compatible model that is suitable for the finite element analysis. This leads to a tremendous amount of overlapping work.

A lot of effort has been made for an automated process conversion from CAD to CAE and to overcome the mentioned bottleneck. Nevertheless, none of the techniques and methods found seems to be applicable in the industry because the automated conversion is not reliable enough to replace the manual correction. The reason is that it is difficult and time-consuming to create a mesh that properly handles complex geometries with many details. Furthermore, this approach causes severe geometry information loss. This can be attributed to the fact that any refinement to capture more details of the computational domain requires the interaction with the design model while the analysis-suitable model is just an approximation of the design model (see Figure 1.1). The direct interaction is usually impossible, and thus the exact information of the original geometry description is never attained.

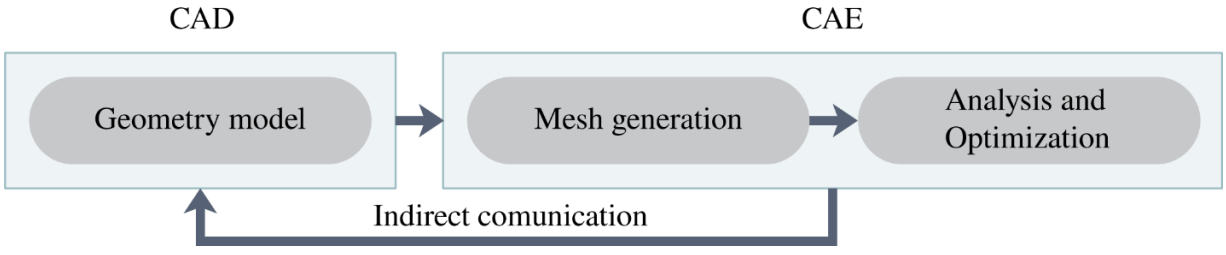

Figure 1.1: Analysis procedure in FEA. Due to the meshing, the computational domain is only an approximation of the CAD object.

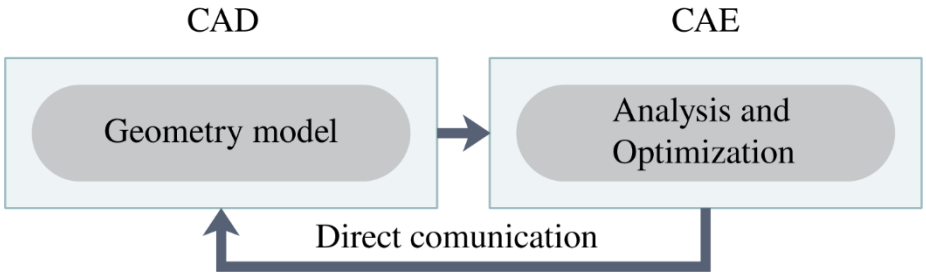

Figure 1.2: Analysis procedure in IGA. No meshing involved, the computational domain is thus kept exactly.

In 2005, Hughes, Cottrell & Bazilievs introduced a new technique, namely Isogeometric Analysis (IGA) [5]. The idea behind this technique is that instead of converting one system to another which is quite difficult to perform flawlessly, one should substitute one system for the other so that the conversion is no longer needed. This is accomplished by using the same basis functions that describe geometry in CAD (i.e. B-splines/NURBS) for analysis. The meshes are therefore exact, and the approximations attain a higher continuity. The computational cost is decreased significantly as the meshes are generated within the CAD. This technique results in a better collaboration between FEA and CAD (see Figure 1.2). Since the pioneering article [5], and the IGA book published in 2009 [2], a vast number of research have been conducted on this subject and successfully applied to many problems ranging from structural analysis [6-8], fluid structure interaction [9-10], electromagnetics [11] and higher-order partial differential equations [12]. IGA gives results with higher accuracy because of the smoothness and the higher-order continuity between elements. For that reason, this fact motivates us to establish a new numerical method beyond the standard finite elements. In this dissertation, an alternative approach based on Bézier extraction will be presented.

1.3 Literature review about materials used in this dissertation

In this dissertation, four material types are considered including laminated composite plate, piezoelectric laminated composite plate, piezoelectric functionally graded porous (PFGP) plate reinforced by graphene platelets (GPLs) and functionally graded piezoelectric material porous plate (FGPMP).

1.3.1. Laminated composite plate

Plates are the most common structural element and are an important part of many engineering areas. They are widely used in civil, aerospace engineering, automotive engineering and many other fields. One of the plate structures greatly studied nowadays is laminated composite plates. Laminated composite plates have excellent mechanical properties, including high strength to weight and stiffness to weight ratios, wear resistance, light weight and so on [13]. Besides possessing the superior material properties, the laminated composites also supply the advantageous design through the arrangement of stacking sequence and layer thickness to obtain the desired characteristics for engineering applications. This explains the considerable attention of many researchers worldwide towards laminated composites. More importantly, their effectiveness and usage depend on the bending behavior, stress distribution and natural vibrations. Thus, the study of their static and dynamic responses is really necessary for the above engineering applications.

This thesis aims to present a more complete and different method from other researchers. Among the applications of structures using IGA are Kirchhoff–Love plate [14-15], isotropic Reissner– Mindlin plates/shells [16-17], laminated composite plates based on the layerwise theory [18] and laminated composite and sandwich/functionally graded plates based on the higher-order shear deformation theory (HSDT) [19-21]. Recently, a research reported by Lezgy-Nazargah et al. [22] was significantly remarked with a refined sinus model for static and free vibration of laminated composite beam using IGA. Moreover, Valizadeh et al. [23] discussed the transient analysis of laminated composite plates using the first-order shear deformation theory (FSDT) based on IGA. It is observed that many researchers have mentioned laminated composite plates. Their studies incorporate many different methods, plate theories and techniques but the investigation of laminated composite plates used IGA based on Bézier extraction and a generalized unconstrained higher-order shear deformation theory (UHSDT) is still incomplete. Hence, this thesis presents a new and complete study for laminated composite plates.

1.3.2. Piezoelectric laminated composite plate

Piezoelectric material is a smart material, in which the electrical and mechanical properties have been coupled. One of the key features of the piezoelectric materials is the ability to make the transformation between the electrical power and mechanical power. Accordingly, when a structure embedded in piezoelectric layers is subjected to mechanical loadings, the piezoelectric material can create electricity. On the contrary, the structure can be changed its shape if an electric field is put on. Due to coupling mechanical and electrical properties, the piezoelectric materials have been extensively applied to create smart structures in aerospace, automotive, military, medical and other areas. In the literature of the plate integrated with piezoelectric layers, there are various numerical methods introduced to predict their behaviors. Mitchell and Reddy [24] presented the classical plate theory (CPT) based on the third-order shear deformation theory (TSDT) to find the Navier solution for composite laminates with piezoelectric laminae. Suleman and Venkayya [25] applied the classical laminate theory (CLT) with the four-node finite element to explore static and vibration analyses of a laminated composite with piezoelectric layers with upon uniformly reduced numerical integration and hourglass maintenance. Victor et al. [26] developed the higher-order finite formulations and an analytical closed-form solution to study the mechanics of adaptive piezoelectric actuators and sensors composite structures. Liew et al. [27] studied post-buclking of piezoelectric FGM plates subjected to thermo-electro-mechanical loadings using a semi-analytical solution with Galerkin-differential quadrature integration algorithm based on HSDT. The radial point interpolation method (RPIM) based on FSDT and the CPT with four-node non-conforming rectangular plate bending element was proposed by Liu et al. [28-29] to calculate and simulate the static deformation and dynamic responses of plates integrated with sensors and actuators. In addition, Hwang and Park [30] studied plates with piezoelectric sensors and actuators using the discrete Kirchhoff quadrilateral (DKQ) element and the Newmark method was used for the direct time responses of the plate subjected to the negative velocity feedback control. An HSDT-

layerwise generalized finite element formulation [31] and the layerwise based on analytical formulation [32] were investigated for piezoelectric composite plates. And FE formulations based on HSDT for analysis of smart laminated plates were studied in ref. [33].

For vibration control, Bailey et al. [34] and Shen et al. [35] investigated smart beams integrated with piezoelectric layers using analytical solutions. Tzou and Tseng [36] developed a piezoelectric thin hexahedron solid element for analysis and control of plates and shells with dispersed piezoelectric sensors and actuators. The meshfree model based on FSDT was combined by Liew et al. [37] to study the shape control of piezo laminated composite plates with the various boundary conditions. Wang et al. [38] used finite element method to investigated dynamic stability analysis of piezoelectric composite plates, in which Lyapunov's energy functional based on the derived general governing equations of movement with active damping was used. Based on CPT, He et al. [39] studied the shape and vibration control of the fuctionally graded materials (FGM) plates integrated with sensors and actuators. Based on HSDT and the element-free IMLS-Ritz method, Selim et al. [40] studied the active vibration control of FGM plates joined piezoelectric layers. In addition, Phung-Van et al. [41] studied the nonlinear transient analysis of piezoelectric FGM plates subjected to thermo-electro-mechanical loads based on the generalized shear deformation theory using IGA.

1.3.3. Piezoelectric functionally graded porous plates reinforced by graphene platelets (PFGP-GPLs)

The porous materials whose excellent properties such as lightweight, excellent energy absorption, heat resistance have been extensively employed in various fields of engineering including (e.g.) aerospace, automotive, biomedical and other areas [42-46]. However, the existence of internal pores leads to a significant reduction in the structural stiffness [47]. In order to overcome this shortcoming, the reinforcement with carbonaceous nanofillers such as carbon nanotubes (CNTs) [48-50] and

graphene platelets (GPLs) [51-52] into the porous materials is an excellent and practical choice to strengthen their mechanical properties.

In recent years, porous materials reinforced by GPLs [53] have been paid much attention to by the researchers due to their superior properties such as lightweight, excellent energy absorption, thermal management [54-56]. The artificial porous materials such as metal foams which possess combinations of both stimulating physical and mechanical properties have been prevalently applied in lightweight structural materials [57-58] and biomaterials [42-43]. The GPLs are dispersed in materials in order to amend the implementation while the weight of structures can be reduced by porosities. With the combined advantages of both GPLs and porosities, the mechanical properties of the material are significantly recovered but still maintain their potential for lightweight structures [59-60]. By modifying the sizes, the density of the internal pores in different directions, as well as GPL dispersion patterns, the FG porous plates reinforced by GPLs (FGP-GPLs) have been introduced to obtain the required mechanical characteristics [61–63].

In the last few years, there have been many studies being conducted to investigate the impacts of GPLs and porosities on the behaviors of structures under various conditions. Based on the Ritz method and Timoshenko beam theory, Kitipornchai et al. [64] and Chen et al. [65] studied the free vibration, elastic buckling and the nonlinear free vibration, post-buckling performances of FG porous beams, respectively. The uniaxial, biaxial, shear buckling and free vibration responses of FGP-GPLs were also investigated by Yang et al. [66] based on FSDT and Chebyshev-Ritz method. Additionally, to investigate the static, free vibration and buckling of FGP-GPLs, Li et al. [67] utilized IGA based on both FSDT and TSDT.

Geometrically nonlinear responses of PFGP-GPLs plates are also analyzed, controlled and presented in this dissertation. For analysis of geometrically nonlinear responses, D. Nguyen-Dinh et al. [68] investigated nonlinear thermo-electro-mechanical dynamic response of shear deformable piezoelectric Sigmoid functionally graded sandwich circular cylindrical shells on elastic foundations.

Moreover, D. Nguyen-Dinh et al. [69] also presented a new approach to investigate nonlinear dynamic response and vibration of imperfect functionally graded carbon nanotube reinforced composite double curved shallow shells. Li et al. [70] presented the nonlinear vibration and dynamic buckling of sandwich FGP-GPLs resting on Winkler-Pasternak elastic foundation applying CPT.

As previously mentioned, most of the studies mainly focused on studying the plates integrated with piezoelectric layers which address only the core layer composed of FGM or FG-CNTRC. Furthermore, the geometrically nonlinear static and dynamic analyses of the piezoelectric FG plates under various loading types are still somewhat limited.

1.3.4. Functionally graded piezoelectric material porous plates (FGPMP)

In practice, the traditional piezoelectric devices are often created from several layers of different piezoelectric materials. In addition, to control vibration, the laminated composite plates are embedded in piezoelectric sensors and actuators called the piezoelectric laminated composite materials. Although these devices have outstanding advantages and wide applications, they have shown some shortcomings such as cracking, delamination and stress concentrations at layers' interfaces. To overcome these disadvantages, FGMs are proposed. FGMs are a new type of composite structure which their material properties vary continuously over the thickness direction by mixing two different materials. Therefore, FGMs will reduce or even remove some disadvantages of piezoelectric laminated composite materials. Some publications about FGMs can be found in [71-73]. Based on the FGM concept, the effective combination of two types of piezoelectric materials in one direction will obtain the functionally graded piezoelectric materials (FGPMs) having many outstanding properties compared with traditional piezoelectric materials [74]. Therefore, FGPMs attract intense attention of researchers for analyzing and designing smart devices in recent years.

Nowadays, there are many modern techniques to fabricate FGMs such as centrifugal solid-particle method, centrifugal mixed-powder method, plasma

spraying, physical vapor deposition (PVD) or multi-step sequential infiltration. Nonetheless, FGMs usually contain some porosities during manufacturing process because inherent imperfection is present in any methods. This issue is relatable to the structure of wood and stone in nature. As commonly known, wood and stone are materials with the presence of porous. This means they are composed of solid and liquid (or gas) phases. For functionally graded piezoelectric material, the existence of internal pores is inevitable in the process of fabrication. The porous materials have been prevalently applied in lightweight structural materials and biomaterial. However, they reduce the structural strength significantly. It is known that the coupled mechanical and electrical behaviors of the imperfect FGPM plates are very different from the perfect FGPM plates. For that reason, investigation of the impact of porosity in FGPM plates is necessary and important to the FGPM technology.

Up to the present, several researchers have studied the electro-mechanical behavior of FG piezoelectric structures. Zhong and Shang [75] calculated an exact three-dimensional solution for a FGPM rectangular plate with fully simply-supported boundary condition and grounded along its four edges. Free and forced vibration control of FG piezoelectric plate under electro-mechanical loading was also examined by Jadhav and Bajoria [76]. Besides, Kiani et al. [77] studied buckling of FG piezoelectric material Timoshenko beams which are subjected to thermo-electrical loading. Using the Mindlin plate theory to model the structure and to adopt the generalized differential quadrature method, Sharma and Parashar [78] analyzed the natural frequencies of annular FGPM plates. Static and free vibration analysis of an FG piezoelectric microplate were presented by Li and Pan [79] based on the modified couple-stress theory. Additionally, Behjat and Khoshravan [80] mentioned geometrical nonlinear for bending and free vibration analysis of FG piezoelectric plates using FEM. Most recently, an analytical approach for free and transient vibration analyses of FGPM plates has been performed by Zhu et al. [81] for general boundary conditions.

Regarding FGPM porous (FGPMP) plates, it can be seen that there are several articles found recently in the literature. For instance, Barati et al. [82] analyzed free vibration of FGPMP plates using an improved four-variable theory where even and uneven porosity distribution were considered. Simultaneously, they investigated buckling of higher-order graded piezoelectric plates with the presence of porosities resting on elastic foundation [83]. Free vibration properties of smart shear deformable plates made of porous magneto-electro-elastic functionally graded (MEE-FG) materials were conducted by Ebrahimi et al. [84]. The coupling of electro-mechanical vibration behavior of FGP plate with porosities in the translation state was also studied by Wang [85]. In addition, Wang and Zu [86] investigated the porosity-dependent nonlinear forced vibrations of functionally graded piezoelectric material (FGPM) plates. It is worth noting that aforementioned works used the analytical approach which is suited to rectangular plates with the simple geometry, while practical applications occur with more complicated geometries. In this matter, finding a suitable numerical method is highly recommended. In other context, the accuracy of numerical solutions for solving FGPMP plates is enhanced significantly with the use of higher-order approximate methods. This reason motivates us to establish a new numerical method beyond the standard finite elements. Also, several numerical results of FGPMP plates may be useful for future references.

1.4 Goal of the dissertation

The dissertation focuses on the development of isogeometric finite element methods in order to analyze and control the responses of the laminated plate structures. So, there are two main aims to be studied. First, a new isogeometric formulation based on Bézier extraction for analysis of the laminated composite plate constructions is presented. Three analyzing forms including static, free vibration and dynamic transient analysis for laminated plate structures including laminated plates, piezoelectric laminated composite plate, piezoelectric functionally graded porous (PFGP) plates reinforced by graphene platelets (GPLs) and functionally graded piezoelectric material porous plates are investigated. Second, an active control

algorithm is applied to control static and transient responses of laminated plates embedded in piezoelectric layers in both linear and nonlinear cases.

1.5 The novelty of dissertation

This dissertation contributes several novelty points coined in the following points:

- A generalized unconstrained higher-order shear deformation theory (UHSDT) is given. This theory not only relaxes zero-shear stresses on the top and bottom surfaces of the plates but also gets rid of the need for shear correction factors. It is written in general form of distributed functions. Two distributed functions which supply better solutions than reference ones are suggested.
- The proposed method is based on IGA which is capable of integrating finite element analysis (FEA) into conventional NURBS-based computer aided design (CAD) design tools. This numerical approach is presented in 2005 by Hughes et al. [5]. However, there are still interesting topics for further research work.
- IGA has surpassed the standard finite elements in terms of effectiveness and reliability for various engineering problems, especially for ones with complex geometry.
- Instead of using conventional IGA, the IGA based on Bézier extraction is used for all the chapters. The key feature of IGA based on Bézier extraction is to replace the globally defined B-spline/NURBS basis functions by Bernstein shape functions which use the same set of shape functions for each element like as the standard FEM. It allows to easily incorporate into existing finite element codes without adding many changes as the former IGA. This is a new point comparing with the previous dissertations in Viet Nam.
- Until now, there exists still a research gap on the porous plates reinforced by graphene platelets embedded in piezoelectric layers using IGA based on

Bézier extraction for both linear and nonlinear analysis. Additionally, the active control technique for control of the static and dynamic responses of this plate type is also addressed.

- In this dissertation, the problems with complex geometries using multipatched approach are also given. This contribution seems different from the previous dissertations which studied IGA in Viet Nam.

1.6 Outline

The dissertation contains seven chapters and is structured as follows:

- Chapter 1 offers introduction and the historical development of IGA. State of the art development of four material types used in this dissertation and the motivation as well as the novelty of the thesis are also clearly described. The organization of the thesis is mentioned to the reader for the review of the content of the dissertation.
- Chapter 2 devotes the presentation of isogeometric analysis (IGA), including B-spline basis functions, non-uniform rational B-splines (NURBS) basis functions, NURBS curves, NURBS surfaces, B-spline geometries, refinement. Furthermore, Bézier extraction, the advantages and disadvantages of IGA comparing with finite element method are also shown in this chapter.
- Chapter 3 provides an overview of plate theories and descriptions of material properties used for the next chapters. First of all, the description of many plate theories including some plate theories to be applied in the chapters. Secondly, the presentation of four material types in this work including laminated composite plate, piezoelectric laminated composite plate, functionally porous plates reinforced by graphene platelets embedded in piezoelectric layers and functionally graded piezoelectric material porous plates.
- Chapter 4 illustrates the obtained results for static, free vibration and transient analysis of the laminated composite plate with various geometries, the direction of the reinforcements and boundary conditions. The IGA based on Bézier extraction is employed for all the chapters. An addition, two

piezoelectric layers bonded at the top and bottom surfaces of laminated composite plate are also consider for static, free vibration and dynamic analysis. Then, for the active control of the linear static and dynamic responses, a displacement and velocity feedback control algorithm are performed. The numerical examples in this chapter show the accuracy and reliability of the proposed method.

- Chapter 5 presents an isogeometric Bézier finite element analysis for bending and transient analyses of functionally graded porous (FGP) plates reinforced by graphene platelets (GPLs) embedded in piezoelectric layers, called PFGP-GPLs. The effects of weight fractions and dispersion patterns of GPLs, the coefficient and types of porosity distribution, as well as external electric voltages on structure's behaviors, are investigated through several numerical examples. These results, which have not been obtained before, can be considered as reference solutions for future work. In this chapter, our analysis of the nonlinear static and transient responses of PFGP-GPLs is also expanded. Then, a constant displacement and velocity feedback control approaches are adopted to actively control the geometrically nonlinear static as well as the dynamic responses of the plates, where the effect of the structural damping is considered, based on a closed-loop control.
- Chapter 6 studies some advantages of the functionally graded piezoelectric material porous plates (FGPMP). The material characteristics of FG piezoelectric plate differ continuously in the thickness direction through a modified power-law formulation. Two porosity models, even and uneven distributions, are employed. To satisfy Maxwell's equation in the quasi-static approximation, an electric potential field in the form of a mixture of cosine and linear variation is adopted. In addition, several FGPMP plates with curved geometries are furthermore studied, which the analytical solution is unknown. Our further study may be considered as a reference solution for future works.

- Finally, chapter 7 closes the concluding remarks and opens some recommendations for future work.

1.7 Concluding remarks

In this chapter, an overview of IGA and the materials; key drivers and the novelty points of this dissertation; and the organization of the dissertation with nine chapters. In next chapter, the isogeometric analysis framework is presented in detail.

Chapter 2
ISOGEOMETRIC ANALYSIS FRAMEWORK

2.1 Introduction

In this chapter, an overview of the advantages of IGA compared to FEM, B-spline, non-uniform rational B-splines (NURBS), isogeometric discretization and Bézier extraction are given. A brief discussion of refinement technique, numerical integration, and summary of IGA procedure is also presented.

2.2 Advantages of IGA compared to FEM

Some advantages of IGA over the conventional FEM are briefly addressed as:

Firstly, computation domain stays preserved at any level of domain discretization no matter how coarse it is. In the context of contact mechanics, this leads to the simplification of contact detection at the interface of the two contact surfaces especially in the large deformation circumstance where the relative position of these two surfaces usually changes significantly. In addition, sliding contact between surfaces can be reproduced precisely and accurately. This is also beneficial for problems that are sensitive to geometric imperfections like shell buckling analysis or boundary layer phenomena in fluid dynamics analysis.

Secondly, NURBS based CAD models make the mesh generation step is done automatically without the need for geometry clean-up or feature removal. This can lead to a dramatical reduction in time consumption for meshing and clean-up steps, which account approximately 80% of the total analysis time of a problem [2].

Thirdly, mesh refinement is effortless and less time-consuming without the need to communicate with CAD geometry. This advantage stems from the same basis functions utilized for both modeling and analysis. It can be readily pointed out that the position to partition the geometry and that the mesh refinement of the computational domain is simplified to knot insertion algorithm which is performed automatically. These partitioned segments then become the new elements and the mesh is thus exact.

Finally, interelement higher regularity with the maximum of C^{p-1} in the absence of repeated knots makes the method naturally suitable for mechanics problems having higher-order derivatives in formulation such as Kirchhoff-Love shell, gradient elasticity, Cahn-Hilliard equation of phase separation… This results from direct utilization of B-spline/NURBS bases for analysis. In contrast with FEM's basis functions which are defined locally in the element's interior with C^0 continuity across element boundaries (and thus the numerical approximation is C^0), IGA's basis functions are not just located in one element (knot span). Instead, they are usually defined over several contiguous elements which guarantee a greater regularity and interconnectivity and therefore the approximation is highly continuous. Another benefit of this higher smoothness is the greater convergence rate as compared to conventional methods, especially when it is combined with a new type of refinement technique, called *k*-refinement. Nevertheless, it is worth mentioning that the larger support of basis does not lead to bandwidth increment in the numerical approximation and thus the bandwidth of the resulted sparse matrix is retained as in the classical FEM's functions [2].

2.3 Some disadvantages of IGA

This method, however, presents some challenges that require some special treatments.

The most significant challenge of making use of B-splines/NURBS in IGA is that its tensor product structure does not permit a true local refinement, any knot insertion will lead to global propagation across the computational domain.

In addition, due to the lack of Kronecker delta property, the application of inhomogeneous Dirichlet boundary condition or exchange of forces/physical data in a coupled analysis are a bit more involved.

Furthermore, owing to the larger support of the IGA's basis functions, the resulted system matrices are relatively denser (containing more nonzero entries) when compared to FEM and the tri-diagonal band structure is lost as well.

2.4. B-spline geometries

2.4.1 B-spline curves

Performing summation over each univariate B-spline basis function multiplied with its associated control point, $\mathbf{P}_i$ a B-spline curve of order p in $\mathbb{R}^d$ is obtained as

$$\mathbf{C}(\xi) = \sum_{i=1}^{n} N_{i,p}(\xi)\mathbf{P}_i = \mathbf{N}(\xi)^{\mathrm{T}}\mathbf{P}, \tag{2. 1}$$

where n is the number of univariate B-spline basis function in ξ direction and the univariate B-spline basis $N_{i,p}(\xi)$ is then defined recursively over p starting with piecewise constants ($p = 0$) as

$$N_{i,0}(\xi) = \begin{cases} 1 & \text{if } \xi_i \le \xi < \xi_{i+1} \\ 0 & \text{otherwise} \end{cases}, \tag{2. 2}$$

$$N_{i,p}(\xi) = \frac{\xi - \xi_i}{\xi_{i+p} - \xi_i} N_{i,p-1}(\xi) + \frac{\xi_{i+p+1} - \xi}{\xi_{i+p+1} - \xi_{i+1}} N_{i+1,p-1}(\xi)$$

where it is assumed that whenever the denominator in an arbitrary coefficient term equals zero, that term is defined to take zero value. Each control point, $\mathbf{P}_i$ is accompanied by its own corresponding basis function which qualifies the influence of control point to the curve. These are similar to nodal coordinates in FEA in the sense that they are the corresponding coefficients of the basis functions, but the non-interpolatory nature of the B-splines does not lead to a usual interpretation of the control point values. Figure 2. 1 illustrates a quartic B-spline curve for a given knot vector $\Xi = \{0,0,0,0,0,1/3,1/3,1/3,2/3,1,1,1,1,1\}$, where the red squares indicate physical knots (element's boundaries) and the two end control points are interpolated as a result of the open knot vector. It can be seen that owing to the multiplicity of four of the knot 1/3, the curve interpolates one control point, and thus the curve is C^0 continuous at this knot.

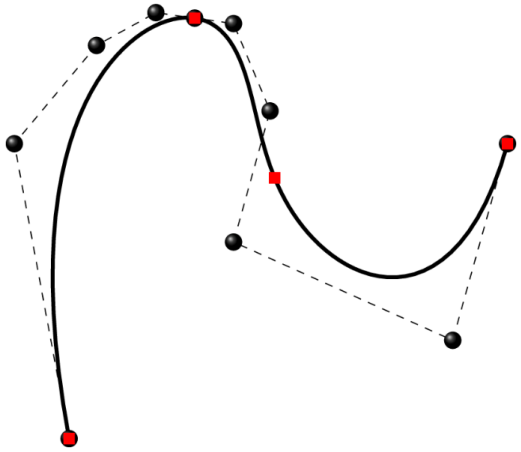

Figure 2. 1: A quartic B-spline curve

A B-spline curve possesses the following properties:

- If $p = n - 1$ (i.e., the order of a B-spline curve is equal to the number of control points minus 1), this B-spline curve reduces to a Bézier curve
- B-spline curve is a piecewise polynomial curve
- Clamped B-spline curve interpolates the two end control points $\mathbf{P}_1$ and $\mathbf{P}_{n+1}$
- Strong convex hull property: an arbitrary B-spline curve is kept inside the convex hull of its control polygon
- Invariance with respect to affine transformations
- Local modification: modifying the position of $\mathbf{P}_i$ affects $\mathbf{C}(\xi)$ only in the interval $\left[\xi_i, \xi_{i+p+1}\right)$
- $\mathbf{C}(\xi)$ is C^{p-k} continuous at a knot of multiplicity k

Each of these Bézier segments is able to join to another at a desired continuity with a maximum of C^{p-1}. This also indicates that an arbitrary curve can be represented by two different approaches (see Figure 2. 2).

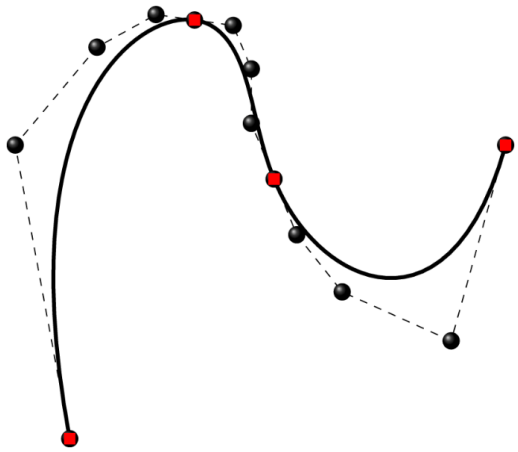

Figure 2. 2: The B-spline curve in Figure 2. 1 can be described by three concatenated Bézier curves. Due to interelement C^0 continuity, this representation produces more control points than the B-spline one.

2.4.2 B-spline surface

A tensor-product B-spline surface of order (p, q) for an arbitrary patch is constructed parametrically by a sum over B-spline functions multiplied with the associated control points as for B-spline curve

$$\mathbf{S}(\xi,\eta)=\sum_{i=1}^{n}\sum_{j=1}^{m}N_{i,j}^{p,q}(\xi,\eta)\mathbf{P}_{i,j}, \tag{2. 3}$$

where m and n are the number of univariate B-spline basis functions in the two parametric directions, $\mathbf{P}_{i,j}$ is the corresponding *control net* formed by connecting $m \times n$ control points, and $N_{i,j}^{p,q}(\xi,\eta)$ is the bivariate B-spline basis function defined as follow:

$$N_{i,j}^{p,q}(\xi,\eta)=N_{i,p}(\xi)M_{j,q}(\eta), \tag{2. 4}$$

Properties of a B-spline surface inherit directly from their univariate counterparts as the result of its tensor product nature.

2.5 Refinement technique

When B-splines is employed as a basis for geometry description and analysis, its polynomial bases can be enriched in several ways without causing any change to the underlying geometry description or the need to interact with the CAD program.

The two elementary refinement strategies of B-splines are called knot insertion and degree elevation which are equivalent to *h*-refinement (subdivision) and *p*-refinement (order elevation) in FEA, respectively. The combination of these two gives rise to the so-called *hp*-refinement in FEA. However, unlike FEA, the order in which *h*- and *p*-refinement are performed in IGA leads to differences in the refined polynomial basis. That means besides the ability to control element size and polynomial order of the basis, the continuity of the basis also easily manipulated which results in a number of different additional degrees of freedom. This entails a whole new refinement strategy, referred to as *k*-refinement. In the following sub-sections, these three refinements are briefly and partially represented for univariate B-splines. For multivariate B-splines, by taking advantage of tensor product structure the parameter space, the univariate algorithms can be independently applied to each parameter direction at a time and likewise for control mesh.

2.5.1 *h*-refinement

This kind of refinement is equivalent to mesh refinement, that is, the mesh size *h* is reduced while the global continuity of the approximation space is kept unchanged. This technique is accomplished via knot insertion. In contrast to mesh refinement in FEA which only produces C^0 continuity between element boundaries, knot insertion provides a much more flexible way to control element size and continuity between elements. The knot insertion technique is based on the following relation

$$\mathbf{C}(\xi)=\sum_{i=1}^{n} N_{i,p}(\xi)\mathbf{P}_i=\sum_{i=1}^{n+m}\overline{N}_{i,p}(\xi)\overline{\mathbf{P}}_i=\overline{\mathbf{C}}(\xi), \tag{2. 5}$$

where $\boldsymbol{\Xi}=\{\xi_1,\xi_2,\ldots,\xi_{n+p+1}\}$ and $\overline{\boldsymbol{\Xi}}=\{\overline{\xi}_1=\xi_1,\overline{\xi}_2,\ldots,\overline{\xi}_{n+m+p+1}=\xi_{n+p+1}\}$ are knot vectors of the original and refined spaces, respectively and *m* is the number of newly inserted knots. The knot insertion requires the reevaluations of both basis functions and corresponding control points. For simplicity, let's consider the insertion of one single knot $\overline{\xi}$ into the knot span $\left[\xi_j,\xi_{j+1}\right)$, where *j* indicates the position in the knot

vector. The $n + 1$ new basis functions are thus derived from the newly extended knot vector $\overline{\boldsymbol{\Xi}}$ and the new control points are computed as a linear combination of the old ones as [90].

$$\overline{\mathbf{P}}_i = \begin{cases} \mathbf{P}_1 & i = 1 \\ \alpha_i \mathbf{P}_i + (1-\alpha_i)\mathbf{P}_{i-1} & 1 < i < n+1, \\ \mathbf{P}_n & i = n+1 \end{cases} \tag{2. 6}$$

where

$$\alpha_i = \begin{cases} 1 & 1 \le i \le j-p \\ \dfrac{\overline{\xi} - \xi_i}{\xi_{i+p} - \xi_i} & j-p+1 \le i \le j. \\ 0 & i \ge j+1 \end{cases} \tag{2. 7}$$

Each single knot insertion only required the evaluation of p new control points and all remaining control points coincide with the old layout. Note that existing knots can be repeated to control the continuity as well as the support of the B-splines by simply inserting its values up to the multiplicity of p. The insertion of existing knots neither affects the polynomial order nor generates new elements. Figure 2. 3 illustrates this process by dividing the second element of the curve into two elements. The original curve is drawn on the left while the refined one is drawn on the right. Their associated basis functions are plotted under each curve. The original one is determined by the knot vector $\Xi = \{0,0,0,0,0,0.33,0.67,1,1,1,1,1\}$ and the control polygon $\mathbf{P}$. Inserting a knot $\overline{\xi} = 0.83$ produces a new control polygon $\overline{\mathbf{P}}$ which has an additional control point and consequently an additional basis function. It is clear that the geometry of the refined curve is the same as the original one, the only change is the number of control points and associated bases that increased by one.

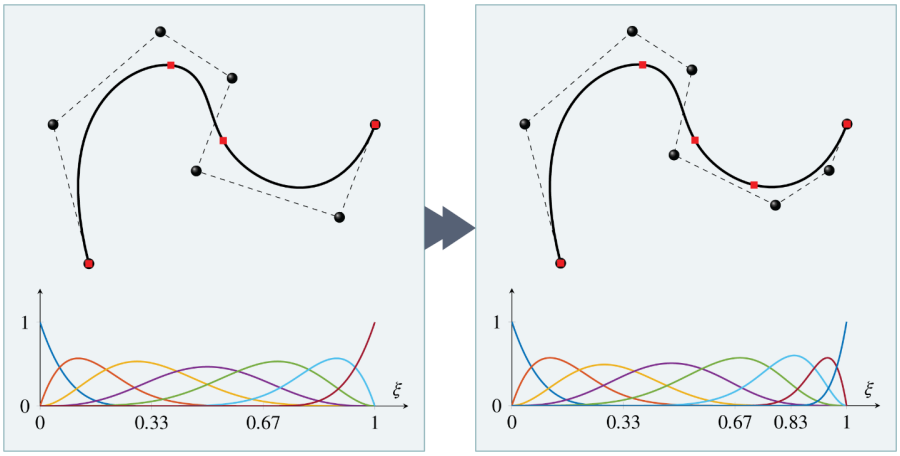

Figure 2. 3: An illustration of *h*-refinement for a B-spline curve.

2.5.2 *p*-refinement

This kind of refinement is equivalent to order raising with fixed interelement regularity. Since a B-spline curve of order p is a piecewise polynomial curve, one can elevate the degree of all spline segments by $t \geq 1$ without changing the curve. Given the incremental order of elevation t, the p-refinement algorithm aims at finding new knot vector $\overline{\boldsymbol{\Xi}} = \left\{\overline{\xi}_0, \ldots, \overline{\xi}_{n+p+t}\right\}$ and new control points $\left\{\overline{\mathbf{P}}_i\right\}$ such that

$$\mathbf{C}(\xi) = \overline{\mathbf{C}}(\xi) = \sum_{i=1}^{\overline{n}} \overline{N}_{i,p+t}(\xi)\overline{\mathbf{P}}_i, \tag{2. 8}$$

where $\overline{n}$ is the number of control points of $\overline{\mathbf{C}}(\xi)$, and $\overline{N}_{i,p+t}(\xi), i = 1, \ldots, \overline{n}$ are the B-spline basis functions of order $k + m$ defined on the knot vector $\overline{\boldsymbol{\Xi}}$. Knot vector $\overline{\boldsymbol{\Xi}}$ and $\overline{n}$ can be inferred directly by the following procedure, given that

$$\boldsymbol{\Xi} = \left\{\xi_1, \ldots, \xi_m\right\} = \left\{\underbrace{a, \ldots, a}_{p+1}, \underbrace{\xi_1, \ldots, \xi_1}_{m_1}, \ldots, \underbrace{\xi_s, \ldots, \xi_s}_{m_s}, \underbrace{b, \ldots, b}_{p+1}\right\}, \tag{2. 9}$$

where $m_1, \ldots, m_s$ are positive integers denoting multiplicities of the internal knots. Due to the fact that $\mathbf{C}(\xi)$ has smoothness up to C^{p-m_i} continuity at the knot ξ_i, $\overline{\mathbf{C}}(\xi)$ must preserve the same regularity at this knot value. To satisfy this constraint, every unique knot in the old knot vector has to be replicated as

$$\overline{\Xi} = \left\{\xi_1,\ldots,\xi_{\overline{m}}\right\} = \left\{\underbrace{a,\ldots,a}_{p+1+t},\underbrace{\xi_1,\ldots,\xi_1}_{m_1+t},\ldots,\underbrace{\xi_s,\ldots,\xi_s}_{m_s+t},\underbrace{b,\ldots,b}_{p+1+t}\right\}, \tag{2. 10}$$

where $\overline{m} = m + (s+2)t$ and $\overline{n} = n + (s+1)t$ [2]. The new control points $\left\{\overline{\mathbf{P}}_i\right\}$ of $\overline{\mathbf{C}}(\xi)$ regarded as a B-spline curve of order $p + t$ can be computed by various algorithms which can be referred in [91-94]. For the sake of simplicity, in this dissertation, the algorithm proposed in [92] is utilized. This algorithm consists of three steps: a) to decompose the B-spline curve into Bézier segments, b) to raise the order of each segment, c) to rejoin the order-elevated Bézier segments to yield the new B-spline curve. This process is demonstrated in Figure 2. 4 , where the order of the curve is increased by one. The original curve is drawn on the left while the refined one is drawn on the right. Their associated basis functions are plotted under each curve. The original quartic one is determined by the knot vector $\Xi = \{0,0,0,0,0,0.33,0.67,1,1,1,1,1\}$ and the control polygon $\mathbf{P}$. Rising the order of the curve by one resulting a quintic curve with the new knot vector $\Xi = \{0,0,0,0,0,0,0.33,0.33,0.67,0.67,1,1,1,1,1,1\}$ and the new control polygon $\overline{\mathbf{P}}$. It can be seen that the geometry of the curve is preserved, but each element is now influenced by one additional control point.

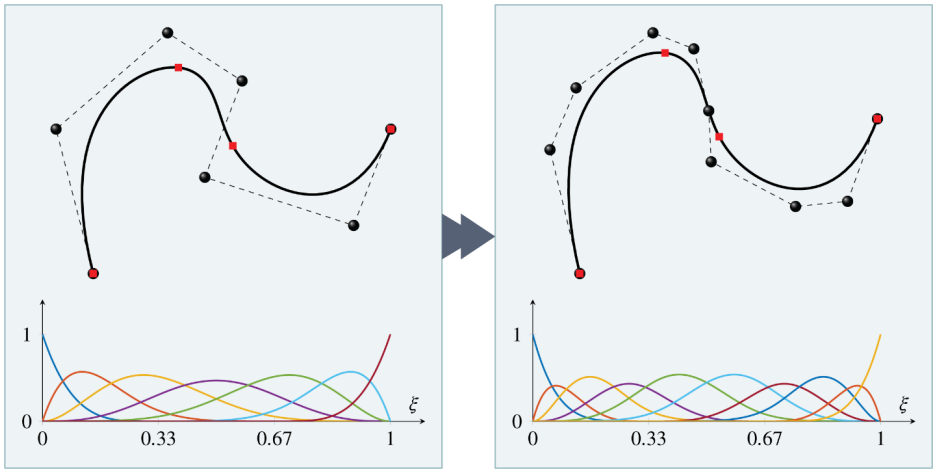

Figure 2. 4: An illustration of *p*-refinement for a B-spline curve.

2.5.3 *k*-refinement

This refinement strategy is equivalent to applying order elevation to the coarse mesh firstly, and then knot insertion. Due to knot insertion conducted after order elevation process, the refined basis achieves both high order and maximum available continuity, i.e. C^{p-1} [95]. This type of refinement is a new additional refinement possibility that cannot be directly compared to classical FEA as *h*- and *p*-refinements.

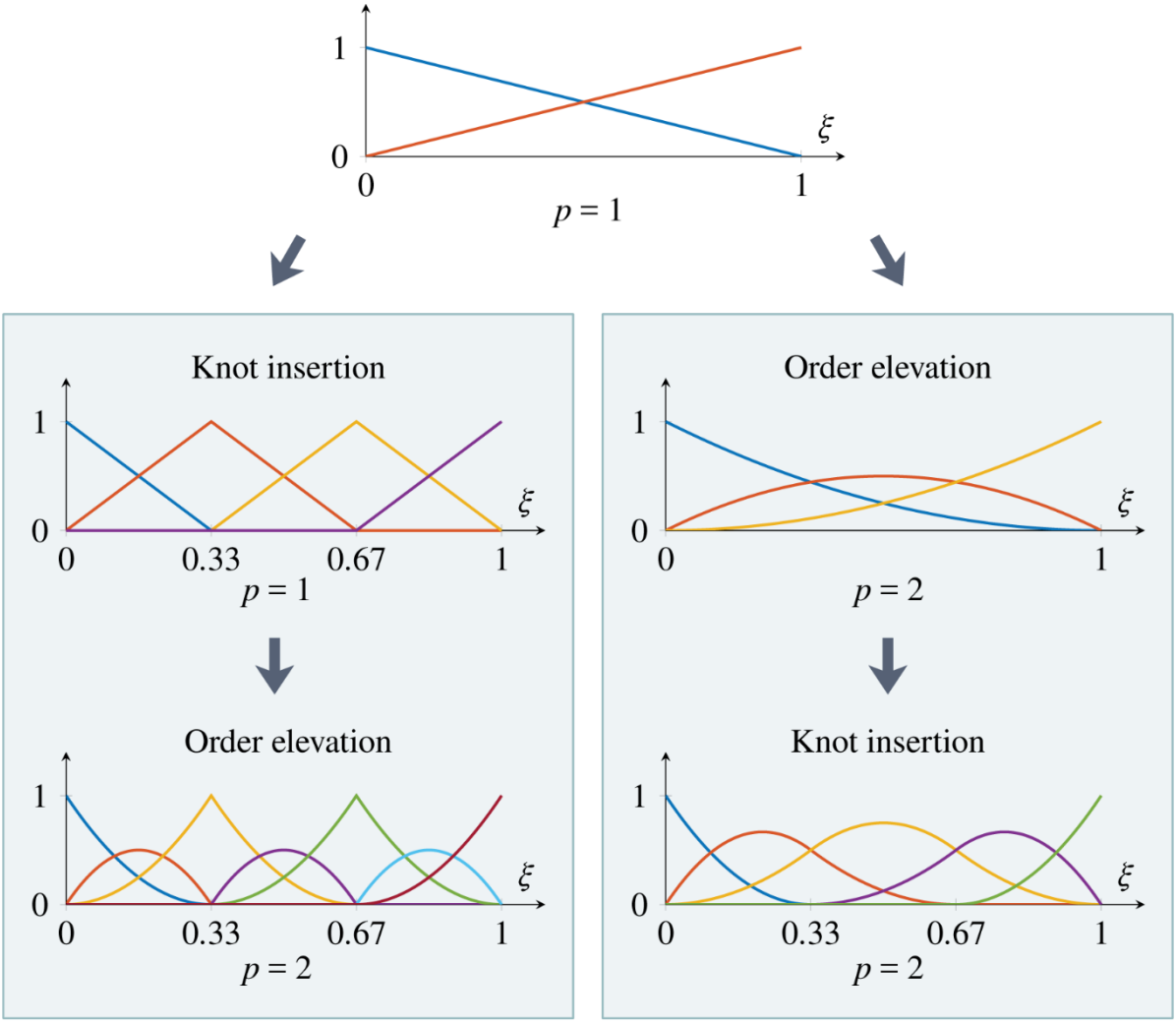

Figure 2. 5: An illustration of *k*-refinement.

Similar to *p*-refinement, *k*-refinement results in an increased number of control points during the refinement procedure. However, while *p*-refinement adds too many degrees of freedom to the whole system, *k*-refinement, on the other hand, can attain the same approximation error with significantly fewer degrees of freedom. An

illustration of *k*-refinement is shown in Figure 2. 5. Classical *p*-refinement compared to *k*-refinement. Let's consider the refinement of one linear element with its bases shown in the top. On the left is the classical *p*-refinement procedure where knot insertion followed by order elevation that produces nine quadratic basis functions with C^0 continuous at element's boundaries. On the right is the new *k*-refinement approach where order elevation followed by knot insertion that gives rise to five quadratic basis functions with interelement continuity of C^1. More detailed discussion on *k*-refinement can be referred in [95].

2.6 NURBS basis function

The geometry representation in CAD as well as in isogeometric analysis is often parametrized by Non-Uniform Rational B-splines (NURBS). NURBS in $\mathbb{R}^d$ are generated from conic projective transformations of B-splines in $\mathbb{R}^{d+1}$. Rational basis functions have the ability to exactly describe a broad range of objects that cannot be exactly described by polynomial basis functions such as conic sections [96].

A NURBS curve is obtained by multiplying every control point's component of the control mesh $\mathbf{P}_i$ with an assigned positive scalar weight w_i following by dividing the Eq. (2. 1) by the weighting function $W(\xi)$ defined as

$$W(\xi) = \sum_{\hat{i}=1}^{n} N_{\hat{i},p}(\xi) w_{\hat{i}}, \tag{2. 11}$$

which gives

$$\mathbf{C}(\xi) = \frac{\sum_{i=1}^{n} N_{i,p}(\xi) \mathbf{P}_i w_i}{W(\xi)} = \sum_{i=1}^{n} R_i^p(\xi) \mathbf{P}_i, \tag{2. 12}$$

where $R_i^p(\xi)$ is the univariate piecewise NURBS basis function defined by

$$R_i^p(\xi) = \frac{N_{i,p}(\xi) w_i}{W(\xi)}. \tag{2. 13}$$

Figure 2. 6 demonstrates two circles that are represented by both NURBS and B-spline in the corresponding solid and dotted curves. Their control points are depicted

by black balls with the associated weights also given for the NURBS case. It is clear that only the NURBS curve is able to represent the circle exactly.

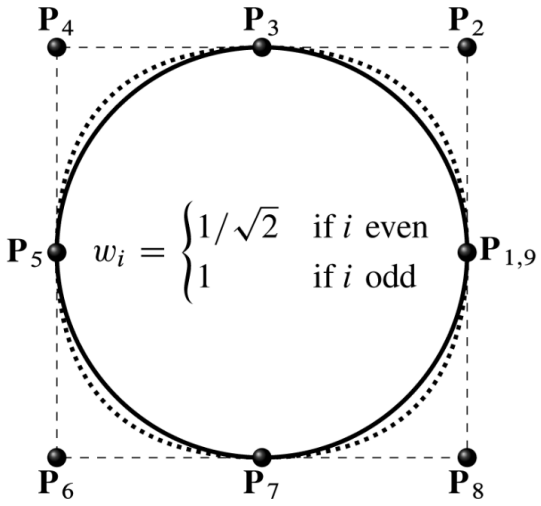

Figure 2. 6: Two representations of the circle. The solid curve is created by NURBS which describes exactly the circle while the dotted curve is created by B-splines which is unable to produce an exact circle.

Most properties of B-Splines also hold for NURBS. In case of equal weights $w_i = const,\ \forall i = 1,\ldots,n$ NURBS become B-Splines. Derivatives of NURBS are more involved than those of B-Splines and are addressed in detail in Subsection 2.5.2. Some important properties of NURBS are given as follows:

- For open knot vectors, NURBS basis functions constitute a partition of unity $\sum_{i=1}^{n} R_i^p(\xi) = 1, \forall \xi$.
- The continuity and support of NURBS basis functions are the same as for B-splines.
- NURBS are pointwise non-negative
- NURBS can represent precisely a wide class of curves, e.g. conic sections.

These properties result in a strong convex hull property. The NURBS surface can be derived by performing projective transformation of Eq. (2. 3) as done before for NURBS curve. The NURBS surface is then defined as

$$\mathbf{S}(\xi,\eta)=\sum_{i=1}^{n}\sum_{j=1}^{m}R_{i,j}^{p,q}(\xi,\eta)\mathbf{P}_{i,j}, \tag{2. 14}$$

where NURBS basis functions in parameter space of two dimensions are defined by

$$R_{i,j}^{p,q}(\xi,\eta)=\frac{N_{i,p}(\xi)M_{j,q}(\eta)w_{i,j}}{W(\xi,\eta)}, \tag{2. 15}$$

in which the bivariate weighting function in the denominator is given by

$$W(\xi,\eta)=\sum_{\hat{i}=1}^{n}\sum_{\hat{j}=1}^{m}N_{\hat{i},p}(\xi)M_{\hat{j},q}(\eta)w_{\hat{i},\hat{j}}, \tag{2. 16}$$

and $w_{i,j}$ is the associated weight to every control point of $m\times n$ control net $\mathbf{P}_{i,j}$. One of the most conic sections that usually encounter in modeling is the circular plate and it can be described exactly by NURBS surface as illustrated in Figure 2. 7. Typically, there are two approaches for parameterizing the same circular NURBS surface at coarse mesh level. The first one is depicted on the left where eighteen control points are used, result in four elements while the second one is shown on the right in which only nine control points are needed that produce only one element. It is worth to mentioning that each parameterization approach surfers from each own singularity. The left one has one singularity at the surface center where nine control points coincide at the same position, and the right one has four singularities at four locations where the four control points $\mathbf{P}_1,\mathbf{P}_3,\mathbf{P}_7,\mathbf{P}_9$ situate. Usually, in analysis, the right one is preferred due to its nice parameterization. Another conic section that often meets in design is the annular plate which is demonstrated in Figure 2. 7. It is important to note that this construction way exhibits an internal interface (indicated by the red line) where the first and last control points in the circumferential direction are met. In analysis, one needs to pay attention to this issue and to figure out a proper way to handle the control variables associated to these control points.

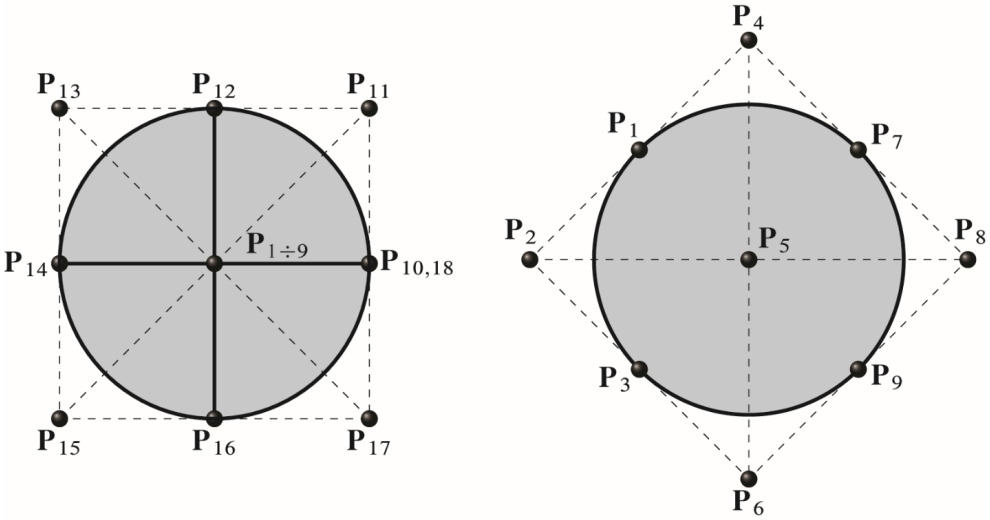

Figure 2. 7: Two representations of the same circular plate.

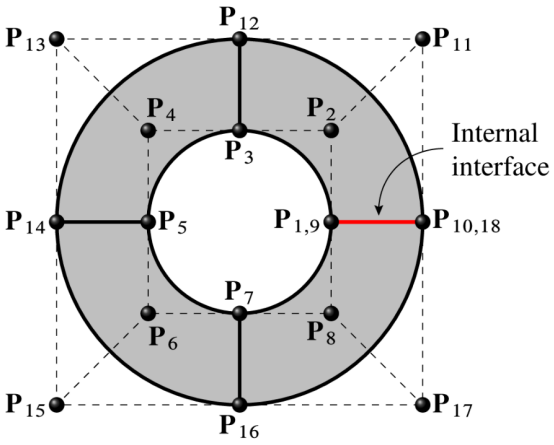

Figure 2. 8: A annular plate represented by NURBS surface.

2.7 Isogeometric discretization

In the isogeometric settings, solution space is approximated by making use of geometry functions (B-spline or NURBS) to guarantee the compatibility between geometry design and analysis phases, that is, it is an isoparametric discretization. Since this dissertation focuses on the composite plate, that is two-dimensional geometry, without loss of generality, a bivariate tensor-product single patch geometry map $\mathbf{F}(\xi,\eta):\widehat{\Omega}\to\Omega$ is considered, where the parameter domain $\widehat{\Omega}$ is a unit square in $\mathbb{R}^2$, $\widehat{\Omega}=[0,1]^2$. The geometrical mapping $\mathbf{F}(\xi,\eta)$ maps any point from the parameter domain to the physical domain via

$$\mathbf{x}(\xi,\eta)=\mathbf{F}(\xi,\eta)=\sum_{i=1}^{n}\sum_{j=1}^{m}R_{i,j}^{p,q}(\xi,\eta)\mathbf{P}_{i,j}, \tag{2. 17}$$

where $\mathbf{P}_{i,j}$ are the control point locations in physical space, $\mathbf{R}_{i,j}^{p,q}(\xi,\eta)$ are the basis functions defined in Eq.(2. 15).

Through the isoparametric concept, B-spline or NURBS basis functions are employed to describe the displacement field and the test functions in spatial coordinates *x* and *y* as

$$\mathbf{u}^{h}\left(\mathbf{x}(\xi,\eta)\right)=\mathbf{u}^{h}(\xi,\eta)=\sum_{i=1}^{n}\sum_{j=1}^{m}R_{i,j}^{p,q}(\xi,\eta)\mathbf{u}_{i,j} \tag{2. 18}$$

where $\mathbf{u}_{i,j}$ is the (*i, j*)-th component of the vector of control variables **u**, obtained from the solution of a discretized PDEs system.

2.8 Numerical integration

To perform isogeometric analysis relied on B-spline/NURBS basis functions, the computational domain is subdivided into elements where the grid size is specified by spans of the knots in parameter space. The parameter space defined by knot vectors is always a line/rectangle/cube depending upon the dimension of parameter space and it is mapped precisely onto geometry which is a physical space. Since the continuities of basis functions are C^{∞} within any non-zero knot span, numerical integration of characteristic components that describe the discretized governing differential equation (e.g. mass matrix, stiffness matrix, load vector, etc.) on each non-zero knot span is conducted analogously as in standard FEA by employing Gaussian quadrature.

In contrast to canonical FEA, the B-spline/NURBS parametric space is local to patches instead of elements. That is, in FEA, each element has its own parameterization where mapping is performed separately and directly from parent to physical elements. On the other hand, the geometrical mapping of B-Spline/NURBS carries a patch comprises with several elements in the parametric space to physical space. That means two mappings are required in order to numerically evaluate the elemental integrals defining the entries of the characteristic matrices or vectors

usually described in physical space. The first one pulls these integrals back to parametric space through a geometrical mapping and the second one further pulls them to the parent space using standard transformation rules where the numerical integration is actually conducted.

For the sake of clarity of the presentation, coordinates in physical, parametric and parent spaces are denoted by **x**, $\hat{\boldsymbol{\xi}}$ and $\tilde{\boldsymbol{\xi}}$, respectively. Elements can be named in the same manner and in the given order as $\Omega^e, \widehat{\Omega}^e, \widetilde{\Omega}^e$. By making use of these notations, the coordinate transformation from parent space to parametric space is formulated by

$$\xi = \frac{1}{2}\left[\left(\xi_{i+1} - \xi_i\right)\tilde{\xi} + \left(\xi_{i+1} + \xi_i\right)\right], \tag{2. 19}$$
$$\eta = \frac{1}{2}\left[\left(\eta_{i+1} - \eta_i\right)\tilde{\eta} + \left(\eta_{i+1} + \eta_i\right)\right],$$

and the Jacobian of this transformation is hence given as follows

$$\det\left(\mathbf{J}_{\tilde{\xi}}\right) = \frac{1}{4}\left(\xi_{i+1} - \xi_i\right)\left(\eta_{i+1} - \eta_i\right). \tag{2. 20}$$

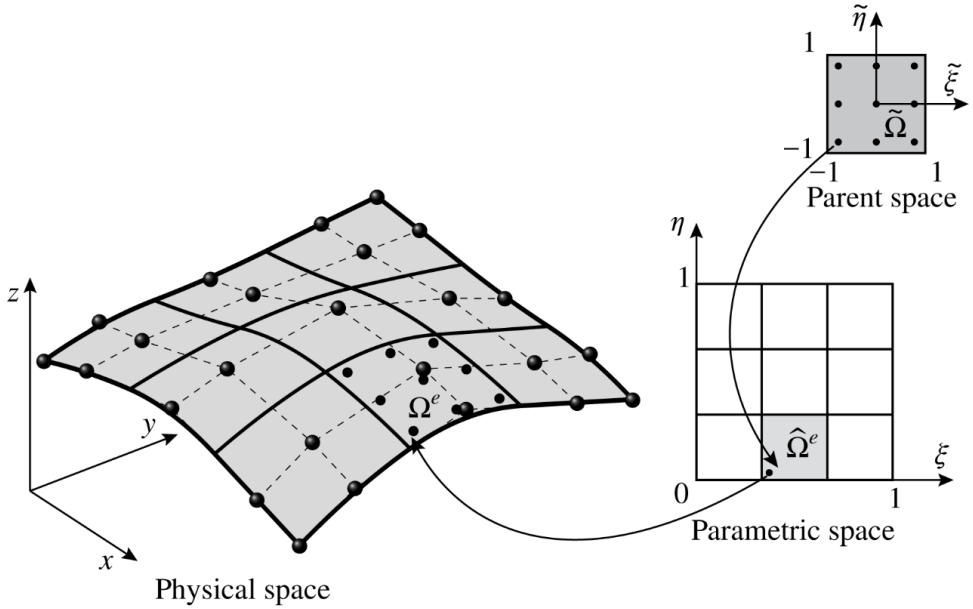

Figure 2. 9: The numerical integration procedure performed in Isogeometric Analysis approach.

To demonstrate this integration procedure, let's take example of the integral of elemental mass matrix which is given by

$$\begin{aligned}\mathbf{M}^e &= \int_{\Omega^e} \mathbf{N}(\mathbf{x})\mathbf{N}(\mathbf{x})\,\mathrm{d}\Omega \\ &= \int_{\widehat{\Omega}^e} \mathbf{N}(\mathbf{F}(\boldsymbol{\xi}))\mathbf{N}(\mathbf{F}(\boldsymbol{\xi}))\det(\mathbf{J}_1)\,\mathrm{d}\widehat{\Omega} \\ &= \int_{\widetilde{\Omega}^e} \mathbf{N}(\widetilde{\boldsymbol{\xi}})\mathbf{N}(\widetilde{\boldsymbol{\xi}})\det(\mathbf{J}_1)\det(\mathbf{J}_{\widetilde{\xi}})\,\mathrm{d}\widetilde{\Omega},\end{aligned} \tag{2. 21}$$

where **N** is the matrix of basis functions, $\mathbf{F}(\boldsymbol{\xi})$ is geometric mapping defined in Eq. (2. 17) and the Jacobian matrix $\mathbf{J}_{\widetilde{\xi}}$ is in turn defined in Eq.(2. 20). The final integral can be carried out using standard Gaussian quadrature where Gauss points are employed (*p* and *q* are orders of B-spline/NURBS basis functions in each parametric direction). Nevertheless, it is noteworthy that Gaussian numerical quadrature is generally sub-optimal and there exist more efficient numerical integration schemes for the IGA [2]. Figure 2. 9 demonstrates these integration mappings, and Figure 2. 10 summarizes essential steps to analyze a problem using the isogeometric framework.

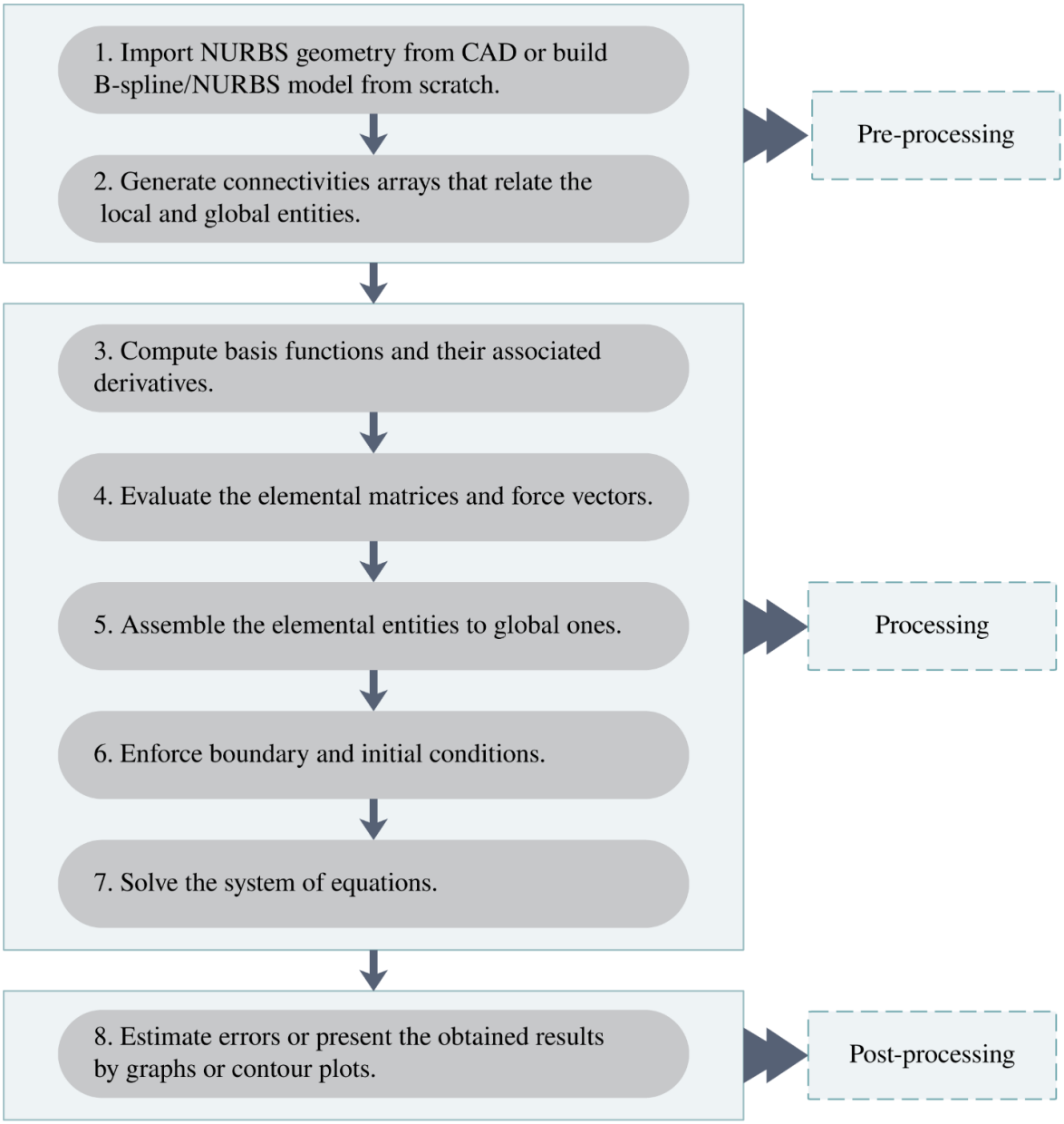

Figure 2. 10: Summary of IGA procedure.

2.9 Bézier extraction

2.9.1 Introduction of Bézier extraction

The main purpose of IGA based on Bézier extraction is to replace the globally defined B-spline/NURBS basis functions by Bernstein shape functions which use the same set of shape functions for each element like as the standard FEM. This allows us to perform a simple integration of standard finite element procedures for smooth, higher-degree basis functions. It is clear that B-spline/NURBS basis functions

spanning the entire domain of structures do not possess a local domain as Lagrangian shape functions. The global structure requires the complicated implementation in the traditional finite element approach. Furthermore, the numerical computation of stiffness formulation needs further transforming into the parent element while basis functions are defined in the parametric space. With Bernstein polynomials as the basis functions in Bézier extraction, computations of IGA are performed easily the same as those do in FEM. Accordingly, the Bernstein basis functions are applied and have the C^0-continuity like the Lagrangian shape functions in FEM.

The native approach for implementing IGA codes as described in foregoing sections exhibits several drawbacks that hinder the integration of IGA to existing the finite element framework. The apparent hindrance is that following this approach, each element takes some different B-spline basis functions as opposed to FEA where the same basis functions are employed for each element. Nevertheless, from the aforementioned observation in Section 2.3.2, each B-spline curve can be expressed as concatenated C^0 Bézier curves. That means it is possible to transform a B-spline patch into a set of piecewise C^0 Bézier elements and use it as the finite element representation of B-spline or NURBS.

2.9.2 Bézier decomposition and Bézier extraction [97-98]

It follows that the same curve can be described by two equivalent formulas as

$$\mathbf{C}(\xi) = \mathbf{N}^{\mathrm{T}}\mathbf{P} = \mathbf{B}^{\mathrm{T}}\mathbf{P}^{b}, \tag{2. 22}$$

where $\mathbf{N}^{\mathrm{T}}$ and $\mathbf{B}^{\mathrm{T}}$ are vectors of B-spline and Bézier basis functions, respectively with the associated control points stored in the corresponding vector $\mathbf{P}$ and $\overline{\mathbf{P}}$. The procedure to identify individual Bézier curves from a B-spline curve is entitled Bézier decomposition. The Bézier decomposition process is usually accomplished via knot insertion by additionally inserting already existing knots until their multiplicities equal to polynomial order and so that the continuities between them are C^0.

Given a knot vector $\boldsymbol{\Xi} = \left\{\xi_1, \xi_2, \ldots, \xi_{n+p+1}\right\}$ and a collection of control points $\mathbf{P} = \left\{\mathbf{P}_i\right\}_{i=1}^{n}$ which determine a B-spline curve. By applying the knot insertion

procedure in Eq. (2. 6) to a set of knots $\left\{\overline{\xi}_1, \overline{\xi}_2, \ldots, \overline{\xi}_j, \ldots, \overline{\xi}_m\right\}$ that needs to be replicated to produce the Bézier decomposition from a B-spline curve, one can write

$$\overline{\mathbf{P}}^{j+1} = \left(\mathbf{C}^j\right)^{\mathrm{T}} \overline{\mathbf{P}}^j, \tag{2. 23}$$

where $\overline{\mathbf{P}}^1 = \mathbf{P}$. Eq. (2. 23) is the matrix form of Eq. (2. 6) obtained when inserting a single knot $\overline{\xi}_j, j = 1, 2, \ldots, m$ to the original knot vector which the matrix $\mathbf{C}^j$ is defined as

$$\mathbf{C}^j = \begin{bmatrix} \alpha_1 & 1-\alpha_2 & 0 & \cdots & & & 0 \\ 0 & \alpha_2 & 1-\alpha_3 & 0 & \cdots & & 0 \\ 0 & 0 & \alpha_3 & 1-\alpha_4 & 0 & \cdots & 0 \\ \vdots & & & & & & \\ 0 & \cdots & & & 0 & \alpha_{(n+j-1)} & 1-\alpha_{(n+j)} \end{bmatrix}, \tag{2. 24}$$

in which $\alpha_i^j, i = 1, 2, \ldots, n+j$ be the *i*-th alpha as given in Eq. (2. 7). By performing the transformation defined in Eq. (2. 24) for every inserted knot $\overline{\xi}_j$, we arrive at the final control points collection $\overline{\mathbf{P}}^{m+1}$ which defined the Bézier segments of the decomposition. Setting $\mathbf{P}^b = \overline{\mathbf{P}}^{m+1}$, follow by defining $\mathbf{C}^{\mathrm{T}} = \left(\mathbf{C}^m\right)^{\mathrm{T}} \left(\mathbf{C}^{m-1}\right)^{\mathrm{T}} \cdots \left(\mathbf{C}^1\right)^{\mathrm{T}}$, one obtains

$$\underbrace{\mathbf{P}^b}_{(n+m)\times d} = \underbrace{\mathbf{C}^{\mathrm{T}}}_{n\times(n+m)} \underbrace{\mathbf{P}}_{n\times d}, \tag{2. 25}$$

which are convex linear combinations of the control points of the B-spline curve, $\mathbf{P}$ and $\mathbf{C}$ is a matrix of so-called *Bézier extraction operator* which rows adding up to unity due to the convex combinations. It is also worthwhile to mention that the information required to construct matrix $\mathbf{C}$ is solely a knot vector, that means the operator holds for both B-splines and NURBS. By combining the two Eqs. (2. 22) and (2. 25), the formulation that relates B-spine basis functions and Bernstein basis functions reads as follows

$$\left.\begin{aligned} \mathbf{N}^{\mathrm{T}}\mathbf{P} &= \mathbf{B}^{\mathrm{T}}\mathbf{P}^b \\ \mathbf{P}^b &= \mathbf{C}^{\mathrm{T}}\mathbf{P} \end{aligned}\right\} \Rightarrow \mathbf{N}^{\mathrm{T}}\mathbf{P} = \mathbf{B}^{\mathrm{T}}\mathbf{C}^{\mathrm{T}}\mathbf{P} \Leftrightarrow \mathbf{N} = \mathbf{C}\mathbf{B}. \tag{2. 26}$$

Hence, the B-Spline basis functions can be obtained by multiplying the same matrix $\mathbf{C}$ with the Bézier basis functions (the Bernstein basis). By the advantage of this approach, the incorporation of IGA to an existing FEA code is simplified to implement an element that utilizes the Bernstein basis and has an entry to load Bézier extraction matrix $\mathbf{C}$. For NURBS, the procedure of applying extraction operator is done as follows.

The formula of weighting functions defined in Eq.(2. 11) can be rewritten in matrix form as

$$W(\xi)=\sum_{\hat{i}=1}^{n} N_{\hat{i},p}(\xi) w_{\hat{i}} = \mathbf{N}^{\mathrm{T}}\mathbf{w} = \left(\mathbf{CB}\right)^{\mathrm{T}}\mathbf{w} = \mathbf{B}^{\mathrm{T}}\mathbf{C}^{\mathrm{T}}\mathbf{w} = \mathbf{B}^{\mathrm{T}}\mathbf{w}^{b} = W^{b}, \tag{2. 27}$$

where $\mathbf{w}^{b}=\mathbf{C}^{\mathrm{T}}\mathbf{w}$ are the corresponding weights of the Bernstein basis functions. Now, one rewrites Eq. (2. 13) in matrix form as follows:

$$\mathbf{R}(\xi)=\frac{1}{W(\xi)}\mathbf{WN}(\xi), \tag{2. 28}$$

in which $\mathbf{W}$ is the diagonal matrix of control points' weights defined as

$$\mathbf{W}=\begin{bmatrix} w_1 & & & \\ & w_2 & & \\ & & \ddots & \\ & & & w_n \end{bmatrix}. \tag{2. 29}$$

Replacing matrix $\mathbf{N}$ in Eq. (2. 28) by the relation in Eq. (2. 26) yields the formula that expresses NURBS basis in terms of Bernstein basis as

$$\mathbf{R}(\xi)=\frac{1}{W(\xi)}\mathbf{WCB}(\xi). \tag{2. 30}$$

The relationship between the NURBS control points, $\mathbf{P}$, and the Bézier control points, $\mathbf{P}^{b}$ is defined as

$$\mathbf{P}^{b}=\left(\mathbf{W}^{b}\right)^{-1}\mathbf{C}^{\mathrm{T}}\mathbf{WP}, \tag{2. 31}$$

where $\mathbf{W}^{b}$ is the diagonal matrix form of the Bézier weights recast from the vector form $\mathbf{w}^{b}$ as

$$\mathbf{W}^b = \begin{bmatrix} w_1^b & & & \\ & w_2^b & & \\ & & \ddots & \\ & & & w_{n+m}^b \end{bmatrix}. \tag{2. 32}$$

For higher-dimension bases, the extraction operators are straightforwardly defined as the tensor product of the univariate ones.

2.10 Concluding remarks

In this chapter, the fundamental developments of Isogeometric Analysis have been addressed which are summarized as follows

- IGA is a concept with the ultimate goal of eliminating the conversion from CAD files to CAE codes. It is accomplished by employing the same basis functions of CAD for analysis.
- B-spline basis functions can readily be computed by the Cox-de Boor algorithm from the so-called knot vector, and its associated derivatives can be expressed as linear combination of the lower order bases.
- B-spline curve is defined by a linear combination of basis functions and corresponding control points. B-spline surface and volume are defined analogously by taking advantage of tensor product structure of B-splines.
- B-splines offers three kinds of mesh refinement, namely *h*-refinement, *p*-refinement and *k*-refinement. While the first two techniques are fairly equivalent to element subdivision and order raising in FEA, respectively, the third one is exclusive to B-splines which results in higher interelement continuity.
- NURBS in $\mathbb{R}^d$ is defined by conic projecting B-splines in $\mathbb{R}^{d+1}$, where the coordinates of the $(d + 1)^{\text{th}}$ dimension are the strictly positive weights. This transformation has the ability to represent exact conic sections.
- NURBS geometry therefore is defined similarly as B-spline one.

- Numerical integration in NURBS-based IGA is performed via two successive mappings, the first one is from natural/parent space to parametric space and the second one is from parametric space to physical space.
- Since the same B-spline/NURBS curve can be represented by concatenated Bézier curves, one can decompose the B-spline/NURBS curve into several C^0 Bézier elements for using in the analysis. This procedure makes the IGA approach backward compatible with conventional FEM codes.

Chapter 3
THEORETICAL BASIS

3.1 Overview

This chapter shows an overview of plate theories; the respective theories used for each of the next chapters; the descriptions of material properties as the main objects of study, including laminated composite plates, piezoelectric laminated composite plates, functionally graded (FG) porous plates reinforced by graphene platelets embedded in piezoelectric layers and functionally graded piezoelectric material porous plates.

3.2 An overview of plate theories

There are various plate theories to analyze the behavior of laminated composite plates [13]. A three-dimensional (3D) elasticity theory has been initially proposed to forecast the exact result of uncomplicated static problems and adjust the correctness of transverse shear stresses [99-101]. However, the computational cost is much higher. For thin structures, the control of the computational cost can become a thoughtful issue. Additionally, the 3D elasticity theory cannot find a solution for practical problems with complex or even slightly complicated geometry and different boundary conditions. Therefore, many equivalent single layer (ESL) plate theories have been then proposed to overcome these disadvantages. By the ESL plate theories, the 3D problems will be transformed into a quasi-2D problem by considering the kinematics of stresses or deformation states through the thickness of the plates. Note that all computations are performed in the reference plane or mid-plane. This thesis uses ESL plate theories to calculate and simulate the behavior of laminated composite plate because of their intrinsic simplicity and small computational cost. In the ESL model, there are many plate theories developed to analyze laminated composite plates. It can be listed that the classical plate theory (CPT), the first-order shear deformation theory (FSDT) and the higher-order shear deformation theories (HSDTs).

3.2.1 The higher-order shear deformation theory

3.2.1.1 The third-order shear deformation theory

To dodge the requirement of a shear correct factor (SCF) and ensure smooth distribution of shear stress, the higher-order shear deformation theories (HSDTs) which use higher-order terms in Taylor's series expansion of the displacement fields in the thickness direction have been developed [108-114]. The third-order shear deformation theory (TSDT) proposed by Reddy [112] is the best common. It has been widely used by the researchers for plates and shells which their thickness expands from thin to thick. In TSDT, the shear stresses satisfy parabolic distributions through the plate thickness that's why SCF is no longer required. An illustration of undeformed and deformed configurations of transverse normal using CLPT, FSDT and TSDT is given in Figure 3. 1.

The displacement field can be expressed as follows

$$\begin{aligned} u(x,y,z,t) &= u_0(x,y,t) + z\beta_x(x,y,t) + z^3\left(-\frac{4}{3h^2}\right)\left(\beta_x + \frac{\partial w_0}{\partial x}\right) \\ v(x,y,z,t) &= v_0(x,y,t) + z\beta_y(x,y,t) + z^3\left(-\frac{4}{3h^2}\right)\left(\beta_y + \frac{\partial w_0}{\partial y}\right); \\ w(x,y,z,t) &= w_0(x,y,t) \end{aligned} \tag{3. 1}$$

The TSDT satisfies the disappearing of transverse shear stresses in the top and bottom surfaces of plates and provides more accurate inter-laminar stress distributions than FSDT.

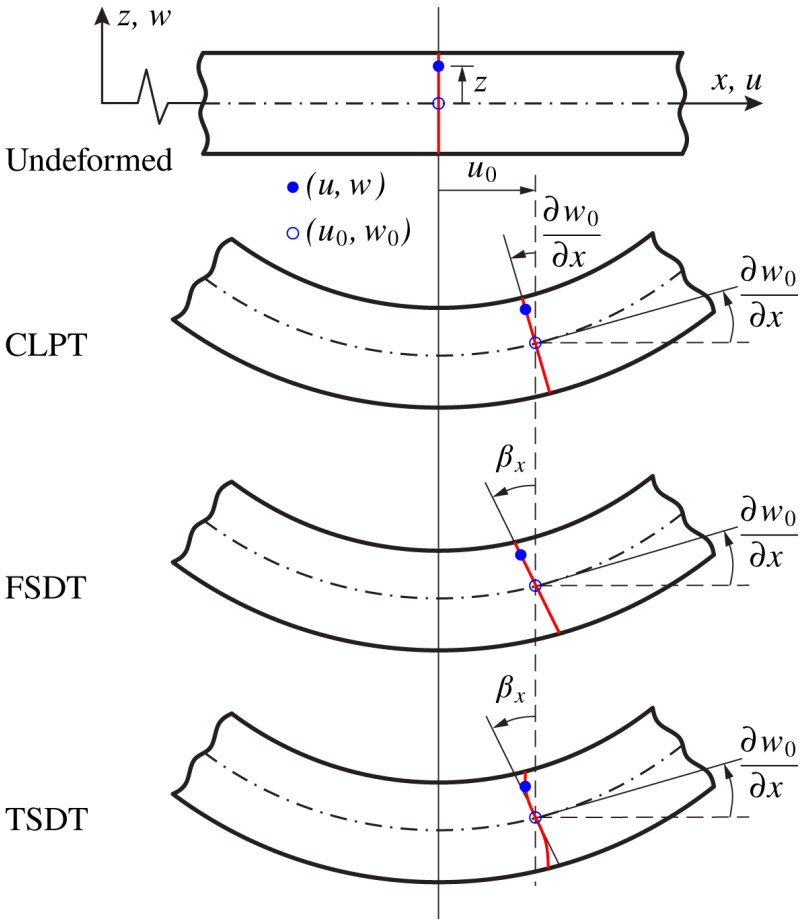

Figure 3. 1. Deformation of transverse normal using CLPT, FSDT and TSDT [13].

3.2.1.2 The generalized higher-order shear deformation theory

There are many higher-order shear deformation theories devised to analyze and simulate the behavior of laminated composite plates. Most common is the higher-order shear deformation theory by the authors in Refs. [18-19, 115-117]; it is derived from the classical plate theory as the following:

$$\begin{aligned} u(x,y,z,t) &= u_0(x,y,t) - z\frac{\partial w_0}{\partial x} + f(z)\beta_x(x,y,t) \\ v(x,y,z,t) &= v_0(x,y,t) - z\frac{\partial w_0}{\partial y} + f(z)\beta_y(x,y,t); \\ w(x,y,z,t) &= w_0(x,y,t) \end{aligned} \tag{3. 2}$$

where *f(z)* is a shape function which determines the distribution of the transverse shear strains and stresses across the thickness of the plates and it is chosen so that the

shear stress-free surface conditions on the top and bottom surfaces of the plate are satisfied. It means that $f'(z)=0$ at $z=\pm h/2$. Under this condition, various distributed functions $f(z)$ have been found and are shown in Table 3. 1. The present theory can be easily extended to other theories in Table 3. 1. This expansion is simply the way to choose the corresponding distribution function *f(z)* along the plate thickness.

Table 3. 1: The various forms of shape function.

Model	$f(z)$	$g(z)=f'(z)$
Reddy [13]	$z-\frac{4z^3}{3h^2}$	$1-4z^2/h^2$
Karama [116]	$ze^{-2(z/h)^2}$	$(1-\frac{4}{h^2}z^2)e^{-2(z/h)^2}$
Arya [115]	$\sin\left(\frac{\pi}{h}z\right)$	$\frac{\pi}{h}\cos(\frac{\pi}{h}z)$
Touratier [117]	$\frac{h}{\pi}\sin(\pi z/h)$	$\cos(\frac{\pi}{h}z)$
Chien [18]	$h\text{artan}(\frac{2z}{h})-z$	$\frac{2}{1+\left(2z/h\right)^2}-1$
Nguyen-Xuan [19]	$\frac{7}{8}z-\frac{2}{h^2}z^3+\frac{2}{h^4}z^5$	$\frac{7}{8}-\frac{6}{h^2}z^2+\frac{10}{h^4}z^4$

Furthermore, Figure 3. 2 shows the shapes of function *f*(*z*) and its derivation $f'(z)$ versus the thickness of the plates, respectively. It can be seen that they fulfill the free stress conditions on the top and bottom of the plates.

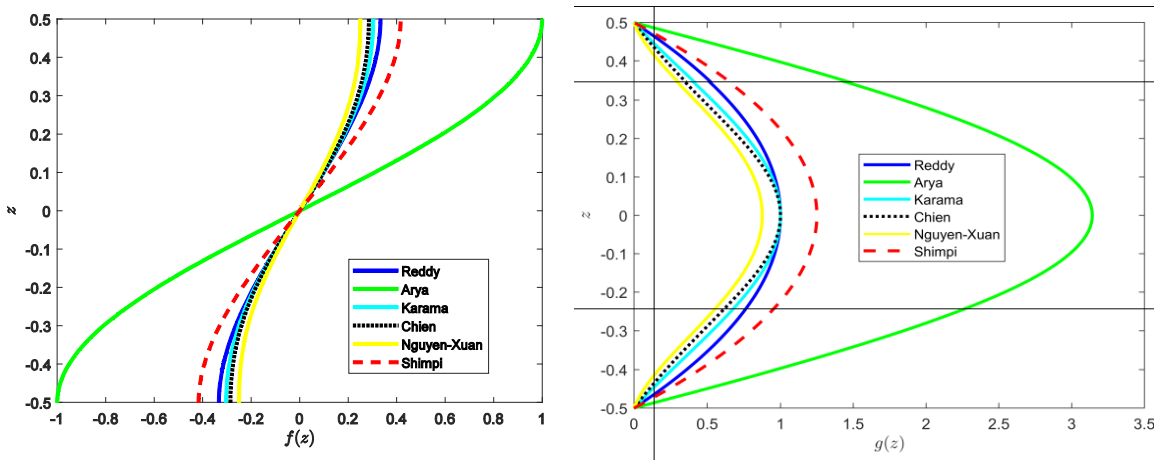

Figure 3. 2. Distribution function $f(z)$ and its derivation $g(z)$ versus the thickness of the plates.

In Eq. (3. 2), if distribution function *f(z)* is equal to zero, the higher-order shear deformation theory will take the form of classical plate theory (see in Eq.(3. 3)).

$$\begin{aligned} u(x,y,z) &= u_0(x,y) - z\frac{\partial w}{\partial x} \\ v(x,y,z) &= v_0(x,y) - z\frac{\partial w}{\partial y}\ ; \left(\frac{-h}{2} \le z \le \frac{h}{2}\right) \\ w(x,y,z) &= w(x,y) \end{aligned} \tag{3. 3}$$

By defining $f(z) = z$ and substituting $\phi_x = -w_{,x} + \beta_x$ for Eq. (3. 4), the first-order shear deformation theory (FSDT) is obtained as

$$\begin{aligned} u(x,y,z) &= u_0(x,y) + z\phi_x \\ v(x,y,z) &= v_0(x,y) + z\phi_y\ ; \\ w(x,y,z) &= w(x,y) \end{aligned} \quad \left(\frac{-h}{2} \le z \le \frac{h}{2}\right) \tag{3. 4}$$

3.2.2 The generalized unconstrained higher-order shear deformation theory (UHSDT)

It can be seen that TSDT contains a cubic-variation of in-plane displacements constrained by the transverse displacement and the rotations. Furthermore, the TSDT assumes that transverse shear stresses vanish on the top and bottom of the plate, which is not entirely accurate. While attempting to solve the problem of shear traction parallel to the surface of plates, Leung [120] proposed an unconstrained third-order shear deformation theory (UTSDT). Additionally, UTSDT is also feasible for

problems involving contact friction or a flow field. Different from the traction-free boundary condition on the top and bottom plate surfaces presented in TSDT of Reddy, this theory allows a finite transverse shear strain on the lower and upper surface of the plate. Although the governing differential equations of UTSDT have a complexity similar to those of TSDT, UTSDT's solutions are more accurate than the TSDT ones compared with the 3D exact solution. The unconstrained third-order shear deformation theory includes seven displacement components, i.e. six in-plane displacements and one transverse displacement.

This thesis contributes an arbitrary novel unconstrained higher-order shear deformation theory (UHSDT) which is used for calculations in chapter 4. Although UHSDT also adopts seven displacement components similar to those of UTSDT, higher-order rotations depend on an arbitrary function $f(z)$ through the plate thickness. In UTSDT [118], the third-order function ($f(z) = z^3$) is used. It can be seen that the profile of the shear stresses through the plate thickness depends on various features such as the number of layers, layer thickness and material properties. Hence, an arbitrary unconstrained higher-order shear deformation theory (UHSDT) is generalized such that it reflects well nonlinear behavior through the plate thickness and can provide better solutions than UTSDT. This motivates us to investigate an unconstrained higher-order shear deformation theory (UHSDT).

The unconstrained theory based on HSDT can be rewritten in a general form using an arbitrary function $f(z)$ as follows:

$$\begin{aligned} u(x,y,z,t) &= u_0(x,y,t) + zu_1(x,y,t) + f(z)u_2(x,y,t) \\ v(x,y,z,t) &= v_0(x,y,t) + zv_1(x,y,t) + f(z)v_2(x,y,t) \\ w(x,y,z,t) &= w(x,y,t) \end{aligned} ; \qquad (3.5)$$

where $u_0(x,y,t), v_0(x,y,t), u_1(x,y,t), v_1(x,y,t), u_2(x,y,t), v_2(x,y,t)$ and $w(x,y,t)$ are seven displacement variables which must be determined. Accordingly, two newly proposed shape functions and shape functions of UTSDT are introduced, where $f(z)$ is the distributed function through the plate thickness. They reflect well nonlinear behavior through the plate thickness and can provide better

solutions than UTSDT. General speaking, $f(z)$ can be defined as a continuous function such that its first derivative is nonlinear through the plate thickness. Moreover, there exists an optimal function $f_{op}(z)$ yielding best accurate solutions. However, the finding of $f_{op}(z)$ remains an open question. Inwhat follows, two functions $f(z)$ are illustrated as shown in Table 3. 2.

Table 3. 2: Three used forms of distributed functions and their derivatives

Model	$f(z)$	$f'(z)$
Leung [120]	z^3	$3z^2$
Model 1	$\arctan(z)$	$\frac{1}{1+z^2}$
Model 2	$\sin(z)$	$\cos(z)$

3.2.3 The C^0-type higher-order shear deformation theory (C^0-type HSDT)

The above-mentioned theories require C^0-continuity and C^1-continuity of the approximate field or the generalized displacement field. The HSDT and the CPT bear the relationship to derivation transverse displacement also called slope components. In some numerical methods, it is often difficult to enforce boundary conditions for slope components due to the unification of the approximation variables. Therefore, a C^0-type HSDT is rather recommended [119-120].

In this thesis, the authors promote a C^0-type HSDT for PFGP-GPLs and FGPMP plates shown in chapters 5 and 6. This theory contributes to increase the novelty of the dissertation.

According to the generalized higher-order shear deformation theory in Eq.(3. 2), the displacement field of any points in the plate has five unknowns and can be rewritten by:

$$\mathbf{u}\left(x,y,z,t\right)=\mathbf{u}^1\left(x,y,t\right)+z\mathbf{u}^2\left(x,y,t\right)+f(z)\mathbf{u}^3\left(x,y,t\right) \tag{3. 6}$$

where

$$\mathbf{u}=\begin{Bmatrix}u\\v\\w\end{Bmatrix};\ \mathbf{u}^1=\begin{Bmatrix}u_0\\v_0\\w_0\end{Bmatrix};\ \mathbf{u}^2=-\begin{Bmatrix}w_{0,x}\\w_{0,y}\\0\end{Bmatrix};\ \mathbf{u}^3=\begin{Bmatrix}\theta_x\\\theta_y\\0\end{Bmatrix} \tag{3. 7}$$

in which u_0, v_0, w_0, θ_x and θ_y are the in-plane, transverse displacements and the rotation components in the *y-z, x-z* planes, respectively; the symbols '*,x*' and '*,y*' denote derivative of any function with respect to *x* and *y* directions, respectively.

To avoid the order of high-order derivation in approximate formulations and easily apply boundary conditions similar to the standard finite element procedure, additional assumptions are made as follows:

$$w_{0,x}=\beta_x\ ;\ w_{0,y}=\beta_y \tag{3. 8}$$

Substituting Eq. (3. 8) to Eq.(3. 7), it can be written:

$$\mathbf{u}^1=\begin{Bmatrix}u_0 & v_0 & w_0\end{Bmatrix}^T;\ \mathbf{u}^2=-\begin{Bmatrix}\beta_x & \beta_y & 0\end{Bmatrix}^T;\ \mathbf{u}^3=\begin{Bmatrix}\theta_x & \theta_y & 0\end{Bmatrix}^T \tag{3. 9}$$

From Eq. (3. 9), it can be seen that the compatible strain fields only request C^0-continuity. This theory is named as the C^0-type higher-order shear deformation theory.

Based on the C^0-type higher-order shear deformation theory, the bending and shear strains are expressed by:

$$\boldsymbol{\varepsilon}=\begin{Bmatrix}\varepsilon_{xx} & \varepsilon_{yy} & \gamma_{xy}\end{Bmatrix}^{\mathrm{T}}=\boldsymbol{\varepsilon}^0+z\boldsymbol{\varepsilon}^1+f(z)\boldsymbol{\varepsilon}^2;\ \boldsymbol{\gamma}=\begin{Bmatrix}\gamma_{xz} & \gamma_{yz}\end{Bmatrix}^{\mathrm{T}}=\boldsymbol{\varepsilon}^{s0}+f'(z)\boldsymbol{\varepsilon}^{s1} \tag{3. 10}$$

where

$$\boldsymbol{\varepsilon}^0=\begin{Bmatrix}u_{0,x}\\v_{0,y}\\u_{0,y}+v_{0,x}\end{Bmatrix};\ \boldsymbol{\varepsilon}^1=-\begin{Bmatrix}\beta_{x,x}\\\beta_{y,y}\\\beta_{x,y}+\beta_{y,x}\end{Bmatrix};\ \boldsymbol{\varepsilon}^2=\begin{Bmatrix}\theta_{x,x}\\\theta_{y,y}\\\theta_{x,y}+\theta_{y,x}\end{Bmatrix}$$
$$\boldsymbol{\varepsilon}^{s0}=\begin{Bmatrix}w_{0,x}-\beta_x\\w_{0,y}-\beta_y\end{Bmatrix};\ \boldsymbol{\varepsilon}^{s1}=\begin{Bmatrix}\theta_x\\\theta_y\end{Bmatrix} \tag{3. 11}$$

in which $f'(z)$ is the derivation of the function $f(z)$ which is chosen later.

3.3 Laminated composite plate

3.3.1 Definition of laminated composite plate

A composite material or composite for short is a material which composed of two or more different materials, including a matrix material and reinforcing (fibers) materials. This combination creates a new material that has mechanical properties more excellent than individual materials including high strength to weight and stiffness to weight ratios, wear resistance, light weight and so on [13, 121].

Laminated composites are formed by two or several lamina layers with different materials assembled together to obtain anticipated mechanical characteristics [13]. Figure 3. 3 shows the process of making a laminated composite from three lamina layers with different fibers.

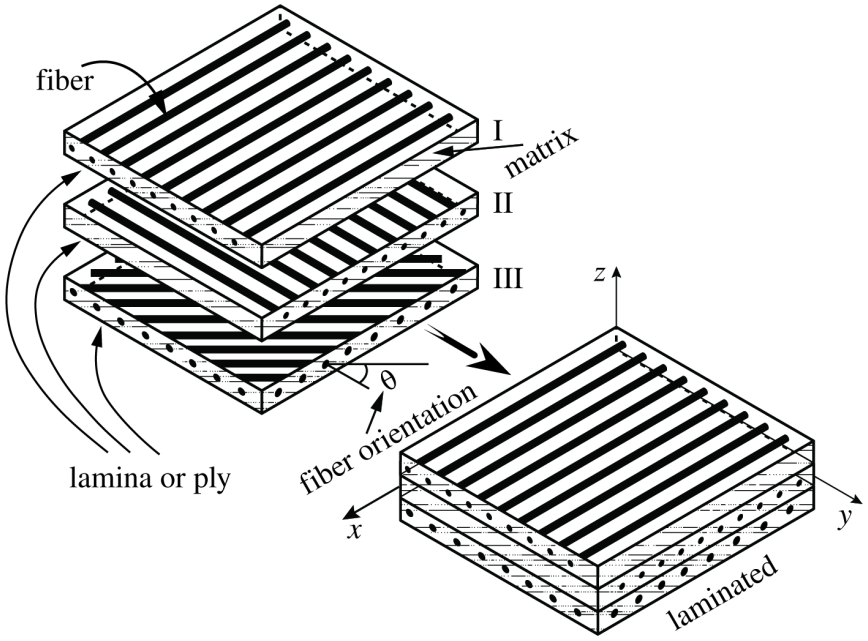

Figure 3. 3. Configuration of a lamina and laminated composite plate.

To set the basic equations of the building block of a composite laminate, there are some assumptions as:

- a lamina is a continuum; i.e., no empty spaces or holes exist.
- a lamina behaves as a linear elastic material; i.e., Hooke's law is used

3.3.2 Constitutive equations of laminated composite plate

The generalized Hooke's law for an anisotropic material is expressed by:

$$\sigma_i = Q_{ij}\varepsilon_j \tag{3. 12}$$

where σ_i are the stress components, ε_j are the strain components and Q_{ij} are the "reduced" material coefficients for 2D problem with *i*, *j* refer to the components of an orthogonal Cartesian coordinate (x_1, x_2, x_3). In general, Q_{ij} have 21 independent elastic constants. For orthotropic materials, the number of material parameters is reduced to 9 in three-dimensional cases.

Figure 3. 4 illustrates the material coordinate system (x_1, x_2, x_3), in which the material coordinate axis x_1 is taken to be parallel or coincide to the fiber, the x_2-axis transverse to the fiber direction in the plane of the lamina, and the x_3-axis is perpendicular to the plane of the lamina.

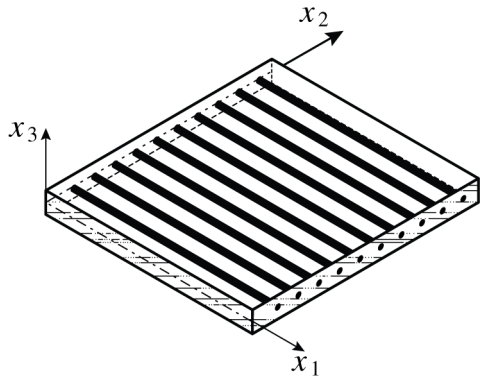

Figure 3. 4. Configuration of a lamina and laminated composite plate.

Using rule of mixture, the lamina constants are defined as follows

$$E_1 = E_f \upsilon_f + E_m \upsilon_m \quad ; \nu_{12} = \nu_f \upsilon_f + \nu_m \upsilon_m$$
$$E_2 = \frac{E_f E_m}{E_f \upsilon_m + E_m \upsilon_f} \quad ; \mathrm{G}_{12} = \frac{G_f G_m}{G_f \upsilon_m + G_m \upsilon_f} \tag{3. 13}$$

where $E_f, E_m; \nu_f, \nu_m; \upsilon_f, \upsilon_m$ and $\mathrm{G}_f, \mathrm{G}_m$ are Young's moduli, Poisson's ratios, volume fractions and the shear modulus, respectively, in which *f* and *m* refer to fiber and matrix of laminated composites, respectively. Besides, $\mathrm{G}_f, \mathrm{G}_m$ are calculated by:

$$G_f = \frac{E_f}{2(1+\nu_f)} \quad ; G_m = \frac{E_m}{2(1+\nu_m)} \tag{3. 14}$$

By neglecting σ_z for each orthotropic layer, the constitutive equation of k^{th} layer in the local coordinate system derived from Hooke's law for a plane stress is given by

$$\begin{Bmatrix} \sigma_1^k \\ \sigma_2^k \\ \tau_{12}^k \\ \tau_{13}^k \\ \tau_{23}^k \end{Bmatrix} = \begin{bmatrix} Q_{11} & Q_{12} & Q_{16} & 0 & 0 \\ Q_{12} & Q_{22} & Q_{26} & 0 & 0 \\ Q_{61} & Q_{62} & Q_{66} & 0 & 0 \\ 0 & 0 & 0 & Q_{55} & Q_{54} \\ 0 & 0 & 0 & Q_{45} & Q_{44} \end{bmatrix}^k \begin{Bmatrix} \varepsilon_1^k \\ \varepsilon_2^k \\ \gamma_{12}^k \\ \gamma_{13}^k \\ \gamma_{23}^k \end{Bmatrix} \tag{3. 15}$$

in which reduced stiffness components, Q_{ij}^k , are expressed by

$$\begin{aligned} &\mathrm{Q}_{11}^k = \frac{E_1^k}{1-\nu_{12}^k \nu_{21}^k};\ \mathrm{Q}_{12}^k = \frac{\nu_{12}^k E_2^k}{1-\nu_{12}^k \nu_{21}^k};\ \mathrm{Q}_{22}^k = \frac{E_2^k}{1-\nu_{12}^k \nu_{21}^k};\ \mathrm{Q}_{66}^k = G_{12}^k; \\ &\mathrm{Q}_{55}^k = G_{13}^k;\ \mathrm{Q}_{44}^k = G_{23}^k \end{aligned} \tag{3. 16}$$

The stress - strain relationship in the global reference system (*x,y,z*) is computed by

$$\begin{Bmatrix} \sigma_{xx}^k \\ \sigma_{yy}^k \\ \tau_{xy}^k \\ \tau_{xz}^k \\ \tau_{yz}^k \end{Bmatrix} = \begin{bmatrix} \bar{Q}_{11} & \bar{Q}_{12} & \bar{Q}_{16} & 0 & 0 \\ \bar{Q}_{12} & \bar{Q}_{22} & \bar{Q}_{26} & 0 & 0 \\ \bar{Q}_{61} & \bar{Q}_{62} & \bar{Q}_{66} & 0 & 0 \\ 0 & 0 & 0 & \bar{Q}_{55} & \bar{Q}_{54} \\ 0 & 0 & 0 & \bar{Q}_{45} & \bar{Q}_{44} \end{bmatrix}^k \begin{Bmatrix} \varepsilon_{xx}^k \\ \varepsilon_{yy}^k \\ \gamma_{xy}^k \\ \gamma_{xz}^k \\ \gamma_{yz}^k \end{Bmatrix} \tag{3. 17}$$

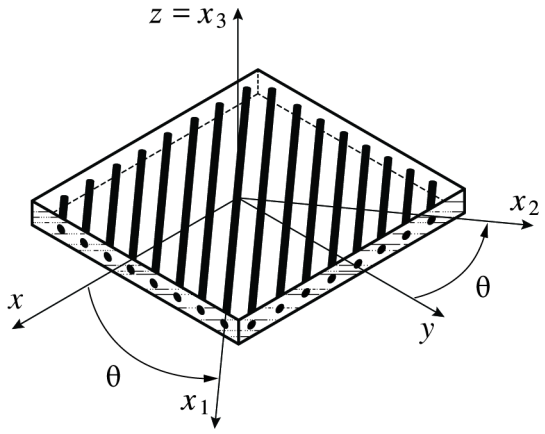

Figure 3. 5. Material and global coordinates of the composite plate.

where $\bar{Q}_{ij}^k$ is the transformed material constant matrix and is written in detail as:

$$
\begin{aligned}
\bar{Q}_{11} &= Q_{11}\cos^4\theta + 2\left(Q_{12}+2Q_{66}\right)\sin^2\theta\cos^2\theta \\
\bar{Q}_{12} &= \left(Q_{11}+Q_{22}-4Q_{66}\right)\sin^2\theta\cos^2\theta + Q_{12}\left(\sin^4\theta+\cos^4\theta\right) \\
\bar{Q}_{22} &= Q_{11}\sin^4\theta + 2\left(Q_{12}+2Q_{66}\right)\sin^2\theta\cos^2\theta + Q_{22}\cos^4\theta \\
\bar{Q}_{16} &= \left(Q_{11}-Q_{22}-2Q_{66}\right)\sin\theta\cos^3\theta + \left(Q_{12}-Q_{22}+2Q_{66}\right)\cos\theta\sin^3\theta \\
\bar{Q}_{26} &= \left(Q_{11}-Q_{22}-2Q_{66}\right)\sin^3\theta\cos\theta + \left(Q_{12}-Q_{22}+2Q_{66}\right)\cos^3\theta\sin\theta \qquad (3.\ 18) \\
\bar{Q}_{26} &= \left(Q_{11}+Q_{22}-2Q_{12}-2Q_{66}\right)\sin^2\theta\cos^2\theta + Q_{66}\left(\sin^4\theta+\cos^4\theta\right) \\
\bar{Q}_{44} &= Q_{44}\cos^2\theta + Q_{55}\sin^2\theta \\
\bar{Q}_{45} &= \left(Q_{55}-Q_{44}\right)\sin\theta\cos\theta \\
\bar{Q}_{55} &= Q_{55}\cos^2\theta + Q_{44}\sin^2\theta
\end{aligned}
$$

Local and global coordinates of the laminated composite is shown in Figure 3. 5.

3.4 Piezoelectric material

3.4.1 Introduce to piezoelectric material

The best-known smart materials are certainly the piezoelectric materials. The growth of intelligent structures combined with sensors and actuators presents a considerable interest in many engineering applications: structural health monitoring, motorized sensors, actuators, vibration and noise suppression, shape control and precision positioning, etc. The piezoelectric effects can be seen as transmissions between electrical and mechanical energy. Such transfers can only occur if the material is comprised of charged particles and can be polarized. When an electric field is applied to piezoelectric structures, the mechanical deformation is produced. And it is known as the converse phenomenon of piezoelectric effect [122-123].

The best popular piezoceramic is the Lead Zirconate Titanate (PZT). It has a recoverable strain of 0.1% and is broadly used as actuator and sensor for a wide range of frequencies, including ultrasonic applications. It is well matched for high accuracy too. Piezopolymers are mainly used as sensors. The next best-known is the Polyvinylidene Fluoride (PVDF). The PVDF was first considered by Kawai (at the end of the ‘60s) and was created commercially available in the early ‘80s. The finding of piezoelectric material has great importance in the European scientific council. After 30 years, this material began to be strongly studied. The main application of

piezoelectric materials was the sea-level transducer by ultrasound waves, which was advanced by Paul Langevin and co-workers in France. And after that, this is extended through many other applications including ultrasonic transducers for sonar and medical purposes, compact piezoelectric motors, structural monitoring or active damping elements, and even ignition systems.

3.4.2 The basic equation of piezoelectric material

This section will introduce the electro-mechanical equations of piezoelectric materials. These equations are based on the IEEE standards (Institute of Electrical and Electronics Engineers Standards) about piezoelectric materials. The equations are widely used to describe the properties of piezoelectric materials. The IEEE standards assume that the piezoelectric material is linear [124]. In this dissertation, the mechanical stress and the electric field are linear.

The linear piezoelectric constitutive equations can be expressed as follow [125-126]

$$\begin{bmatrix} \boldsymbol{\sigma} \\ \mathbf{D} \end{bmatrix} = \begin{bmatrix} \mathbf{c} & -\mathbf{e}^T \\ \mathbf{e} & \mathbf{g} \end{bmatrix} \begin{bmatrix} \bar{\boldsymbol{\varepsilon}} \\ \mathbf{E} \end{bmatrix} \tag{3. 19}$$

where $\bar{\boldsymbol{\varepsilon}}$ and $\boldsymbol{\sigma}$ are the strain vector and the stress vector, respectively; $\mathbf{c}$ denotes the elastic constant matrix. The electric field vector **E**, can be defined as

$$\mathbf{E} = -\text{grad}\phi = -\nabla\phi \tag{3. 20}$$

Note that, for the type of piezoelectric materials considered in this work the stress piezoelectric constant matrices **e,** the strain piezoelectric constant matrices **d** and the dielectric constant matrices **g** can be written as follows [41]

$$\mathbf{e} = \begin{bmatrix} 0 & 0 & 0 & 0 & e_{15} \\ 0 & 0 & 0 & e_{15} & 0 \\ e_{31} & e_{32} & e_{33} & 0 & 0 \end{bmatrix}; \mathbf{d} = \begin{bmatrix} 0 & 0 & 0 & 0 & d_{15} \\ 0 & 0 & 0 & d_{15} & 0 \\ d_{31} & d_{32} & d_{33} & 0 & 0 \end{bmatrix}; \quad \mathbf{g} = \begin{bmatrix} p_{11} & 0 & 0 \\ 0 & p_{22} & 0 \\ 0 & 0 & p_{33} \end{bmatrix} \tag{3. 21}$$

3.5 Piezoelectric functionally graded porous plates reinforced by graphene platelets (PFGP-GPLs)

In this study, a plate model like as a sandwich plate with length a, width b and total thickness of $h = h_c + 2h_p$ in which h_c and h_p are the thicknesses of the porous layer which is called core and the piezoelectric face layers, respectively, is shown in Figure 3. 6

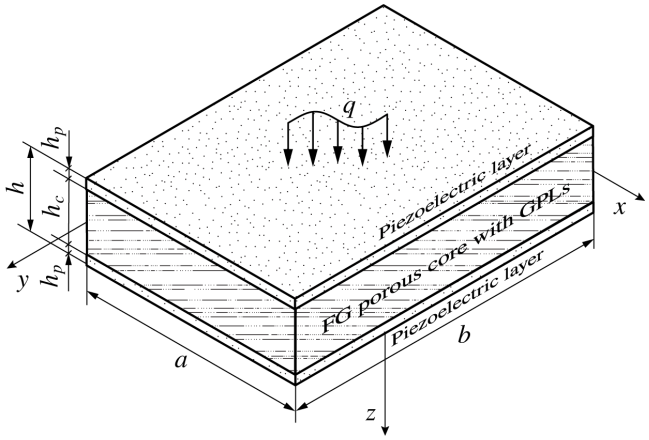

Figure 3. 6. Configuration of a piezoelectric FG porous plate reinforced by GPLs.

Three different porosity distribution types along the thickness direction of plates including two types of non-uniformly symmetric and a uniform are illustrated in Figure 3. 7. In addition, three GPL dispersion patterns shown in Figure 3. 8 are investigated for each porosity distribution. In each pattern, the GPL volume fraction V_{GPL} is assumed to vary smoothly along the thickness direction. As can be seen in Figure 3. 8, E_1' and E_2' denote the maximum and minimum Young's moduli of the non-uniformly distributed porous material without GPLs, respectively, while E' is Young's modulus of uniform porosity distribution.

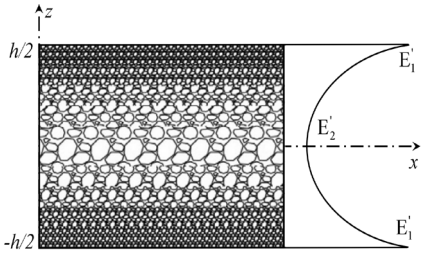

(a) Non-uniform porosity distribution 1

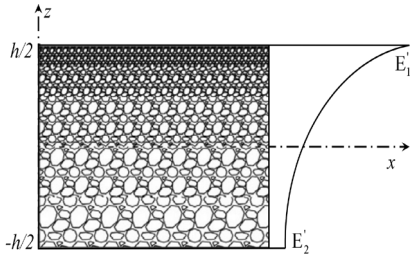

(b) Non-uniform porosity distribution 2

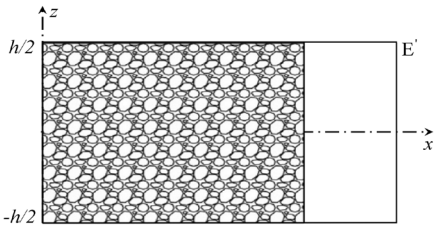

(c) Uniform porosity distribution

Figure 3. 7. Porosity distribution types [127]

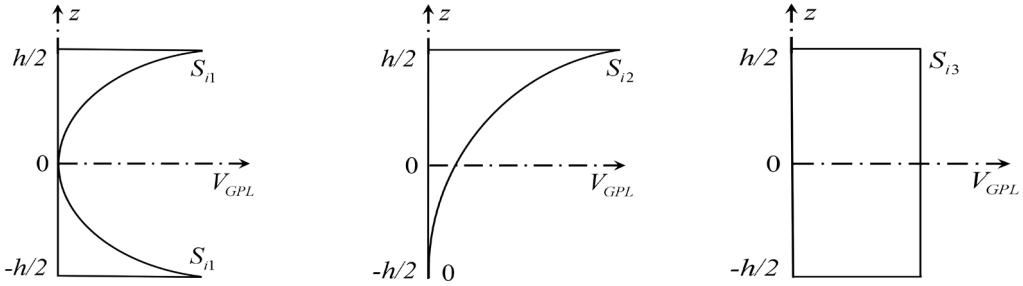

(a) Pattern A (b) Pattern B (c) Pattern C

Figure 3. 8. Three dispersion patterns A, B and C of the GPLs for each porosity distribution type [127].

The material properties including Young's moduli $E(z)$, shear modulus $G(z)$ and mass density $\rho(z)$ which alter along the thickness direction for different porosity distribution types can be expressed as

$$\begin{cases} E(z) = E_1\left[1 - e_0\lambda(z)\right], \\ G(z) = E(z)/\left[2(1+v(z))\right], \\ \rho(z) = \rho_1\left[1 - e_m\lambda(z)\right], \end{cases} \tag{3. 22}$$

where

$$\lambda(z)=\begin{cases}\cos(\pi z/h_c), & \text{Non-uniform porosity distribution 1}\\ \cos(\pi z/2h_c+\pi/4), & \text{Non-uniform porosity distribution 2}\\ \lambda, & \text{Uniform porosity distribution}\end{cases} \tag{3.23}$$

in which $E_1 = E_1'$ and $E_1 = E'$ for types of non-uniformly and uniform porosity distribution, respectively. ρ_1 denotes the maximum value of mass density of the porous core. The coefficient of porosity e_0 can be determined by

$$e_0 = 1 - E_2^{'} / E_1^{'} \tag{3.24}$$

Through Gaussian Random Field (GRF) scheme [40], the mechanical characteristic of closed- cell cellular solids is given as

$$\frac{E(z)}{E_1} = \left(\frac{\rho(z)/\rho_1 + 0.121}{1.121}\right)^{2.3} for\left(0.15 < \frac{\rho(z)}{\rho_1} < 1\right) \tag{3.25}$$

Then, the coefficient of mass density e_m in Eq. (3. 22) is possibly stated as

$$e_m = \frac{1.121\left(1 - \sqrt[2.3]{1 - e_0\lambda(z)}\right)}{\lambda(z)} \tag{3.26}$$

Also according to the closed-cell GRF scheme [128], Poisson's ratio $\nu(z)$ is derived as

$$v(z) = 0.221p^{'} + v_1(0.342p^{'2} - 1.21p^{'} + 1), \tag{3.27}$$

in which ν_1 represents the Poisson's ratio of the metal matrix without internal pores and p' is given as

$$p^{'} = 1.121\left(1 - \sqrt[2.3]{1 - e_0\lambda(z)}\right) \tag{3.28}$$

It should be noted that to obtain a meaningful and fair comparison, the mass per unit of surface M of the FG porous plates with different porosity distributions is set to be equivalent and can be calculated by

$$M = \int_{-h_c/2}^{h_c/2} \rho(z)dz \tag{3.29}$$

Then, the coefficient λ in Eq. (3. 23) for uniform porosity distribution can be defined as

$$\lambda = \frac{1}{e_0} - \frac{1}{e_0}\left(\frac{M/\rho_1 h + 0.121}{0.121}\right)^{2.3} \tag{3.30}$$

The volume fraction of GPLs alters along the thickness of the plate for three dispersion patterns depicted in Figure 3. 8 can be given as

$$V_{GPL} = \begin{cases} S_{i1}\left[1-\cos(\pi z/h_c)\right], & \text{Pattern A} \\ S_{i2}\left[1-\cos(\pi z/2h_c + \pi/4)\right], & \text{Pattern B} \\ S_{i3}, & \text{Pattern C} \end{cases} \tag{3.31}$$

where S_{i1}, S_{i2} and S_{i3} are the maximum values of GPL volume fraction and $i = 1,2,3$ corresponds to two non-uniform porosity distributions 1, 2 and the uniform distribution, respectively.

The relationship between the volume fraction V_{GPL} and weight fractions Λ_{GPL} is given by

$$\frac{\Lambda_{GPL}\rho_m}{\Lambda_{GPL}\rho_m + \rho_{GPL} - \Lambda_{GPL}\rho_{GPL}} \int_{-h_c/2}^{h_c/2} \left[1 - e_m\lambda(z)\right] dz = \int_{-h_c/2}^{h_c/2} V_{GPL}\left[1 - e_m\lambda(z)\right] dz. \tag{3.32}$$

By the Halpin-Tsai micromechanical model [129-131], Young's modulus E_1 is determined as

$$E_1 = \frac{3}{8}\left(\frac{1+\zeta_L\eta_L V_{GPL}}{1-\eta_L V_{GPL}}\right)E_m + \frac{5}{8}\left(\frac{1+\zeta_w\eta_w V_{GPL}}{1-\eta_w V_{GPL}}\right)E_m, \tag{3.33}$$

in which

$$\zeta_L = \frac{2l_{GPL}}{t_{GPL}}, \quad \zeta_w = \frac{2w_{GPL}}{t_{GPL}}, \quad \eta_L = \frac{(E_{GPL}/E_m) - 1}{(E_{GPL}/E_m) + \zeta_L}, \tag{3.34}$$

$$\eta_w = \frac{(E_{GPL}/E_m) - 1}{(E_{GPL}/E_m) + \zeta_w},$$

where w_{GPL}, l_{GPL} and t_{GPL} denote the average width, length and thickness of GPLs, respectively; E_{GPL} and E_m are Young's moduli of GPLs and metal matrix, respectively. Then, the mass density ρ_1 can be determined and Poison's ratio ν_1 of the GPLs reinforced for porous metal matrix according to the rule of mixture is written as

$$\rho_1 = \rho_{GPL} V_{GPL} + \rho_m V_m, \tag{3. 35}$$

$$\nu_1 = \nu_{GPL} V_{GPL} + \nu_m V_m \tag{3. 36}$$

where ρ_{GPL}, ν_{GPL} and V_{GPL} are the mass density, Poisson's ratio and volume fraction of GPLs, respectively; while ρ_m, ν_m and $V_m = 1 - V_{GPL}$ represent the mass density, Poisson's ratio and volume fraction of metal matrix, respectively.

3.6 Functionally graded piezoelectric material porous plates (FGPMP)

Consider a FGPMP plate with the length *a*, the width *b* and the thickness *h*. The plate is made of a mixture of two different materials PZT-4 and PZT-5H materials subjected to an electric potential $\Phi(x,y,z,t)$ as shown in Figure 3.9, in which the fully material 1 and material 2 surfaces are distributed at the top ($z = h/2$) and bottom $(z = -h/2)$ plates, respectively. Two types of FG piezoelectric porous plates consisting of FGPMP-I and FGPMP-II are considered in this study. For a type of even distribution, FGPMP-I, the effective material properties of piezoelectric porous plates through the thickness direction are computed by a modified power-law model [82-83]:

$$\begin{aligned}
&c_{ij}(z) = \left(c_{ij}^u - c_{ij}^l\right)\left(\frac{z}{h} + \frac{1}{2}\right)^g + c_{ij}^l - \frac{\alpha}{2}\left(c_{ij}^u + c_{ij}^l\right); \\
&(i,j) = \{(1,1),(1,2),(1,3),(3,3),(5,5),(6,6)\} \\
&e_{ij}(z) = \left(e_{ij}^u - e_{ij}^l\right)\left(\frac{z}{h} + \frac{1}{2}\right)^g + e_{ij}^l - \frac{\alpha}{2}\left(e_{ij}^u + e_{ij}^l\right);\ (i,j) = \{(3,1),(3,3),(3,5)\} \\
&k_{ij}(z) = \left(k_{ij}^u - k_{ij}^l\right)\left(\frac{z}{h} + \frac{1}{2}\right)^g + k_{ij}^l - \frac{\alpha}{2}\left(k_{ij}^u + k_{ij}^l\right);\ \ (i,j) = \{(1,1),(3,3)\} \\
&\rho(z) = \left(\rho^u - \rho^l\right)\left(\frac{z}{h} + \frac{1}{2}\right)^g + \rho^l - \frac{\alpha}{2}\left(\rho^u + \rho^l\right)
\end{aligned} \tag{3.37}$$

where c_{ij}, e_{ij} and k_{ij} are defined as above, *g* is the power index that represents the material distribution across the plate thickness, ρ is the material density; the symbols

u and l denote the material properties of the upper (material 1) and lower surfaces (material 2), respectively, and α is the porosity volume fraction.

Type of uneven distribution, FGPMP-II, the porosities are concentrated around the cross-section middle-surface and the amount of porosity discharges at the top and bottom of the cross-section. In this case, the effective material properties are computed by:

$$
\begin{aligned}
&c_{ij}(z)=\left(c_{ij}^{u}-c_{ij}^{l}\right)\left(\frac{z}{h}+\frac{1}{2}\right)^{g}+c_{ij}^{l}-\frac{\alpha}{2}\left(c_{ij}^{u}+c_{ij}^{l}\right)\left(1-\frac{2|z|}{h}\right)\ ;\\
&(i,j)=\{(1,1),(1,2),(1,3),(3,3),(5,5),(6,6)\}\\
&e_{ij}(z)=\left(e_{ij}^{u}-e_{ij}^{l}\right)\left(\frac{z}{h}+\frac{1}{2}\right)^{g}+e_{ij}^{l}-\frac{\alpha}{2}\left(e_{ij}^{u}+e_{ij}^{l}\right)\left(1-\frac{2|z|}{h}\right);\ (i,j)=\{(3,1),(3,3),(3,5)\}\\
&k_{ij}(z)=\left(k_{ij}^{u}-k_{ij}^{l}\right)\left(\frac{z}{h}+\frac{1}{2}\right)^{g}+k_{ij}^{l}-\frac{\alpha}{2}\left(k_{ij}^{u}+k_{ij}^{l}\right)\left(1-\frac{2|z|}{h}\right);(i,j)=\{(1,1),(3,3)\}\\
&\rho(z)=\left(\rho^{u}-\rho^{l}\right)\left(\frac{z}{h}+\frac{1}{2}\right)^{g}+\rho^{l}-\frac{\alpha}{2}\left(\rho^{u}+\rho^{l}\right)\left(1-\frac{2|z|}{h}\right)
\end{aligned}
\qquad (3.\ 38)
$$

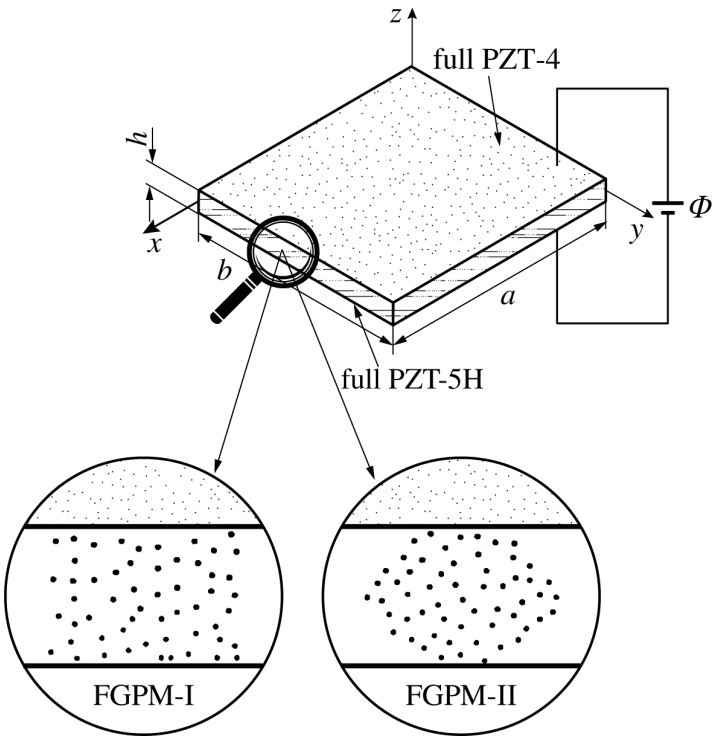

Figure 3.9. Geometry and cross sections of a FGPMP plate made of PZT-4/PZT-5H.

In order to show the influence of porosity volume fraction on material properties, the variation of elastic coefficient c_{11} of porous FGPM plate made of PZT-4/PZT-5H versus the thickness is studied with various power index values as depicted in Figure 3.10. It can be seen that the elastic coefficient of perfect FGPM, $\alpha = 0$, is continuous through the top surface (PZT-4 rich) to the bottom surface (PZT-5H rich) as shown in Figure 3.10a. As $g = 0$, the elastic coefficient is constant through the plate thickness. The profiles of c_{11} are also plotted in Figure 3.10b and Figure 3.10c for porous FGPMP-I and FGPMP-II, respectively. As seen, there has the same profile for the perfect FGPM and FGPMP-I type with porosities. However, the magnitude of the elastic coefficient of porous FGPMP-I is lower than that of perfect FGPM. Therefore, the stiffness of the FGPMP is decreased with the presence of the porous parameter. Moreover, when the porosities are distributed around the cross section mid-zone and the amount of porosity diminishes on the top and bottom of the cross-section, FGPMP-II type, the elastic coefficient is maximum on the bottom and top surface and decreases towards middle zone direction as indicated in Figure 3.10c. Figure 3.10d displays the influence of porosities on the elastic coefficient. It is found that the elastic coefficient's amplitude of FGPMP-II plate is equal to that of perfect FGPM on the bottom and top surface, and equal to that of FGPMP-I plate at the mid-surface.

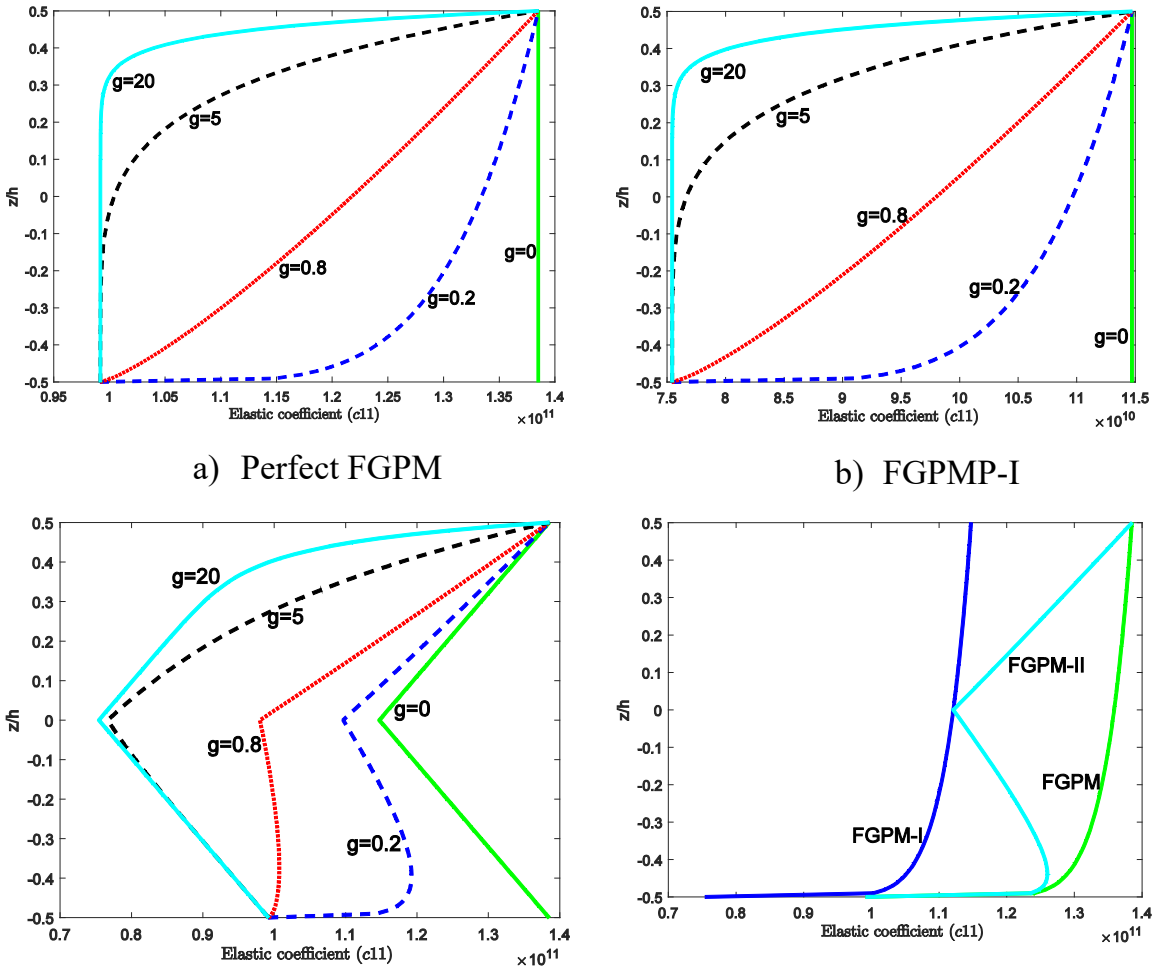

a) Perfect FGPM

b) FGPMP-I

c) FGPMP-II

d) FGPMP, g=0.1

Figure 3.10. Variation of elastic coefficient c_{11} of FGPMP plate made of PZT-4/PZT-5H with $\alpha = 0.2$.

3.7 Concluding remarks

In this chapter, an overview of plate theories used in all the next chapters are given. In addition, the fundamentals of several materials are provided such as laminated composite plates, piezoelectric laminated composite plates, piezoelectric functionally graded porous plates reinforced by graphene platelets and functionally graded piezoelectric material porous plates.

Chapter 4
ANALYZE AND CONTROL THE LINEAR RESPONSES OF THE PIEZOELECTRIC LAMINATED COMPOSITE PLATES

4.1 Overview

In this chapter, an isogeometric finite element formulation based on Bézier extraction for the non-uniform rational B-splines (NURBS) in combination with a generalized unconstrained higher-order shear deformation theory (UHSDT) is presented for analysis of static, free vibration and transient responses of plates. This chapter based on two papers in refs. [98, 148]. Two types of plates such as the laminated composite plates and the piezoelectric laminated composite plates are studied. In addition, for the piezoelectric laminated composite plates, the active response control of structures is also investigated. The displacement field is approximated according to the proposed model and the linear transient formulation for plates is solved by Newmark time integration. The presented method relaxes zero-shear stresses at the top and bottom surfaces of the plates and no shear correction factors are used. NURBS can be written in terms of Bernstein polynomials and the Bézier extraction operator as section 2.9. Through the thickness of each piezoelectric layer, the electric potential variation is assumed to be linear. A closed-loop system is used for active control of the piezoelectric laminated composite plates. The accuracy and reliability of the proposed method are verified by comparing its numerical predictions with those of other available numerical approaches.

4.2 Laminated composite plate formulation based on Bézier extraction for NURBS

4.2.1 The weak form for laminated composite plates

The unconstrained theory based on HSDT (UHSDT) which is presented in 3.2.2 section is used for model 1 and model 2, in which $f(z) = \arctan(z)$ and $f(z) = \sin(z)$,

respectively. Therefore, the UHSDT can be called the unconstrained inverse trigonometric shear deformation theory (UITSDT) and the unconstrained sinusoidal shear deformation theory (USSDT), respectively. By the assumption that a linear constitutive relationship is employed for the analysis of the laminated composite plate embedded in piezoelectric layers, the formulation for each field is approximated separately.

The in-plane strain vector $\boldsymbol{\varepsilon}_p$ is thus expressed by the following equation

$$\boldsymbol{\varepsilon}_p = [\varepsilon_{xx} \;\; \varepsilon_{yy} \;\; \gamma_{xy}]^T = \boldsymbol{\varepsilon}_0 + z\boldsymbol{\varepsilon}_1 + f(z)\boldsymbol{\varepsilon}_2 \tag{4. 1}$$

and the transverse shear strain vector $\boldsymbol{\gamma}$ has the following form

$$\boldsymbol{\gamma} = \begin{bmatrix} \gamma_{xz} & \gamma_{yz} \end{bmatrix}^T = \boldsymbol{\varepsilon}_0^s + f'(z)\boldsymbol{\varepsilon}_1^s \tag{4. 2}$$

where $f'(z)$ is derivative of $f(z)$ function and

$$\boldsymbol{\varepsilon}_0 = \begin{bmatrix} u_{0,x} \\ v_{0,y} \\ v_{0,x} + u_{0,y} \end{bmatrix}, \boldsymbol{\varepsilon}_1 = \begin{bmatrix} u_{1,x} \\ v_{1,y} \\ v_{1,x} + u_{1,y} \end{bmatrix}, \boldsymbol{\varepsilon}_2 = \begin{bmatrix} u_{2,x} \\ v_{2,y} \\ v_{2,x} + u_{2,y} \end{bmatrix}, \boldsymbol{\varepsilon}_0^s = \begin{bmatrix} u_1 + w_{,x} \\ v_1 + w_{,y} \end{bmatrix}, \tag{4. 3}$$

$$\boldsymbol{\varepsilon}_1^s = \begin{bmatrix} u_2 \\ v_2 \end{bmatrix}$$

A weak form of the static model for the plates under transverse loading q_0 can be written as

$$\int_\Omega \delta\boldsymbol{\varepsilon}_p^T \bar{\mathbf{D}} \boldsymbol{\varepsilon}_p \mathrm{d}\Omega + \int_\Omega \delta\boldsymbol{\gamma}^T \bar{\mathbf{D}}_s \boldsymbol{\gamma} \mathrm{d}\Omega = \int_\Omega \delta w q_0 \mathrm{d}\Omega \tag{4. 4}$$

where q_0 is the transverse loading per unit area.

From Hooke's law and the linear strains given by Eqs.(4. 1) and (4. 2), the stress is computed by

$$\boldsymbol{\sigma} = \begin{bmatrix} \boldsymbol{\sigma}_p \\ \boldsymbol{\tau} \end{bmatrix} = \underbrace{\begin{bmatrix} \bar{\mathbf{D}} & \mathbf{0} \\ \mathbf{0} & \bar{\mathbf{D}}_s \end{bmatrix}}_{\mathbf{c}} \underbrace{\begin{bmatrix} \boldsymbol{\varepsilon}_p \\ \boldsymbol{\gamma} \end{bmatrix}}_{\boldsymbol{\varepsilon}} = \mathbf{c}\boldsymbol{\varepsilon} \tag{4. 5}$$

where $\boldsymbol{\sigma}_p$ and $\boldsymbol{\tau}$ are the in-plane stress component and shear stress; $\bar{\mathbf{D}}$ and $\bar{\mathbf{D}}_s$ are material constant matrices given in the form of

$$\bar{\mathbf{D}}=\begin{bmatrix}\mathbf{A} & \mathbf{B} & \mathbf{E}\\ \mathbf{B} & \mathbf{D} & \mathbf{F}\\ \mathbf{E} & \mathbf{F} & \mathbf{H}\end{bmatrix};\bar{\mathbf{D}}_s=\begin{bmatrix}\mathbf{A}_s & \mathbf{B}_s\\ \mathbf{B}_s & \mathbf{D}_s\end{bmatrix} \tag{4. 6}$$

in which

$$\begin{gathered}(A_{ij},B_{ij},D_{ij},E_{ij},F_{ij},H_{ij})=\int_{-h/2}^{h/2}(1,z,z^2,f(z),zf(z),f^2(z))\bar{Q}_{ij}\mathrm{d}z;\\ i,j=1,2,6\\ (A_s^{ij},B_s^{ij},D_s^{ij})=\int_{-h/2}^{h/2}\left[1,f'(z),(f^{'}(z))^2\right]\bar{Q}_{ij}\mathrm{d}z;\ i,j=4,5\end{gathered} \tag{4. 7}$$

where $\bar{Q}_{ij}$ is the transformed material constant matrix (see section 3.3.2 for further details).

For forced vibration analysis of the plates, a weak form can be derived from the following undamped dynamic equilibrium equation as follows:

$$\int_\Omega \delta\boldsymbol{\varepsilon}_p^T\bar{\mathbf{D}}\boldsymbol{\varepsilon}_p\mathrm{d}\Omega+\int_\Omega \delta\boldsymbol{\gamma}^T\bar{\mathbf{D}}_s\boldsymbol{\gamma}\mathrm{d}\Omega+\int_\Omega \delta\tilde{\mathbf{u}}^T\mathbf{m}\ddot{\tilde{\mathbf{u}}}\mathrm{d}\Omega=\int_\Omega \delta wq(x,y,t)\mathrm{d}\Omega \tag{4. 8}$$

where the mass matrix **m** is calculated in a consistent form as follows

$$\mathbf{m}=\begin{bmatrix}I_1 & I_2 & I_4\\ I_2 & I_3 & I_5\\ I_4 & I_5 & I_6\end{bmatrix},(I_1,I_2,I_3,I_4,I_5,I_6)=\int_{-h/2}^{h/2}\rho\left(1,z,z^2,f(z),zf(z),f^2(z)\right)\mathrm{d}z \tag{4. 9}$$

in which ρ is the mass density,

$$\tilde{\mathbf{u}}=\begin{Bmatrix}\mathbf{u}_1\\ \mathbf{u}_2\\ \mathbf{u}_3\end{Bmatrix},\mathbf{u}_1=\begin{Bmatrix}u_0\\ v_0\\ w\end{Bmatrix};\mathbf{u}_2=\begin{Bmatrix}u_1\\ v_1\\ 0\end{Bmatrix};\mathbf{u}_3=\begin{Bmatrix}u_2\\ v_2\\ 0\end{Bmatrix} \tag{4. 10}$$

and $q(x,y,t)$ is the transverse loading per unit area which is the function depending on time and space.

It should be noted that no external forces are required in the free vibration problems, and the terms on the right-hand side of Eq.(4. 8) is thus equivalent to zero.

4.2.2 Approximated formulation based on Bézier extraction for NURBS

By using the Bézier extraction for NURBS, the displacement field **u** of the plate is approximated as follows

$$\mathbf{u}^h(\xi,\eta)=\sum_{A}^{m\times n}R_A^e(\xi,\eta)\mathbf{d}_A \tag{4. 11}$$

where $n\times m$ is the number of basis functions, $R_A^e(\xi,\eta)$ is a NURBS basis function for two-dimensional problems which is written in form of the linear combination of Bézier extraction operator and Bernstein polynomials, $\mathbf{P}_A$ is the control point A and $\mathbf{d}_A=\begin{bmatrix}u_{0A} & v_{0A} & u_{1A} & v_{1A} & u_{2A} & v_{2A} & w_A\end{bmatrix}^T$ is the vector of nodal degrees of freedom associated with control point A.

By substituting Eq. (4. 11) with Eq.(4. 1), the in-plane and shear strains can be rewritten as

$$\begin{bmatrix}\boldsymbol{\varepsilon}_p & \boldsymbol{\gamma}\end{bmatrix}^T=\sum_{A=1}^{m\times n}\begin{bmatrix}\mathbf{B}_A^m & \mathbf{B}_A^{b1} & \mathbf{B}_A^{b2} & \mathbf{B}_A^{s_1} & \mathbf{B}_A^{s_2}\end{bmatrix}^T\mathbf{q}_A \tag{4. 12}$$

in which

$$\mathbf{B}_A^m=\begin{bmatrix}R_{A,x} & 0 & 0 & 0 & 0 & 0 & 0\\ 0 & R_{A,y} & 0 & 0 & 0 & 0 & 0\\ R_{A,y} & R_{A,x} & 0 & 0 & 0 & 0 & 0\end{bmatrix},\ \mathbf{B}_A^{b1}=\begin{bmatrix}0 & 0 & R_{A,x} & 0 & 0 & 0 & 0\\ 0 & 0 & 0 & R_{A,y} & 0 & 0 & 0\\ 0 & 0 & R_{A,y} & R_{A,x} & 0 & 0 & 0\end{bmatrix}$$

$$\mathbf{B}_A^{b2}=\begin{bmatrix}0 & 0 & 0 & 0 & R_{A,x} & 0 & 0\\ 0 & 0 & 0 & 0 & 0 & R_{A,y} & 0\\ 0 & 0 & 0 & 0 & R_{A,y} & R_{A,x} & 0\end{bmatrix} \tag{4. 13}$$

$$\mathbf{B}_A^{s1}=\begin{bmatrix}0 & 0 & R_A & 0 & 0 & 0 & R_{A,x}\\ 0 & 0 & 0 & R_A & 0 & 0 & R_{A,y}\end{bmatrix},\ \mathbf{B}_A^{s2}=\begin{bmatrix}0 & 0 & 0 & 0 & R_A & 0 & 0\\ 0 & 0 & 0 & 0 & 0 & R_A & 0\end{bmatrix}$$

By substituting Eq. (4. 12) with Eq.(4. 4), the formulation of static analysis is obtained in the following form

$$\mathbf{Kd} = \mathbf{F} \tag{4. 14}$$

where the global stiffness matrix **K** is given by

$$\mathbf{K} = \int_{\Omega} \left[\begin{Bmatrix} \mathbf{B}^{m} \\ \mathbf{B}^{b1} \\ \mathbf{B}^{b2} \end{Bmatrix}^{T} \begin{bmatrix} \mathbf{A} & \mathbf{B} & \mathbf{E} \\ \mathbf{B} & \mathbf{D} & \mathbf{F} \\ \mathbf{E} & \mathbf{F} & \mathbf{H} \end{bmatrix} \begin{Bmatrix} \mathbf{B}^{m} \\ \mathbf{B}^{b1} \\ \mathbf{B}^{b2} \end{Bmatrix} + \begin{Bmatrix} \mathbf{B}^{s1} \\ \mathbf{B}^{s2} \end{Bmatrix}^{T} \begin{bmatrix} \mathbf{A}_{\mathrm{s}} & \mathbf{B}_{\mathrm{s}} \\ \mathbf{B}_{\mathrm{s}} & \mathbf{D}_{\mathrm{s}} \end{bmatrix} \begin{Bmatrix} \mathbf{B}^{s1} \\ \mathbf{B}^{s2} \end{Bmatrix} \right] \mathrm{d}\Omega \tag{4. 15}$$

and the load vector **F** is calculated as

$$\mathbf{F} = \int_{\Omega} q_0 \mathbf{R}_0 \mathrm{d}\Omega \tag{4. 16}$$

in which

$$\mathbf{R}_0 = \begin{bmatrix} 0 & 0 & 0 & 0 & 0 & 0 & R_A \end{bmatrix} \tag{4. 17}$$

For free vibration analysis, one has

$$\mathbf{M}\ddot{\mathbf{d}} + \mathbf{Kd} = \mathbf{0} \tag{4. 18}$$

where the global mass matrix **M** is described as

$$\mathbf{M} = \int_{\Omega} \left\{ \begin{bmatrix} \mathbf{N_0} \\ \mathbf{N_1} \\ \mathbf{N_2} \end{bmatrix}^{T} \begin{bmatrix} I_1 & I_2 & I_4 \\ I_2 & I_3 & I_5 \\ I_4 & I_5 & I_6 \end{bmatrix} \begin{bmatrix} \mathbf{N_0} \\ \mathbf{N_1} \\ \mathbf{N_2} \end{bmatrix} \right\} \mathrm{d}\Omega \tag{4. 19}$$

with

$$\mathbf{N}_0 = \begin{bmatrix} R_A & 0 & 0 & 0 & 0 & 0 & 0 \\ 0 & R_A & 0 & 0 & 0 & 0 & 0 \\ 0 & 0 & 0 & 0 & 0 & 0 & R_A \end{bmatrix}; \tag{4. 20}$$

$$\mathbf{N_1} = \begin{bmatrix} 0 & 0 & R_A & 0 & 0 & 0 & 0 \\ 0 & 0 & 0 & R_A & 0 & 0 & 0 \\ 0 & 0 & 0 & 0 & 0 & 0 & 0 \end{bmatrix}; \mathbf{N_2} = \begin{bmatrix} 0 & 0 & 0 & 0 & R_A & 0 & 0 \\ 0 & 0 & 0 & 0 & 0 & R_A & 0 \\ 0 & 0 & 0 & 0 & 0 & 0 & 0 \end{bmatrix}$$

And for forced vibration analysis, undamped dynamic discrete equations can be expressed from Eq.(4. 8)

$$\mathbf{M}\ddot{\mathbf{d}} + \mathbf{Kd} = \mathbf{F}(t) \tag{4. 21}$$

To solve this second order time-dependent problem, several methods have been proposed such as Wilson, Newmark, Houbolt, Crank-Nicholson, etc. Here, Eq.(4. 21) is solved by the Newmark direct integration scheme.

4.3 Theory and formulation of the piezoelectric laminated composite plates

4.3.1 Variational forms of piezoelectric composite plates

The summation of kinetic energy, strain energy, dielectric energy and external work named the generalized energy function is written in the following form [28]

$$L = \int \left(\frac{1}{2}\rho \dot{\mathbf{u}}^T \dot{\mathbf{u}} - \frac{1}{2}\boldsymbol{\sigma}^T \boldsymbol{\varepsilon} + \frac{1}{2}\mathbf{D}^T \mathbf{E} + \mathbf{u}^T \mathbf{f}_s - \phi \mathbf{q}_s \right) \mathrm{d}\Omega + \sum \mathbf{u}^T \mathbf{F}_p - \sum \phi \mathbf{Q}_p \qquad (4.\ 22)$$

where ρ is the mass density, $\mathbf{u}$ and $\dot{\mathbf{u}}$ are the mechanical displacement and velocity; ϕ is the electric potential; $\mathbf{f}_s$ and $\mathbf{F}_p$ are the mechanical surface loads and point loads; $\mathbf{q}_s$ and $\mathbf{Q}_p$ are the surface charges and point charges.

The Galerkin weak form of piezoelectric structures derived by using Hamilton's variational principle can be possibly written as

$$\delta \Pi = 0 \qquad (4.\ 23)$$

The material behavior of actuators and sensors made of the piezoelectric composite can be modeled as the following constitutive equations [125]

$$\begin{bmatrix} \boldsymbol{\sigma} \\ \mathbf{D} \end{bmatrix} = \begin{bmatrix} \mathbf{c} & -\mathbf{e}^T \\ \mathbf{e} & \mathbf{g} \end{bmatrix} \begin{bmatrix} \boldsymbol{\varepsilon} \\ \mathbf{E} \end{bmatrix} \qquad (4.\ 24)$$

in which **c**, the elasticity matrix, is defined as

$$\mathbf{c} = \begin{bmatrix} \mathbf{A} & \mathbf{B} & \mathbf{L} & \mathbf{0} & \mathbf{0} \\ \mathbf{B} & \mathbf{G} & \mathbf{F} & \mathbf{0} & \mathbf{0} \\ \mathbf{L} & \mathbf{F} & \mathbf{H} & \mathbf{0} & \mathbf{0} \\ \mathbf{0} & \mathbf{0} & \mathbf{0} & \mathbf{A}_s & \mathbf{B}_s \\ \mathbf{0} & \mathbf{0} & \mathbf{0} & \mathbf{B}_s & \mathbf{D}_s \end{bmatrix} \qquad (4.\ 25)$$

in which

$$\begin{aligned} (\mathbf{A}, \mathbf{B}, \mathbf{G}, \mathbf{L}, \mathbf{F}, \mathbf{H}) &= \int_{-h/2}^{h/2} \left(1, z, z^2, f(z), zf(z), f^2(z)\right) \bar{Q}_{ij} \mathrm{d}z \quad i, j = 1, 2, 6 \\ (\mathbf{A}_s, \mathbf{B}_s, \mathbf{D}_s) &= \int_{-h/2}^{h/2} \left(1, f'(z), \left(f'(z)\right)^2\right) \bar{Q}_{ij} \mathrm{d}z \quad i, j = 4, 5 \end{aligned} \qquad (4.\ 26)$$

where $\bar{Q}_{ij}$ is calculated as in Eq.(3. 18).

4.3.2 Approximated formulation of electric potential field

To approximate the electric potential field, each thin piezoelectric layer is discretized into a lot of finite sublayers through the thickness dimension. Besides, the electric potential variation is assumed to be linear in each sublayer and is approximated throughout the piezoelectric layer thickness as follows [150]:

$$\phi^i(z) = \mathbf{N}_\phi^i \boldsymbol{\phi}^i \tag{4. 27}$$

where $\mathbf{N}_\phi^i$ is the shape functions for the electric potential with p = 1, and $\boldsymbol{\phi}^i$ is the vector containing the electric potentials at the top and bottom surfaces of the i-th sublayer, $\boldsymbol{\phi}^i = \begin{bmatrix} \phi^{i-1} & \phi^i \end{bmatrix}$ $(i = 1,2,....,n_{sub})$ in which n_{sub} is the number of piezoelectric layers.

For each piezoelectric sublayer element, values of electric potentials are assumed to be equal at the same height along the thickness [125]. The electric field **E** can be rewritten as

$$\mathbf{E} = -\nabla \mathbf{N}_\phi^i \boldsymbol{\phi}^i = -\mathbf{B}_\phi \boldsymbol{\phi}^i \tag{4. 28}$$

in which

$$\mathbf{B}_\phi = \begin{Bmatrix} 0 & 0 & \dfrac{1}{h_p} \end{Bmatrix} \tag{4. 29}$$

in which h_p is the thickness of piezoelectric layer. Note that, for the type of piezoelectric materials considered in this work the piezoelectric constant matrix **e** and the dielectric constant matrix **g** of the k^{th} orthotropic layer in the local coordinate system are written as follows [150]

$$\mathbf{e}^{(k)} = \begin{bmatrix} 0 & 0 & 0 & 0 & e_{15} \\ 0 & 0 & 0 & e_{15} & 0 \\ e_{31} & e_{32} & e_{33} & 0 & 0 \end{bmatrix}^{(k)} \quad ; \quad \mathbf{g}^{(k)} = \begin{bmatrix} p_{11} & 0 & 0 \\ 0 & p_{22} & 0 \\ 0 & 0 & p_{33} \end{bmatrix}^{(k)} \tag{4. 30}$$

However, the laminate is usually made of several orthotropic layers with different directions of orthotropy and consequently different characteristic directions

for the dielectric and piezoelectric properties. So, the piezoelectric stress constant matrix **e** and the dielectric constant matrices **g** for the k^{th} orthotropic lamina in the global coordinate system is given by

$$\mathbf{e}^{(k)}=\begin{bmatrix}0&0&0&0&\overline{e}_{15}&0\\0&0&0&\overline{e}_{15}&0&0\\\overline{e}_{31}&\overline{e}_{32}&\overline{e}_{33}&0&0&0\end{bmatrix}^{(k)}\quad;\quad\mathbf{g}^{(k)}=\begin{bmatrix}\overline{p}_{11}&0&0\\0&\overline{p}_{22}&0\\0&0&\overline{p}_{33}\end{bmatrix}^{(k)}\tag{4. 31}$$

where $\overline{e}_{ij}$ and $\overline{p}_{ii}$ are transformed material constants of the k^{th} lamina and are calculated similarly to $\overline{Q}_{ij}$ in Eq. (3. 18).

4.3.3 Governing equations of motion

The elementary governing equation of motion can be derived in the following form

$$\begin{bmatrix}\mathbf{M}_{uu}&0\\0&0\end{bmatrix}\begin{bmatrix}\ddot{\mathbf{d}}\\\ddot{\boldsymbol{\phi}}\end{bmatrix}+\begin{bmatrix}\mathbf{K}_{uu}&\mathbf{K}_{u\phi}\\\mathbf{K}_{\phi u}&-\mathbf{K}_{\phi\phi}\end{bmatrix}\begin{bmatrix}\mathbf{d}\\\boldsymbol{\phi}\end{bmatrix}=\begin{bmatrix}\mathbf{f}\\\mathbf{Q}\end{bmatrix},\tag{4. 32}$$

where

$$\begin{aligned}&\mathbf{K}_{uu}=\int_{\Omega}\mathbf{B}_u^T\mathbf{c}\mathbf{B}_u\mathrm{d}\Omega\quad;\quad\mathbf{K}_{u\phi}=\int_{\Omega}\mathbf{B}_u^T\tilde{\mathbf{e}}^T\mathbf{B}_{\phi}\mathrm{d}\Omega\\&\mathbf{K}_{\phi\phi}=\int_{\Omega}\mathbf{B}_{\phi}^T\mathbf{g}\mathbf{B}_{\phi}\mathrm{d}\Omega\quad;\quad\mathbf{M}_{uu}=\int_{\Omega}\tilde{\mathbf{N}}^T\mathbf{m}\tilde{\mathbf{N}}\mathrm{d}\Omega\end{aligned}\tag{4. 33}$$

in which

$$\begin{aligned}&\tilde{\mathbf{e}}=\begin{bmatrix}\mathbf{e}_m^T&z\mathbf{e}_m^T&f(z)\mathbf{e}_m^T&\mathbf{e}_s^T&f'(z)\mathbf{e}_s^T\end{bmatrix},\\&\mathbf{e}_m=\begin{bmatrix}0&0&0\\0&0&0\\e_{31}&e_{32}&e_{33}\end{bmatrix};\mathbf{e}_s=\begin{bmatrix}0&e_{15}\\e_{15}&0\\0&0\end{bmatrix}\end{aligned}\tag{4. 34}$$

and $\mathbf{B}_u=[\mathbf{B}^m\ \mathbf{B}^{b1}\ \mathbf{B}^{b2}\ \mathbf{B}^{s1}\ \mathbf{B}^{s2}]^T$; **m** and $\tilde{\mathbf{N}}$ are defined similar to Eqs. (4. 13) and (4. 20).

Since the electric field **E** exists only according to the *z* direction, $\mathbf{K}_{u\phi}$ in Eq.(4. 33) can be rewritten as

$$\mathbf{K}_{u\phi}=\int_{\Omega}\left(\left(\mathbf{B}^m\right)^T e_m{}^T\mathbf{B}_{\phi}+z\left(\mathbf{B}^{b1}\right)^T e_m{}^T\mathbf{B}_{\phi}+f(z)\left(\mathbf{B}^{b2}\right)^T e_m{}^T\mathbf{B}_{\phi}\right)\mathrm{d}\Omega\tag{4. 35}$$

Substituting the second line of Eq. (4. 32) into the first line, the shortened form is obtained as

$$\mathbf{M}\ddot{\mathbf{d}} + \left(\mathbf{K}_{uu} + \mathbf{K}_{u\phi}\mathbf{K}_{\phi\phi}^{-1}\mathbf{K}_{\phi u}\right)\mathbf{d} = \mathbf{F} + \mathbf{K}_{u\phi}\mathbf{K}_{\phi\phi}^{-1}\mathbf{Q} \qquad (4.\ 36)$$

4.4 Active control analysis

Now considering a composite plate integrated piezoelectric with *n (n ≥ 2)* layers (See Figure 4. 1). The sensor layer at the bottom is denoted with the subscript *s* and the charge $Q = 0$.

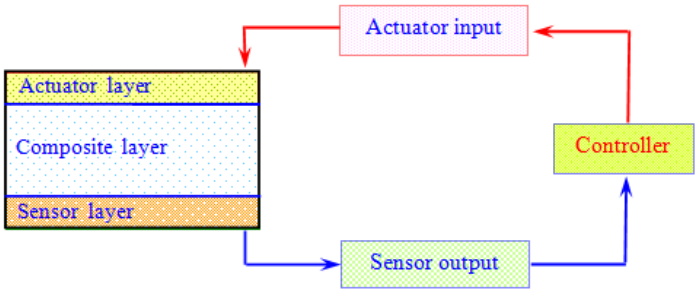

Figure 4. 1 . A schematic diagram of a laminated plate with integrated piezoelectric sensors and actuators.

The constant gains G_d and G_v of the control of displacement feedback and that of velocity one [28] are hence used to couple the input actuator voltage vector $\boldsymbol{\phi}_a$ and the output sensor voltage vector $\boldsymbol{\phi}_s$ as

$$\boldsymbol{\phi}_a = G_d\boldsymbol{\phi}_s + G_v\dot{\boldsymbol{\phi}}_s \qquad (4.\ 37)$$

Without the external charge Q, the generated potential on the sensor layer can be derived from the second equation of Eq. (4. 32) as

$$\boldsymbol{\phi}_s = \left[\mathbf{K}_{\phi\phi}^{-1}\right]_s \left[\mathbf{K}_{\phi u}\right]_s \mathbf{d}_s \qquad (4.\ 38)$$

Eq.(4. 38) above shows that, when an external force deforms the plate, the electric charges are generated in the sensor layer and then amplified through the closed loop control to be converted into the signal. This signal is then sent to the distributed actuator and generates an input voltage for the actuators. Finally, a resultant force

arises through the converse piezoelectric effect and this force actively controls the static response of the smart laminated composite plates.

Substituting Eqs. (4. 37) and (4. 38) into Eq. (4. 32), ones obtain

$$\begin{aligned}\mathbf{Q}_a = &\left[\mathbf{K}_{uu}\right]_a \mathbf{d}_a - G_d \left[\mathbf{K}_{\phi\phi}\right]_a \left[\mathbf{K}_{\phi\phi}^{-1}\right]_s \left[\mathbf{K}_{\phi u}\right]_s \mathbf{d}_s - \ldots \\ &G_v \left[\mathbf{K}_{\phi\phi}\right]_a \left[\mathbf{K}_{\phi\phi}^{-1}\right]_s \left[\mathbf{K}_{\phi u}\right]_s \dot{\mathbf{d}}_s\end{aligned} \tag{4. 39}$$

Substituting Eqs. (4. 37) and (4. 39) into Eq.(4. 36), one writes

$$\mathbf{M}\ddot{\mathbf{d}} + \mathbf{C}\dot{\mathbf{d}} + \mathbf{K}^*\mathbf{d} = \mathbf{F} \tag{4. 40}$$

where

$$\mathbf{K}^* = \mathbf{K}_{uu} + G_d \left[\mathbf{K}_{u\phi}\right]_s \left[\mathbf{K}_{\phi\phi}^{-1}\right]_s \left[\mathbf{K}_{\phi u}\right]_s \tag{4. 41}$$

and the active damping matrix, **C**, can be computed by

$$\mathbf{C} = G_v \left[\mathbf{K}_{u\phi}\right]_a \left[\mathbf{K}_{\phi\phi}^{-1}\right]_s \left[\mathbf{K}_{\phi u}\right]_s \tag{4. 42}$$

Without effect of the structural damping, Eq.(4. 40) can be rewritten as

$$\mathbf{M}\ddot{\mathbf{d}} + \mathbf{K}^*\mathbf{d} = \mathbf{F} \tag{4. 43}$$

For static analyses, Eq. (4. 40) reduces to

$$\mathbf{K}^*\mathbf{d} = \mathbf{F} \tag{4. 44}$$

4.5 Results and discussions

This section, several examples through a series of benchmark problems for the laminated composite plates with various geometric features, fiber orientation angles and boundary conditions using isogeometric Bézier elements for NURBS are considered. Note that, the boundary conditions for Bézier elements are applied equally to conventional IGA since the element topology is unchanged. The boundary conditions of the plate are used: clamped (C), simply supported (S) or free (F) edges. Thus, the symbol CFSF stands for clamped, free, simply supported and free boundary conditions along the edges of the plate.

For easy reference, the abbreviations of the below-mentioned methods are listed as follows:

- RPIM-UTSDT – The unconstrained third-order plate theory using the radial point interpolator meshless method by Dinis et al. [132].

- DQM-FSDT – The moving least squares differential quadrature method based on FSDT by Liew et al. [133]
- IGA-ITSDT – The isogeometric analysis based on a new inverse trigonometric shear deformation theory by Thai et al. [134].
- IGA-TSDT – The proposed isogeometric approach using the third-order shear deformation theory of Reddy [13,112].
- IGA-UTSDT – The proposed isogeometric approach using the unconstrained third-order plate theory of Leung [120].
- IGA-UITSDT – The proposed isogeometric approach using Bézier extraction combined the unconstrained inverse trigonometric shear deformation theory.
- IGA-USSDT– The proposed isogeometric approach using Bézier extraction combined with the unconstrained sinusoidal shear deformation theory.

The properties of materials used in this study are given below:

- Material I [13]:

  $E_1 = 25E_2, G_{12} = G_{13} = 0.5E_2, G_{23} = 0.2E_2, \nu_{12} = 0.25$

- Material II [135]:

  - Isotropic plate: $E = 5.6$ GPa, $\nu = 0.15$, $G = E/2(1+\nu)$

  - Faceplate: $E = 1.08 \times 10^4$ MPa, $\nu = 0.15$ and middle layer: the graphite/epoxy laminae [136]:

  $E_1 = 181$ GPa, $E_2 = 10.3$ GPa, $G_{12} = G_{13} = 7.17$ GPa, $G_{23} = 2.87$ GPa, $\nu_{12} = 0.28$

- Material III [133]:

  $E_1 = 40E_2, G_{12} = G_{13} = 0.6E_2, G_{23} = 0.5E_2, \nu_{12} = 0.25, \rho = 1$

- Material IV [137]:

  $E_1 = 172.369$ GPa, $E_2 = 6.895$ GPa, $G_{12} = G_{13} = 3.448$ GPa, $G_{23} = 1.379$ GPa, $\nu_{12} = 0.25$, $\rho = 1603.03$ kg/m^3

In this section, due to the square and circular composite plates are essential structural parts in modern engineering structures, two examples including a four-layer ($0^0/90^0/90^0/0^0$) square plate and a laminated circular plate are studied for static

problem. For the sake of simplicity and consistency, these two examples are also employed for vibration analysis. All layers of the laminated plate are assumed to be of the same thickness and made of the same linearly elastic composite materials.

4.5.1. Static analysis of the four-layer [$0^0/90^0/90^0/0^0$] square laminated plate

A four-layer fully simply supported square laminated plate subjected to a sinusoidal pressure defined as $q(x,y) = q_0 \sin(\frac{\pi x}{a})\sin(\frac{\pi y}{b})$ is considered, as shown in Figure 4. 2. The length to width ratio is a/b = 1 and the length to thickness ratios are a/h = 4, 10, 20 and 100, respectively. Material *I* is used.

The normalized displacement and stresses are defined as

$$\begin{aligned}&\bar{w} = (100E_2h^3)w(\frac{a}{2},\frac{a}{2},0)/qa^4; \bar{\sigma}_{xx} = \frac{h^2}{qa^2}\sigma_{xx}(\frac{a}{2},\frac{a}{2},\frac{h}{2}); \bar{\sigma}_{yy} = \frac{h^2}{qa^2}\sigma_{yy}(\frac{a}{2},\frac{a}{2},\frac{h}{4})\\ &\bar{\sigma}_{xy} = \frac{h^2}{qa^2}\sigma_{xy}(0,0,\frac{h}{2}); \bar{\sigma}_{xz} = \frac{h}{qa}\sigma_{xz}(0,\frac{a}{2},0); \bar{\sigma}_{yz} = \frac{h}{qa}\sigma_{yz}(\frac{a}{2},0,0)\end{aligned} \quad (4.45)$$

The convergence and accuracy of solutions using quadratic (p = 2), cubic (p = 3) and quartic (p = 4) Bézier elements at mesh level of 7x7, 11x11 and 15x15 elements is investigated as depicted in Table 4. 1. Figure 4. 3 illustrates Bézier control mesh of a square plate using 7x7, 11x11 and 15x15 cubic Bézier elements, respectively. The relative error percentages compared with the exact 3D elasticity solution [138] are also given in the parentheses. Table 4. 1 reveals that the obtained results correlate well with the exact value. It is observed that as the number of orders of polynomial and a mesh increase the obtained results converge to exact solutions. Throughout this test, nearly the same values of solutions are obtained for cubic and quartic elements at the mesh level of 11x11 and 15x15 elements in terms of both displacement and stresses. However, for quartic elements, the number of degrees of freedom is much greater than that of cubic elements. As a result, this leads to an increase in computational cost. Thereby, for practical choice, a cubic Bézier element with a mesh of 11x11 elements can be assigned for all numerical examples tested below.

Table 4. 2 displays the obtained results along with other solutions for the normalized displacement and stresses. The obtained results based on the proposed model are compared with those of the other reference ones based on the unconstrained third-order theory using Navier's series solution (UTSDT [120]) and using the numerical solution of RPIM-UTSDT. Additionally, IGA-UITSDT is also compared with the Reddy's analytical solutions- TSDT [13] and the exact 3D elasticity approach of Pagano [138]. It is found that IGA-UITSDT is a stronger competitor than other reference numerical techniques for all ratios a/h. Comparing with IGA-UTSDT, IGA-UITSDT and IGA-USSDT give the results slightly better, especially for thick plates. The obtained results from IGA-UITSDT are alike with IGA-USSDT yet IGA-UITSDT seem to be slightly better than IGA-USSDT. Normalized displacement and stresses of the proposed method conform well to the analytical solutions [120,138]. For a thick plate with $a/h = 4$ and 10, the obtained results are more accurate than other reference solutions. They even move beyond TSDT by Reddy [13]. Moreover, the shear stresses of the proposed model are close to those of the exact 3D elasticity solution [138].

Figure 4. 4 plots the distribution of stresses through the thickness of a four-layer square plate with $a/h = 4$. It can be seen that our results match well with those of the IGA-TSDT solutions. Notably, the transverse shear stresses of UTSDT and UITSDT based on IGA are non-zero at the top and bottom surfaces of the plate. This discrepancy is owing to that by using UTSDT and UITSDT, the transverse shear stresses relax at the boundary layer. However, such a non-zero amount (Table 4. **2** and Figure 4. 4) is only slight. Thus, the obtained results are accurate under bending loads, whereas contact friction or a flow field along the boundary layer is not within the research scope of this thesis. Efforts are underway to investigate the behavior of UITSDT in the presence of surface shear traction.

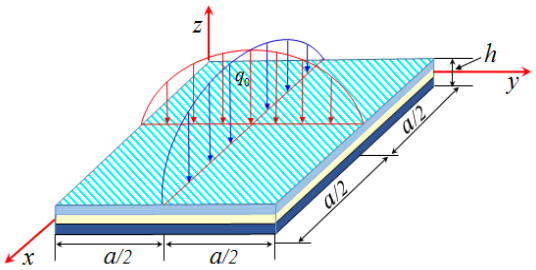

Figure 4. 2. Geometry attention of a laminated plate under a sinusoidally distributed load.

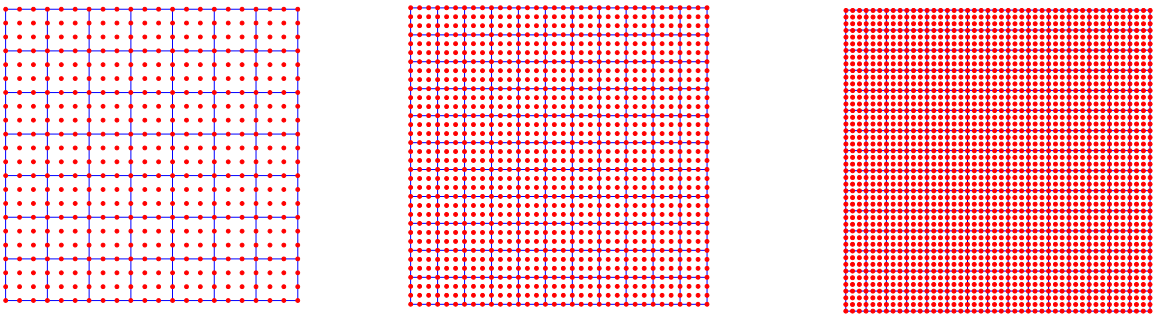

a) (b) (c)

Figure 4. 3. Bézier control mesh of a square plate using cubic Bézier elements: (a) 7x7; (b) 11x11 and (c) 15x15.

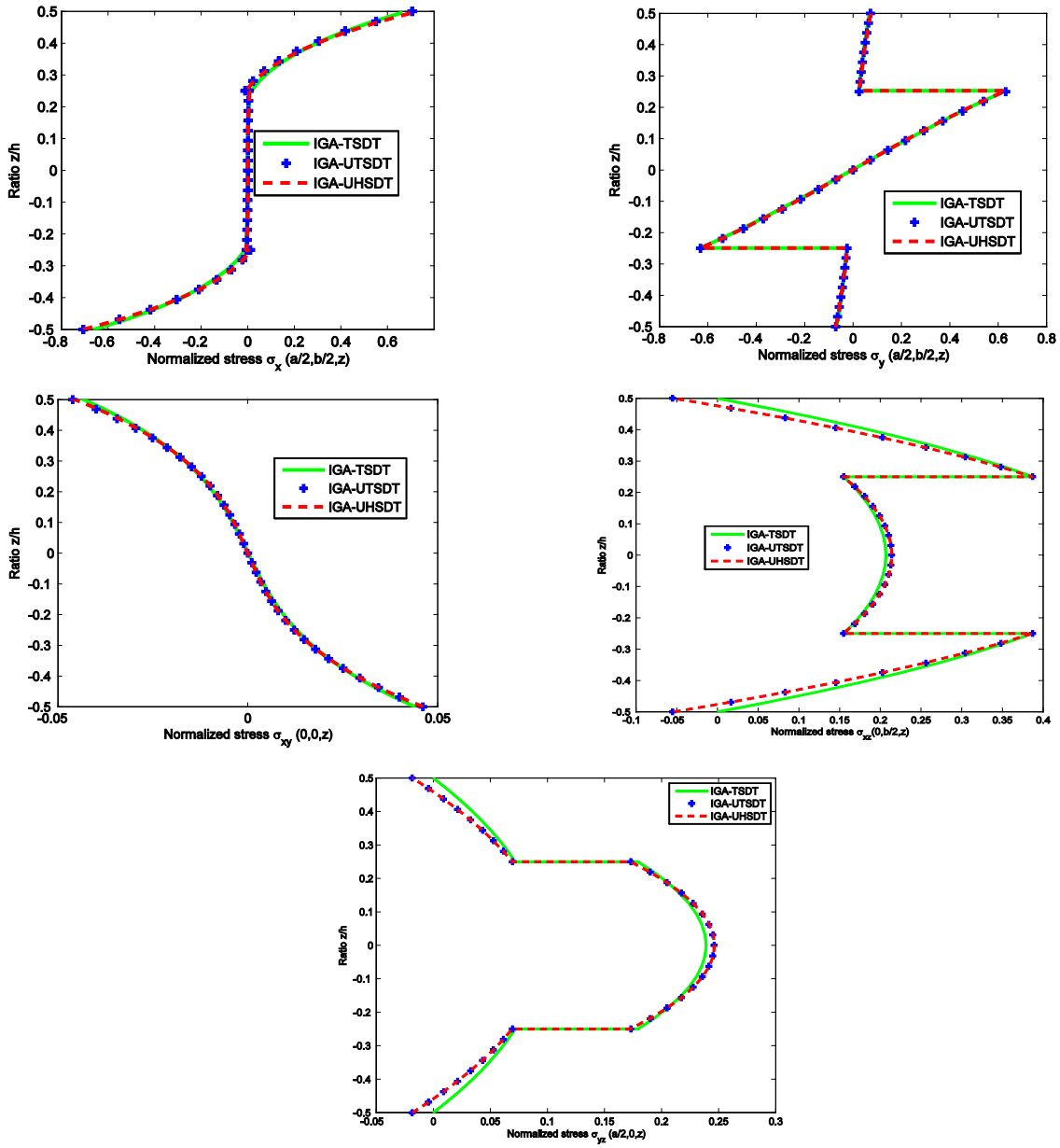

Figure 4. 4. Comparison of the normalized stress distributions through the thickness of a four-layer $[0^0/90^0/90^0/0^0]$ laminated composite square plate ($a/h = 4$).

Table 4. 1: Convergence of the normalized displacement and stresses of a four-layer $[0^0/90^0/90^0/0^0]$ laminated composite square plate ($a/h = 4$).

Order	Mesh (DOFs)	Method	$\overline{w}$	$\overline{\sigma}_{xx}$	$\overline{\sigma}_{yy}$	$\overline{\sigma}_{xz}$	$\overline{\sigma}_{yz}$	$\overline{\sigma}_{xy}$
	11x11 (3703)	IGA-UITSDT	1.90300 (2.61%)	0.7010 (2.64%)	0.6268 (5.46%)	0.2132 (2.64%)	0.2451 (15.77%)	0.0460 (1.49%)

	15x15	IGA-	1.90308	0.7032	0.6287	0.2137	0.2457	0.0460
	(6727)	UITSDT	(2.61%)	(2.33%)	(5.17%)	(2.42%)	(15.57%)	(1.49%)
p=3	7x7	IGA-	1.90301(2.61%)	0.7058	0.6311	0.2140	0.2460	0.0460
	(3388)	UITSDT		(1.97%)	(4.81%)	(2.28%)	(15.46%)	(1.49%)
	11x11	IGA-	1.90307	0.7041	0.6296	0.2142	0.2462	0.0461
	(8092)	UITSDT	(2.61%)	(2.20%)	(5.03%)	(2.19%)	(15.3%)	(1.28%)
	15x15	IGA-	1.90308	0.7058	0.6311	0.2142	0.2462	0.0461
	(14812)	UITSDT	(2.61%)	(1.97%)	(4.81%)	(2.19%)	(15.3%)	(1.28%)
p=4	7x7	IGA-	1.90309	0.7017	0.6274	0.2136	0.2455	0.0461
	(5887)	UITSDT	(2.61%)	(2.54%)	(5.41%)	(2.46%)	(15.63%)	(1.28%)
	11x11	IGA-	1.90309	0.7041	0.6296	0.2140	0.2460	0.0461
	(14175)	UITSDT	(2.61%)	(2.20%)	(5.03%)	(2.28%)	(15.46%)	(1.28%)
	15x15	IGA-	1.90309	0.7049	0.6303	0.2140	0.2462	0.0461
	(26047)	UITSDT	(2.61%)	(2.10%)	(4.93%)	(2.28%)	(15.39%)	(1.28%)
		Elasticity [138]	**1.9540**	**0.7200**	**0.6630**	**0.2190**	**0.2910**	**0.0467**

Table 4. 2: Normalized displacement and stresses of a simply supported $[0^0/90^0/90^0/0^0]$ square laminated plate under a sinusoidally distributed load.

a/*h*	Method	$\overline{w}$	$\overline{\sigma}_{xx}$	$\overline{\sigma}_{yy}$	$\overline{\sigma}_{xy}$	$\overline{\sigma}_{xz}$	$\overline{\sigma}_{yz}$
4	TSDT [13]	1.8937	0.6651	0.6322	0.044	0.2064	0.2389
	RPIM-UTSDT [132]	1.9024	0.7044	0.6297	0.0478	0.2169	0.2494
	UTSDT [120]	1.9023	0.7057	0.6309	0.0461	0.2064	0.2389
	IGA-UTSDT	1.9023	0.7040	0.6294	0.0461	0.2138	0.2460
	IGA- UITSDT	1.9031	0.7041	0.6296	0.0460	0.2142	0.2462
	IGA- USSDT	1.9030	0.7040	0.6295	0.0460	0.2140	0.2460
	Elasticity [138]	1.9540	0.7200	0.6630	0.0467	0.2190	0.2910
10	TSDT [13]	0.7147	0.5456	0.3888	0.0268	0.2640	0.1531
	RPIM-UTSDT [132]	0.7204	0.5599	0.3903	0.0280	0.2887	0.1580
	UTSDT [120]	0.7204	0.5609	0.3911	0.0273	0.2843	0.1593
	IGA-UTSDT	0.7204	0.5596	0.3901	0.0273	0.2842	0.1593
	IGA- UITSDT	0.7204	0.5596	0.3902	0.0274	0.2832	0.1612

	IGA- USSDT	0.7203	0.5599	0.3901	0.0272	0.2842	0.1611
	Elasticity [138]	0.7430	0.5590	0.4010	0.0275	0.3010	0.1960
20	TSDT [13]	0.5060	0.5393	0.3043	0.0228	0.2825	0.1234
	RPIM-UTSDT [132]	0.5077	0.5425	0.3046	0.0233	0.3120	0.1167
	UTSDT [120]	0.5078	0.5436	0.3052	0.0230	0.3066	0.1279
	IGA-UTSDT	0.5078	0.5424	0.3045	0.0229	0.3066	0.1278
	IGA- UITSDT	0.5078	0.5424	0.3045	0.0229	0.3079	0.1278
	IGA- USSDT	0.5076	0.5422	0.3044	0.0228	0.3078	0.1276
	Elasticity [138]	0.5170	0.5430	0.3090	0.0230	0.3280	0.1560
100	TSDT [13]	0.4343	0.5387	0.2708	0.0213	0.2897	0.1117
	RPIM-UTSDT [132]	0.4321	0.5351	0.2700	0.0220	0.2986	0.0704
	UTSDT [120]	0.4344	0.5389	0.2709	0.0214	0.3154	0.1153
	IGA-UTSDT	0.4344	0.5376	0.2702	0.0213	0.3153	0.1152
	IGA- UITSDT	0.4344	0.5389	0.2709	0.0213	0.3153	0.1152
	IGA- USSDT	0.4343	0.5384	0.2708	0.0213	0.3153	0.1152
	Elasticity [138]	0.4347	0.5390	0.2710	0.0214	0.3390	0.1410

4.5.2 Static analysis of laminated circular plate subjected to a uniform distributed load

Next, the circular plate such as isotropic, multilayered symmetrical isotropic and laminated composite plates are considered. Material *II* is used. A plate of diameter $a = 2R$ and thickness $h = 2H$ with clamped boundary is shown in Figure 4. 5a. A NURBS quadratic function is enough to model exactly the circular geometry with an only single element using 9 control points as shown in Figure 4. 5b. Table 4. 3 summarizes data of the circular plate and Figure 4. 6 shows the 11x11 cubic Bézier element mesh used for the analysis. All plates in this section subject to the uniform distributed load $q = 0.12$ MPa [135].

First of all, the isotropic plates with different ratios of radius to thickness (R/H = 40, 20, 10 and 7) are studied. The plate has radial R=100mm and thickness $2H$ =20mm. Timoshenko and Goodier [48] and Luo et al. [135] gave a set of three-

dimensional solutions and close three-dimensional linear analytical solutions for axially symmetrical isotropic circular plates as follow,

$$w = q_0(1-r^2)^2 \frac{3(1-\upsilon^2)}{128Eh^3}$$
$$\sigma_r = q_0\left[\frac{2+\upsilon}{8}\frac{z^3}{h^3} - \frac{3(3+\upsilon)}{32}\frac{r^2 z}{h^3} - \frac{3}{8}\frac{z}{h}\right] \quad (4.46)$$

Table 4. 4 shows the results of the displacement in the center of the plate $w(0,0,0)$ and in-plan stress σ_x in the top surface of the plate with $r^2 = x^2 + y^2$. The obtained results are compared with the close three-dimensional linear analytical solutions of Luo et al. [135], Ansys software (ANS) [135] using element Solid45, the "pb-2 Ritz" theory of Liew [135,140,141] and IGA-UTSDT. It can be observed that the obtained results agree well with other reference solutions in terms of deflection and stress. Between IGA-UTSDT model and IGA- UITSDT model is not much different and they close to solutions of Liew [135,140,141] using "pb-2 Ritz" theory. It is clear that the obtained transverse displacement and in-plane stress decrease as the thickness of the plate increases.

Secondly, a three-layer symmetrical isotropic circular plate with the same thickness including two faceplates and middle layer and a laminated composite circular plate with the arrangement of fiber orientation angles is ($0^0/90^0/90^0/0^0$) and ($0^0/90^0/0^0$) and ($0^0/90^0$) are considered. The geometry is similar to above example and material *II* is used. The results of the deflection of the present theory, solutions of Luo et al. [135], the "pb-2 Ritz" theory of Liew [140,141], Ansys [135], and IGA-UTSDT are shown in Table 4. 5. It is clear that the present theory and IGA-UTSDT are closer to reference solutions than Ansys's solutions. For laminated composite plate, it can be found that the deflection will be increased when the number of layers decreases with the same thickness of the plate. Although no having a reference for the laminated composite circular plate, the obtained results from isotropic and

multilayer isotropic plate verify the reliability and effectiveness of the proposed method.

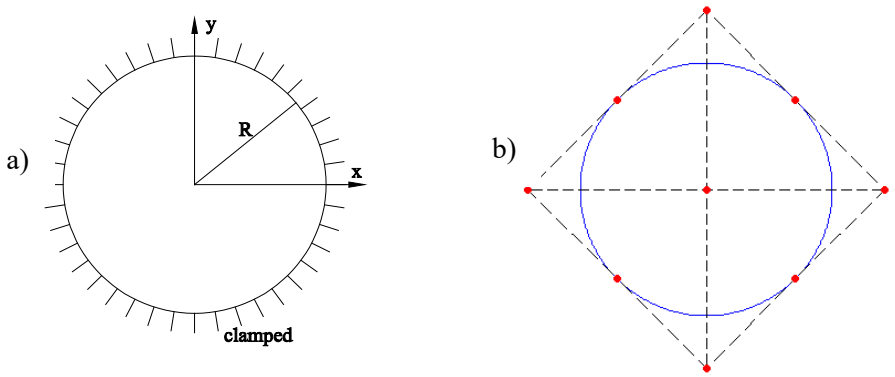

Figure 4. 5. a. Geometry and b. Coarse mesh and control points of a circular plate.

Table 4. 3: Control points and weights for a circular plate with a radius of $R = 0.5$.

i	1	2	3	4	5	6	7	8	9
x_i	$-\sqrt{2}/4$	$-\sqrt{2}/2$	$-\sqrt{2}/4$	0	0	0	$\sqrt{2}/4$	$\sqrt{2}/2$	$\sqrt{2}/4$
y_i	$\sqrt{2}/4$	0	$-\sqrt{2}/4$	$\sqrt{2}/2$	0	$-\sqrt{2}/2$	$\sqrt{2}/4$	0	$-\sqrt{2}/4$
w_i	1	$\sqrt{2}/2$	1	$\sqrt{2}/2$	1	$\sqrt{2}/2$	1	$\sqrt{2}/2$	1

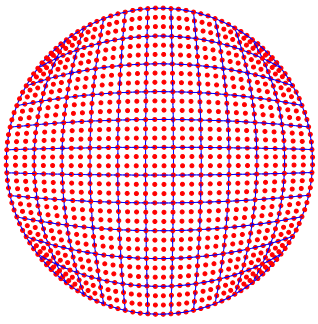

Figure 4. 6. A mesh of 11×11 cubic Bézier elements.

Table 4. 4: The transverse displacement $w(0,0,0)$ and in-plane stress σ_x of isotropic circular plate with various R/H ratios.

Method/Author		R/H			
		40	20	10	7
Luo et al. [135]	$w(0,0,0)$ $\text{x}10^2$(mm)	331.8	41.47	5.18	1.78
Pb-2 Ritz [140,141]		328.2	42.12	5.81	2.24
ANS [135]		310.8	37.16	5.02	1.75
IGA-UTSDT		317.0	40.69	5.61	2.17
IGA- UITSDT		316.9	40.58	5.54	2.11
IGA- USSDT		317.1	40.57	5.54	2.10
Luo et al. [135]	σ_x (MPa)	-	-	1.21	-
Pb-2 Ritz [140,141]		-	-	1.41	-
ANS [135]		-	-	1.23	-
IGA-UTSDT		21.15	5.21	1.31	0.65
IGA- UITSDT		21.15	5.20	1.29	0.64
IGA- USSDT		21.14	5.21	1.30	0.65

Table 4. 5: The deflection $w(0,0,0)\text{x}10^2$ (mm) of three-layer symmetrical isotropic and laminated composite circular plates.

Plate	Method				
	Luo et al. [135]	ANS [135]	Pb-2 Ritz [140,141]	IGA-UTSDT	IGA-UITSDT
Three-layer isotropic	6.0	6.2	6.0	6.09	6.08
$(0^0/90^0/90^0/0^0)$	-	-	-	0.775	0.773
$(0^0/90^0/0^0)$	-	-	-	0.874	0.881
$(0^0/90^0)$	-	-	-	1.157	1.134

4.5.3 Free vibration of laminated composite square plate

Consider a four-layer ($0^0/90^0/90^0/0^0$) plate with simply supported boundary condition. Material III is employed. The effects of the length to thickness *a/h* and various elastic modulus ratios E_1 / E_2 are studied. The normalized frequency $\bar{\omega}$ is calculated as $\bar{\omega} = (\omega a^2 / h)(\rho / E_2)^{1/2}$ in which ω is natural frequency.

The first normalized frequencies of IGA-UITSDT are listed under various modulus ratios E_1/E_2 and with $a/h = 5$ (Table 4. 6). The obtained results are compared with analytical solutions based on the HSDT [137], the moving least squares differential quadrature method (DQM) [133] based on the FSDT, the meshfree method using multiquadric radial basis functions (RBFs) [142], wavelets functions [143] based on the FSDT and IGA-UTSDT. A good agreement is found for the present method in comparison with other ones. It is also seen that the present results match very well with the exact solutions [137] indicating that the proposed method has high reliability.

Interestingly, Table 4. 7 reveals the influence of the length to thickness ratios with $E_1 / E_2 = 40$. The obtained results are compared with those of Zhen and Wanji [144] based on a global-local higher-order theory (GLHOT), Cho et al. [145] based on HSDT, Matsunaga [146] based on a global–local higher-order theory and IGA-UTSDT. As expected, the present method yields excellent results when compared with other published solutions for all ratios *a*/*h*. According to Table 4. 6, IGA-UITSDT model gives solutions slightly better than IGA-UTSDT model compared with Exact-HSDT model in terms of the normalized frequencies.

Table 4. 6: The first non-dimensional frequency parameter of a four-layer $[0^0/90^0/90^0/0^0]$ laminated composite square plate ($a/h = 5$).

Method	E_1/E_2			
	10	20	30	40
RBFs-FSDT [142]	8.2526	9.4974	10.2308	10.7329
Wavelets-FSDT [143]	8.2794	9.5375	10.2889	10.8117

DQM-FSDT [133]	8.2924	9.5613	10.3200	10.8490
Exact-HSDT [137]	8.2982	9.5671	10.3260	10.8540
IGA-UTSDT	8.2693	9.5442	10.2470	10.7873
IGA-UITSDT	8.2702	9.5455	10.2698	10.7926
IGA- USSDT	8.2703	9.5455	10.2697	10.7925

Table 4. 7: The non-dimensional frequency parameter of a four-layer $[0^0/90^0/90^0/0^0]$ simply supported laminated square plate ($E_1 / E_2 = 40$).

Method/Authors	*a*/*h*						
	4	5	10	20	25	50	100
GLHOT [144]	9.2406	10.7294	15.1658	17.8034	18.2404	18.9022	19.1566
Matsunaga [146]	9.1988	10.6876	15.0721	17.6369	18.0557	18.6702	18.8352
Cho *et al.* [145]	-	10.6730	15.0660	17.535	18.0540	18.6700	18.8350
IGA-UTSDT	9.2710	10.7873	15.0949	17.6434	18.0599	18.6713	18.8355
IGA-UITSDT	9.2704	10.7926	15.0949	17.6434	18.0599	18.6713	18.8355
IGA- USSDT	9.2704	10.7924	15.0945	17.6433	18.0598	18.6715	18.8354

4.5.4 Free vibration of laminated circular plate

A circular four-layer $[\theta^0 / -\theta^0 / -\theta^0 / \theta^0]$ laminated plate and various fiber orientation angles $\theta = 0^0, 15^0, 30^0$ and 45^0 are studied. Material parameter *III* is also used. The circular plate has a radius to thickness ratio of 5 ($R/h = 5$) and element mesh is similar to the 4.3.1.2 section. The normalized frequencies are defined as $\bar{\omega} = (\omega a^2 / h)(\rho / E_2)^{1/2}$ in which "*a*" is the diameter of the circular plate.

The effect of the ply angles θ on the non-dimensional fundamental frequency of the simply supported and clamped circular plate is investigated and the numerical results are presented in Table 4. 8. The solutions are compared with those of DQM-FSDT [133] and IGA-UTSDT. Additionally, the first six normalized frequencies derived from the proposed method in comparison with those of DQM-FSDT [133], IGA-ITSDT [134] and IGA-UTSDT in two cases $\theta^0 = 15^0$ and $\theta^0 = 45^0$ are also given in Table 4. 9. The results obtained also match well with other published solutions. Figure 4. 7 provides the first six-mode shapes of a circular four-layer [45^0/-

45^0/-45^0/45^0] clamped laminated plate with R/h = 5 and the normalized frequencies, respectively. These mode shapes describe well the physical vibration of the plate.

Table 4. 8: First non-dimensional frequency parameters of a four-layer $[\theta^0 / -\theta^0 / -\theta^0 / \theta^0]$ laminated circular plate (R/h = 5).

BC	Method	θ^0			
		0^0	15^0	30^0	45^0
Simply supported	DQM-FSDT [133]	16.512	16.495	16.947	17.147
	IGA-UTSDT	16.467	16.472	16.852	17.172
	IGA-UITSDT	16.471	16.479	16.882	17.175
Clamped	DQM-FSDT [133]	22.211	22.774	24.071	24.752
	IGA-UTSDT	22.910	23.232	24.176	24.730
	IGA-UITSDT	22.891	23.211	24.166	24.712

Table 4. 9: First six non-dimensional frequency parameters of a four-layer $[\theta^0 / -\theta^0 / -\theta^0 / \theta^0]$ clamped laminated circular plate (R/h = 5).

θ^0	Method	Modes					
		1	2	3	4	5	6
15^0	DQM-FSDT [133]	22.774	31.455	43.350	43.469	52.872	57.386
	IGA-ITSDT [134]	23.609	31.774	43.956	47.115	55.772	58.924
	IGA-UTSDT	23.232	31.910	44.340	46.057	54.809	58.200
	IGA-UITSDT	23.211	31.901	44.319	46.087	54.804	58.168
45^0	DQM-FSDT [133]	24.752	39.181	43.607	56.759	56.967	65.571
	IGA-ITSDT [134]	24.660	37.898	46.250	54.204	59.017	71.368
	IGA-UTSDT	24.730	37.925	44.566	54.383	57.342	67.496
	IGA-UITSDT	24.712	37.802	44.579	54.135	57.260	67.535

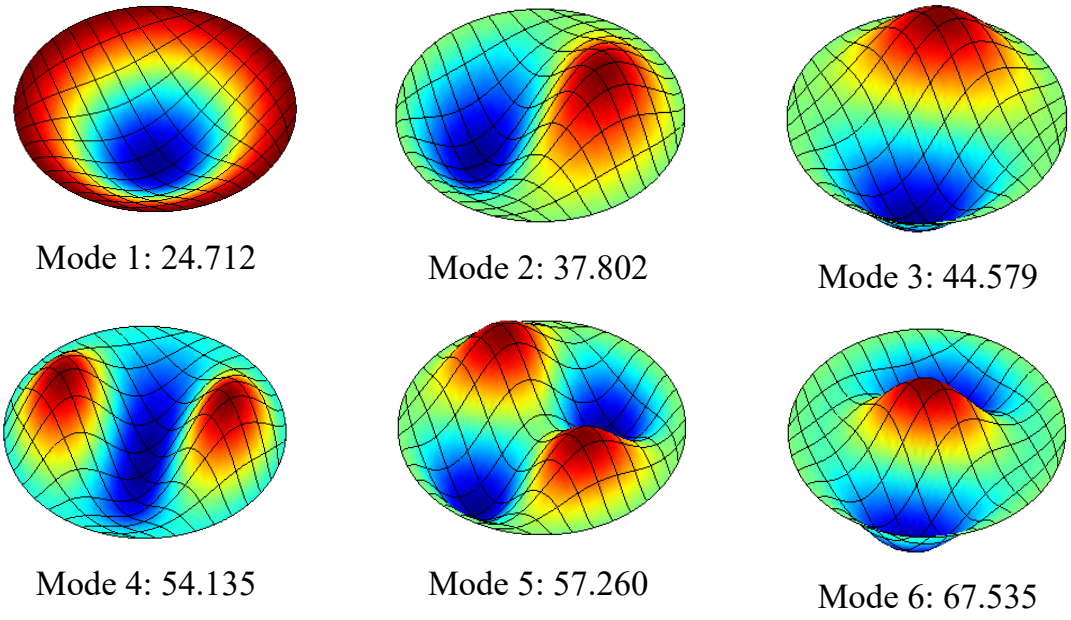

Figure 4. 7. Six mode shapes of a four-layer [45^0/-45^0/-45^0/45^0] clamped laminated circular plate with $R/h = 5$.

4.5.5 Transient analysis

One numerical example of a square laminated plate with $a = 5h$ and $a = 20h$ is studied for transient analysis subjected to various dynamic loadings. The dynamic loading, the intensive high load happened in a very short time, is one of the most challenging situations that the laminated composite plate may undergo during its operation. The obtained results are verified by comparing with other numerical or analytical solutions available in the literature. All layers of the laminated plate are assumed to have the same thicknesses and material properties. The time step $\Delta t =$ 0.1ms is chosen.

First, a fully simply supported three-layer square laminated plate sorted as [0^0/90^0/0^0] is considered. Material *IV* is used. Length and thickness of the plates are assumed to be $a = 5h$ and $h = 0.1524m$, respectively. Khdeir and Reddy [147] first studied this benchmark solution. It is to be noted that the analytical results obtained from the works of Khdeir and Reddy [147] are called exact solutions to date in the absence of three-dimensional elasticity solution for laminated composite plates. The plate is subjected to a sinusoidally distributed transverse load including step, triangular, sine and explosive blast loads as Eq.(4. 48)

$$q(x,y,t) = q_0 \sin(\frac{\pi x}{a}) \sin(\frac{\pi y}{b}) F(t) \tag{4. 47}$$

in which,

$$F(t) = \begin{cases} \begin{Bmatrix} 1 & 0 \le t \le t_1 \\ 0 & t > t_1 \end{Bmatrix} & \text{Step loading} \\ \begin{Bmatrix} 1 - t/t_1 & 0 \le t \le t_1 \\ 0 & t > t_1 \end{Bmatrix} & \text{Triangular loading} \\ \begin{Bmatrix} \sin(\pi t/t_1) & 0 \le t \le t_1 \\ 0 & t > t_1 \end{Bmatrix} & \text{Sine loading} \\ e^{-\gamma t} & \text{Explosive blast} \end{cases} \tag{4. 48}$$

where $t_1 = 0.006$ s ; $\gamma = 330$ s^{-1} and $q_0 = 68.9476$ MPa .

Displacement at the center of the plate and the dimensionless normal stress response in the time domain are given. The dimensionless normal stress is defined as

$$\bar{\sigma}_{xx} = \sigma_{xx}(a/2, b/2, h/2)/q_0 \tag{4. 49}$$

Figure 4. 8 shows the variation of the displacement at the center of the plate as a function under various dynamic loadings. The present solutions (IGA-UITSDT) are compared to the exact solutions obtained by Khdeir and Reddy [147] based on HSDT. According to Figure 4. 8 and Figure 4. 9, the graphs of central deflection and dimensionless normal stress relatively coincide and the difference between the results obtained and the exact solutions is negligible and acceptable. It can be seen that the stress response curve is very similar to the displacement response curve.

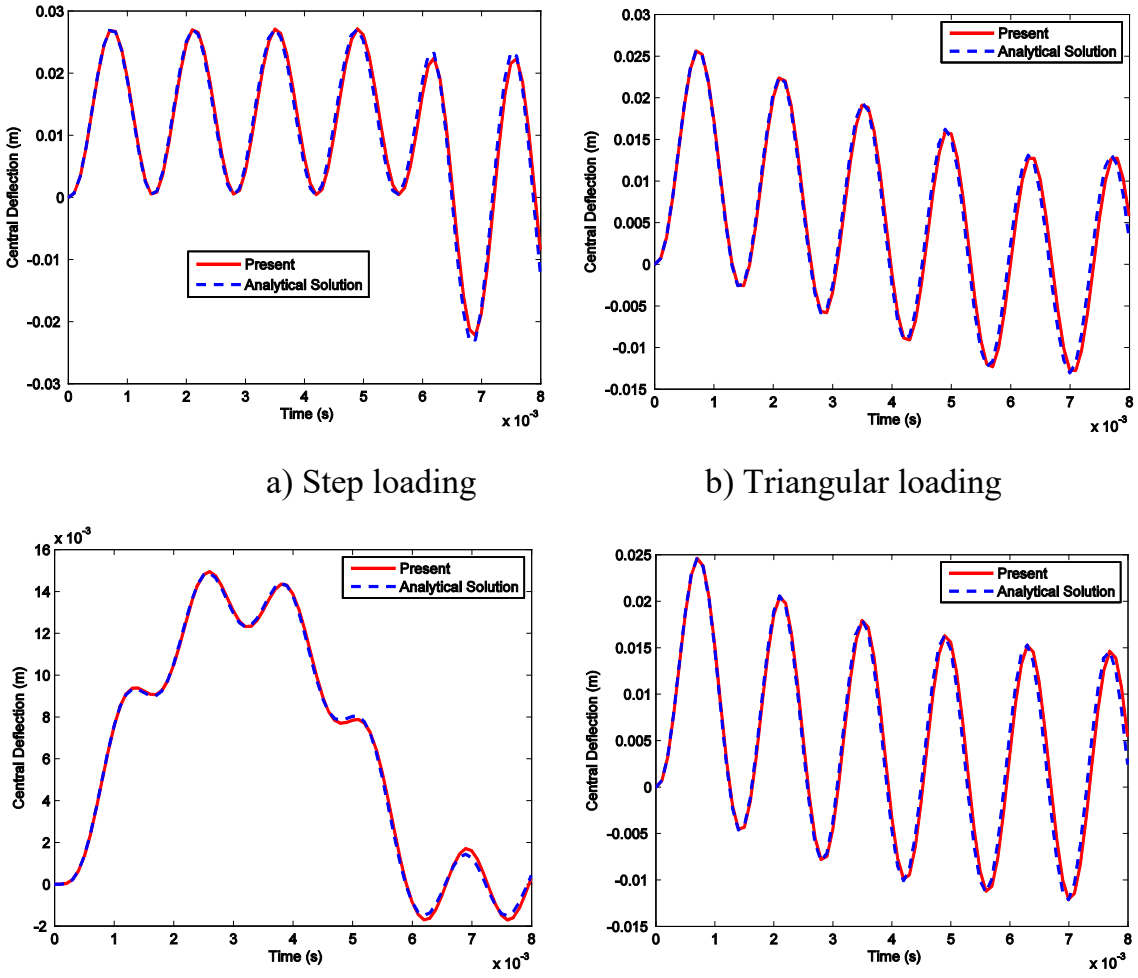

a) Step loading b) Triangular loading

c) sine loading d) explosive blast loading

Figure 4. 8. Central deflection for a $[0^0/90^0/0^0]$ square laminated plate subjected to various dynamic loadings.

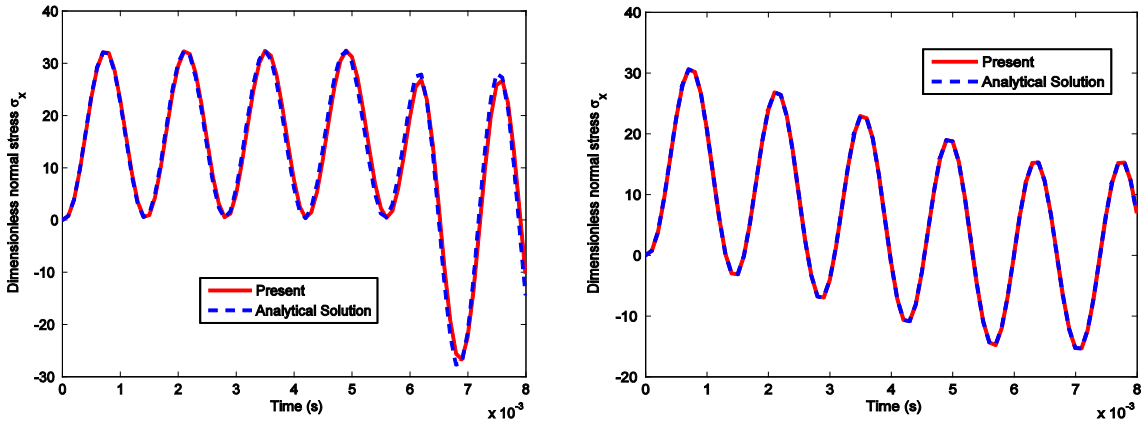

a) Step loading b) Triangular loading

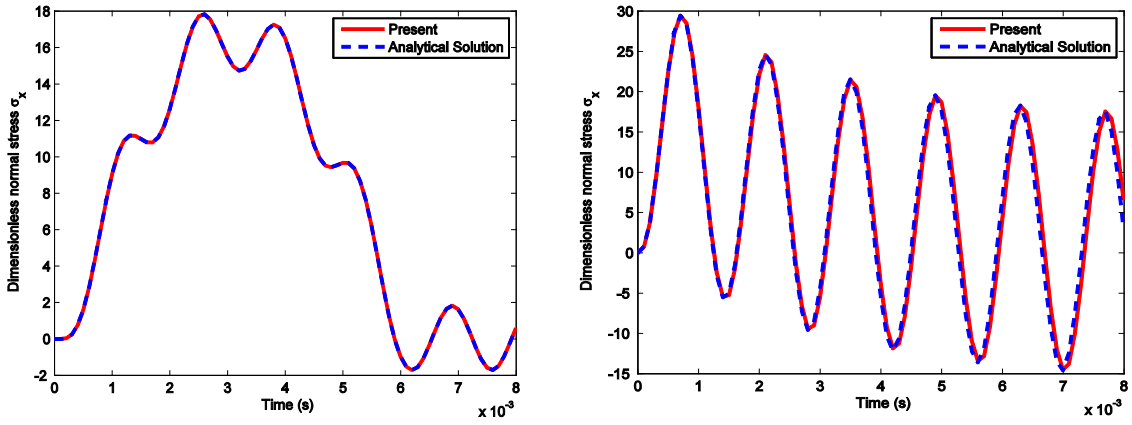

c) sine loading d) explosive blast loading

Figure 4. 9. Dimensionless normal stress for a $[0^0/90^0/0^0]$ square laminated plate subjected to various dynamic loadings.

Second, a fully simply supported three-layer square laminated plate sorted as $[0^0/90^0/0^0]$ is considered. The length and thickness of the square plate are assumed to be $a = 20h$ and $h = 0.0381$m, respectively. Wang et al. [149] also studied this example, which is chosen here to demonstrate the accuracy of IGA in the dynamic analysis of plates under different transient loads with $q_0 = 3.448$ MPa. Figure 4. 10 shows the time histories of central deflection of the plate under various dynamic loadings. The obtained results of IGA-UITSDT are compared with those obtained by Wang et al. [149] using the strip element method (SEM) and IGA-UTSDT. The dimensionless normal stress response $\bar{\sigma}_{xx}$ in the time domain for step loading and the comparison of IGA-UITSDT solutions with those of SEM are also given in Figure 4. 11. As expected, the reliability of the proposed method is apparent when the results obtained coincide perfectly with reference solutions for both displacement and stress. Again, the stress response curve is not different from the displacement response curve. Thereby, this comment is similar to other load cases.

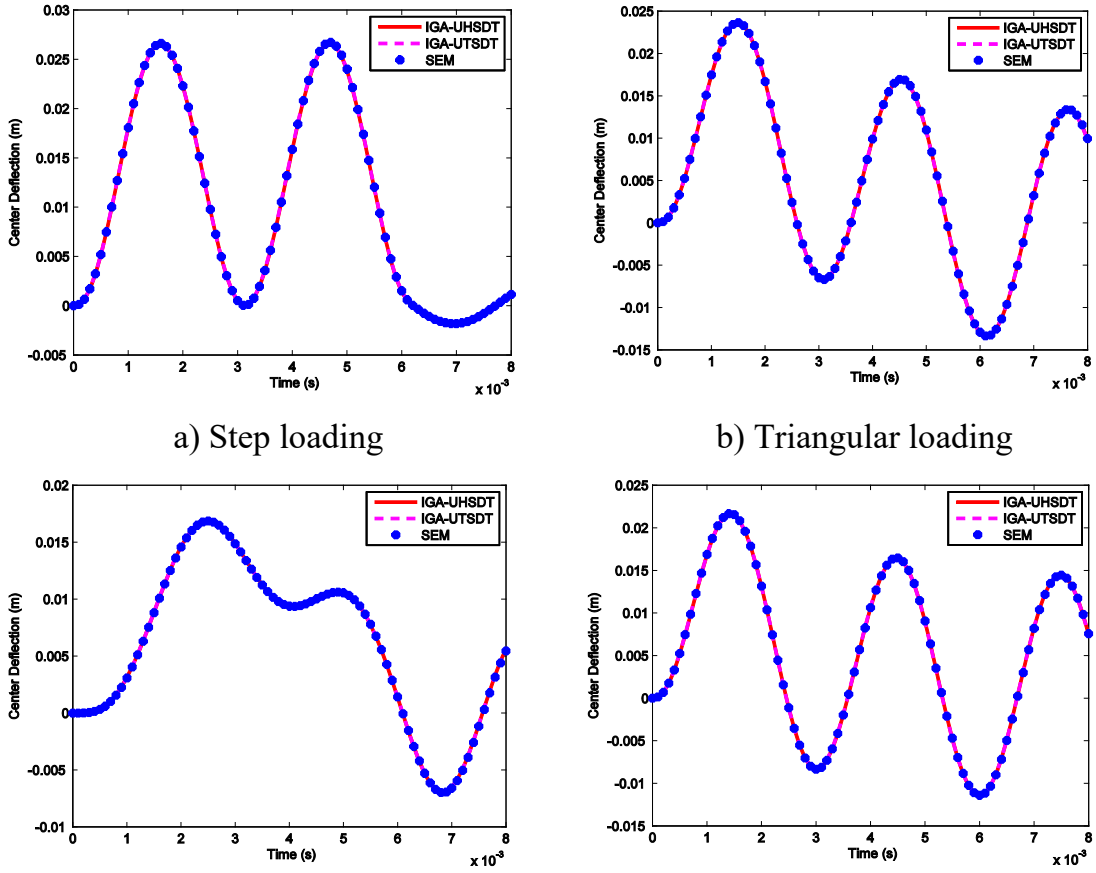

a) Step loading

b) Triangular loading

c) sine loading

d) explosive blast loading

Figure 4. 10. Central deflection versus time for a [0^0/90^0/0^0] square laminated plate subjected to various dynamic loadings.

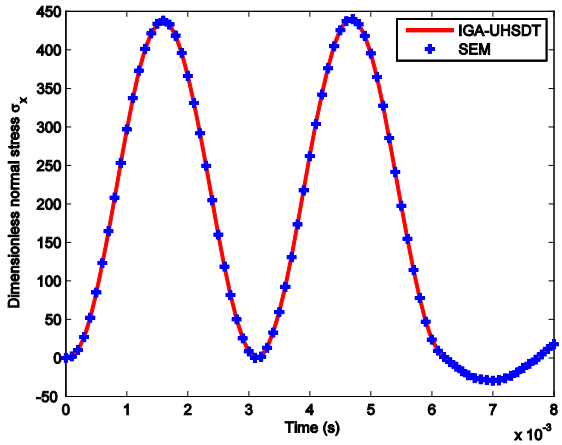

Figure 4. 11. Dimensionless normal stress $\bar{\sigma}_{xx}$ versus time for a [0^0/90^0/0^0] square laminated plate under step loading.

4.5.6 Static analysis of the square piezoelectric laminated composite plate

A simply supported square laminated plate ($20\,\text{cm} \times 20\,\text{cm}$) subjected to a uniform load q = 100 N/m^2 is considered. This plate is bonded by piezoelectric ceramics on both the lower and upper surfaces symmetrically. It consists of four composite layers and two outer piezo-layers denoted by *pie*. The laminate configuration of the composite plate is $[pie/\text{-}\theta/\theta]_s$ and $[pie/\text{-}\theta/\theta]_{as}$ where subscript "*s*" indicates symmetric laminate, and the subscript "*as*" anti-symmetric laminate, and θ is the fiber orientation angle of the layers. The non-piezoelectric composite plate is 1mm thick, and its layers have the same thickness each. The piezo-layer has the thickness of 0.1mm. Table 4. 10 shows the material properties of the plate made of T300/976 graphite/epoxy layers, and of the piezoceramic as PZT-G1195N.

Table 4. 10: The properties of the piezoelectric composite plates

Properties	PZT-4	PZT-G1195N	T300/979	Gr/Ep
E_{11} (GPa)	81.3	63.0	150	132.38
E_{22} (GPa)	81.3	63.0	9.0	10.76
E_{33} (GPa)	64.5	63.0	9.0	10.76
G_{12} (GPa)	30.6	24.2	7.1	3.61
G_{13} (GPa)	25.6	24.2	7.1	5.65
G_{23} (GPa)	25.6	24.2	2.5	5.65
ν_{11}	0.33	0.30	0.3	0.24
ν_{23}	0.43	0.30	0.3	0.24
ν_{13}	0.43	0.30	0.3	0.49
ρ (kg/m^3)	7600	7600	1600	1578
$d_{31} = d_{32}$ (m/V)	-1.22e-10	2.54e-10	-	-
d_{15} (m/V)	-	-	-	-
p_{11} (F/m)	1475	15.3e-9	-	-
p_{22} (F/m)	1475	15.3e-9	-	-
p_{33} (F/m)	1300	15.0e-9	-	-

First of all, the SSSS piezoelectric composite plate with different fiber orientation angles including [*pie*/-15/15]$_{as}$, [*pie*/-30/30]$_{as}$, [*pie*/-45/45]$_{as}$ and [*pie*/-45/45]$_{s}$ is investigated. A control Bézier mesh with 13x13 quadratic and cubic elements should be used here. Table 4. 11 displays the central point deflection of the piezoelectric composite plate subjected to the uniform load and different input voltages. The results of IGA-UITSDT can be seen to agree well with those of Refs. [28,151]. And Figure 4. 12 shows the deflection of the plate with various input voltages 0V, 5V, 8V, 10V. The deflection decreases to increase the input voltage as expected. It's because the input voltage induces an upward deflection of the plate due to the piezoelectric effect. This upward contribution becomes prevalent for an input voltage of 10V. Again, it can be seen that the obtained results and those of Refs. [28,151] are the same. In addition, the fiber orientation angle increases, the deflection of the plate decreases. For the input electric voltage of $10V$, the profile of deflection of the plate is different from those with other electric voltages due to the electric field vector **E** generates the electric field force. This electric field force is opposite to the mechanical force. Therefore, with the same mechanical loading the bigger of the input voltage make the smaller of displacement. However, it should be limitted the value of the input voltage in order to restrict the demolition of structures.

Table 4. 11: Central control point/node deflection of the simply supported piezoelectric composite plate subjected to a uniform load and different input voltages (10^{-4} m).

Input voltage	Scheme	Method			
		CS-DSG3 [151]	RPIM [28]	IGA-USSDT	IGA-UITSDT
0V	[*pie* /-45/45]$_{s}$	-0.6326	-0.6038	-0.6230	-0.6356
	[*pie*/-45/45]$_{as}$	-0.6323	-0.6217	-0.6205	-0.6139
	[*pie* /-30/30]$_{as}$	-0.6688	-0.6542	-0.6572	-0.6656
	[*pie* /-15/15]$_{as}$	-0.7442	-0.7222	-0.7400	-0.7436
5V	[*pie* /-45/45]$_{s}$	-0.2863	-0.2717	-0.2767	-0.2845

	[*pie* /-45/45]$_{as}$	-0.2801	-0.2717	-0.2744	-0.2820
	[*pie* /-30/30]$_{as}$	-0.2957	-0.2862	-0.2882	-0.2965
	[*pie* /-15/15]$_{as}$	-0.3259	-0.3134	-0.3192	-0.3281
10V	[*pie* /-45/45]$_{s}$	0.0721	0.0757	0.0788	0.0689
	[*pie* /-45/45]$_{as}$	0.0601	0.0604	0.0720	0.0602
	[*pie* /-30/30]$_{as}$	0.0774	0.0819	0.0805	0.0686
	[*pie* /-15/15]$_{as}$	0.0924	0.0954	0.1015	0.0887

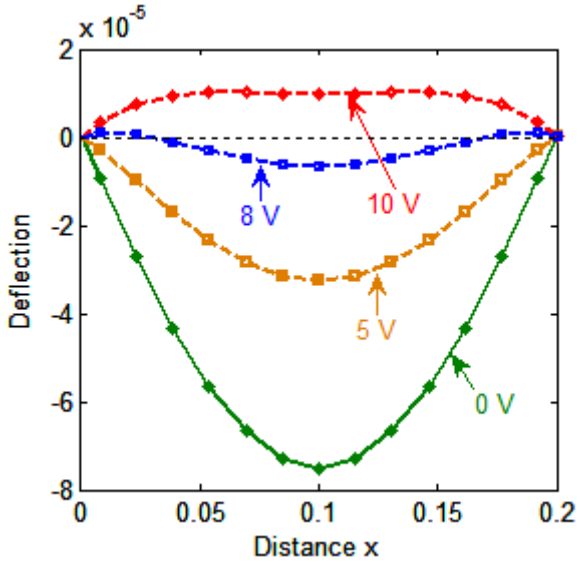

(a) [*pie*/-15/15]$_{as}$

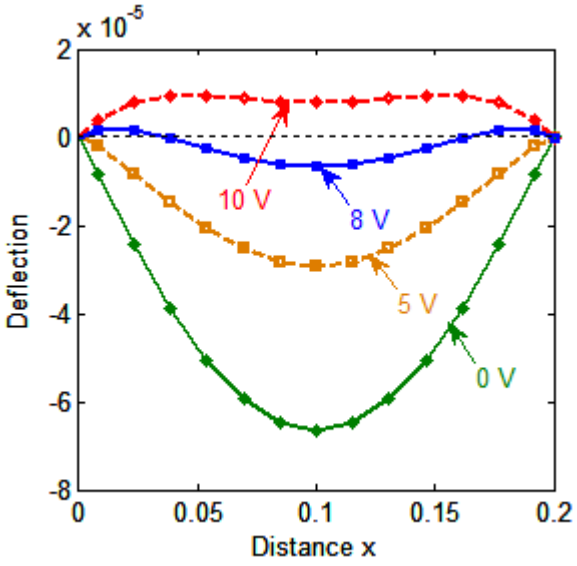

(b) [*pie*/-30/30]$_{as}$

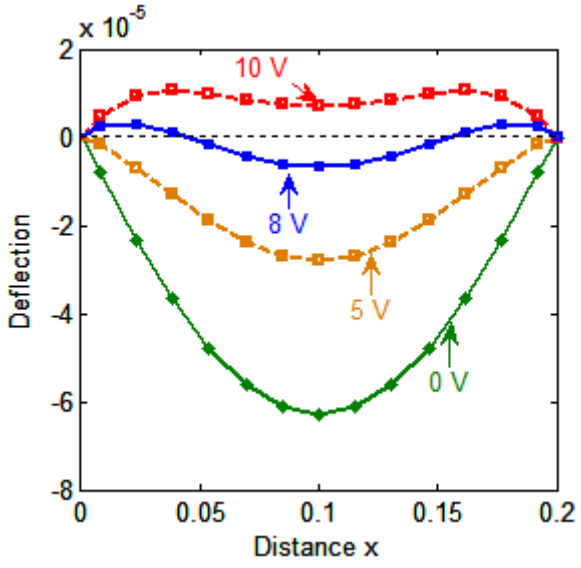

(c) [*pie*/-45/45]$_{as}$

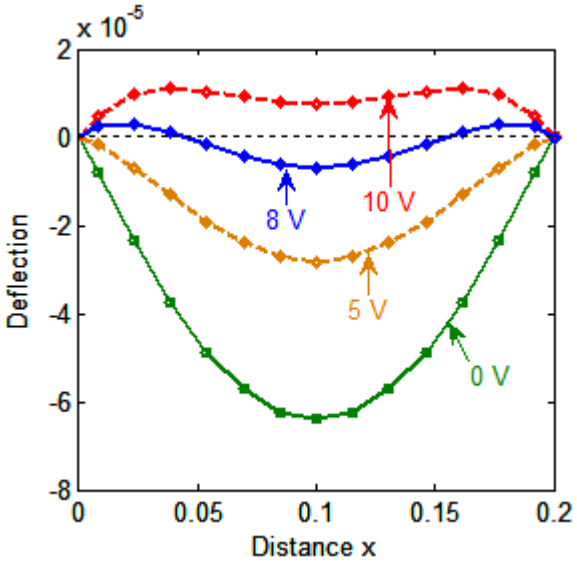

(d) [*pie*/-45/45]$_{s}$

Figure 4. 12. Centerline deflection of a simply supported piezoelectric composite plate subjected uniform load and different input voltages.

Next, Figure 4. 13 shows a deflection of the CFFF piezoelectric composite plate [*pie*/-45/45]$_{as}$ subjected to a uniform loading and various actuator input voltages. It can be seen that when the actuator input voltage becomes bigger, the deflection becomes upward. And these results agree well with and similar to what illustrated in [28,152]. Furthermore, the deflection of the plate with different boundary conditions (CFFF, SSFF, SSSS) is shown in Figure 4. 14. The proposed method is seen to agree well with RPIM method [28].

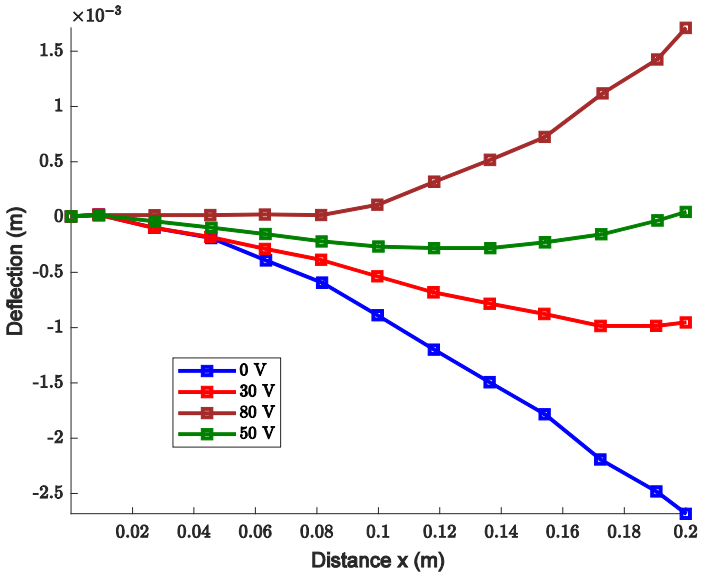

Figure 4. 13. Effect of actuator input voltages to deflection of the piezoelectric composite plate [*pie*/-45/45]$_{as}$ subjected to the uniform loading.

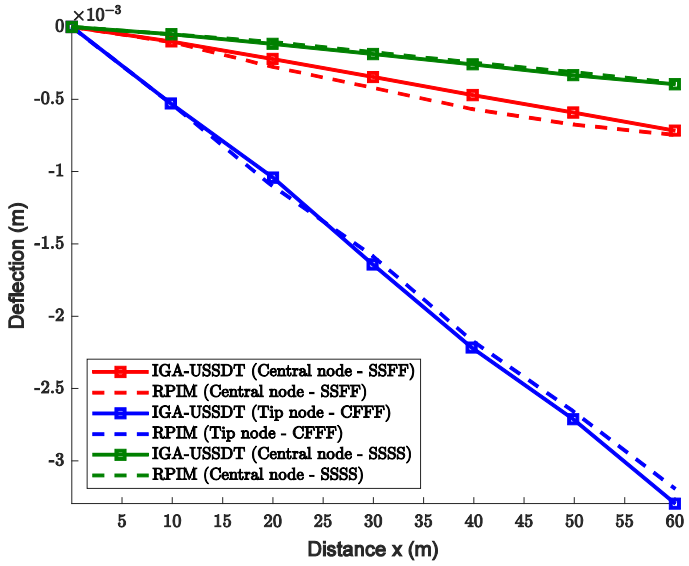

Figure 4. 14. The deflection of the piezoelectric composite plates with various boundary conditions.

4.5.7 Free vibration analysis of an elliptic piezoelectric composite plate

An elliptical plate with two boundary conditions: CCCC and SSSS is considered. The elliptical plate radiuses are $a = 5$ and $b = 2.5$ and plotted in Figure 4. 15a. The thickness of plate h and the piezoelectric layer have the thickness of $a/20$ and $h/10$ respectively. The material properties are chosen similarly to those in section 4.5.6. The first ten natural frequencies of the CCCC and SSSS plate calculated with a mesh of 19×19 quaratic elements (Figure 4. 15b) are displayed in

Table 4. ***12*** and Table 4. 13, respectively. It can be seen that when the fiber orientation angle decreases, frequency also decreases. And Figure 4. 16 plots the shape of the first six eigenmodes of the SSSS elliptical plate.

a) b)

Figure 4. 15. Geometry and element mesh of a clamped elliptical plate.

Table 4. 12. The first ten natural frequencies of the CCCC elliptical piezoelectric composite plate.

Mode	[*pie*/-45/45]*as*	[-45/*pie*/45]*as*	[*pie*/-30/30]*as*	[*pie*/-15/15]*as*
1	59.543	53.653	55.229	52.748
2	86.457	80.141	83.640	81.477
3	120.812	112.629	121.134	121.464
4	143.947	129.963	131.951	125.143
5	163.347	152.547	167.923	161.383
6	181.928	169.248	170.306	172.071
7	217.185	203.880	215.048	206.189
8	224.924	212.437	226.657	223.331
9	256.960	233.666	235.318	235.197
10	274.291	261.147	267.152	259.949

Table 4. 13. The first ten natural frequencies of the SSSS elliptical piezoelectric composite plate.

Mode	[*pie*/-45/45]*as*	[-45/*pie*/45]*as*	[*pie*/-30/30]*as*	[*pie*/-15/15]*as*
1	37.851	35.283	36.105	34.493
2	68.929	64.783	67.823	66.012
3	104.971	95.174	96.955	91.774
4	104.990	97.936	105.106	104.753
5	144.999	134.474	140.279	132.761
6	147.919	139.184	147.598	143.180
7	192.075	178.037	181.186	143.354
8	196.683	187.094	181.329	150.895
9	198.162	187.671	189.551	179.857
10	198.647	197.126	190.016	182.146

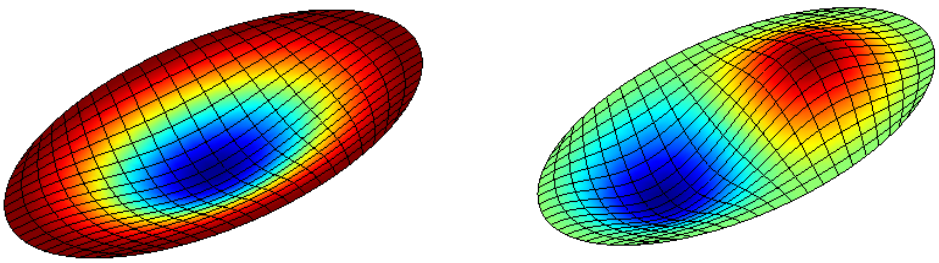

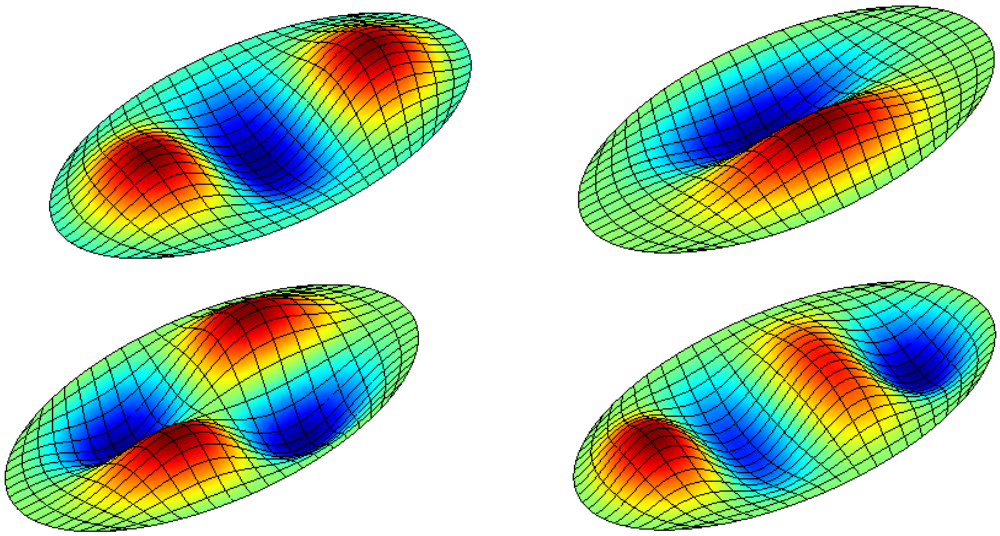

Figure 4. 16. Six mode shapes of a clamped laminated elliptical plate.

4.5.8 Dynamic control of piezoelectric laminated composite plate

A piezoelectric composite plate subjected to a uniform load q = 100 N/m^2 with the geometry, boundary conditions and material properties specified in section 4.5.6 is considered. The stacking sequence of the composite plate is [*pie*/-45/45]$_s$.

First, the control of the static deflection is studied. In Figure 4. 17, the effect of the displacement feedback control gain G_d on the static deflection of the plate is given, and that when G_d becomes bigger, the deflections become smaller, similarly to what illustrated in [28]. The explanation of this is that when the external load deforms the plate, electric charges are generated in the sensor layer; they are then amplified through the closed-loop control. The converted signal is then sent to the distributed actuator and generates an input voltage for the actuator. A resultant force is generated through the converse piezoelectric effect and this force actively controls the static response of the laminated plate. Next, the CFFF plate is assumed to be subjected to a harmonic uniform load $F = q\sin(\bar{\omega}t)$, where $\bar{\omega}$ is chosen as the first natural angular frequency. Figure 4. 18 shows the transient responses of the center point of the piezoelectric composite plate with and without the velocity feedback gain. It can be seen that the response with control is smaller than that without control, as expected due to an increase in the active damping.

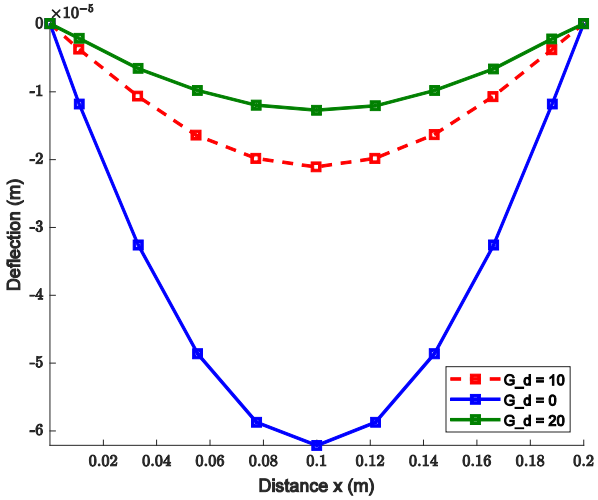

Figure 4. 17. Effect of G_d of the displacement feedback control on static deflections of the SSSS square piezoelectric composite plate with [*pie*/-45/45]$_s$.

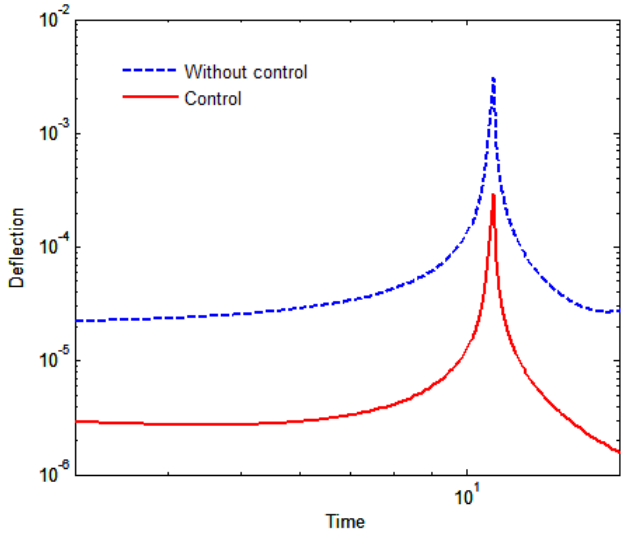

Figure 4. 18. Effect of G_v on the dynamic deflection response of a CFFF piezoelectric composite plate subjected to a uniform load.

4.6 Concluding remarks

This chapter presents an isogeometric finite element formulation using Bézier extraction for NURBS in combination with a generalized unconstrained theory for static, free vibration and transient analysis of laminated composite plates. Thanks to the Bézier extraction, the implementation of IGA becomes significantly easier with Bernstein basis functions, which have a close resemblance to Lagrange shape

functions as using C^0 continuous Bézier elements. This approach seems to be a reasonable choice due to the basis functions are given on localized form and the way of implementation in IGA is similar to in FEM. In terms of obtained results, although the present approach relaxes the non-zero transverse shear stresses at the lower and upper surface of the plate and no shear correction factor is used, the solutions correlated well with the solutions derived from other higher-order shear deformation theories for all examples. The UITSDT formulation is highly flexible and generalizable owing to the ability to select an arbitrary function $f(z)$ through the plate thickness. Throughout the static, free vibration and transient analysis, numerical results indicated that the proposed method achieves high reliability as compared with other published solutions and slightly better than the UTSDT using IGA based on Bézier extraction. The combination of the best advantage of IGA in terms of exact geometry and Bézier extraction which can integrate IGA into existing finite element codes along with a generalized unconstrained theory created a significant contribution in this chapter.

In addition, a displacement and velocity feedback control algorithm for the active control of the static deflection and of the dynamic response of the plates through a closed-loop control with bonded or embedded distributed piezoelectric sensors and actuators is used. Some numerical examples are shown for the analysis of the static deflection, natural vibration mode and dynamic control of piezoelectric laminated plates with different stacking schemes. The closed-loop control algorithm based on displacements and velocities feedback is applied to reduce vibration attitudes of the piezoelectric composite plates. Gain factors of the displacement and velocity rise, the deflections decrease accordingly.

As expected, the proposed approach may provide a reliable source of reference when laminated composite plates are calculated with other methods.

Chapter 5:
ANALYSIS AND CONTROL THE RESPONSES OF PIEZOELECTRIC FUNCTIONALLY GRADED POROUS PLATES REINFORCED BY GRAPHENE PLATELETS

5.1 Overview

In this chapter, an isogeometric Bézier finite element for bending and transient analyses of functionally graded porous (FGP) plates reinforced by graphene platelets (GPLs) embedded in piezoelectric layers is presented. It is named as PFGP-GPLs for a short. This chapter is written based on ref. [153]. Both linear and nonlinear respones of structures are given. The plates are constituted by a core layer, which contains the internal pores and GPLs dispersed in the metal matrix either uniformly or non-uniformly according to three different patterns, and two piezoelectric layers perfectly bonded on the top and bottom surfaces of host plate. The modified HalpinTsai micromechanical model is used to estimate the effective mechanical properties which vary continuously along the thickness direction of the core layer. In addition, the electric potential is assumed to vary linearly through the thickness for each piezoelectric sublayer. A generalized C^0-type higher-order shear deformation theory (C^0 - HSDT) presented in section 3.2.3 is used. The effects of weight fractions and dispersion patterns of GPLs, the coefficient and distribution types of porosity, as well as external electrical voltages on structure's behaviors, are investigated through several numerical examples. In addition, the present theory is developed further to analyze and control geometrically nonlinear responses of PFGP-GPLs plates. The geometrically nonlinear equations are solved by the Newton - Raphson iterative procedure and the Newmark's time integration scheme. The influences of the porosity coefficients, weight fractions of GPLs as well as the external electrical voltage on the

geometrically nonlinear behaviors of the plates with different porosity distributions and GPL dispersion patterns are investigated through numerical examples. Then, a constant displacement and velocity feedback control approaches are adopted to active control the geometrically nonlinear static as well as the dynamic responses of the FG porous plates, where the effect of the structural damping is considered, based on a closed - loop control with piezoelectric sensors and actuators.

5.2 Theory and formulation of PFGP-GPLs plate

The configuration of a PFGP-GPLs plate is considered and illustrated in Figure 3. 6. Lower and upper layers of the FG porous plate are embedded in two piezoelectric layers. In this chapter, the C^0-HSDT with the function *f(z)* is chosen $f(z) = h\text{artan}(\frac{2z}{h}) - z$ [134]. Due to the formulation for each field should be approximated independently, the approximation of electric potential field is given in 4.3.2 section in chapter 4.

For a plate bending, the strain vector is presented by

$$\varepsilon_{ij} = \frac{1}{2}\left(\frac{\partial u_i}{\partial x_j} + \frac{\partial u_j}{\partial x_i}\right) + \frac{1}{2}\frac{\partial u_k}{\partial x_i}\frac{\partial u_k}{\partial x_j} \tag{5. 1}$$

Employing the von Kármán assumptions, the strain-displacement relations can be rewritten as

$$\boldsymbol{\varepsilon} = \left\{\varepsilon_{xx} \quad \varepsilon_{yy} \quad \gamma_{xy}\right\}^{\mathrm{T}} = \boldsymbol{\varepsilon}^0 + z\boldsymbol{\varepsilon}^1 + f(z)\boldsymbol{\varepsilon}^2; \quad \boldsymbol{\gamma} = \left\{\gamma_{xz} \quad \gamma_{yz}\right\}^{\mathrm{T}} = \boldsymbol{\varepsilon}^{s0} + f'(z)\boldsymbol{\varepsilon}^{s1} \tag{5. 2}$$

where

$$\boldsymbol{\varepsilon}^0 = \begin{Bmatrix} u_{0,x} \\ v_{0,y} \\ u_{0,y} + v_{0,x} \end{Bmatrix} + \frac{1}{2}\begin{bmatrix} w_{,x}^2 \\ w_{,y}^2 \\ 2w_{,xy} \end{bmatrix} = \boldsymbol{\varepsilon}^0{}_L + \boldsymbol{\varepsilon}^0{}_{NL}; \; \boldsymbol{\varepsilon}^1 = -\begin{Bmatrix} \beta_{x,x} \\ \beta_{y,y} \\ \beta_{x,y} + \beta_{y,x} \end{Bmatrix}; \tag{5. 3}$$

$$\boldsymbol{\varepsilon}^2 = \begin{Bmatrix} \theta_{x,x} \\ \theta_{y,y} \\ \theta_{x,y} + \theta_{y,x} \end{Bmatrix}$$

$$\boldsymbol{\varepsilon}^{s0}=\begin{Bmatrix} w_{0,x}-\beta_x \\ w_{0,y}-\beta_y \end{Bmatrix};\ \boldsymbol{\varepsilon}^{s1}=\begin{Bmatrix} \theta_x \\ \theta_y \end{Bmatrix}$$

in which the nonlinear component is computed as

$$\boldsymbol{\varepsilon}_{NL}=\frac{1}{2}\begin{bmatrix} w_{,x} & 0 \\ 0 & w_{,y} \\ w_{,y} & w_{,x} \end{bmatrix}\begin{Bmatrix} w_{,x} \\ w_{,y} \end{Bmatrix}=\frac{1}{2}\mathbf{A}_\theta\boldsymbol{\theta} \tag{5. 4}$$

5.2.1 Approximation of mechanical displacement

Based on the Bézier extraction of NURBS, the mechanical displacement field of the FG porous plate can be approximated as follows

$$\mathbf{u}^h\left(\xi,\eta\right)=\sum_{A}^{m\times n}R_A^e\left(\xi,\eta\right)\mathbf{d}_A \tag{5. 5}$$

where $n\times m$ is the number of basis functions. Meanwhile $R_A^e\left(\xi,\eta\right)$ denotes a NURBS basis function presented in the consistent form of the linear grouping of Bézier extraction operator and Bernstein polynomials and $\mathbf{d}_A=\begin{bmatrix} u_{0A} & v_{0A} & w_A & \beta_{xA} & \beta_{yA} & \theta_{xA} & \theta_{yA} \end{bmatrix}^T$ is the vector of nodal degrees of freedom associated with control point A.

By substituting Eq. (5. 5) for Eq. (3.13) the in-plane and shear strains can be rewritten as

$$\begin{bmatrix}\boldsymbol{\varepsilon}\ \boldsymbol{\gamma}\end{bmatrix}^T=\sum_{A=1}^{m\times n}\left(\mathbf{B}_A^L+\frac{1}{2}\mathbf{B}_A^{NL}\right)\mathbf{d}_A \tag{5. 6}$$

where $\mathbf{B}_A^L=\begin{bmatrix}\mathbf{B}_A^1 & \mathbf{B}_A^2 & \mathbf{B}_A^3 & \mathbf{B}_A^{s_1} & \mathbf{B}_A^{s_2}\end{bmatrix}^T$

$$\mathbf{B}_A^1=\begin{bmatrix} R_{A,x} & 0 & 0 & 0 & 0 & 0 & 0 \\ 0 & R_{A,y} & 0 & 0 & 0 & 0 & 0 \\ R_{A,y} & R_{A,x} & 0 & 0 & 0 & 0 & 0 \end{bmatrix},\ \mathbf{B}_A^2=-\begin{bmatrix} 0 & 0 & 0 & R_{A,x} & 0 & 0 & 0 \\ 0 & 0 & 0 & 0 & R_{A,y} & 0 & 0 \\ 0 & 0 & 0 & R_{A,y} & R_{A,x} & 0 & 0 \end{bmatrix}$$

$$\mathbf{B}_A^3=\begin{bmatrix} 0 & 0 & 0 & 0 & 0 & R_{A,x} & 0 \\ 0 & 0 & 0 & 0 & 0 & 0 & R_{A,y} \\ 0 & 0 & 0 & 0 & 0 & R_{A,y} & R_{A,x} \end{bmatrix} \tag{5. 7}$$

$$\mathbf{B}_A^{s1}=\begin{bmatrix} 0 & 0 & R_{A,x} & -R_A & 0 & 0 & 0 \\ 0 & 0 & R_{A,y} & 0 & -R_A & 0 & \end{bmatrix},\ \mathbf{B}_A^{s2}=\begin{bmatrix} 0 & 0 & 0 & 0 & 0 & R_A & 0 \\ 0 & 0 & 0 & 0 & 0 & 0 & R_A \end{bmatrix}$$

and $\mathbf{B}_A^{NL}$ is calculated by

$$\mathbf{B}_A^{NL}=\begin{bmatrix} w_{A,x} & 0 \\ 0 & w_{A,y} \\ w_{A,y} & w_{A,x} \end{bmatrix}\begin{bmatrix} 0 & 0 & R_{A,x} & 0 & 0 & 0 & 0 \\ 0 & 0 & R_{A,x} & 0 & 0 & 0 & 0 \end{bmatrix}=\mathbf{A}_\theta\mathbf{B}_A^g \tag{5. 8}$$

5.2.2 Governing equations of motion

The elementary governing equation of motion can be derived in the following form:

$$\begin{bmatrix} \mathbf{M}_{uu} & 0 \\ 0 & 0 \end{bmatrix}\begin{bmatrix} \ddot{\mathbf{d}} \\ \ddot{\boldsymbol{\phi}} \end{bmatrix}+\begin{bmatrix} \mathbf{K}_{uu} & \mathbf{K}_{u\phi} \\ \mathbf{K}_{\phi u} & -\mathbf{K}_{\phi\phi} \end{bmatrix}\begin{bmatrix} \mathbf{d} \\ \boldsymbol{\phi} \end{bmatrix}=\begin{bmatrix} \mathbf{f} \\ \mathbf{Q} \end{bmatrix}, \tag{5. 9}$$

where

$$\mathbf{K}_{uu}=\int_\Omega(\mathbf{B}^L+\mathbf{B}^{NL})^T\mathbf{c}(\mathbf{B}^L+\tfrac{1}{2}\mathbf{B}^{NL})\mathrm{d}\Omega \quad ; \quad \mathbf{K}_{u\phi}=\int_\Omega(\mathbf{B}^L)^T\tilde{\mathbf{e}}^T\mathbf{B}_\phi\mathrm{d}\Omega \tag{5. 10}$$
$$\mathbf{K}_{\phi\phi}=\int_\Omega\mathbf{B}_\phi^T\mathbf{g}\mathbf{B}_\phi\mathrm{d}\Omega \quad ; \quad \mathbf{M}_{uu}=\int_\Omega\tilde{\mathbf{N}}^T\mathbf{m}\tilde{\mathbf{N}}\mathrm{d}\Omega \quad ; \quad \mathbf{f}=\int_\Omega\overline{q}_0\overline{\mathbf{N}}\mathrm{d}\Omega$$

in which

$$\tilde{\mathbf{e}}=\begin{bmatrix}\mathbf{e}_m^T & z\mathbf{e}_m^T & f(z)\mathbf{e}_m^T & \mathbf{e}_s^T & f'(z)\mathbf{e}_s^T\end{bmatrix};\overline{\mathbf{N}}=\begin{bmatrix}0 & 0 & R_A & 0 & 0 & 0 & 0\end{bmatrix}; \tag{5. 11}$$

where

$$e_m = \begin{bmatrix} 0 & 0 & 0 \\ 0 & 0 & 0 \\ e_{31} & e_{32} & e_{33} \end{bmatrix}; e_s = \begin{bmatrix} 0 & e_{15} \\ e_{15} & 0 \\ 0 & 0 \end{bmatrix} \tag{5. 12}$$

The global mass matrix $\mathbf{M}_{uu}$ is described as

$$\mathbf{M}_{uu} = \int_{\Omega} \left\{ \begin{Bmatrix} \mathbf{N_0} \\ \mathbf{N_1} \\ \mathbf{N_2} \end{Bmatrix}^T \begin{bmatrix} \mathbf{I}_1 & \mathbf{I}_2 & \mathbf{I}_4 \\ \mathbf{I}_2 & \mathbf{I}_3 & \mathbf{I}_5 \\ \mathbf{I}_4 & \mathbf{I}_5 & \mathbf{I}_6 \end{bmatrix} \begin{Bmatrix} \mathbf{N_0} \\ \mathbf{N_1} \\ \mathbf{N_2} \end{Bmatrix} \right\} \mathrm{d}\Omega \tag{5. 13}$$

where

$$\mathbf{I_0} = \begin{bmatrix} \mathbf{I}_1 & \mathbf{I}_2 & \mathbf{I}_4 \\ \mathbf{I}_2 & \mathbf{I}_3 & \mathbf{I}_5 \\ \mathbf{I}_4 & \mathbf{I}_5 & \mathbf{I}_6 \end{bmatrix}; \tag{5. 14}$$

$$\left(I_1, I_2, I_3, I_4, I_5, I_6\right) = \int_{-h/2}^{h/2} \rho\left(1, z, z^2, f(z), zf(z), f^2(z)\right) \mathrm{d}z$$

$$\mathbf{N}_0 = \begin{bmatrix} R_A & 0 & 0 & 0 & 0 & 0 & 0 \\ 0 & R_A & 0 & 0 & 0 & 0 & 0 \\ 0 & 0 & R_A & 0 & 0 & 0 & 0 \end{bmatrix}; \tag{5. 15}$$

$$\mathbf{N_1} = -\begin{bmatrix} 0 & 0 & 0 & R_A & 0 & 0 & 0 \\ 0 & 0 & 0 & 0 & R_A & 0 & 0 \\ 0 & 0 & 0 & 0 & 0 & 0 & 0 \end{bmatrix}; \ \mathbf{N_2} = \begin{bmatrix} 0 & 0 & 0 & 0 & 0 & R_A & 0 \\ 0 & 0 & 0 & 0 & 0 & 0 & R_A \\ 0 & 0 & 0 & 0 & 0 & 0 & 0 \end{bmatrix}$$

Substituting the second line of Eq. (5. 9) into the first line, Eq. (5. 9) can be expressed

$$\mathbf{M}_{uu}\ddot{\mathbf{d}} + \left(\mathbf{K}_{uu} + \mathbf{K}_{u\phi}\mathbf{K}_{\phi\phi}^{-1}\mathbf{K}_{\phi u}\right)\mathbf{d} = \mathbf{F} + \mathbf{K}_{u\phi}\mathbf{K}_{\phi\phi}^{-1}\mathbf{Q} \tag{5. 16}$$

$$\Leftrightarrow \mathbf{M}\ddot{\mathbf{d}} + \bar{\mathbf{K}}\mathbf{d} = \bar{\mathbf{F}}$$

5.3 Numerical results

5.3.1 Linear analysis

5.3.1.1 Convergence and verification studies

In this section, the accuracy and reliability of the proposed method are verified through a numerical example which has just been reported by Li et al. [70]. The free

vibration analysis for a sandwich FG porous square plate reinforced by GPLs with simply supported boundary condition (SSSS) is considered. That means the right side of Eq.(5. 16) is zeros vector. The initial parameters of plate are given as: $a = b = 1$ m, $h = 0.005a$, $h_p = 0.1h$, $h_p = 0.8h$, $e_0 = 0.5$. The sandwich plate includes isotropic metal face layers (Aluminum) and a porous core layer which is constituted by the uniformly distributed porous reinforced with uniformly distributed GPLs along the thickness. In this example, the copper is chosen as the metal matrix of the core layer whose material properties, as well as metal face ones, are given in Table 5. 1. For the GPLs, the parameters are used as follows: $l_{GPL} = 2.5\mu m$, $w_{GPL} = 1.5\mu m$, $t_{GPL} = 1.5nm$ and $\Lambda_{GPL} = 1wt.\%$.

Table 5. 1. Material properties

Properties	Core						Piezoelectric
	Ti-6Al-4V	Alumium oxide	Al	Al_2O_3	Cu	GPL	PZT-G1195N
Elastic properties							
E_{11} (GPa)	105.70	320.24	70	380	130	1010	63.0
E_{22} (GPa)	105.70	320.24	70	380	130	1010	63.0
E_{33} (GPa)	105.70	320.24	70	380	130	1010	63.0
G_{12} (GPa)	-	-	-	-	-	-	24.2
G_{13} (GPa)	-	-	-	-	-	-	24.2
G_{23} (GPa)	-	-	-	-	-	-	24.2
ν_{12}	0.2981	0.26	0.3	0.3	0.34	0.186	0.30
ν_{13}	0.2981	0.26	0.3	0.3	0.34	0.186	0.30
ν_{23}	0.2981	0.26	0.3	0.3	0.34	0.186	0.30
Mass density	4429	3750	2702	3800	8960	1062.5	7600
Piezoelectric coefficients							
d_{31} (m/V)							254 x10^{-12}
d_{32} (m/V)	-	-	-	-	-	-	254x 10^{-12}
Electric permittivity							
p_{11} (F/m)	-	-	-	-	-	-	15.3x10^{-9}
p_{22} (F/m)	-	-	-	-	-	-	15.3 x 10^{-9}
p_{33} (F/m)	-	-	-	-	-	-	15.3 x 10^{-9}

The convergence and accuracy of present formulation using quadratic ($p = 2$) Bézier elements at mesh levels of 7x7, 11x11, 15x15, 17x17 and 19x19 elements are studied, as shown in Figure 5. 1.

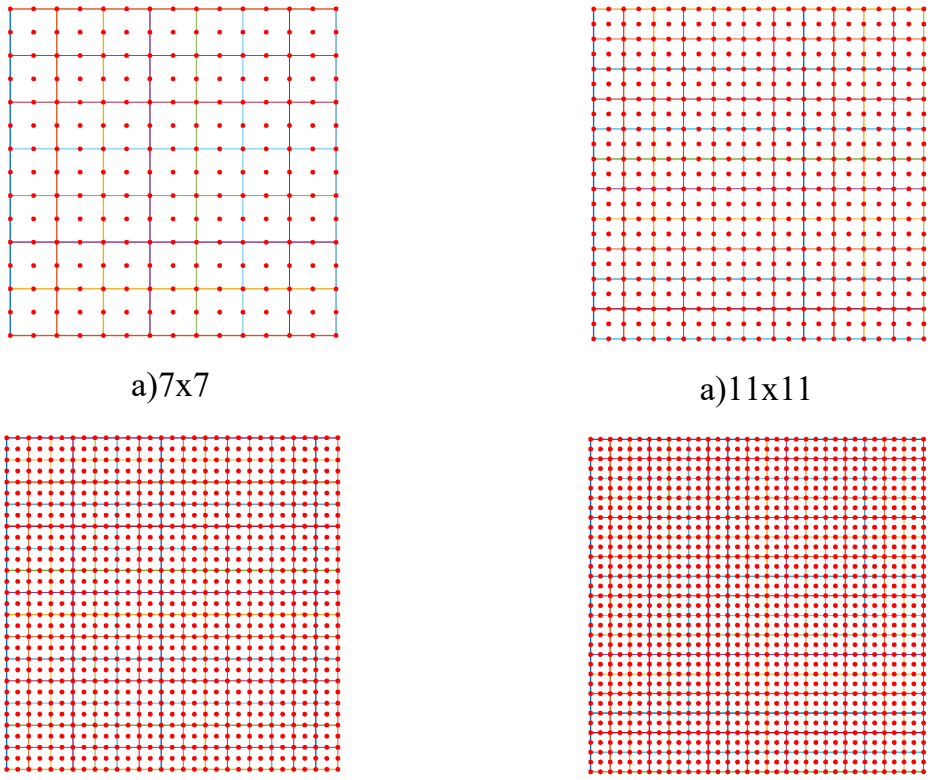

Figure 5. 1. Bézier control mesh of a square sandwich functionally graded porous plate reinforced by GPL using quadratic Bézier elements.

The natural frequencies generated from the proposed method are compared with analytical solutions [70] based on CPT. Table 5. 2 lists the natural frequencies of the first four m and n values with different Bézier control mesh. Noted that mode 1, mode 5, mode 11 and mode 21 of the vibration correspond with $n = 1, m = 1; n = 3,\ m = 1; n = 3,\ m = 3$ and $n = 3,\ m = 5$. These modes are carefully chosen because of the active vibration in the middle region of the plate where has more damage than other regions [154]. Furthermore, the relative error percentages compared with the analytical solutions are also given in the corresponding column. It can be seen that obtained results from the present approach agree well with the analytical solutions [70] for all selected modes. In addition, Table 5. 2 also reveals that the same accuracy of natural frequency is almost obtained for all modes using quadratic elements at mesh levels of 17x17 and 19x19 elements. The difference between the two mesh levels is not significant. As a result, for a practical point of

view, the mesh of 17x17 quadratic Bézier elements is applied to model the square plate for all numerical examples.

Table 5. 2: Comparison of convergence of the natural frequency (rad/s) for a sandwich simply supported FGP square plater reinforced by GPLs with different Bézier control meshes.

Mesh	Mode type (*m,n*)	Methods		
		Present	Analytical [70]	Relative error* (%)
7x7	(1,1)	161.1793	160.6964	+0.30050
	(1,3)	854.1663	803.4820	+6.30808
	(3,3)	1540.242	1446.2676	+6.49774
	(3,5)	2885.639	2731.8389	+5.62994
11x11	(1,1)	160.7703	160.6964	+0.04598
	(1,3)	822.1301	803.4820	+2.32091
	(3,3)	1466.455	1446.2676	+1.39584
	(3,5)	2799.861	2731.8389	+2.48998
15x15	(1,1)	160.7038	160.6964	+0.00460
	(1,3)	812.5604	803.4820	+1.12988
	(3,3)	1455.374	1446.2676	+0.62964
	(3,5)	2766.213	2731.8389	+1.25828
17x17	(1,1)	160.7008	160.6964	+0.00273
	(1,3)	810.1388	803.4820	+0.82849
	(3,3)	1452.617	1446.2676	+0.43907
	(3,5)	2755.097	2731.8389	+0.85138
19x19	(1,1)	160.6970	160.6964	+0.00037
	(1,3)	810.1320	803.4820	+0.82764
	(3,3)	1452.603	1446.2676	+0.43810
	(3,5)	2755.087	2731.8389	+0.85100

$$\text{*Relative error}=\frac{\text{Present value-Analytical value}}{\text{Analytical value}}.100\%$$

5.3.1.2 Static analysis

In this example, the static analysis of a cantilevered piezoelectric FGM square plate with a size length 400 mm × 400 mm is considered. The FGM core layer is

made of Ti-6A1-4V and aluminum oxide whose the effective properties mechanical is described based on the rule of mixture [152]. The plate is bonded by two piezoelectric layers which are made of PZT-G1195N on both the upper and lower surfaces symmetrically. The thickness of the FGM core layer is 5 mm and the thickness of each piezoelectric layer is 0.1 mm. All material properties of the core and piezoelectric layers are listed in Table 5. 1. Note that, as power index $n = 0$ implies the FG plate consists only of Ti-6A1-4V while n tends to ∞, the FG plate almost totally consists of aluminum oxide.

Firstly, the effect of input electric voltages on the deflection of the cantilevered piezoelectric FGM square plate subjected to a uniformly distributed load of 100 $\mathrm{N/m^2}$ is examined. Table 5. 3 shows the tip node deflection of FG plate corresponding to various input electric voltages. These results agree well with the reference solutions [56] all cases. In addition, the centerline deflection of piezoelectric FGM square plate only subjected to input electric voltage of $10V$ is displayed in Figure 5. 2. As expected, the obtained results are in good agreement with the reference solution, which is reported by Nguyen-Quang et al. [156]. For further illustration, the centerline deflection of piezoelectric FGM square plate subjected to simultaneously electro-mechanical load is shown in Figure 5. 3. The observation indicates that when the input voltage increases, the deflection of the plate becomes smaller because the piezoelectric effect makes the displacement of FGM plate going upward.

Table 5. 3: Tip node deflection of the cantilevered piezoelectric FGM plate subjected to a uniform load and different input voltages (10^{-3} m).

Input voltages (V)	Ti-6Al-4V		Aluminum oxide	
	Present	CS-DSG3 [156]	Present	CS-DSG3 [156]
0	-0.25437	-0.25460	-0.08946	-0.08947
20	-0.13328	-0.13346	-0.04608	-0.04609
40	-0.01229	-0.01232	-0.00271	-0.00271

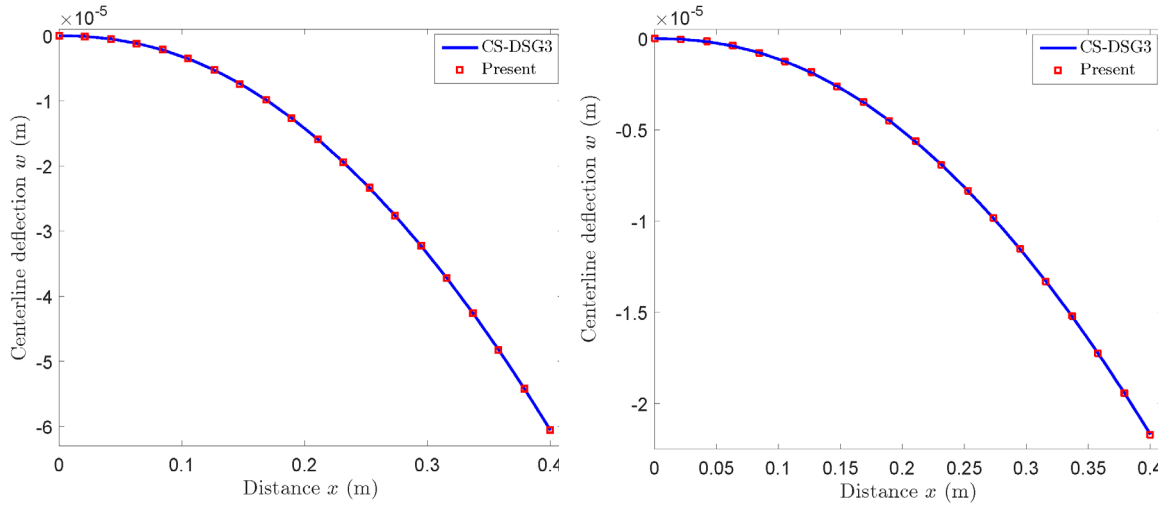

(a) Ti-6Al-4V (b) Aluminum oxide

Figure 5. 2: Profile of the centerline deflection of square piezoelectric FGM plate subjected to input voltage of 10V.

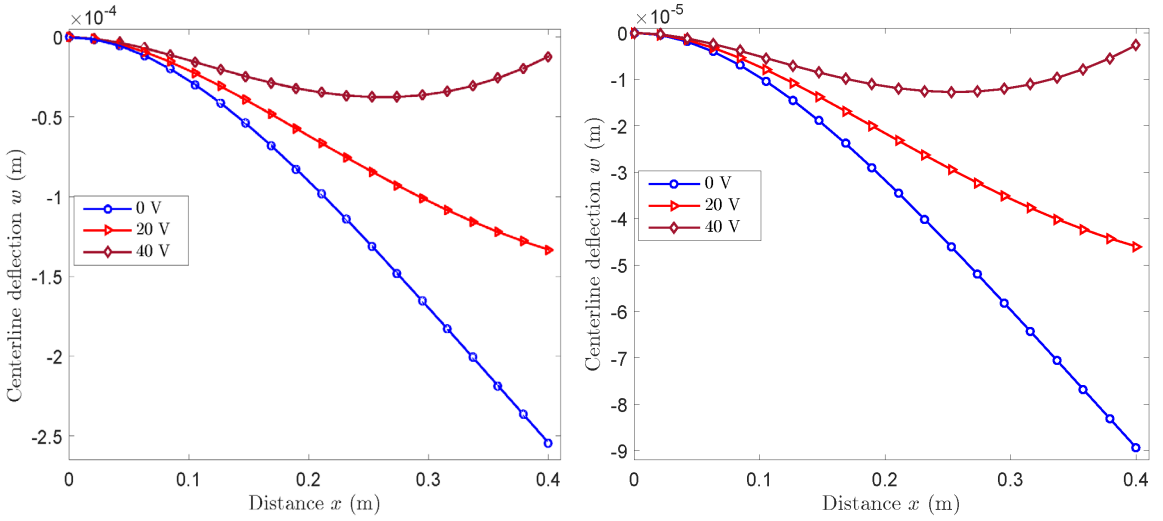

(a) Ti-6Al-4V (b) Aluminum oxide

Figure 5. 3: Profile of the centerline deflection of square piezoelectric FGM plate under a uniform loading and different input voltages.

Next, an FG porous plate reinforced by GPLs integrated with piezoelectric layers, PFGP-GPLs, which has the same geometrical dimensions, boundary conditions and pressure loading with above example is investigated. The material

properties of porous core and face layers, as well as GPL dimensions, are given as the same in Section 5.3.1.1 Table 5. 4 presents the deflection of tip node of cantilever PFGP-GPLs plate with $\Lambda_{GPL} = 0$ and various porosity coefficients under a uniform loading and different input electric voltages. Through our observation, at a specific of input electrical voltage, an increase in porosity coefficients leads to in the deflection of PFGP-GPL plate because the stiffness of plate will decrease significantly as the higher density and larger size of internal pores. Conversely, the deflection of PFGP-GPL plate decreases when the input voltage increases. Meanwhile, Table 5. 5 shows the tip node deflection of a cantilever PFGP-GPL plate for three GPL dispersion patterns with $\Lambda_{GPL} = 1$ *wt*.% and $e_0 = 0.2$ under a uniform loading and different input electric voltages. As expected, the effective stiffness of PFGP-GPLs plate can be greatly reinforced after adding a number of GPLs into matrix materials.

The careful observation shows that the dispersion pattern A dispersed GPLs symmetric through the midplane of plate provides the smallest deflection while the asymmetric dispersion pattern B has the largest deflection. As a result, the dispersion pattern A yields the best reinforcing performance for the static analysis of PFGP-GPLs plate. Besides, for any specific weight fractions, the GPLs dispersion patterns, input electric voltages and porosity coefficients, the porosity distribution 1 always provides the best reinforced performance as evidenced by obtaining the smallest deflection. This comment is clearly shown in Figure 5. 4 which shows the effect of porosity coefficients and GPL weight fractions on the tip deflection of PFGP-GPL plates with input electric voltage of 0V. Possibly to see that the combination between the porosity distribution 1 and GPL dispersion pattern A makes the best structural performance for FG porous square plate compared with all considered combinations.

Figure 5. 5 shows the profile of the centerline deflection of the cantilever PFGP-GPLs plate for various core types and input electric voltages under electro-mechanic loading. Accordingly, four core types constituted by the porosity distribution type 1, the GPL dispersion pattern A and two values of the porosity

coefficients and weight fraction of GPLs are considered in this example. It is observed that the stiffness of the plate is significantly improved when reinforced by GPLs. Besides, the centerline deflection of the plate tends to go backward to the input electric voltage due to the piezoelectric effect. Therefore, if the porous core layer of plate reinforced by GPLs combines with the piezoelectric material, the displacements of the structure will significantly decrease.

Table 5. 4: Tip node deflection $w.10^{-3}$ (m) of a cantilever PFGP-GPLs plate for various porosity coefficients with $\Lambda_{GPL}=0$ under a uniform loading and different input voltages.

Input voltages (V)	e_0 0.0	0.1	0.2	0.4	0.6
	Non-uniform porosity 1				
0	-0.2055	-0.2131	-0.2213	-0.2395	-0.2606
20	-0.1096	-0.1136	-0.1178	-0.1271	-0.1381
40	-0.0137	-0.0140	-0.0142	-0.0148	-0.0156
	Non-uniform porosity 2				
0	-0.2055	-0.2182	-0.2330	-0.2721	-0.3348
20	-0.1096	-0.1162	-0.1238	-0.1438	-0.1761
40	-0.0137	-0.0141	-0.0145	-0.0155	-0.0174
	Uniform porosity				
0	-0.2055	-0.2193	-0.2352	-0.2558	-0.3332
20	-0.1096	-0.1167	-0.1248	-0.1453	-0.1750
40	-0.0137	-0.0141	-0.0144	-0.0154	-0.0168

Table 5. 5: Tip node deflection $w.10^{-3}$ (m) of a cantilever PFGP-GPLs plate for three GPL patterns with $\Lambda_{GPL}=1wt\%$ and e_0 =0.2 under a uniform loading and different input voltages.

GPL patterns	Input voltages (V) 0	20	40	60

	Non-uniform porosity 1	
A	-1.1938 -0.6299 -0.0664	0.4971
B	-1.5325 -0.8107 -0.0898	0.6311
C	-1.4852 -0.7867 -0.0879	0.6108
	Non-uniform porosity 2	
A	-1.2567 -0.6616 -0.0670	0.5276
B	-1.6308 -0.8607 -0.0917	0.6772
C	-1.5657 -0.8274 -0.0894	0.6486
	Uniform porosity	
A	-1.2666 -0.6667 -0.0669	0.5328
B	-1.6243 -0.8576 -0.0911	0.6754
C	-1.5801 -0.8348 -0.0895	0.6559

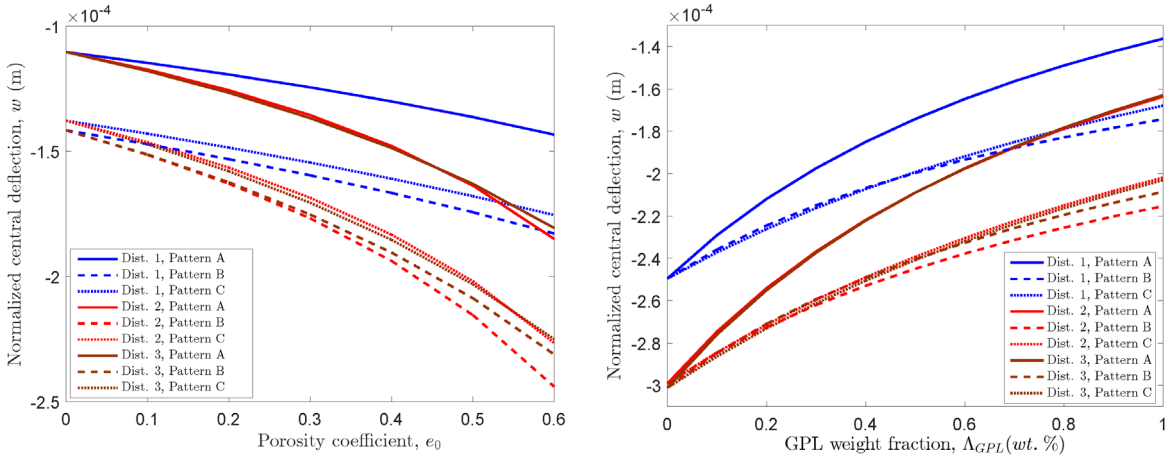

(a) Effect of porosity coefficients with $\Lambda_{GPL} = 1wt\%$

(b) Effect of GPL weight fractions with $e_0 = 0.5$

Figure 5. 4: Effect of porosity coefficients and GPL weight fractions on deflection of PFGP-GPL plates with input voltage of 0V.

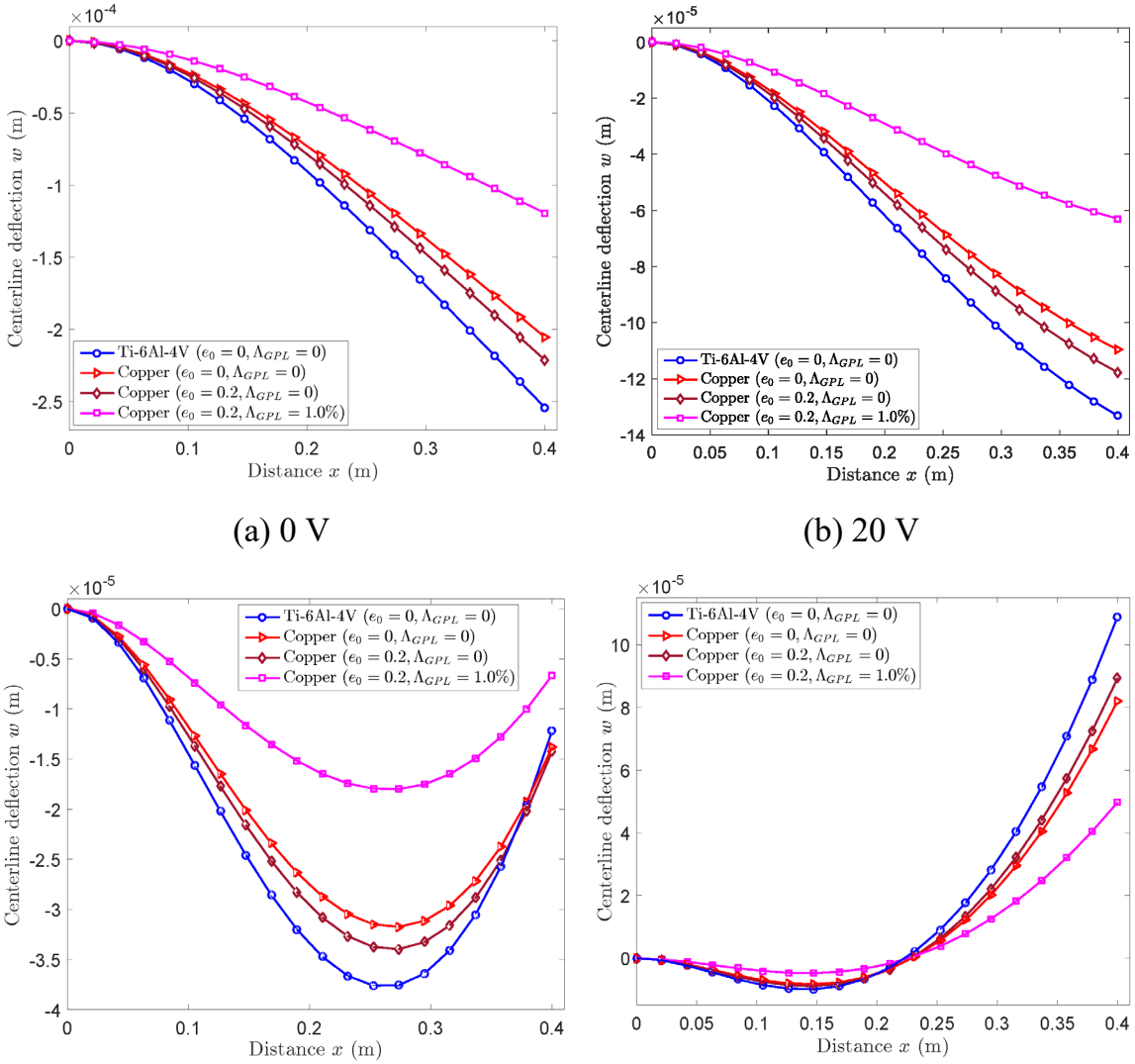

Figure 5. 5: Profile of the centerline deflection of a cantilever PFGP-GPLs plate with many kinds of cores under a uniform loading and different input voltages.

5.3.1.3 Transient analysis

Firstly, a SSSS FGM $\left(\mathrm{Al}/\mathrm{Al_2O_3}\right)$ square plate with 0.2 m in length and 0.01 m in thickness is studied to verify this approach. For this problem, the FG plate is subjected to the transverse load sinusoidally distributed in the spatial domain and varying with time including step, triangular, sinusoidal and explosive blast loads. In the Eqs. (4. 47) and (4. 48), the values of $t_1 = 0.003$ s ; $\gamma = 330$ s^{-1} and $q_0 = 15$ MPa;

and $F(t)$ is plotted as shown in Figure 5. 6. The chosen time step $\Delta t = 2.10^{-5}$ in this study.

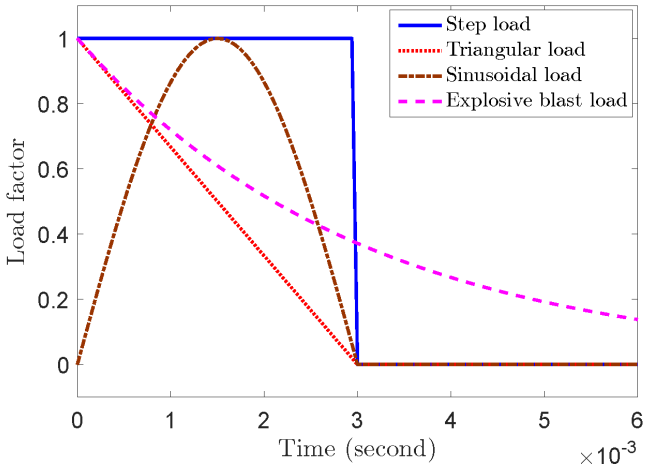

Figure 5. 6: Time history of load factors.

Figure 5. 7 shows the transient responses according to the normalized central deflections $w = w/h$ of the FGM plate with power index of FGM $n = 1$. The obtained results of present solution using IGA through Bézier extraction based on C^0-HSDT are compared with those obtained by Nguyen et al. [157] based on a polygonal finite element method and the quadratic serendipity shape functions. As expected, the results from this approach completely coincide with those of the reference solution.

Next, a SSSS FGP-GPL plate not bonded by piezoelectric layers while the initial parameters and loads are similar to SSSS FGM $\left(\mathrm{Al}/\mathrm{Al_2O_3}\right)$ square plate is considered. Figure 5. 8 shows the variation of the normalized central deflections as a function versus time under various dynamic loadings and different porosity coefficients for porosity distribution 1 and $\Lambda_{GPL} = 0$. Meanwhile, the variation of the normalized central deflections for porosity distribution 1, dispersion pattern A with $\Lambda_{GPL} = 1wt\%$ is also shown in Figure 5. 9. It can be seen that the transient responses of FGP-GPL plate proportionally alter correspondingly to various porosity coefficients. Accordingly, the amplitudes of the normalized central deflection increase with the increase in the porosity coefficient values due to the reduction in

the plate stiffness. As seen in Figure 5. 9 the transient responses of FGP-GPL plate are significantly smaller compared to dynamic responses in Figure 5. 8 as expected.

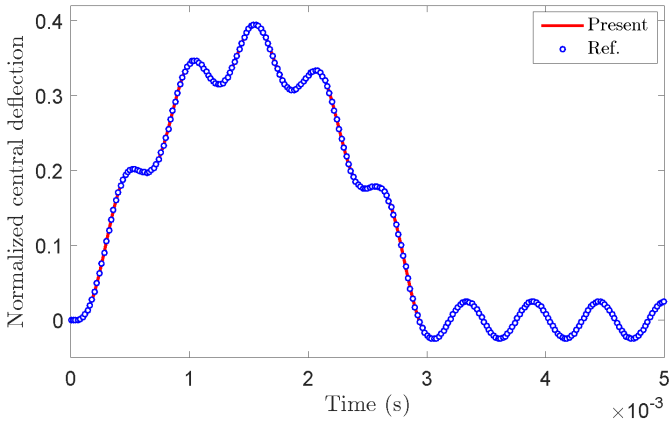

Figure 5. 7: Transient responses of normalized central deflection of a simply supported square Al/Al_2O_3 plate under sinusoidal loading.

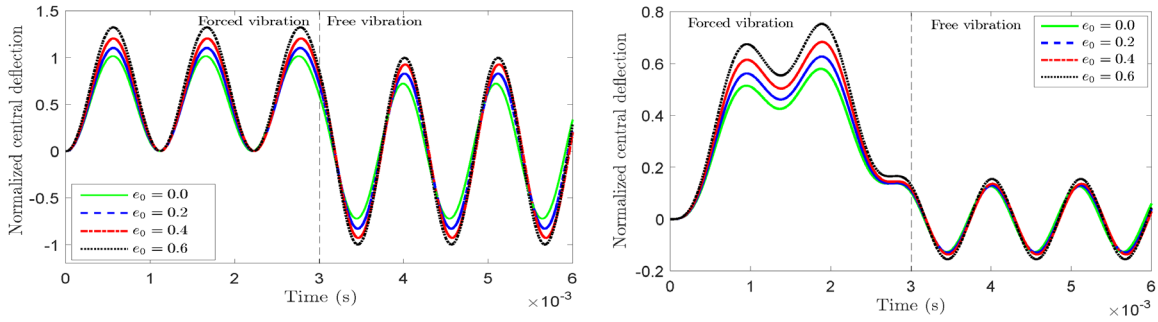

(a) Step load

(b) Sinusoidal load

Figure 5. 8: Influence of different porosity coefficients to the transient responses of FGP-GPL plate for porosity distribution 1 and $\Lambda_{GPL} = 0$ under various dynamic loadings.

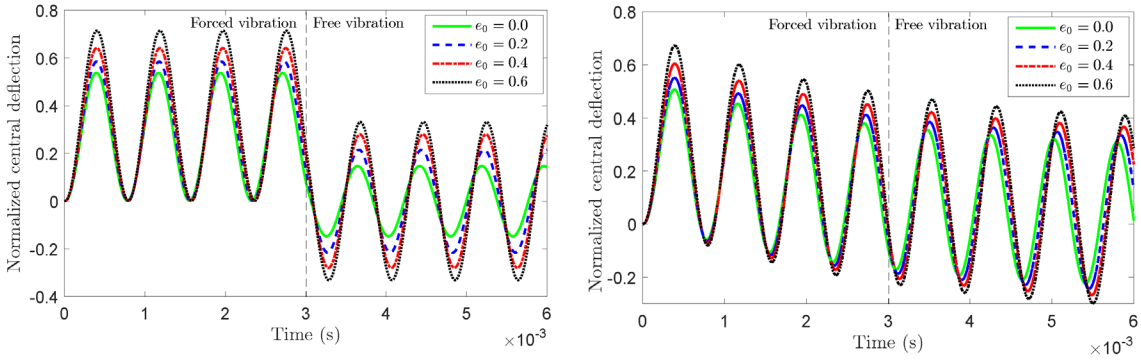

(a) Step load (d) Explosive blast load

Figure 5. 9: Influence of different porosity coefficients to the transient responses of FGP-GPL plate for porosity distribution 1, $\Lambda_{GPL} = 1wt\%$ and pattern A under various dynamic loadings.

The influence of the weight fraction and dispersion pattern of GPLs on the transient responses of FGP-GPL plate is investigated in this example. The influence of different weight fraction values and distribution reinforcements on the transient responses of FGP-GPL plate with uniform porosity distribution and e_0 =0.2 subjected to step loading is shown in Figure 5. 10. Clearly, the dynamic responses of the FGP-GPL plate are considerably affected by weight fraction values. Furthermore, like as static analysis, the amplitude of the dynamic response of FGP-GPL, which is constituted by nonuniform porosity distribution 1 and GPL dispersion pattern A, is the smallest for all the combination of three porosity distributions and GPL dispersion patterns, respectively. As a result, the choice of the non-uniform porosity distribution 1 and the type of GPL dispersion pattern A clearly heads for FGP-GPL plate. In addition, the profile of the normalized centerline deflection with some cases for various dynamic loadings (porosity distribution 1, dispersion pattern A) is shown in Figure 5. 11. In this specific figure, three cases are considered including a solid plate, a porous plate with e_0 =0.4 and a porous plate reinforced by GPLs with $\Lambda_{GPL} = 1wt\%$. It is found that the FGP-GPL in case 3 gives the smallest amplitude of the dynamic response. Therefore, the FG porous plates reinforcement by GPLs is necessary and meaningful to improve the performance structure.

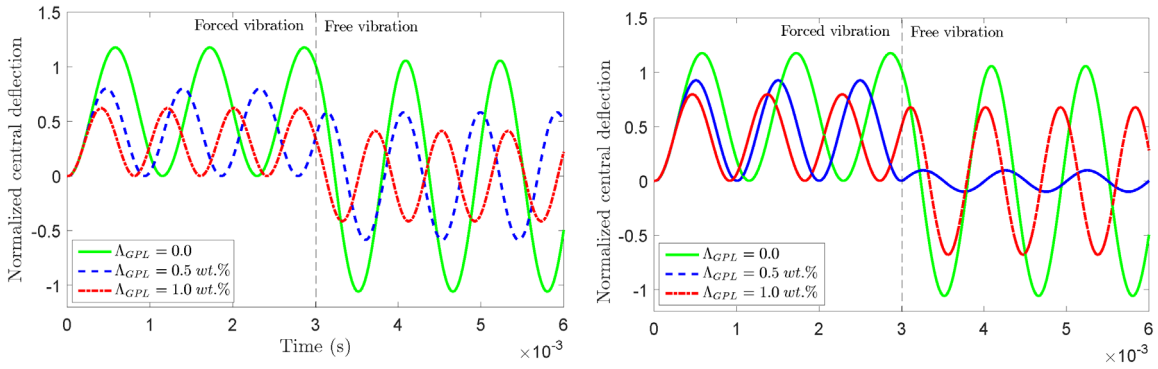

(a) Pattern A (b) Pattern B

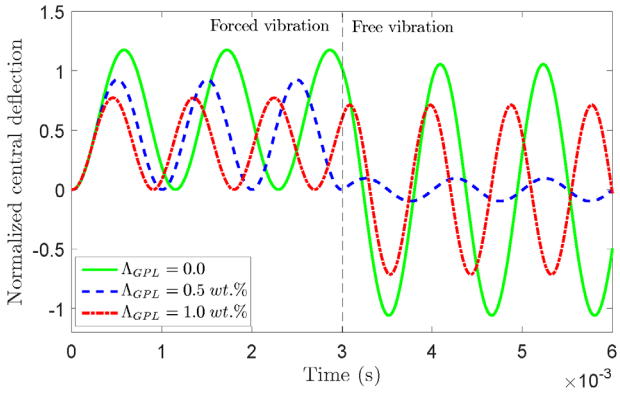

(c) Pattern C

Figure 5. 10: Influence of different weight fraction values to the transient responses of FGP-GPL plate for three GPLs dispersion patterns with uniform porosity distribution and e_0 =0.2 subjected to step loading.

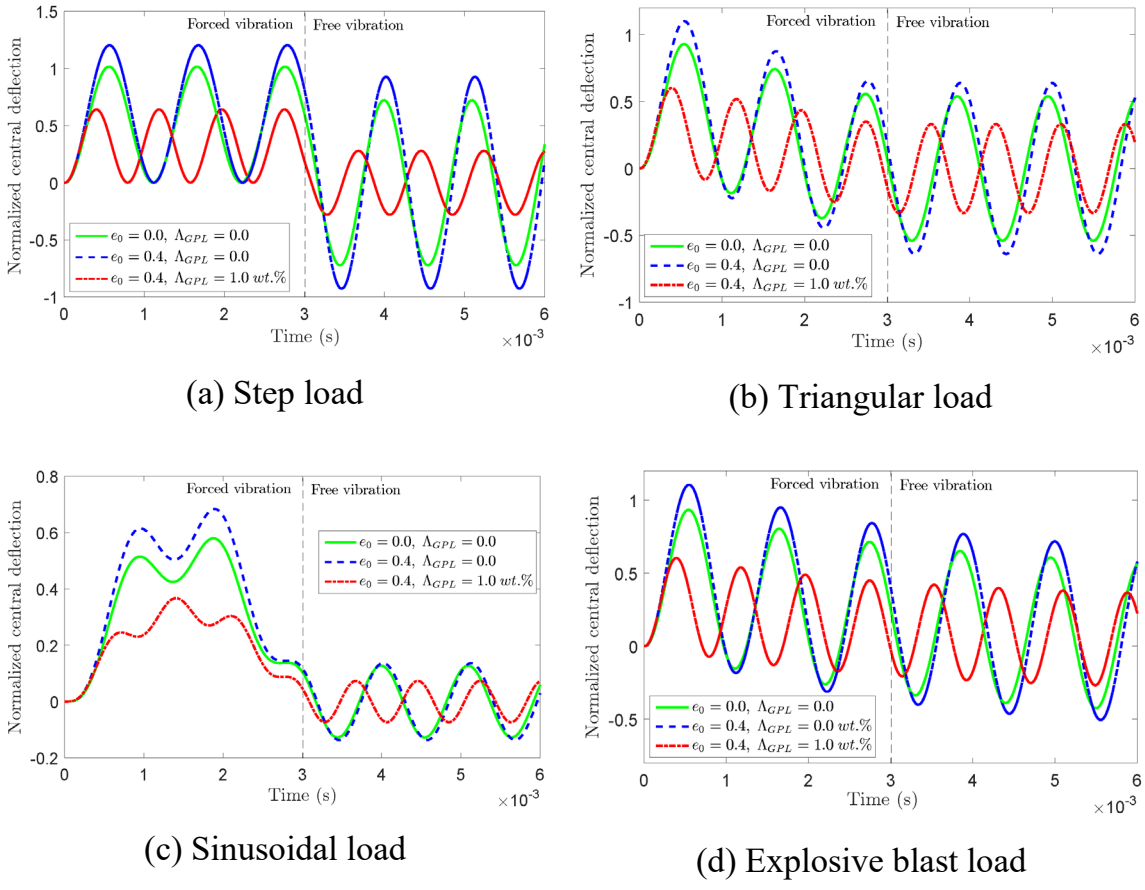

(a) Step load

(b) Triangular load

(c) Sinusoidal load

(d) Explosive blast load

Figure 5. 11: The profile of the normalized centerline deflection of FGP-GPL plate with some cases for porosity distribution 1, pattern A under various dynamic loadings.

In the last example, the above FGP-GPL plate is bonded by piezoelectric layers on both the upper and lower surfaces of the plate, called PFGP-GPL, with the thickness of each piezoelectric layer h_p = 1mm. In this example, the effect of the different porosity coefficients on the transient responses of FGP-GPL and PFGP-GPL plates with the porosity distribution 1 in case of $\Lambda_{GPL} = 0$ is examined. The time histories of the normalized central deflection of FGP-GPL and PFGP-GPL plates are shown in Figure 5. 12. It is found that the amplitude of dynamic response in case of PFGP-GPL plate is smaller than in case of FGP-GPL plate while the porous plate gives the deflection bigger than the solid plate. Note that this comparison is given

since the thickness of the piezoelectric layer is very thin. Combined with the piezoelectric material, the dynamic response of structure will be greatly reduced.

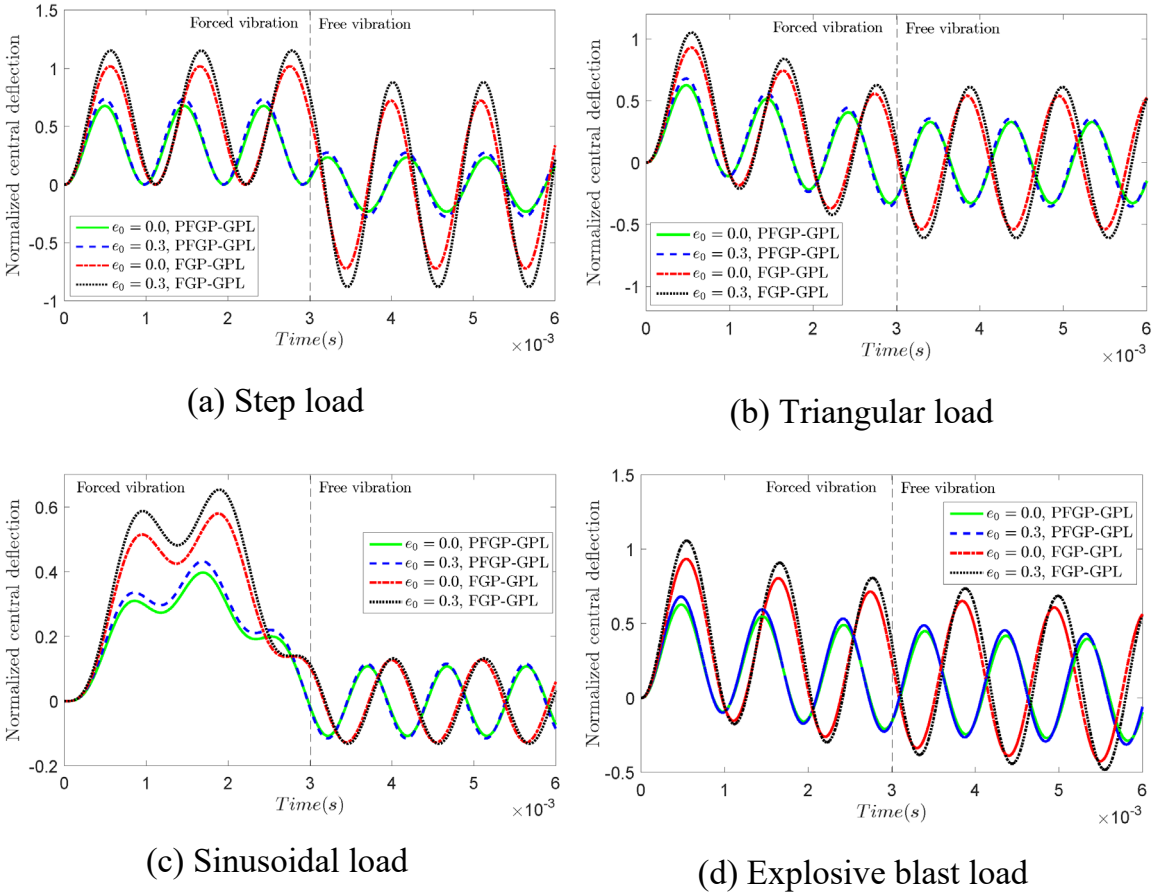

(a) Step load

(b) Triangular load

(c) Sinusoidal load

(d) Explosive blast load

Figure 5. 12: Effect of different porosity coefficients to the transient responses of FGP-GPL and PFGP-GPL plate forporosity distribution 1 and $\Lambda_{GPL}=0$ under various dynamic loadings.

Furthermore, the effect of the different weight fraction values on the transient responses of FGP-GPL and PFGP-GPL plate corresponding to three porosity distributions with dispersion pattern A and e_0 = 0.2 under sinusoidal loading is also depicted in Figure 5. 13. Figure 5. 14 gives the variation of the normalized central deflections as a function subjected to step loading with various weight fractions for three GPL dispersion patterns, uniform porosity distribution and e_0 = 0.2. From Figure 5. 13 and Figure 5. 14, the PFGP-GPL plate with $\Lambda_{GPL}=1wt\%$ provides the smallest normalized central deflection value. In addition, the profile of the normalized centerline deflection of FGP-GPL and PFGP-GPL plates for some cases with porosity

distribution 1, dispersion pattern *A* under the explosive blast loading is plotted in Figure 5. 15. It is observed that the plate with the presence of porosities, reinforced by GPLs and embedded in thin piezoelectric layer provides a very small deflection when compared with other cases. As expected, the combination of porosity distribution 1, the type of GPL dispersion pattern *A* and integration with piezoelectric material is so great in order to decrease the response of structures.

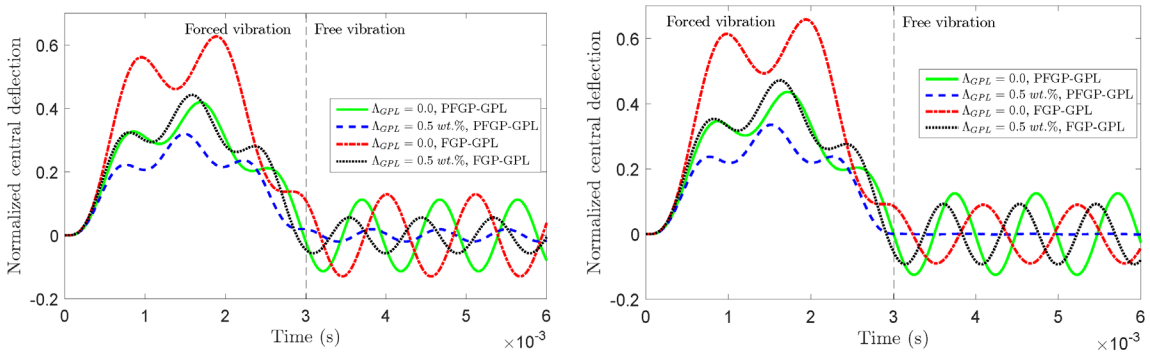

(a) Non-uniform porosity distribution 1 (b) Uniform porosity distribution

Figure 5. 13: Effect of different weight fraction values to the transient responses of FGP-GPL and PFGP-GPL plate for three porosity distributions with pattern *A* and e_0 = 0.2 under sinusoidal loading.

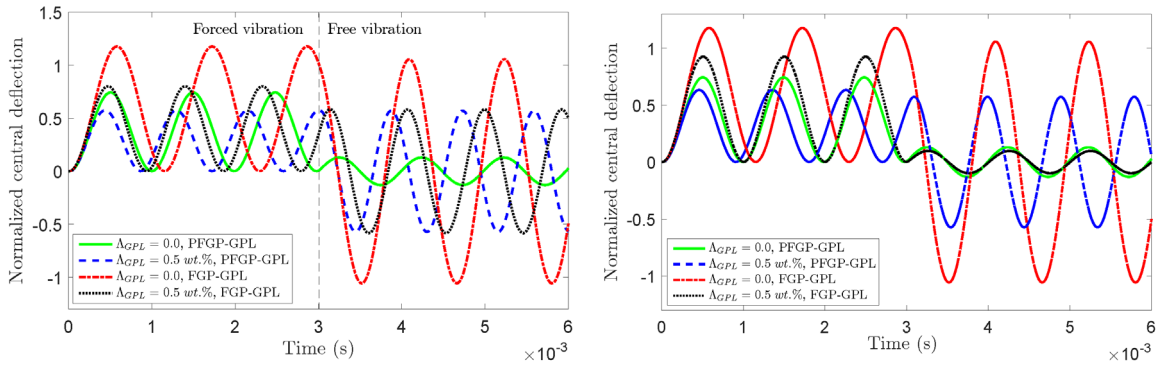

(a) Pattern A (b) Pattern B

Figure 5. 14: Effect of different weight fraction values to the transient responses of FGP-GPL and PFGP-GPL plate for two GPLs dispersion patterns with uniform porosity distribution and e_0 = 0.2 under step loading.

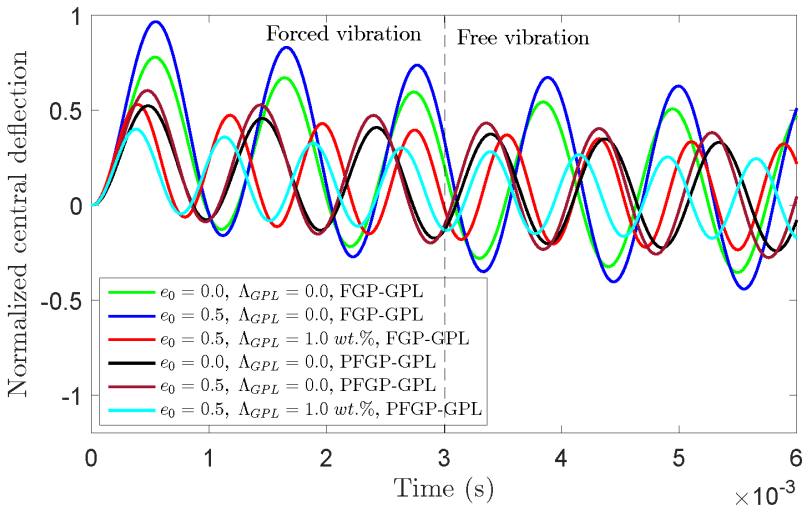

Figure 5. 15: The profile of the normalized centerline deflection of FGP-GPL and PFGP-GPL plate for some cases with porosity distribution 1, pattern A under the explosive blast loading.

5.3.2 Nonlinear analysis

In this study, the Newton-Raphson iterative procedure [159] is employed to obtain the solutions of the nonlinear problems. Accordingly, the iterations, where the solutions of the current time step can be obtained based on the solutions of the previous time step, are repeated until the solutions converge. For the geometrically nonlinear dynamic analysis of the FG plate under various dynamic loadings, which the equations of dynamic problem depend on both the time domain and unknown displacement vector, the Newmark's integration scheme is adopted. In all numerical examples, the PZT-G1195N piezoelectric layer is employed and perfectly bonded on the top and bottom surfaces of the FG plate structure as well as ignored the adhesive layers.

5.3.2.1 Validation analysis

In this section, various numerical studies regarding the geometrically nonlinear static and dynamic analyses of the isotropic as well as the piezoelectric FG square plates are carried out in order to demonstrate the accuracy and stability of the present approach. Firstly, a fully clamped (CCCC) isotropic square plate is considered to show the validity of the present formulation for the geometrically

nonlinear analysis. The plate is subjected to uniformly distributed load while the width-to-thickness ratio (a/h) is taken equal to 100. The material properties of the plate are $E = 3 \times 10^7$ psi and $\nu = 0.316$. In this example, the normalized central deflection and load parameter can be defined as $w = w/h$ and $P = q_0 a^4/(Eh^2)$, respectively. Table 5. 6 presents the normalized central deflections of the isotropic square plate which are compared with those of the Levy's analytical solution [160], Urthaler and Reddy's mixed FEM using FSDT [161] and Nguyen et al. [162] based on IGA and refined plate theory (RPT). As can be observed that the proposed results are in good agreement with the existing analytical solution as well as other approximate results.

Table 5. 6: Normalized central deflection *w* of CCCC isotropic square plate under the uniform load with *a*/*h* = 100.

P	Present	Analytical [160]	MXFEM [161]	IGA-RPT [162]
17.79	0.2348	0.237	0.2328	0.2365
38.3	0.4663	0.471	0.4738	0.4692
63.4	0.6873	0.695	0.6965	0.6908
95.0	0.8983	0.912	0.9087	0.9024
134.9	1.1016	1.121	1.1130	1.1060
184.0	1.2960	1.323	1.3080	1.3008
245.0	1.4875	1.521	1.5010	1.4926
318.0	1.6728	1.714	1.6880	1.6784
402.0	1.8492	1.902	1.8660	1.8552

Next, in order to verify the accuracy of the proposed approach for the geometrically nonlinear transient analysis, a fully simply supported (SSSS) orthotropic square plate subjected to uniform load with $q_0 = 1.0$ MPa is conducted in this example. The material properties and the geometry of plate are considered as follows: Young's modulus $E_1 = 525\text{Pa}$, $E_2 = 21\text{Pa}$, shear modulus $G_{12} = G_{23} = G_{13} = 10.5\text{Pa}$, Poisson's ratio $\nu = 0.25$, mass density $\rho = 800\text{kg/m}^3$, length of the plate $L = 0.25\text{m}$ and thickness $h = 5$ mm. Figure 5. 16 depicts the geometrically nonlinear transient response of the square plate subjected to a uniform load. It can be seen that the present results are in an excellent agreement with those obtained from the finite strip method, which was reported by Chen et al. [163].

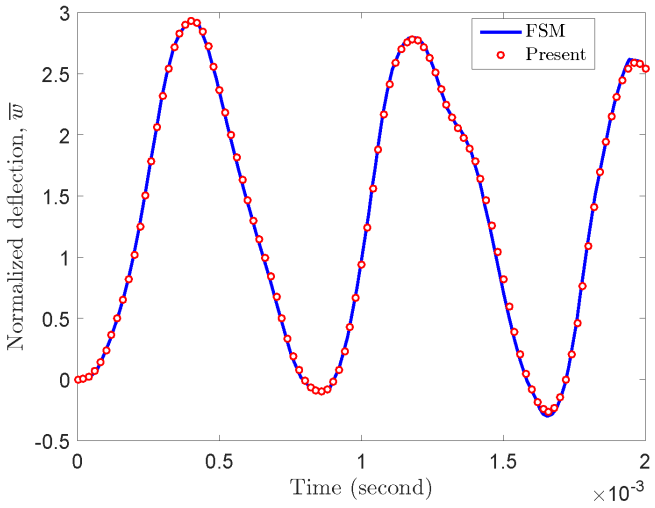

Figure 5. 16: Normalized nonlinear transient central deflection of a square orthotropic plate under the uniform load.

Last but not least, a cantilever piezoelectric FG square plate is exhaustively presented to demonstrate the accuracy and validity of the present method for the static analysis of the FG plates integrated with piezoelectric layers. The FG plate which is bonded by two piezoelectric layers on both the upper and the lower surfaces is made of aluminum oxide and Ti-6A1-4V materials whose material properties are given in Table 5. 1. In this study, the rule of mixture [164] is utilized to describe the distribution of the ceramic and metal phases in the core layer. The plate has a side length $a = b = 0.4\text{m}$ while the thickness of the FG core layer and each piezoelectric layer are $h_c = 5$ mm and $h_p = 0.1\text{mm}$, respectively. The cantilever piezoelectric FG plate is simultaneously subjected to a uniformly distributed load with $q_0 = 100\ \text{N}/\text{m}^2$ and various input voltage values. The centerline linear deflections of the piezoelectric FG square plate are plotted in Figure 5. 17 while the tip node deflections are also listed in Table 5. 7 with various material index n. The results which are generated from the proposed method are compared with those reported in [156] using a cell-based smoothed discrete shear gap method (CS-DSG3) based on FSDT. It can be observed that the results obtained by the present formulation generally agree well with the reference solutions.

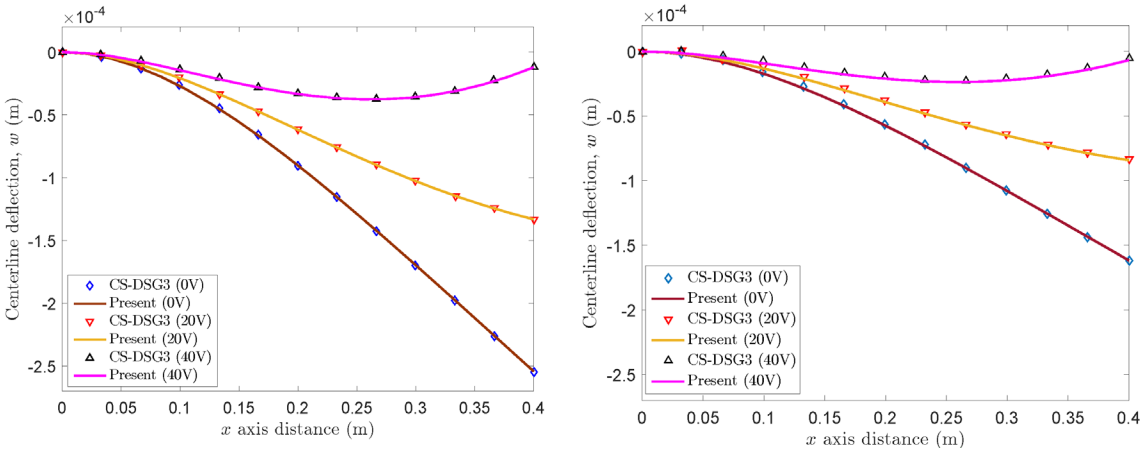

(a) $n = 0$ (b) $n = 0.5$

Figure 5. 17: Centerline linear deflections of the cantilever piezoelectric FG plate under the uniform loading and various actuator input voltages with $n = 0$ and $n = 0.5$.

Table 5. 7: Tip node deflection of the cantilever piezoelectric FGM plate subjected to the uniform load and various input voltages (x 10^{-4} m).

n	Method	Input voltages (V)		
		0	20	40
n=0	Present	-2.5437	-1.3328	-0.1229
	CS-DSG3 [156]	-2.5460	-1.3346	-0.1232
n =0.5	Present	-1.6169	-0.8418	-0.0667
	CS-DSG3 [156]	-1.6199	-0.8440	-0.0681
n=5	Present	-1.1233	-0.5808	-0.0382
	CS-DSG3 [156]	-1.1266	-0.5820	-0.0375
$n = \infty$	Present	-0.8946	-0.4608	-0.0271
	CS-DSG3 [156]	-0.8947	-0.4609	-0.0271

In the next part, investigations into the geometrically nonlinear static and dynamic responses of the piezoelectric FG porous square plate reinforced by GPLs will be presented.

5.3.2.2 Geometrically nonlinear static analysis

Firstly, the geometrically nonlinear static analysis of a piezoelectric FG plate subjected to a uniform load with parameter load $q = q_0 \times 10^3$ is addressed. A SSSS piezoelectric FG square plate which is made of aluminum oxide and Ti-6A1-4V has a side length $a = b = 0.2$m, thickness of FG core layer $h_c = 2$ mm and thickness of

each piezoelectric layer $h_p = 0.1$ mm. Figure 5. 18 illustrates the influence of the material index n on the normalized linear and nonlinear central deflections of the piezoelectric FG plates under mechanical load. As can be seen that, by increasing the material index n, the deflection of the piezoelectric FG plate decreases gradually. The largest deflection is obtained when material index $n = 0$, where the plate consists only of Ti-6A1-4V leads to the decrease in the bending stiffness. Furthermore, the values of the central deflection of the geometrically nonlinear analysis are always smaller than that of the linear one and this difference reduces with the increase of the material index.

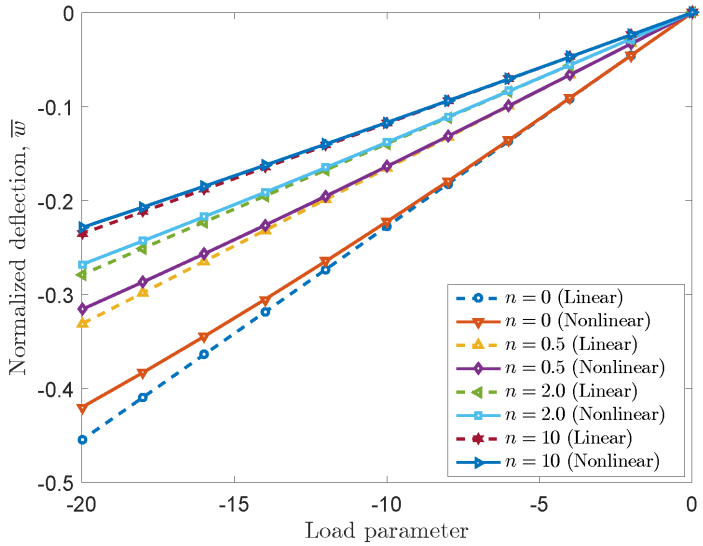

Figure 5. 18: Effect of the material index *n* on the linear and nonlinear central deflections of the piezoelectric FG plate under the mechanical load.

Next, a SSSS piezoelectric FG plate with a porous core layer which is constituted by combining two porosity distribution types and three GPL dispersion patterns, respectively, is considered in this example. The piezoelectric FG plate is subjected to a sinusoidally distributed load which is defined as $q = q_0 sin(\pi x/a) sin(\pi y/b)$ in which $q_0 = 1.0$MPa. The plate has a side length $a = b = 0.4$ m, the thickness of the FG porous core layer $h_c = 20$ mm and thickness of each piezoelectric layer $h_p = 1$ mm. In this study, the copper is chosen as the metal matrix whose material properties are given in Table 5. 1 while the dimensions of GPLs are $l_{GPL} = 2.5$ µm, $w_{GPL} =$

1.5 μm, $t_{GPL} = 1.5$ nm. Figure 5. 19 examines the influence of the porosity coefficients on the nonlinear deflection of the piezoelectric FG porous plate with GPL dispersion pattern A ($\Lambda_{GPL} = 1.0wt.\%$) for two porosity distribution types, respectively. It can be observed that an increase of the porosity coefficients leads to the rise in the nonlinear deflection of the FG porous plate since the higher density of internal pores in material yields the reduction in stiffness of plate structures. In addition, Figure 5. 20 depicts the effect of the weight fraction and the GPL dispersion patterns on the nonlinear deflection of the piezoelectric FG porous plate with $e_0 = 0.2$ and two porosity distribution types, respectively. It can be observed that the effective stiffness of the FG porous core layer is greatly strengthened when adding a small amount of GPLs ($\Lambda_{GPL} = 1.0wt.\%$) into the metal matrix as evidenced by decreasing the nonlinear deflection of the FG plate. More importantly, the reinforcing effect of GPLs also depends significantly on the dispersion of GPLs in the material matrix. Accordingly, with the same weight fraction of GPLs, the dispersion pattern A, where GPLs are dispersed symmetrically through the midplane of the porous core layer, the plate achieves the smallest nonlinear deflection while the asymmetric dispersion pattern B provides the largest one. For further illustration, Figure 5. 21 depicts the variation of the nonlinear deflection of the piezoelectric FG porous plate reinforced by GPLs which is constituted by porosity distribution 1 and three different GPL dispersion patterns corresponding to parameter load 10, respectively.

The combined influences of two porosity distribution types and three GPL dispersion patterns on the nonlinear deflection of the piezoelectric FG porous plate with $\Lambda_{GPL} = 1.0wt.\%$ and $e_0 = 0.4$ are also investigated. As evidently depicted in Figure 5. 22 for all the considered associations, the combination between the porosity distribution 1 and the GPL dispersion pattern A obtains the best reinforcing performance in the geometrically nonlinear static analysis of the piezoelectric FG porous plate. This observation indicated that the plate structures, where the internal pores are distributed on the midplane and GPLs are dispersed around the top and bottom surfaces, can provide the optimum reinforcement.

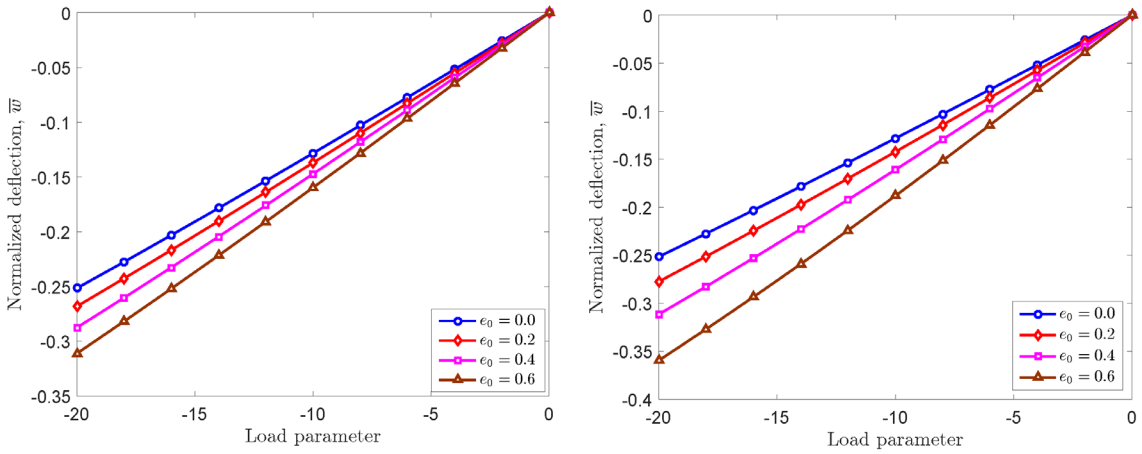

(a) Porosity distribution 1 (b) Porosity distribution 2

Figure 5. 19: Effect of the porosity coefficients on the nonlinear deflection of the piezoelectric FG porous square plate with GPL dispersion pattern A and $\Lambda_{GPL} = 1wt\%$.

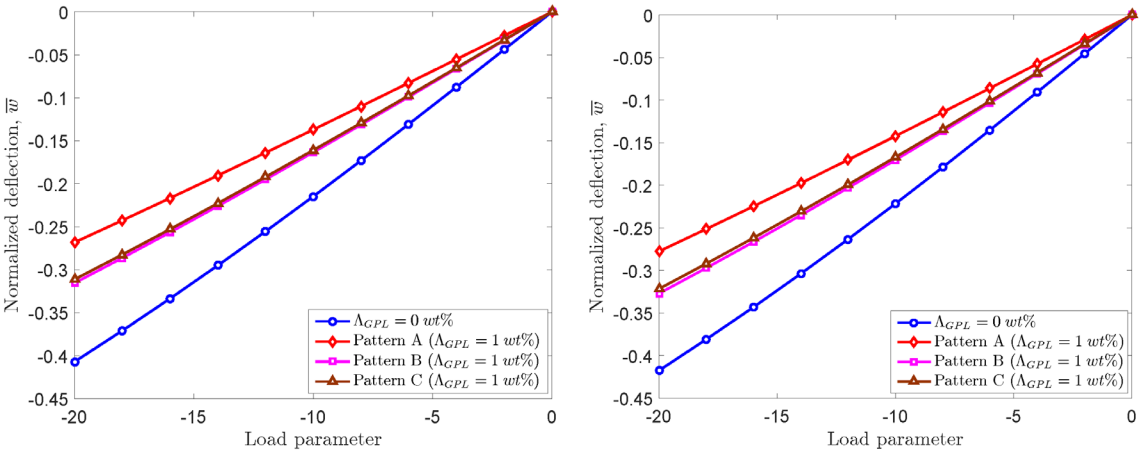

(a) Porosity distribution 1 (b) Porosity distribution 2

Figure 5. 20: Effect of the weight fractions and dispersion patterns of GPLs on the nonlinear deflection of the piezoelectric FG porous square plate with $e_0 = 0.2$.

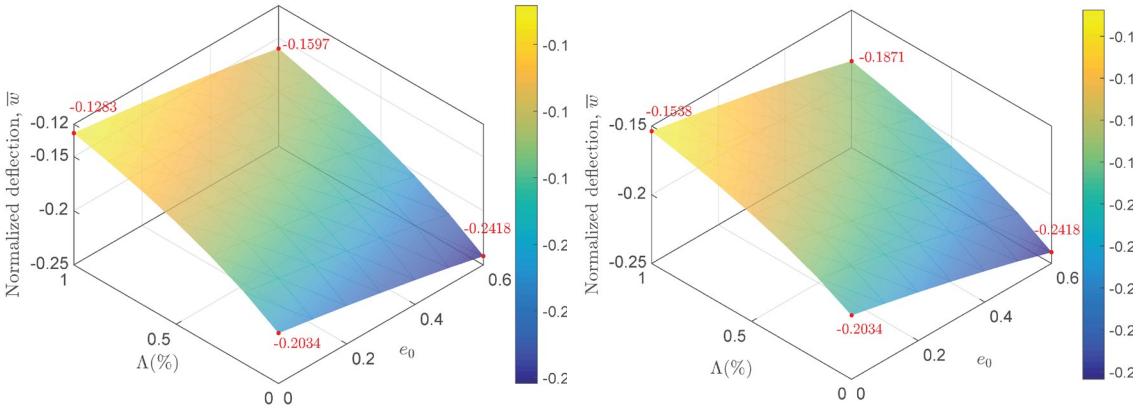

(a) Pattern A (b) Pattern B

Figure 5. 21: Effect of the porosity coefficients and weight fractions of GPLs on the nonlinear deflection of piezoelectric FG porous square plate for porosity distribution 1 and different GPL dispersion patterns.

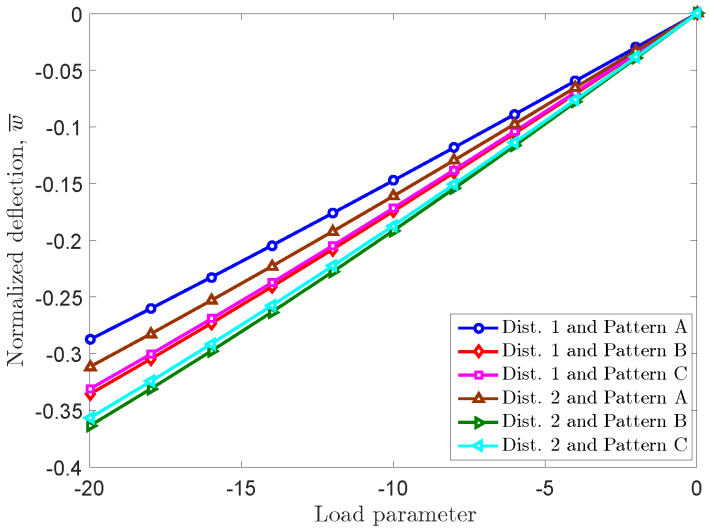

Figure 5. 22: Effect of the porosity distributions and GPL dispersion patterns on the nonlinear deflection of the piezoelectric FG porous square plate with $e_0 = 0.4$ and $\Lambda_{GPL} = 1wt\%$.

5.3.2.3 Geometrically nonlinear dynamic analysis

In this part, the geometrically nonlinear dynamic responses of a CCCC piezoelectric FG porous plate reinforced by GPLs are studied. The dimensions and the material properties of the FG plate are the same previous example. The plate is assumed to be subjected to time-dependent sinusoidally distributed transverse loads.

In Eqs. (4. 47) and (4. 48), given $t_1 = 0.003$ s ; $\gamma = 330$ s^{-1} and $q_0 = 100$ MPa. Figure 5. 23 illustrates the influence of the porosity coefficient on the nonlinear transient response of the piezoelectric FG porous plate with porosity distribution 1 and dispersion pattern A ($\Lambda_{GPL} = 1.0wt.\%$) under step and sinusoidal loads, respectively. It can be seen that by increasing the porosity coefficients, the amplitude of the transverse deflection of the FG porous plate can be increased while the period of motion does not seem to affect. It can be concluded that the presence of porosities in the core layer of the FG plate reduces the capacity of itself against external excitation. Furthermore, Figure 5. 24 demonstrates the influence of the weight fraction and the dispersion pattern of GPLs on the nonlinear transient response of the piezoelectric FG porous plate with $e_0 = 0.2$ and porosity distribution 2 corresponding to triangular and explosive blast loads, respectively. As expected, a smaller magnitude of the deflection can be obtained when the weight fraction of GPLs in metal matrix increase. Again, the dispersion of GPLs into the metal matrix also affects the reinforcing performance of structure that dispersion pattern *A* provides the smallest magnitude of the deflection.

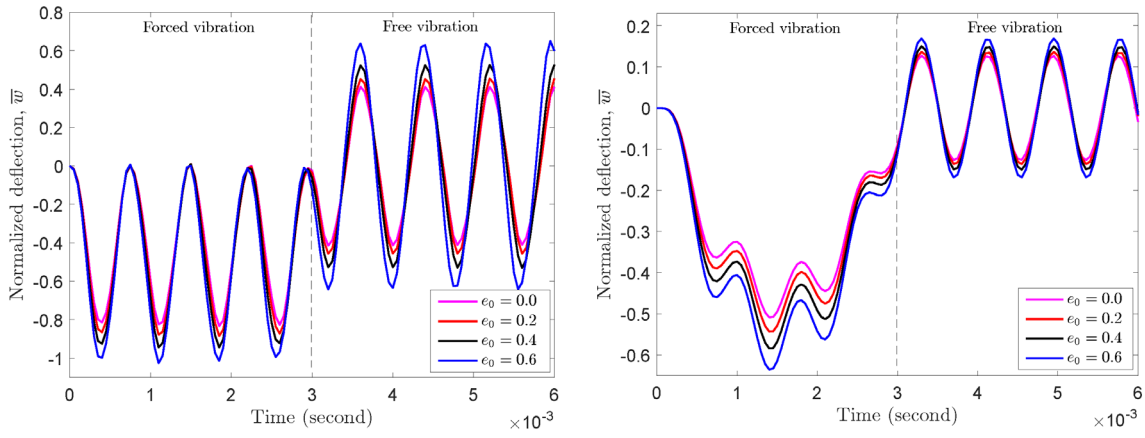

(a) Step load (b) Sinusoidal load

Figure 5. 23: Effect of the porosity coefficients on the nonlinear dynamic responses of the CCCC piezoelectric FG porous plate with GPL dispersion pattern A and $\Lambda_{GPL} = 1wt\%$.

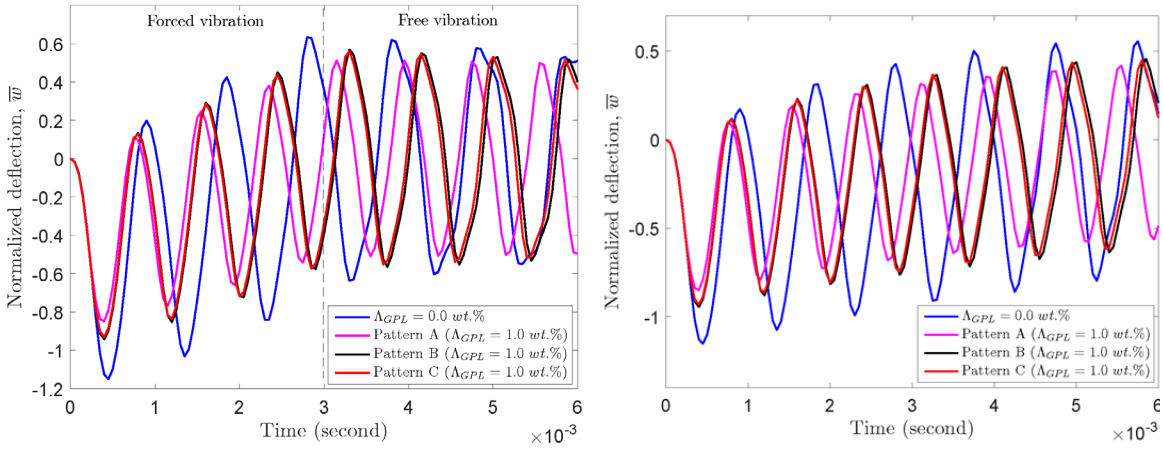

(a) Triangular load (b) Explosive blast load

Figure 5. 24: Effect of the weight fractions and dispersion patterns of GPLs on the nonlinear dynamic responses of the CCCC piezoelectric FG porous square plate with porosity distribution 2 and $e_0 = 0.2$.

Next, the combined influences of various porosity distribution types and the GPL dispersion patterns on the nonlinear dynamic response of the piezoelectric FG plate is also examined and indicated in Figure 5. 25. For this specific example, the porous core layer of the piezoelectric plate has the porosity coefficient $e_0 = 0.4$ and the GPL weight fraction $\Lambda_{GPL} = 1.0wt.\ \%$. As clearly demonstrated in Figure 5. 25 the combination between the porosity distribution 1 and the GPL dispersion pattern A always provides the best reinforcement as evidenced by obtaining the smallest amplitude of the deflection. Moreover, the dynamic responses of the linear and nonlinear of the FG porous plate with porosity distribution 2 ($e_0 = 0.3$) and the GPL dispersion pattern C ($\Lambda_{GPL} = 1.0wt.\%$) under triangular and sinusoidal loads are also considered and depicted in Figure 5. 26. As can be observed, the geometrically nonlinear responses generally obtain smaller magnitudes of the deflection and periods of motion.

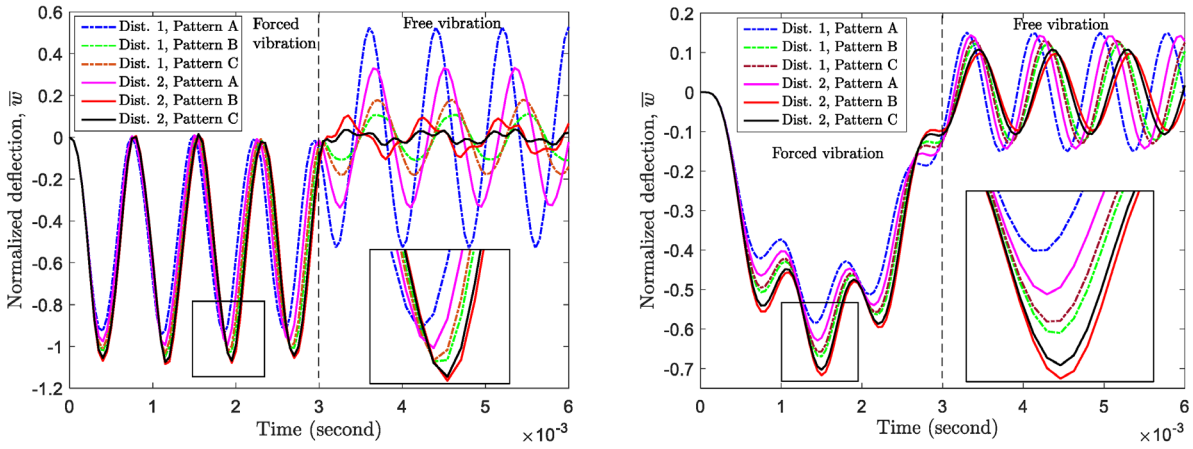

(a) Step load (b) Sinusoidal load

Figure 5. 25: Effect of the porosity distributions and GPL dispersion patterns on the nonlinear dynamic responses of the CCCC piezoelectric FG porous square plate with $e_0 = 0.2$ and $\Lambda_{GPL} = 1wt\%$.

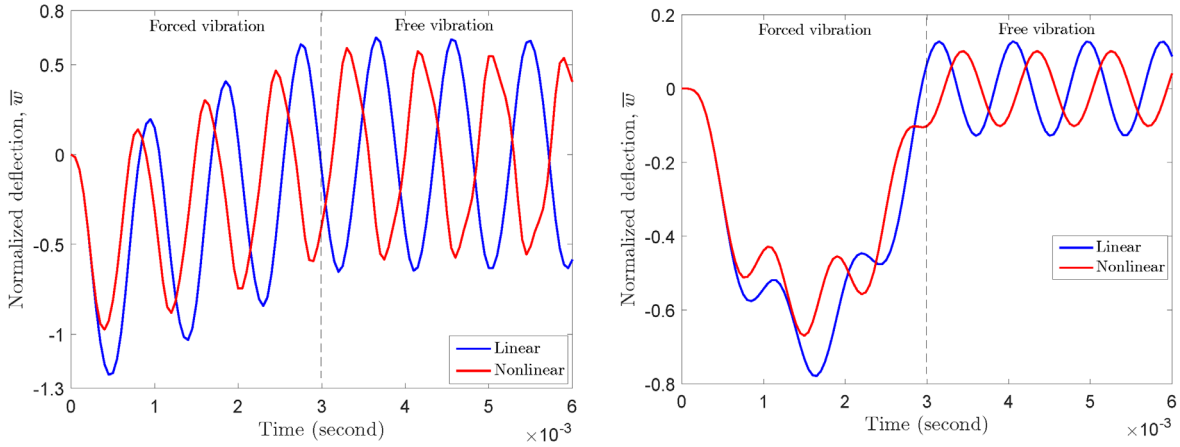

(a) Triangular load (b) Sinusoidal load

Figure 5. 26: Linear and nonlinear dynamic responses of the CCCC piezoelectric FG porous square plate with porosity distribution 2 $e_0 = 0.3$ and dispersion pattern C ($\Lambda_{GPL} = 1wt\%$).

5.3.2.4 Static and dynamic responses active control

In this section, the active control for the static and dynamic responses of the FG porous plate reinforced by GPLs using integrated sensors and actuators is investigated. Firstly, the active control for the linear static responses of a SSSS FG plate which is subjected to a uniformly distributed load with $q_0 = 100\mathrm{N/m^2}$ is

investigated to verify the accuracy of the proposed approach. The FG plate composed of Ti-6A1-4V and aluminum oxide materials with material index $n = 2$ and has the side length $a = b = 0.2$m while the thickness of core FG layer and each piezoelectric layer are taken to be 1 mm and 0.1 mm, respectively. Figure 5. 27 illustrates the linear static deflections of the FG plate with various displacement feedback control gains G_d. As can be observed that the present results agree well with the reference solution reported in [156] who employed the CS-DSG3 based on FSDT. As expected, when the displacement feedback control gain G_d increases, the linear static deflection of the FG plate decreases. Furthermore, the active control for the linear dynamic responses of the FG plate is also investigated based on a constant velocity feedback control algorithm G_v and closed-loop control. In this specific example, the FG plate is initially subjected to a uniform load $q_0 = 100\text{N/m}^2$ and then the load is suddenly removed. In this study, the modal superposition is adopted in order to reduce the computational cost and the first six modes are considered in the modal space analysis, while the initial modal damping ratio for each mode is assumed to be 0.8 %. Figure 5. 28 shows the linear dynamic responses of the central deflection of the FG plate. The results which are generated from the present method agree well with the reference solution [156].

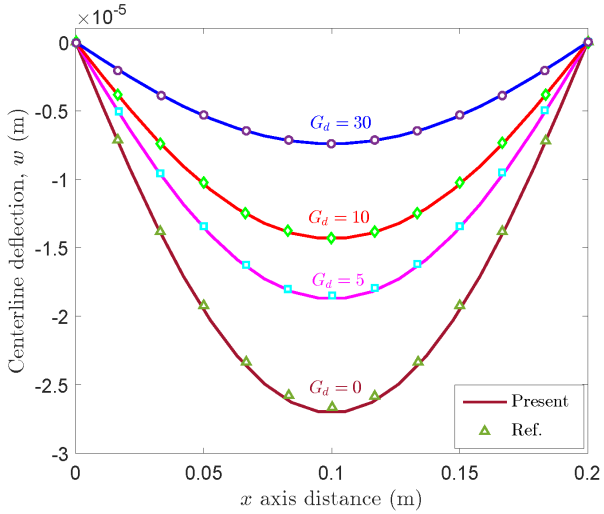

Figure 5. 27: Effect of the displacement feedback control gain G_d on the linear static responses of the SSSS plate subjected to uniformly distributed load.

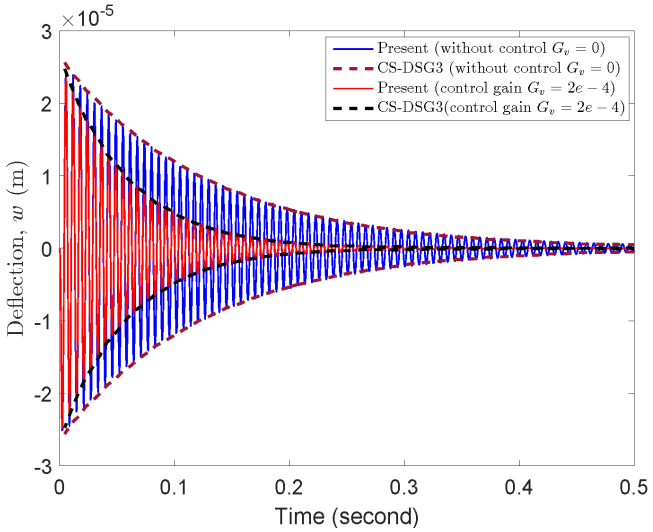

Figure 5. 28: Effect of the velocity feedback control gain G_v on the linear dynamic response of the SSSS FG square plate.

Next, the active control for the nonlinear static responses of the SSSS FG porous plate reinforced with GPLs is further investigated in this part. The FG plate consisting of the combination of the porosity distribution 1 and GPL dispersion pattern A, which provides the best structural performance, is selected to study. The material properties of the FG porous plate are the same in Sub-section 5.2.3.2. The plate has a side length $a = b = 0.4$m, the thickness of the FG porous core layer $h_c = 20$ mm and thickness of each piezoelectric layer $h_p = 1$ mm under sinusoidally distributed load which is defined as $q = q_0 sin(\pi x/a) sin(\pi y/b)$ with $q_0 = 1.0$MPa. Figure 5. 29 depicts the nonlinear static deflection of the FG porous reinforced by GPLs with the porosity coefficient $e_0 = 0.4$ and the GPL weight fraction $\Lambda_{GPL} = 1.0wt.\%$ corresponding to various displacement feedback control gains. It can be observed that the deflection of the FG porous plate decreases significantly when the displacement feedback control gain increase.

In the last example, the active control for the geometrically nonlinear dynamic responses of the CCCC FG porous plate reinforced by GPLs is conducted. The plate has both length and width set the same at 0.2 m with the thickness of core layer $h_c = 10$ mm and each piezoelectric layer $h_p = 0.1$ mm. The FG plate with the porosity distribution 1 ($e_0 = 0.4$) and dispersion pattern A ($\Lambda_{GPL} = 1.0wt.\%$) is subjected to

sinusoidally distributed transverse loads. Figure 5. 30 illustrates the nonlinear dynamic responses of the central deflection of the FG plate corresponding to various velocity feedback control gains G_v. It can be observed that when the control gain G_v is equal to zero corresponding to without control case, the nonlinear dynamic response of the FG porous plate still attenuates with respect to time since the effect of the structural damping is considered in this study. More importantly, the geometrically nonlinear dynamic response can be suppressed faster in the case controlled by higher velocity feedback control gain values. As a result, depending on the specific cases, the responses of the FG porous plate structures including deflection, oscillation time or even both can be controlled to satisfy an expectation by designing an appropriate value for the velocity feedback control gain. It should be noted that the feedback control gain values could not be increased without limit since piezoelectric materials have their own breakdown voltage values. In addition, Figure 5. 31 depicts the influence of the velocity feedback control gain G_v on the linear and nonlinear responses of the CCCC FG porous square plate subjected to step load. As expected, the geometrically nonlinear dynamic responses provide smaller magnitudes of the deflection and periods of motion.

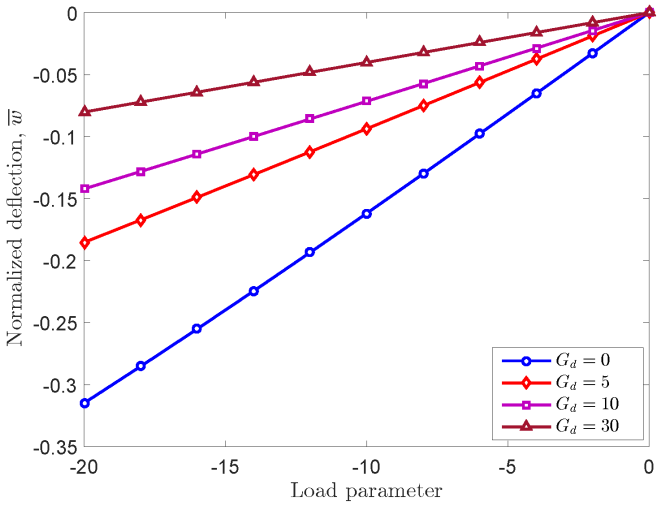

Figure 5. 29: Effect of the displacement feedback control gain G_d on the nonlinear static responses of the SSSS FG porous plate with porosity distribution 1 ($e_0 = 0.4$) and dispersion pattern A ($\Lambda_{GPL} = 1wt\%$).

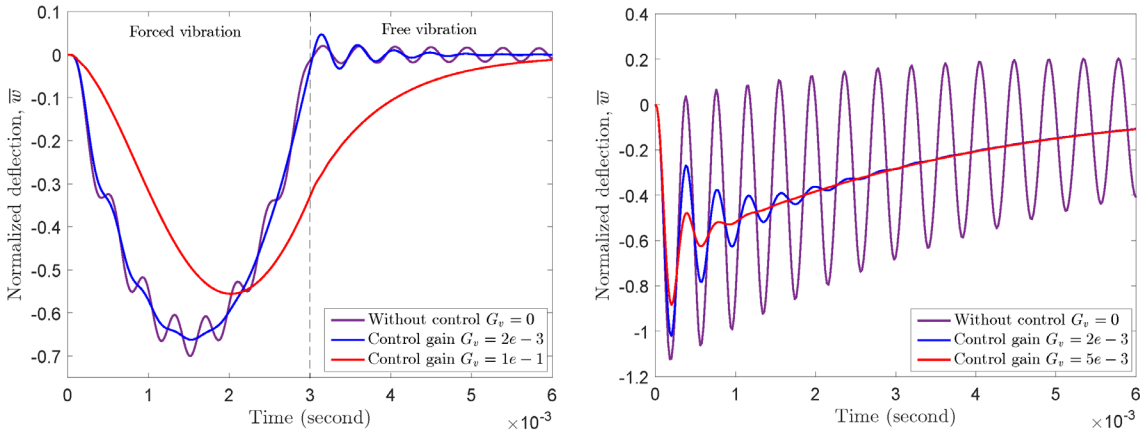

(a) Sinusoidal load (b) Explosive blast load

Figure 5. 30: Effect of the velocity feedback control gain G_v on the nonlinear dynamic responses of the CCCC FG porous square plate subjected to dynamic loadings.

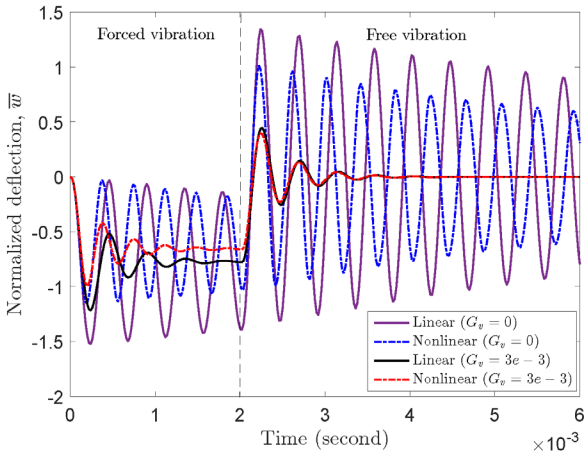

Figure 5. 31: Effect of the velocity feedback control gain G_v on the linear and nonlinear dynamic responses of the CCCC FG porous square plate subjected to step load.

5.4 Concluding remarks

An effective numerical model within the framework of an isogeometric analysis (IGA) based on the Bézier extraction in associated with the C^0-HSDT has been investigated for the bending and transient responses of PFGP-GPLs plates subjected to static and dynamic loadings. An addition, the geometrically nonlinear static and

dynamic responses for PFGP-GPLs plates are also given. The combination of the IGA with the most advantage in terms of exact geometries and the Bézier extraction leading to integrating the IGA into the existing FEM structure becomes easily and efficiently. The core layer of plate constituted by the combination of three porosity distribution types and dispersion pattern of GPLs, respectively is considered. The mechanical displacement field is approximated through the C^0-HSDT model applying IGA and Bézier extraction while the electric potential is assumed to vary linearly along the thickness of each piezoelectric sublayer. By the static and transient analyses, the influences of different parameters including external electric voltage, porosity distribution type, porosity coefficient, dispersion pattern and weight fraction of GPL on the behaviors of PFGP-GPLs plates are exhaustively studied. Interestingly, the obtained results agree well with extant studies or available solutions in the literature. Furthermore, numerical solutions for PFGP-GPLs has been achieved, while analytical solutions for them have not been found yet. The control algorithms based on the constant displacement and velocity feedbacks were utilized to control the geometrically nonlinear static and dynamic responses of the FG porous plate reinforced with GPLs. Some remarkable conclusions show the following significant contributions

- The suggested approach has been successfully employed to study the static and transient problems of PFGP-GPL.
- The stiffness of FG porous plate greatly decreases due to porosity coefficients. However, the stiffness of the plates remarkably increases as the FG porous plate is reinforced by GPLs. The obtained results in term of displacements and periods of motions as well as amplitude of the transient response for the FG porous plate without GPLs are greater than those achieved for the FG porous plate with GPLs. Can be concluded that if a very small amount of graphene is added into the matrix material of structures, their stiffness will be increased significantly.

- For FGP-GPL plate which is bonded by piezoelectric layers, the obtained results accompany with piezoelectric phenomenon as the PFGP-GPL plate is subjected to electro-mechanic loading. The higher external electric voltage yields the smaller displacement. The amplitude of the transient response of FGP-GPLs without piezoelectric layers is bigger than that of FGP-GPLs embedded piezoelectric layers.
- After adding a small amount of GPLs into the metal matrix, the stiffness of the structures is significantly improved while an increase of the porosity coefficients leads to the decrease of the reinforcing effect. For all the combinations, the association between the porosity distribution type 1 with internal pores distributed on the midplane and the GPL dispersion pattern *A*, where GPLs are dispersed around the top and bottom surfaces, obtained the best reinforcing performance.
- For geometrically nonlinear static responses control of the FG porous plates, two effective algorithms are considered including the input voltage control with opposite signs applied across the thickness of two piezoelectric layers and the displacement feedback control algorithm. In addition, the dynamic response of the FG porous plate can be expectantly suppressed based on the effectiveness of the velocity feedback control algorithm.
- Finally, the combined advantages of both the porous architecture and GPL reinforcement into material matrices is a good choice to provide the advanced ultra-light high-strength structures in engineering.

Chapter 6
FREE VIBRATION ANALYSIS OF THE FUNCTIONALLY GRADED PIEZOELECTRIC MATERIAL POROUS PLATES

6.1 Overview

In this chapter, a functionally graded piezoelectric material (FGPM) plate with the presence of porosities is investigated. It is named FGPMP plate for short. This chapter is written based on the paper [174]. The FGPM plate is considered in both perfect and imperfect forms. Material properties of FGPMP plates vary continuously through the thickness direction and are computed by a modified power-law formula. Two porosity models including even and uneven distributions are employed. To satisfy the Maxwell's equation in the quasi-static approximation, an electric potential field in the form of a mixture of a cosine and linear variation is adopted. A C^0-type higher-order shear deformation theory (C^0-type HSDT), which is mentioned in section 3.2.3, is used in this chapter. An isogeometric finite element method based on Bézier extraction also is performed. The FGPMP plates with the influence of external electric voltages, power-law index, porosity coefficient, porosity distribution; geometrical parameters, aspect ratios, and various boundary conditions are studied. Obtained results are compared with the analytical solution as well as those of several available numerical approaches. In addition, several FGPMP plates with curved geometries studied furthermore. Although these geometries have not had any analytical solutions, they could be considered as reference solutions for future work.

6.2 Functionally graded piezoelectric material plate formulation based on Bézier extraction for NURBS

6.2.1 Kinematics of FGPMP plates

A FGPMP plate model is shown in Figure 3.9 and the material properties of FG Piezoelectric Material Porous plates are presented in section 3.6. C^0-type HSDT

exhibited in section 3.2.5 is used in order to compute the free vibration frequencies of the plate.

The function of the electrical potential is chosen so that the distribution of electric and magnetic potentials through the plate thickness is fulfilled Maxwell's equation in the quasi-static approximation by [82-83]:

$$\Phi(x,y,z,t) = g(z)\phi(x,y,t) + \frac{2z}{h}V_0 e^{i\omega t} \tag{6. 1}$$

where V_0 is the applied electric voltage, $g(z)$ is an arbitrary distributed function of z-coordinate, $\phi(x,y,t)$ expresses the function of the electrical potential in reference plane and ω is the eigen value. In this paper, $g(z)$ is given as $g(z) = -\cos(\pi z/h)$.

According to Eq.(6. 1), the electric fields (E_x, E_y and E_z) become:

$$\begin{aligned} E_x &= -\Phi_{,x} = -g(z)\phi_{,x} \;;\; E_y = -\Phi_{,y} = -g(z)\phi_{,y}; \\ E_z &= -\Phi_{,z} = -g'(z)\phi - \frac{2V_0}{h}e^{i\omega t} \end{aligned} \tag{6. 2}$$

For a piezo-electrically actuated FG piezoelectric porous plate, the constitutive relations are described by:

$$\begin{aligned} \sigma_{ij} &= C_{ijkl}\varepsilon_{kl} - e_{kij}E_k \\ D_i &= e_{ikl}\varepsilon_{kl} + k_{ik}E_k \end{aligned} \tag{6. 3}$$

where σ_{ij}, ε_{kl}, D_i and E_k are stress, strain, electric displacement and electric field components, respectively; C_{ijkl}, e_{ijk} and k_{ik} define elastic, piezoelectric and dielectric constants, respectively.

The electric field vector **E** can be expressed as

$$\mathbf{E} = -\text{grad}\phi = -\nabla\phi \tag{6. 4}$$

The formulations in Eq.(6. 3) are also clearly rewritten following matrix forms as:

$$\boldsymbol{\sigma}^b = \begin{Bmatrix} \sigma_{xx} \\ \sigma_{yy} \\ \sigma_{xy} \end{Bmatrix} = \begin{bmatrix} \tilde{c}_{11} & \tilde{c}_{12} & 0 \\ \tilde{c}_{12} & \tilde{c}_{22} & 0 \\ 0 & 0 & \tilde{c}_{66} \end{bmatrix} \begin{Bmatrix} \varepsilon_{xx} \\ \varepsilon_{yy} \\ \varepsilon_{xy} \end{Bmatrix} - \begin{bmatrix} 0 & 0 & \tilde{e}_{31} \\ 0 & 0 & \tilde{e}_{31} \\ 0 & 0 & 0 \end{bmatrix} \begin{Bmatrix} 0 \\ 0 \\ E_z \end{Bmatrix} E_z = \mathbf{C}^b \boldsymbol{\varepsilon}^b - \mathbf{C}_c^b \mathbf{E}^b$$

$$\boldsymbol{\tau}^s = \begin{Bmatrix} \tau_{xz} \\ \tau_{yz} \end{Bmatrix} = \begin{bmatrix} \tilde{c}_{55} & 0 \\ 0 & \tilde{c}_{44} \end{bmatrix} \begin{Bmatrix} \gamma_{xz} \\ \gamma_{yz} \end{Bmatrix} - \begin{bmatrix} \tilde{e}_{15} & 0 \\ 0 & \tilde{e}_{14} \end{bmatrix} \begin{Bmatrix} E_x \\ E_y \end{Bmatrix} = \mathbf{C}^s \boldsymbol{\gamma} - \mathbf{C}_c^s \mathbf{E}^s \tag{6. 5}$$

$$\mathbf{D}^p = \begin{Bmatrix} D_x \\ D_y \end{Bmatrix} = \begin{bmatrix} \tilde{e}_{15} & 0 \\ 0 & \tilde{e}_{14} \end{bmatrix} \begin{Bmatrix} \gamma_{xz} \\ \gamma_{yz} \end{Bmatrix} + \begin{bmatrix} \tilde{k}_{11} & 0 \\ 0 & \tilde{k}_{22} \end{bmatrix} \begin{Bmatrix} E_x \\ E_y \end{Bmatrix} = \mathbf{C}_c^s \boldsymbol{\gamma} + \mathbf{C}^k \mathbf{E}^s$$

$$D^z = \tilde{e}_{31}\varepsilon_x + \tilde{e}_{32}\varepsilon_y + \tilde{k}_{33}E_z$$

where $\tilde{c}_{ij}$, $\tilde{e}_{ij}$ and $\tilde{k}_{ij}$ define the reduced constants of FGPMP plates and they are expressed by:

$$\begin{aligned} &\tilde{c}_{11} = c_{11} - \frac{c_{13}^2}{c_{33}}, \tilde{c}_{12} = c_{12} - \frac{c_{13}^2}{c_{33}}, \tilde{c}_{66} = c_{66} \\ &\tilde{e}_{31} = e_{31} + \frac{c_{13}e_{33}}{c_{33}}, \tilde{k}_{11} = k_{11}, \tilde{k}_{33} = k_{33} + \frac{e_{33}^2}{c_{33}} \end{aligned} \tag{6. 6}$$

Now, Hamilton's principle is used to obtain the governing equations of free vibration for FGPMP plates:

$$\int_0^t \left(\delta\Pi_S - \delta\Pi_K + \delta\Pi_I\right) \mathrm{d}t = 0 \tag{6. 7}$$

where Π_S, Π_K and Π_I are strain energy, kinetic energy and potential energy from initial stress which is generated from applying electric voltage, respectively.

The strain energy $\delta\Pi_S$ is defined as

$$\delta\Pi_S = \int_{\hat{V}} \begin{pmatrix} \sigma_{xx}\delta\varepsilon_{xx} + \sigma_{yy}\delta\varepsilon_{yy} + \tau_{xy}\delta\gamma_{xy} + \tau_{xz}\delta\gamma_{xz} + \tau_{yz}\delta\gamma_{yz} - \ldots \\ D_x\delta E_x - D_y\delta E_y - D_z\delta E_z \end{pmatrix} \mathrm{d}\hat{V} \tag{6. 8}$$

Substituting Eq. (6. 5) into Eq. (6. 8), the discrete Galerkin weak form can be rewritten as

$$\delta\Pi_S = \int_{\hat{V}} \left(\begin{array}{l} \left(\delta\boldsymbol{\varepsilon}^b\right)^T \mathbf{C}^b \boldsymbol{\varepsilon}^b - \left(\delta\boldsymbol{\varepsilon}^b\right)^T \mathbf{C}_c^b \mathbf{E}^b + \delta\boldsymbol{\gamma}^T \mathbf{C}^s \boldsymbol{\gamma} - \delta\boldsymbol{\gamma}^T \mathbf{C}_c^s \mathbf{E}^s - \\ \left(\delta\mathbf{E}^s\right)^T \mathbf{C}_c^s \boldsymbol{\gamma} - \left(\delta\mathbf{E}^s\right)^T \mathbf{C}^k \mathbf{E}^s \end{array} \right) \mathrm{d}\hat{V} - \int_{\hat{V}} \left(\delta E_z\right)^T \left(\tilde{e}_{31}\varepsilon_x + \tilde{e}_{32}\varepsilon_y + \tilde{k}_{33} E_z \right) \mathrm{d}\hat{V} \tag{6. 9}$$

in which

$$\varepsilon_x = \varepsilon_x^0 + z\varepsilon_x^1 + f(z)\varepsilon_x^2;\ \varepsilon_y = \varepsilon_y^0 + z\varepsilon_y^1 + f(z)\varepsilon_y^2 \tag{6. 10}$$

Eq. (6. 9) can be split into two independent integrals following to middle surface and *z*-axis direction as:

$$\begin{array}{l} \delta\Pi_S = \int_\Omega \left(\hat{\boldsymbol{\varepsilon}}^b\right)^T \hat{\mathbf{C}}^b \delta\hat{\boldsymbol{\varepsilon}}^b \mathrm{d}\Omega + \left(\int_\Omega \left(\boldsymbol{\phi}^b\right)^T \hat{\mathbf{C}}_c^{b1} \boldsymbol{\varepsilon}^0 \mathrm{d}\Omega + \int_\Omega \left(\boldsymbol{\phi}^b\right)^T \hat{\mathbf{C}}_c^{b2} \boldsymbol{\varepsilon}^1 \mathrm{d}\Omega + \int_\Omega \left(\boldsymbol{\phi}^b\right)^T \hat{\mathbf{C}}_c^{b3} \boldsymbol{\varepsilon}^2 \mathrm{d}\Omega \right) + \\ \int_\Omega \left(\hat{\boldsymbol{\varepsilon}}^s\right)^T \hat{\mathbf{C}}^s \delta\boldsymbol{\varepsilon}^s \mathrm{d}\Omega + \int_\Omega \left(\boldsymbol{\phi}^s\right)^T \hat{\mathbf{C}}_c^s \delta\boldsymbol{\varepsilon}^s \mathrm{d}\Omega + \int_\Omega \left(\boldsymbol{\varepsilon}^s\right)^T \hat{\mathbf{C}}_c^s \delta\boldsymbol{\phi}^s \mathrm{d}\Omega + \int_\Omega \left(\boldsymbol{\phi}^s\right)^T \hat{\mathbf{C}}^k \delta\boldsymbol{\phi}^s \mathrm{d}\Omega + \\ \left(\begin{array}{l} \int_\Omega \varepsilon_x^0 \tilde{e}_{31}^1 \delta\phi^z \mathrm{d}\Omega + \int_\Omega \varepsilon_x^1 \tilde{e}_{31}^2 \delta\phi^z \mathrm{d}\Omega + \int_\Omega \varepsilon_x^2 \tilde{e}_{31}^3 \delta\phi^z \mathrm{d}\Omega + \int_\Omega \varepsilon_y^0 \tilde{e}_{32}^1 \delta\phi^z \mathrm{d}\Omega + \int_\Omega \varepsilon_y^1 \tilde{e}_{32}^2 \delta\phi^z \mathrm{d}\Omega + \\ \int_\Omega \varepsilon_y^2 \tilde{e}_{32}^3 \delta\phi^z \mathrm{d}\Omega + \int_\Omega \phi^z \hat{\tilde{k}}_{33} \delta\phi^z \mathrm{d}\Omega - e^{i\omega t} \int_{-h/2}^{h/2} g'(z)\, dz \int_\Omega \frac{2V_0}{h} \tilde{k}_{33} \delta\phi^z \mathrm{d}\Omega \end{array} \right) \end{array} \tag{6. 11}$$

The left side of Eq. (6. 11) can be rewritten under compact forms as:

$$\delta\Pi_S = \delta\Pi_1 + \delta\Pi_2 + \delta\Pi_3 + \delta\Pi_4 + \delta\Pi_5 + \delta\Pi_6 + \delta\Pi_7 \tag{6. 12}$$

where

$$\delta\Pi_1 = \int_\Omega \left(\hat{\boldsymbol{\varepsilon}}^b\right)^T \hat{\mathbf{C}}^b \delta\hat{\boldsymbol{\varepsilon}}^b \mathrm{d}\Omega;$$

$$\delta\Pi_2 = \int_\Omega \left(\boldsymbol{\phi}^b\right)^T \hat{\mathbf{C}}_c^{b1} \boldsymbol{\varepsilon}^0 \mathrm{d}\Omega + \int_\Omega \left(\boldsymbol{\phi}^b\right)^T \hat{\mathbf{C}}_c^{b2} \boldsymbol{\varepsilon}^1 \mathrm{d}\Omega + \int_\Omega \left(\boldsymbol{\phi}^b\right)^T \hat{\mathbf{C}}_c^{b3} \boldsymbol{\varepsilon}^2 \mathrm{d}\Omega;$$

$$\delta\Pi_3 = \int_\Omega \left(\hat{\boldsymbol{\varepsilon}}^s\right)^T \hat{\mathbf{C}}^s \delta\boldsymbol{\varepsilon}^s \mathrm{d}\Omega;\ \delta\Pi_4 = \int_\Omega \left(\boldsymbol{\phi}^s\right)^T \hat{\mathbf{C}}_c^s \delta\boldsymbol{\varepsilon}^s \mathrm{d}\Omega;\ \delta\Pi_5 = \int_\Omega \left(\boldsymbol{\varepsilon}^s\right)^T \hat{\mathbf{C}}_c^s \delta\boldsymbol{\phi}^s \mathrm{d}\Omega; \tag{6. 13}$$

$$\delta\Pi_6 = \int_\Omega \left(\boldsymbol{\phi}^s\right)^T \hat{\mathbf{C}}^k \delta\boldsymbol{\phi}^s \mathrm{d}\Omega;$$

$$\delta\Pi_7 = \int_\Omega \varepsilon_x^0 \tilde{e}_{31}^1 \delta\phi^z \mathrm{d}\Omega + \int_\Omega \varepsilon_x^1 \tilde{e}_{31}^2 \delta\phi^z \mathrm{d}\Omega + \int_\Omega \varepsilon_x^2 \tilde{e}_{31}^3 \delta\phi^z \mathrm{d}\Omega + \int_\Omega \varepsilon_y^0 \tilde{e}_{32}^1 \delta\phi^z \mathrm{d}\Omega + \int_\Omega \varepsilon_y^1 \tilde{e}_{32}^2 \delta\phi^z \mathrm{d}\Omega +$$

$$\int_\Omega \varepsilon_y^2 \tilde{e}_{32}^3 \delta\phi^z \mathrm{d}\Omega + \int_\Omega \phi^z \hat{\tilde{k}}_{33} \delta\phi^z \mathrm{d}\Omega - e^{i\omega t} \int_{-h/2}^{h/2} g'(z)\, dz \int_\Omega \frac{2V_0}{h} \tilde{k}_{33} \delta\phi^z \mathrm{d}\Omega$$

For details, we need to rewrite the above terms as follows:

$$\delta\Pi_1 = \int_\Omega \left(\hat{\boldsymbol{\varepsilon}}^b\right)^T \hat{\mathbf{C}}^b \delta\hat{\boldsymbol{\varepsilon}}^b \mathrm{d}\Omega$$

where

$$\hat{\boldsymbol{\varepsilon}}^b = \left\{\boldsymbol{\varepsilon}^0 \quad \boldsymbol{\varepsilon}^1 \quad \boldsymbol{\varepsilon}^2\right\}^T; \hat{\mathbf{C}}^b = \begin{bmatrix} \mathbf{A}^b & \mathbf{B}^b & \mathbf{E}^b \\ \mathbf{B}^b & \mathbf{D}^b & \mathbf{F}^b \\ \mathbf{E}^b & \mathbf{F}^b & \mathbf{H}^b \end{bmatrix}$$

$$\left(\mathbf{A}^b, \mathbf{B}^b, \mathbf{D}^b, \mathbf{E}^b, \mathbf{F}^b, \mathbf{H}^b\right) = \int_{-h/2}^{h/2} \left(1, z, z^2, f(z), z f(z), f^2(z)\right) \begin{bmatrix} \tilde{c}_{11} & \tilde{c}_{12} & 0 \\ \tilde{c}_{12} & \tilde{c}_{22} & 0 \\ 0 & 0 & \tilde{c}_{66} \end{bmatrix} \mathrm{d}z \tag{6. 14}$$

$$\delta\Pi_2 = \int_\Omega \left(\boldsymbol{\phi}^b\right)^T \hat{\mathbf{C}}_c^{b1} \delta\boldsymbol{\varepsilon}^0 \mathrm{d}\Omega + \int_\Omega \left(\boldsymbol{\phi}^b\right)^T \hat{\mathbf{C}}_c^{b2} \delta\boldsymbol{\varepsilon}^1 \mathrm{d}\Omega + \int_\Omega \left(\boldsymbol{\phi}^b\right)^T \hat{\mathbf{C}}_c^{b3} \delta\boldsymbol{\varepsilon}^2 \mathrm{d}\Omega = \int_\Omega \left(\boldsymbol{\phi}^b\right)^T \hat{\mathbf{C}}_c^b \delta\hat{\boldsymbol{\varepsilon}}^b \mathrm{d}\Omega$$

where

$$\hat{\mathbf{C}}_c^b = \left[\hat{\mathbf{C}}_c^{b1} \quad \hat{\mathbf{C}}_c^{b2} \quad \hat{\mathbf{C}}_c^{b3}\right]; \hat{\mathbf{C}}_c^{b1} = \int_{-h/2}^{h/2} g'(z) \begin{bmatrix} 0 & 0 & \tilde{e}_{31} \\ 0 & 0 & \tilde{e}_{31} \\ 0 & 0 & 0 \end{bmatrix} \mathrm{d}z;$$

$$\hat{\mathbf{C}}_c^{b2} = \int_{-h/2}^{h/2} z g'(z) \begin{bmatrix} 0 & 0 & \tilde{e}_{31} \\ 0 & 0 & \tilde{e}_{31} \\ 0 & 0 & 0 \end{bmatrix} \mathrm{d}z; \ \hat{\mathbf{C}}_c^{b3} = \int_{-h/2}^{h/2} f(z) g'(z) \begin{bmatrix} 0 & 0 & \tilde{e}_{31} \\ 0 & 0 & \tilde{e}_{31} \\ 0 & 0 & 0 \end{bmatrix} \mathrm{d}z \tag{6. 15}$$

$$\delta\Pi_3 = \int_\Omega \left(\hat{\boldsymbol{\varepsilon}}^s\right)^T \hat{\mathbf{C}}^s \delta\boldsymbol{\varepsilon}^s \mathrm{d}\Omega$$

where

$$\hat{\boldsymbol{\varepsilon}}^s = \left\{\boldsymbol{\varepsilon}^{s0} \quad \boldsymbol{\varepsilon}^{s1}\right\}^T; \hat{\mathbf{C}}^s = \begin{bmatrix} \mathbf{A}_s & \mathbf{B}_s \\ \mathbf{B}_s & \mathbf{D}_s \end{bmatrix};$$

$$\left(\mathbf{A}_s; \mathbf{B}_s; \mathbf{D}_s\right) = \int_{-h/2}^{h/2} (1, f'(z), f'^2(z)) \begin{bmatrix} \tilde{c}_{55} & 0 \\ 0 & \tilde{c}_{44} \end{bmatrix} \mathrm{d}z \tag{6. 16}$$

$$\delta\Pi_4 = \int_\Omega \left(\boldsymbol{\phi}^s\right)^T \hat{\mathbf{C}}_c^s \delta\boldsymbol{\varepsilon}^s \mathrm{d}\Omega \ \text{ and } \ \delta\Pi_5 = \int_\Omega \left(\boldsymbol{\varepsilon}^s\right)^T \hat{\mathbf{C}}_c^s \delta\boldsymbol{\phi}^s \mathrm{d}\Omega$$

where

$$\hat{\mathbf{C}}_c^s = \begin{bmatrix} \mathbf{A}_c^s & \mathbf{B}_c^s \\ \mathbf{B}_c^s & \mathbf{D}_c^s \end{bmatrix}; \left(\mathbf{A}_c^s; \ \mathbf{B}_c^s; \ \mathbf{D}_c^s \ \right) = \int_{-h/2}^{h/2} g(z)[1, f'(z), f'^2(z)] \begin{bmatrix} \tilde{e}_{15} & 0 \\ 0 & \tilde{e}_{14} \end{bmatrix} \mathrm{d}z \tag{6. 17}$$

$$\delta\Pi_6 = \int_\Omega \left(\boldsymbol{\phi}^s\right)^T \hat{\mathbf{C}}^k \delta\boldsymbol{\phi}^s \mathrm{d}\Omega$$

where

$$\hat{\mathbf{C}}^k = \int_{-h/2}^{h/2} g(z) g(z) \begin{bmatrix} \tilde{k}_{11} & 0 \\ 0 & \tilde{k}_{22} \end{bmatrix} \mathrm{d}z \tag{6. 18}$$

$$\delta\Pi_7 = \int_\Omega \varepsilon_x^0 \tilde{e}_{31}^1 \delta\phi^z \mathrm{d}\Omega + \int_\Omega \varepsilon_x^1 \tilde{e}_{31}^2 \delta\phi^z \mathrm{d}\Omega + \int_\Omega \varepsilon_x^2 \tilde{e}_{31}^3 \delta\phi^z \mathrm{d}\Omega + \int_\Omega \varepsilon_y^0 \tilde{e}_{32}^1 \delta\phi^z \mathrm{d}\Omega +$$

$$\int_\Omega \varepsilon_y^1 \tilde{e}_{32}^2 \delta\phi^z \mathrm{d}\Omega + \int_\Omega \varepsilon_y^2 \tilde{e}_{32}^3 \delta\phi^z \mathrm{d}\Omega + \int_\Omega \phi^z \hat{\tilde{k}}_{33} \delta\phi^z \mathrm{d}\Omega - e^{i\omega t} \int_{-h/2}^{h/2} g'(z) dz \int_\Omega \frac{2V_0}{h} \tilde{k}_{33} \delta\phi^z \mathrm{d}\Omega$$

in which

$$\tilde{e}_{31}^{1}=\int_{-h/2}^{h/2}g'(z)\tilde{e}_{31}\mathrm{d}z\;;\;\tilde{e}_{31}^{2}=\int_{-h/2}^{h/2}zg'(z)\tilde{e}_{31}\mathrm{d}z\;;\;\tilde{e}_{31}^{3}=\int_{-h/2}^{h/2}f(z)g'(z)\tilde{e}_{31}\mathrm{d}z$$

$$\tilde{e}_{32}^{1}=\int_{-h/2}^{h/2}g'(z)\tilde{e}_{32}\mathrm{d}z\;;\;\tilde{e}_{32}^{2}=\int_{-h/2}^{h/2}zg'(z)\tilde{e}_{32}\mathrm{d}z\;;\;\tilde{e}_{32}^{3}=\int_{-h/2}^{h/2}f(z)g'(z)\tilde{e}_{32}\mathrm{d}z \qquad (6.\ 19)$$

$$\hat{\tilde{k}}_{33}=\int_{-h/2}^{h/2}g'(z)g'(z)\tilde{k}_{33}\mathrm{d}z$$

Note that when $g(z)=0$ at $z=\pm h/2$ and $g(z)$ is an even function, $\int_{-h/2}^{h/2}g'(z)\mathrm{d}z=0$. Hence, $\delta\Pi_7$ is not affected by the applied electric voltage V_0.

The variation of the kinetic energy of the mass system can be written as

$$\delta\Pi_K=\int_\Omega\delta\hat{\mathbf{u}}^T\hat{\mathbf{m}}\ddot{\hat{\mathbf{u}}}\mathrm{d}\Omega \qquad (6.\ 20)$$

where

$$\hat{\mathbf{u}}=\begin{Bmatrix}\mathbf{u}^1\\ \mathbf{u}^2\\ \mathbf{u}^3\end{Bmatrix};\quad \hat{\mathbf{m}}=\begin{bmatrix}\mathbf{I}_1 & \mathbf{I}_2 & \mathbf{I}_4\\ \mathbf{I}_2 & \mathbf{I}_3 & \mathbf{I}_5\\ \mathbf{I}_4 & \mathbf{I}_5 & \mathbf{I}_6\end{bmatrix} \qquad (6.\ 21)$$

in which the mass inertia terms $\mathbf{I}_i$ (i=1:6) are calculated as Eq.(6. 22):

$$(\mathbf{I}_1,\mathbf{I}_2,\mathbf{I}_3,\mathbf{I}_4,\mathbf{I}_5,\mathbf{I}_6)=\int_{-h/2}^{h/2}\rho(z)\left(1,z,z^2,f(z),zf(z),f^2(z)\right)\begin{bmatrix}1&0&0\\0&1&0\\0&0&1\end{bmatrix}\mathrm{d}z \qquad (6.\ 22)$$

The potential energy obtained from external applied electric voltage can be written by

$$\delta\Pi_I=\int_\Omega\delta\begin{Bmatrix}w_{0,x}\\ w_{0,y}\end{Bmatrix}^{\mathrm{T}}\begin{bmatrix}N_x^0 & N_{xy}^0\\ N_{xy}^0 & N_y^0\end{bmatrix}\begin{Bmatrix}w_{0,x}\\ w_{0,y}\end{Bmatrix}\mathrm{d}\Omega=N^I\int_\Omega\left(\frac{\partial w}{\partial x}\frac{\partial\delta w}{\partial x}+\frac{\partial w}{\partial y}\frac{\partial\delta w}{\partial y}\right)\mathrm{d}\Omega \qquad (6.\ 23)$$

where

$$N_{xy}^0=0,N_x^0=N_y^0=N^I=-e^{i\omega t}\int_{-h/2}^{h/2}\tilde{e}_{31}\frac{2V_0}{h}dz \qquad (6.\ 24)$$

6.2.2 Approximated formulation

By using the Bézier extraction of NURBS, the displacement field **u** of the plate is approximated as follows

$$\mathbf{u}(\xi,\eta)=\sum_{A}^{m\times n}R_A^e(\xi,\eta)\mathbf{d}_A \tag{6. 25}$$

where $n\times m$ is the number of basis functions, $R_A^e(\xi,\eta)$ is a NURBS basis function which is written in the compact form of the linear combination of Bézier extraction operator and Bernstein polynomials and $\mathbf{d}_A=\{u_{0A}\quad v_{0A}\quad w_{0A}\quad \beta_{xA}\quad \beta_{yA}\quad \theta_{xA}\quad \theta_{yA}\}^T$ is the vector of nodal degrees of freedom associated with control point A.

The electric field **E** in Eq. (6. 4) can be rewritten as

$$\mathbf{E}=-\nabla\mathbf{N}_\phi\boldsymbol{\phi}_A=-\mathbf{B}_\phi\boldsymbol{\phi}_A \tag{6. 26}$$

in which $\boldsymbol{\phi}_A$ is electric potential related to control point A and $\mathbf{N}_\phi$ is the shape functions for the electric potential.

Substituting Eq.(6. 25) to Eq.(3. 11), the first component of Eq. (6. 12), $\delta\Pi_1$ is approximated based on Bézier extraction of NURBS as

$$\delta\Pi_1=\delta\mathbf{d}^T\mathbf{K}_1\mathbf{d} \tag{6. 27}$$

where

$$\mathbf{K}_1=\int_\Omega\hat{\mathbf{B}}_u^T\hat{\mathbf{C}}^b\hat{\mathbf{B}}_u\mathrm{d}\Omega;\ \hat{\mathbf{B}}_u=\begin{bmatrix}\mathbf{B}_1 & \mathbf{B}_2 & \mathbf{B}_3\end{bmatrix}^T \tag{6. 28}$$

and

$$\mathbf{B}_1=\sum_{A=1}^{mxn}\begin{bmatrix}R_{A,x}&0&0&0&0&0&0\\0&R_{A,y}&0&0&0&0&0\\R_{A,y}&R_{A,x}&0&0&0&0&0\end{bmatrix};\ \mathbf{B}_2=-\sum_{A=1}^{mxn}\begin{bmatrix}0&0&0&R_{A,x}&0&0&0\\0&0&0&0&R_{A,y}&0&0\\0&0&0&R_{A,y}&R_{A,x}&0&0\end{bmatrix};$$
$$\mathbf{B}_3=\sum_{A=1}^{mxn}\begin{bmatrix}0&0&0&0&0&R_{A,x}&0\\0&0&0&0&0&0&R_{A,y}\\0&0&0&0&0&R_{A,y}&R_{A,x}\end{bmatrix} \tag{6. 29}$$

The second component of Eq. (6. 12), $\delta\Pi_2$ is obtained by substituting Eqs.(6. 25) and (6. 26) to Eqs. (3. 11) and (6. 13).

$$\delta\Pi_2=\delta\boldsymbol{\phi}^T\mathbf{K}_2\mathbf{d} \tag{6. 30}$$

where

$$\mathbf{K}_2 = \int_\Omega \left(\mathbf{B}_\phi^b\right)^T \hat{\mathbf{C}}_c^b \hat{\mathbf{B}}_u \mathrm{d}\Omega \; ; \; \mathbf{B}_\phi^b = -\sum_{A=1}^{mxn} \begin{bmatrix} 0 \\ 0 \\ R_A \end{bmatrix} \tag{6. 31}$$

The third component of Eq. (6. 12), $\delta\Pi_3$, is given as

$$\delta\Pi_3 = \delta\mathbf{d}^T \mathbf{K}_3 \mathbf{d} \tag{6. 32}$$

where

$$\mathbf{K}^3 = \int_\Omega \left(\mathbf{B}^s\right)^T \hat{\mathbf{C}}^s \mathbf{B}^s \mathrm{d}\Omega; \; \mathbf{B}_s = \begin{bmatrix} \mathbf{B}_s^1 & \mathbf{B}_s^2 \end{bmatrix}^T \tag{6. 33}$$

and

$$\mathbf{B}_s^1 = \sum_{A=1}^{mxn} \begin{bmatrix} 0 & 0 & R_{A,x} & -R_A & 0 & 0 & 0 \\ 0 & 0 & R_{A,y} & 0 & -R_A & 0 & 0 \end{bmatrix}; \mathbf{B}_s^2 = \sum_{A=1}^{mxn} \begin{bmatrix} 0 & 0 & 0 & 0 & 0 & R_A & 0 \\ 0 & 0 & 0 & 0 & 0 & 0 & R_A \end{bmatrix} \tag{6. 34}$$

The fourth term of Eq. (6. 12), $\delta\Pi_4$, becomes

$$\delta\Pi_4 = \delta\boldsymbol{\phi}^T \mathbf{K}_4 \mathbf{d} \tag{6. 35}$$

where

$$\mathbf{K}_5 = \int_\Omega \left(\mathbf{B}_\phi^s\right)^T \hat{\mathbf{C}}_c^s \mathbf{B}^s \mathrm{d}\Omega; \;\; \mathbf{B}_\phi^s = -\sum_{A=1}^{mxn} \begin{bmatrix} R_{A,x} \\ R_{A,y} \end{bmatrix} \tag{6. 36}$$

The next term of Eq. (6. 12), $\delta\Pi_5$ is similar to $\delta\Pi_4$, in which $\mathbf{K}_5$ is the transpose matrix of $\mathbf{K}_5$

$$\mathbf{K}_5 = \int_\Omega \left(\mathbf{B}^s\right)^T \hat{\mathbf{C}}_c^s \mathbf{B}_\phi^s \mathrm{d}\Omega; \tag{6. 37}$$

The one more term of Eq. (6. 12), $\delta\Pi_6$ has form

$$\delta\Pi_6 = \delta\boldsymbol{\phi}^T \mathbf{K}^6 \boldsymbol{\phi} \tag{6. 38}$$

$$\mathbf{K}_6 = \int_\Omega \left(\mathbf{B}_\phi^s\right)^T \hat{\mathbf{C}}^k \mathbf{B}_\phi^s \mathrm{d}\Omega; \tag{6. 39}$$

The final term of Eq. (6. 12), $\delta\Pi_7$ is given as

$$\delta\Pi_7 = \delta\mathbf{d}^T \mathbf{K}_{71} \boldsymbol{\phi} + \delta\mathbf{d}^T \mathbf{K}_{72} \boldsymbol{\phi} + \delta\boldsymbol{\phi}^T \mathbf{K}_{73} \boldsymbol{\phi} \tag{6. 40}$$

where

$$\mathbf{K}_7 = \mathbf{K}_7 + \mathbf{K}_{72} + \mathbf{K}_{73} = \tag{6. 41}$$
$$\int_\Omega \left(\mathbf{B}_x\right)^T \hat{\mathbf{E}}_x \mathbf{B}_z \mathrm{d}\Omega + \int_\Omega \left(\mathbf{B}_y\right)^T \hat{\mathbf{E}}_y \mathbf{B}_z \mathrm{d}\Omega + \int_\Omega \left(\mathbf{B}_z\right)^T \hat{\tilde{k}}_{33} \mathbf{B}_z \mathrm{d}\Omega;$$
$$\hat{\mathbf{E}}_x = \begin{bmatrix} \tilde{e}_{31}^1 & \tilde{e}_{31}^2 & \tilde{e}_{31}^3 \end{bmatrix}^T ; \hat{\mathbf{E}}_y = \begin{bmatrix} \tilde{e}_{32}^1 & \tilde{e}_{32}^2 & \tilde{e}_{32}^3 \end{bmatrix}^T ;$$
$$\mathbf{B}_x = \begin{bmatrix} \mathbf{B}_x^1 & \mathbf{B}_x^2 & \mathbf{B}_x^3 \end{bmatrix}^T ; \mathbf{B}_y = \begin{bmatrix} \mathbf{B}_y^1 & \mathbf{B}_y^2 & \mathbf{B}_y^3 \end{bmatrix}^T$$

and

$$\mathbf{B}_x^1 = \sum_{A=1}^{mxn} \begin{bmatrix} R_{A,x} & 0 & 0 & 0 & 0 & 0 & 0 \end{bmatrix}; \mathbf{B}_x^2 = -\sum_{A=1}^{mxn} \begin{bmatrix} 0 & 0 & 0 & R_{A,x} & 0 & 0 & 0 \end{bmatrix};$$
$$\mathbf{B}_x^3 = \sum_{A=1}^{mxn} \begin{bmatrix} 0 & 0 & 0 & 0 & 0 & R_{A,x} & 0 \end{bmatrix}; \mathbf{B}_y^1 = \sum_{A=1}^{mxn} \begin{bmatrix} 0 & R_{A,y} & 0 & 0 & 0 & 0 & 0 \end{bmatrix}; \tag{6. 42}$$
$$\mathbf{B}_y^2 = -\sum_{A=1}^{mxn} \begin{bmatrix} 0 & 0 & 0 & 0 & R_{A,x} & 0 & 0 \end{bmatrix}; \mathbf{B}_y^3 = \sum_{A=1}^{mxn} \begin{bmatrix} 0 & 0 & 0 & 0 & 0 & 0 & R_{A,y} \end{bmatrix};$$
$$\mathbf{B}_z = -\sum_{A=1}^{mxn} R_A$$

The potential energy in Eq. (6. 23) is also approximated as

$$\delta\Pi_I = \delta \mathbf{d}^T \mathbf{K}_I \mathbf{d} \tag{6. 43}$$

where

$$\mathbf{K}_I = \int_\Omega \left(\mathbf{B}_I\right)^{\mathrm{T}} \begin{bmatrix} -2\tilde{e}_{31} V_0 & 0 \\ 0 & -2\tilde{e}_{31} V_0 \end{bmatrix} \mathbf{B}_I \mathrm{d}\Omega \; ; \mathbf{B}_I = \sum_{A=1}^{mxn} \begin{bmatrix} 0 & 0 & R_{A,x} & 0 & 0 & 0 & 0 \\ 0 & 0 & R_{A,y} & 0 & 0 & 0 & 0 \end{bmatrix} \tag{6. 44}$$

The elementary governing equation of motion can be generally derived by substituting Eqs.(6. 9),(6. 20),(6. 23) into Eq.(6. 7) as:

$$\begin{bmatrix} \mathbf{M} & 0 \\ 0 & 0 \end{bmatrix} \begin{bmatrix} \ddot{\mathbf{d}} \\ \ddot{\boldsymbol{\phi}} \end{bmatrix} + \begin{bmatrix} \mathbf{K}_{uu} & \mathbf{K}_{u\phi} \\ \mathbf{K}_{\phi u} & \mathbf{K}_{\phi\phi} \end{bmatrix} \begin{bmatrix} \mathbf{d} \\ \boldsymbol{\phi} \end{bmatrix} = \begin{bmatrix} 0 \\ 0 \end{bmatrix} \tag{6. 45}$$

where

$$\mathbf{K}_{uu} = \mathbf{K}^1 + \mathbf{K}^3 - \mathbf{K}_I \quad ; \quad \mathbf{K}_{u\phi} = -\left(\mathbf{K}^5 + \mathbf{K}^{71} + \mathbf{K}^{72}\right);$$
$$\mathbf{K}_{\phi u} = -\left(\mathbf{K}^2 + \mathbf{K}^4\right) \quad ; \quad \mathbf{K}_{\phi\phi} = -\left(\mathbf{K}^6 + \mathbf{K}^{73}\right) \tag{6. 46}$$

Substituting the second line of Eq. (6. 45) into the first line, the shortened form is obtained as

$$\mathbf{M}\ddot{\mathbf{d}} + \left(\mathbf{K}_{uu} - \mathbf{K}_{u\phi}\mathbf{K}_{\phi\phi}^{-1}\mathbf{K}_{\phi u}\right)\mathbf{d} = 0 \tag{6. 47}$$

The governing equation of free vibration problem can be formulated by the following form

$$\left(\mathbf{K} - \omega^2\mathbf{M}\right)\mathbf{d} = 0 \tag{6. 48}$$

where the global stiffness matrix $\mathbf{K}$ is given as

$$\mathbf{K} = \mathbf{K}_{uu} - \mathbf{K}_{u\phi}\mathbf{K}_{\phi\phi}^{-1}\mathbf{K}_{\phi u} \tag{6. 49}$$

and the global mass matrix $\mathbf{M}$ is described like as Eq.(5. 13).

6.3 Numerical examples and discussions

Since the square and circular plates are important structural parts in engineering structures, four examples for square and circular porous functionally graded piezoelectric plates with various geometric from simple to complex, different boundary conditions and two types of porous distribution using isogeometric finite elements based on Bézier extraction are considered. In addition, the cubic function $f(z) = z - \frac{4z^3}{3h^2}$ [112,158] is employed in the following examples, but the use of other forms of *f(z)* in the present formulation is straightforward.

Two types of Dirichlet boundary conditions are used as:

- Simply supported:
  - Rectangular plate

$u_0 = w_0 = \theta_x = \beta_x = 0$ at $y = 0, b$ and $v_0 = w_0 = \theta_y = \beta_y = 0$ at $x = 0, a$

  - Circular plate

$u_0 = v_0 = w_0 = 0$ at boundaries

- Fully clamped:

$u_0 = v_0 = w_0 = \beta_x = \beta_y = \theta_x = \theta_y = 0$ at boundaries.

Table 6. 1. Material properties [165-166].

Properties	PZT-4(*)	PZT-5A(*)	PZT-4(**)	PZT-5H(**)
$c_{11}=c_{22}$ (GPa)	138.499	99.201	139	126
c_{12}	77.371	54.016	77.8	79.1
c_{13}	73.643	50.778	74	83.9
c_{33}	114.745	86.856	115	117
c_{55}	25.6	21.1	25.6	23
c_{66}	30.6	22.6	30.6	23.5
e_{31} (Cm^{-2})	-5.2	-7.209	-5.2	-6.5
e_{33}	15.08	15.118	15.1	23.3
e_{15}	12.72	12.322	12.7	17
k_{11} ($C^2m^{-2}N^{-1}$)	1.306 x10^{-9}	1.53 x10^{-9}	6.46 x10^{-9}	15.05 x10^{-9}
k_{33}	1.115 x10^{-9}	1.5 x10^{-9}	5.62 x10^{-9}	13.02 x10^{-9}

(*): Material properties are given in [165].

(**): Material properties are given in [166].

6.3.1 Square plates

6.3.1.1 The square FGPMP plate

A square FGPM plate (a/b =1) subjected to various electric voltages and boundary conditions is condsidered. The length to thickness ratio is given as a/h = 100. The accuracy and reliability of the present method are verified by analytical solutions which are given in the literature. Material properties are given in Table 6. 1. The non-dimensional frequency parameter $\tilde{\omega}$ is defined as $\tilde{\omega} = \omega b^2 / h\sqrt{(\rho / c_{11})}_{PZT-4}$. First, the convergence and accuracy of solutions using quadratic (p = 2) Bézier elements at mesh levels of 7x7, 11x11, 15x15 and 17x17 elements are investigated as depicted in Table 6. 2 for a perfect FGPM plate with simply supported boundary conditions. Figure 6. 1 illustrates Bézier control mesh of a square FGPM plate using 7x7, 11x11, 15x15 and 17x17 quadratic Bézier elements. The first non-dimensional frequency is compared with the analytical solution reported by Barati et al. [82] using a refined four-variable plate theory. The relative error percentages compared with the analytical solution [82] are also given in the parentheses. Table 6. 2 reveals that the obtained results correlate well with the

analytical value. It is observed that the present results converge well to the reference solution when increasing the number of elements. Throughout this test, the same accuracy of non-dimensional frequency is almost obtained for all external electric voltages using quadratic elements at mesh levels of 15x15 and 17x17 elements. The difference between them is not significant. So, the mesh of 15x15 quadratic Bézier elements is chosen for all numerical examples.

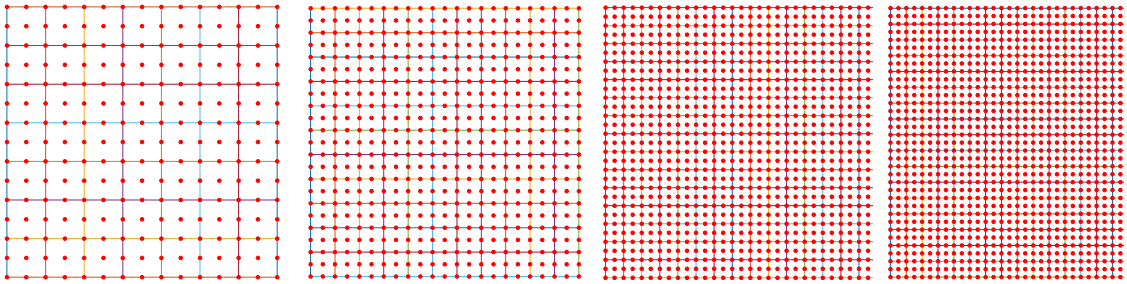

(a) (b) (c) (d)

Figure 6. 1. Bézier control mesh of a square FGPM plate using quadratic Bézier elements: (a) 7x7; (b) 11x11 (c) 15x15 and (d) 17x17.

Table 6. 2. Comparison of convergence of the first non-dimensional frequency $\tilde{\omega}$ of a perfect FGPM plate ($\alpha = 0$) with different electric voltages for the simply supported boundary condition.

			Power index		
V_0	Methods	Mesh	g=0.2	g=1	g=5
		7x7	6.2275	6.0239	5.8747
-500	Present		(+0.349%)	(+0.349%)	(+0.346%)
		11x11	6.2136	6.0106	5.8618
			(+0.129%)	(+0.135%)	(+0.125%)
		15x15	6.2099	6.0070	5.8584
			(+0.070%)	(+0.067%)	(+0.067%)
		17x17	6.2098	6.0070	5.8582
			(+0.070%)	(+0.067%)	(+0.067%)
	Analytical [82]		6.20555	6.00294	5.85444
		7x7	6.0529	5.8395	5.6822
0	Present		(+0.375%)	(+0.371%)	(+0.370%)

		11x11	6.0386	5.8258	5.6689
			(+0.138%)	(+0.136%)	(+0.136%)
		15x15	6.0348	5.8221	5.6653
			(+0.075%)	(+0.072%)	(+0.072%)
		17x17	6.0347	5.8220	5.6652
			(+0.075%)	(+0.072%)	(+0.072%)
	Analytical [82]		6.03027	5.81787	5.66120
		7x7	5.8730	5.6491	5.4829
500	Present		(+0.397%)	(+0.397%)	(+0.398%)
		11x11	5.8583	5.6349	5.4691
			(+0.146%)	(+0.145%)	(+0.146%)
		15x15	5.8544	5.6311	5.4654
			(+0.079%)	(+0.078%)	(+0.078%)
		17x17	5.8544	5.6310	5.4653
			(+0.079%)	(+0.078%)	(+0.078%)
	Analytical [82]		5.84974	5.62671	5.46113

Table 6. 3 displays obtained results of FGPMP plates compared with the analytical solutions for the non-dimensional frequency. Note that material properties used for Table 6. 2 and Table 6. 3 are consulted from Ref. [165] given in Table 6. 1. It is seen that present results agree well with the reference solutions [82] for both FGPMP-I and FGPMP-II types under a variety of electric voltages and power-law exponents**.**

Table 6. 3: Comparison of the first dimensionless frequency $\tilde{\omega}$ of an imperfect FGPM plate ($\alpha = 0.2$) with different electric voltages for the simply supported boundary conditions.

V_0	Methods	FGPMP-I			FGPMP-II		
		g=0.2	g=1	g=5	g=0.2	g=1	g=5
-500	Present	6.2526	5.9951	5.8089	6.3810	6.1584	5.9952
	Analytical [82]	6.2481	5.99103	5.80503	6.37713	6.15487	5.99172
0	Present	6.0797	5.8099	5.6136	6.2111	5.9782	5.8064
	Analytical [82]	6.0751	5.80571	5.60954	6.20715	5.97455	5.80282
500	Present	5.9018	5.6186	5.4112	6.0365	5.7924	5.6113
	Analytical [82]	5.8970	5.61429	5.40698	6.03238	5.78861	5.60756

In Table 6. 4, the first dimensionless frequency $\tilde{\omega}$ of FGPM plate without porosities for several boundary conditions is presented. Five boundary conditions including CCCC, SCSC, CFCF, CCFF and SCFS are studied. Material properties referred in Ref. [166] are used. The obtained solutions are compared with those reported by Zhu et al. [167] using the analytical approach and FSDT. It can be seen that an excellent agreement is found for various boundary conditions, electric voltages and power index values. Also, numerical solutions for square FGPMP plates with different boundary conditions are given in Table 6. 5. It can be seen that the non-dimensional frequency reduces as the power index value rises for both perfect and imperfect FGPMP plates with all kinds of given boundary conditions. This observation found is due to expansion of gradient index resulting in deduction of the plate stiffness since volume fraction of PTZ-4 decreases. Additionally, with the same porosity coefficient value, the obtained results for first dimensionless frequency of the FGPMP-I type are lower than those of the FGPMP-II type. This means that porosity distribution has much influence on free vibration responses of FGPMP plates. An important point is that the sign of applied electric voltage also affects the behavior of plate significantly. Particularly, negative value of electric initial loading leads to bigger frequencies than those of the positive one. Clearly, the external applied electric voltage will produce the axial compressive and tensile forces which increase and decrease the stiffness of plate when suppling positive and negative electric voltage, respectively. Moreover, the first dimensionless frequency also changes for different boundary conditions regarding the stiffness of plate. For example, the fully clamped FGPMP plate has highest frequencies since the stiffness plate is biggest.

Table 6. 4: Comparison of non-dimensional frequency $\tilde{\omega}$ of a perfect FGPM plate with different boundary conditions ($\alpha = 0$).

		g=0.1		*g*=1		*g*=2		*g*=6	
BC	V_0	Ref.[167]	Present	Ref.[167]	Present	Ref.[167]	Present	Ref.[167]	Present
	-200	9.483	9.5000	9.083	9.0993	8.988	8.9999	8.865	8.8736
	0	9.426	9.4438	9.011	9.0277	8.910	8.9220	8.780	8.7880

CC	200	9.369	9.3873	8.938	8.9554	8.831	8.8433	8.694	8.7015
CC									
	-200	7.670	7.6778	7.354	7.3590	7.280	7.2807	7.184	7.1811
SC	0	7.606	7.6142	7.272	7.2779	7.192	7.1925	7.088	7.0843
SC	200	7.540	7.5500	7.190	7.1959	7.102	7.1031	6.989	6.9861
	-200	5.721	5.7509	5.475	5.5075	5.417	5.4477	5.342	5.3718
CF	0	5.699	5.7000	5.410	5.4425	5.346	5.3769	5.264	5.2940
CF	200	5.617	5.6484	5.343	5.3764	5.273	5.3048	5.185	5.2146
	-200	1.796	1.7960	1.743	1.7435	1.733	1.7339	1.720	1.7212
CC	0	1.695	1.6960	1.616	1.6170	1.596	1.5968	1.571	1.5712
FF	200	1.586	1.5879	1.474	1.4765	1.441	1.4427	1.400	1.4004
	-200	4.311	4.3085	4.138	4.1357	4.099	4.0949	4.047	4.0430
SC	0	4.231	4.2290	4.036	4.0341	3.988	3.9844	3.926	3.9216
FS	200	4.149	4.1474	3.931	3.9291	3.873	3.8697	3.800	3.7952

Table 6. 5: Non-dimensional frequency $\tilde{\omega}$ of an imperfect FGPM plate ($\alpha = 0.2$) with different boundary conditions.

V_0	BCs	FGPMP-I				FGPMP-II			
		g=0.1	*g*=1	*g*=2	*g*=6	*g*=0.1	*g*=1	*g*=2	*g*=6
-					8.8148	9.7806	9.3412	9.2331	9.0967
200	CCCC	9.6109	9.0947	8.9702					
	SCSC	7.7663	7.3553	7.2573	7.1349	7.9034	7.5537	7.4685	7.3610
	CFCF	5.8161	5.5036	5.4286	5.3355	5.9191	5.6525	5.5875	5.5057
	CCFF	1.8100	1.7421	1.7302	1.7149	1.8419	1.7840	1.7736	1.7600
	SCFS	4.3538	4.1323	4.0811	4.0177	4.4311	4.2418	4.1974	4.1416
0	CCCC	9.5583	9.0230	8.8904	8.7254	9.7273	9.2714	9.1565	9.0118
	SCSC	7.7067	7.2741	7.1670	7.0338	7.8430	7.4746	7.3818	7.2650
	CFCF	5.7683	5.4385	5.3561	5.2542	5.8704	5.5891	5.5179	5.4285
	CCFF	1.7106	1.6153	1.5899	1.5585	1.7467	1.6605	1.6385	1.6110
	SCFS	4.2792	4.0304	3.9679	3.8908	4.3555	4.1427	4.0887	4.0211
200	CCCC	9.5053	8.9505	8.8099	8.6350	9.6736	9.2010	9.0791	8.9261
	SCSC	7.6466	7.1919	7.0756	6.9311	7.7822	7.3948	7.2940	7.1676
	CFCF	5.7201	5.3721	5.2822	5.1710	5.8219	5.5247	5.4470	5.3498

CCFF	1.6150	1.4744	1.4318	1.3790	1.6445	1.5240	1.4875	1.4421
SCFS	4.2028	3.9251	3.8503	3.7582	4.2782	4.0405	3.9761	3.8958

Figure 6. 2 displays the distribution of dimensionless frequency versus power index values with SSSS boundary condition, a=b=100h and V_0 =0 for both FGPMP-I and FGPMP-II types. It can be seen that the influence of α, porosity coefficient, on the natural frequency of FGPMP plate is remarkable. Clearly, as power index value increases, the first non-dimension frequency decreases for all α. Interestingly, obtained results reduce as α increases for FGPMP-I type. However, this phenomenon is inversed for FGPMP-II type. Therefore, it can be claimed that the value of porosity coefficient and its distribution type have a significant impact on the free vibration response of FGPMP plates.

The influence of applied electric voltages on dimensionless frequency for various porosity coefficient is also depicted in Figure 6. 3. The FGPMP plate has a=b=100h, g=1 with simply supported boundary conditions. As observed, the value of the first non-dimensional frequency continuously decreases as applied electric voltage changes from -500 Volt to 0 Volt and then +500 Volt for two distributions of porosity. Again, the increase of porosity coefficient leads to the reduction of dimensionless frequency for FGPMP-I case. The same observation can be also found for FGPMP-II case.

The variation of fundamental frequency parameters of FGPMP plates versus power index values and electric voltages for various boundary conditions is plotted in Figure 6. 4 and Figure 6. 5, respectively. According to these Figures, the dimensionless frequency decreases as gradient index value and electric voltage increase for all boundary conditions. Moreover, the first six mode shapes and respectively numerical results for CCFF FGPMP-I porous plate are illustrated in Figure 6. 6.

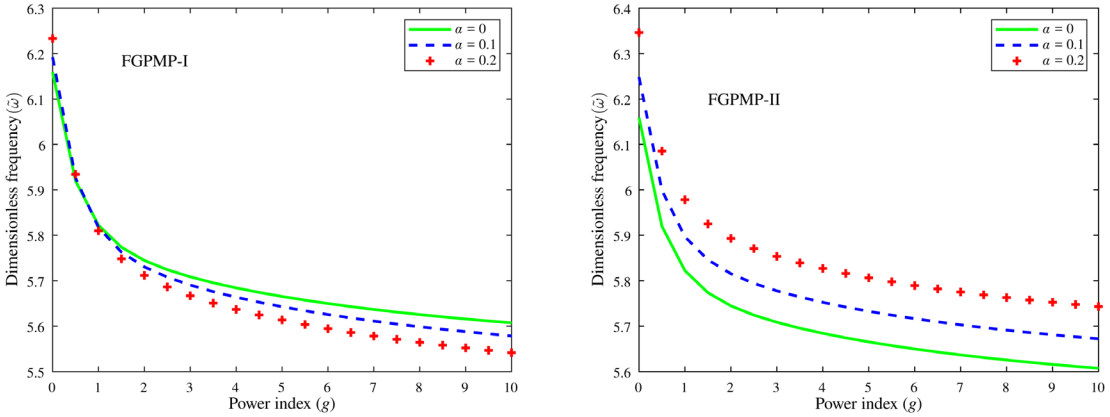

Figure 6. 2. Profile of the dimensionless frequency of FGPMP plates versus power index for various porosity coefficients ($a = b = 100h$, $V_0 = 0$).

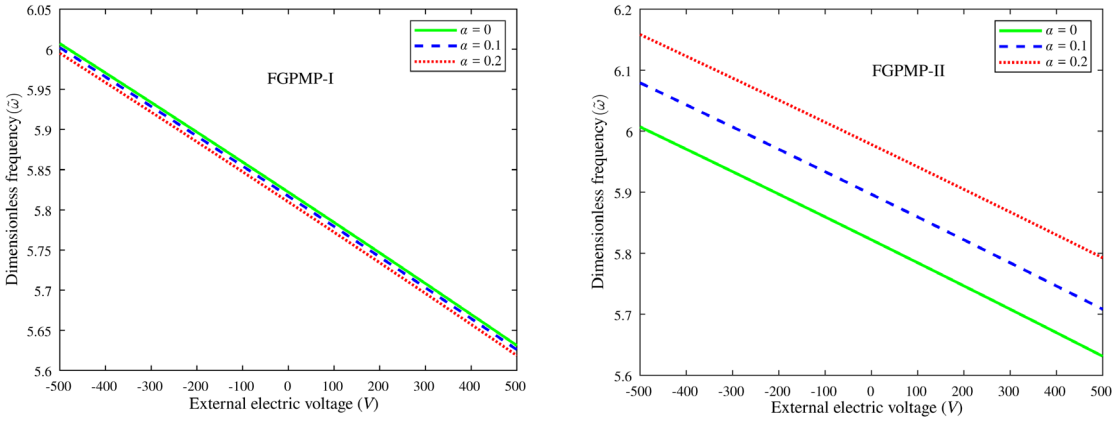

Figure 6. 3. Profile of the dimensionless frequency of FGPMP plates versus electric voltage for various porosity coefficients ($a = b = 100h$, $g = 1$).

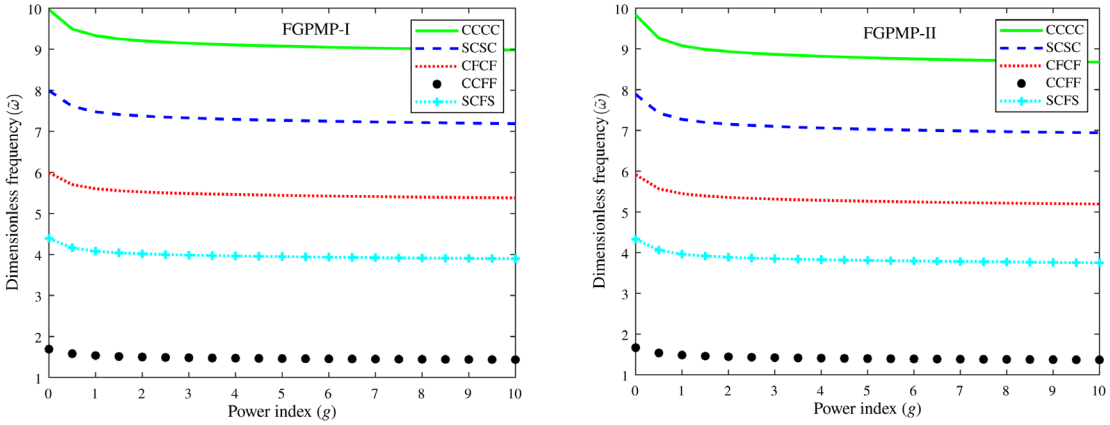

Figure 6. 4. Profile of the frequency of FGPMP plates versus power index values for various boundary conditions ($\alpha = 0.2$, $a = b = 100h$, $V_0 = 200$).

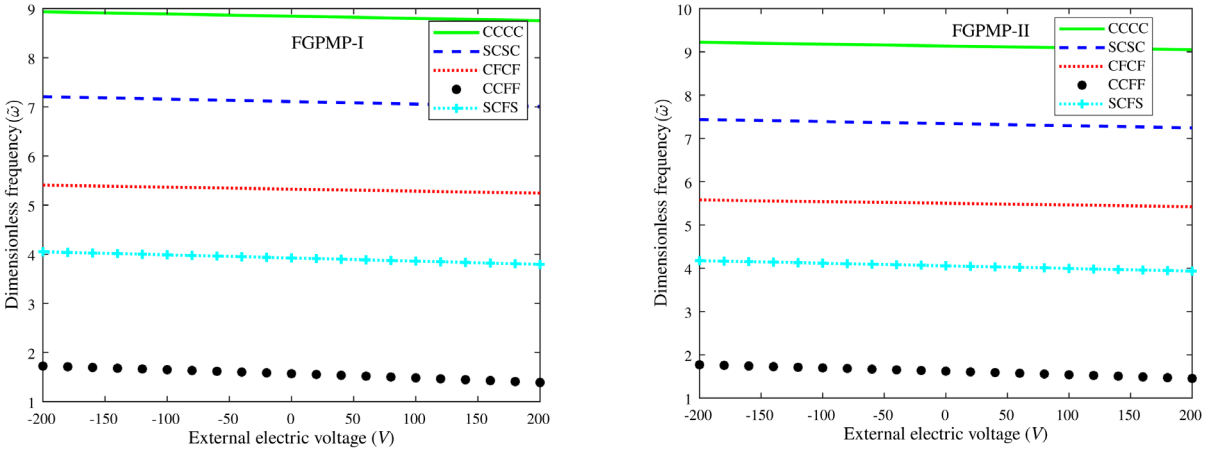

Figure 6. 5. Profile of the dimensionless frequency of FGPMP plates ($\alpha = 0.2$) versus electric voltage values for various boundary conditions ($a = b = 100h$, g=6).

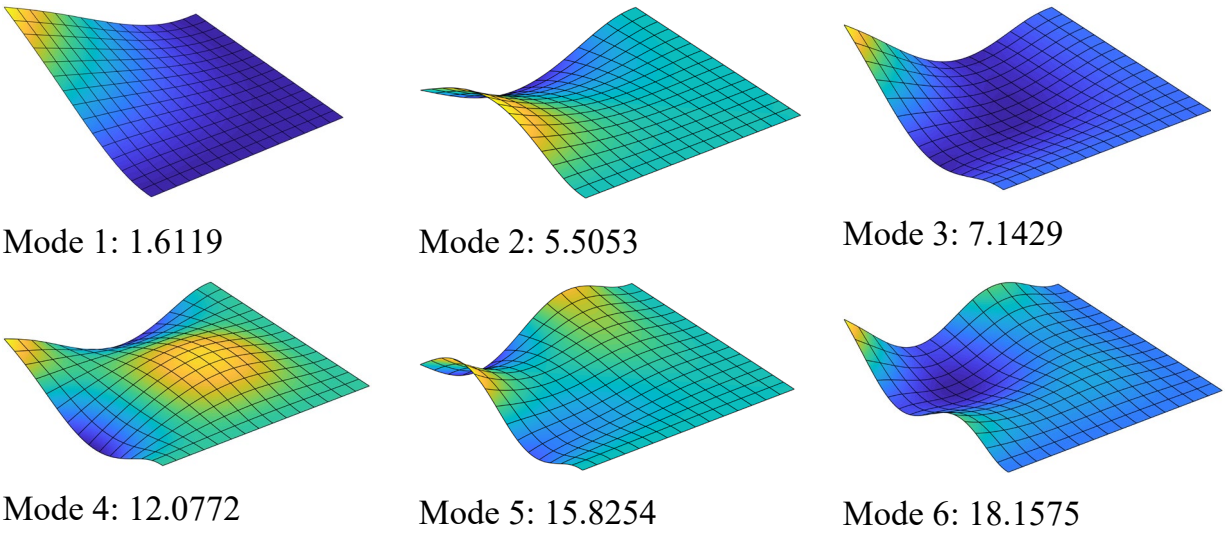

Figure 6. 6. Six mode shapes of a square FGPMP-I porous plate ($\alpha = 0.2$) plate for CCFF boundary condition ($a = b = 100h$, g=2).

6.3.1.2 FGP square plate with a complicated cutout

A square domain with a complicated cutout, as shown in Figure 6. 7a is studied. Figure 6. 7b illustrates a mesh of 336 control points with quadratic Bézier elements. The simply supported and fully clamped boundary conditions are used. First, in order to validate the effectiveness and accuracy of the present solution in comparison with other ones, the FG square plate with a hole of complicated shape made of zirconia (ZrO_2-2) and aluminum (Al) is studied. Material parameters are given as:

$E_c = 200\text{GPa};\ \nu_c = 0.3;\ \rho_c = 3000\text{kg/m}^3$ and $\rho_m = 2707\text{kg/m}^3$ where "c" and "m" are the symbols of ceramic and metal, respectively. The non-dimensional frequency is normalized by $\tilde{\omega} = \omega \frac{a^2}{h}\sqrt{\rho_c / E_c}$. A comparison of the first six non-dimensional frequencies between the present solution with those given in [168] based on 3D elasticity theory using IGA is shown in Table 6. 6. Simultaneously, the obtained solution with various power index values is also compared with those reported in [169] using mesh-free method with naturally stabilized nodal integration based on TSDT. It can be seen that the present solution has good agreement with that reported in Refs. [168] and [169] for both different power index values and two condition boundaries. Non-dimensional frequency parameters decrease with increasing of gradient index values.

Next, the behavior of a FGPMP plate is analyzed. Material properties are given in [165]. The non-dimensional frequencies are calculated by $\tilde{\omega} = \omega b^2 / h\sqrt{\left(\rho / c_{11}\right)_{PZT-4}}$. Numerical solution for non-dimensional frequencies of perfect and imperfect FGPM plate is listed in Table 6. 7 and Table 6. 8, respectively. Influence of electric voltages, boundary conditions and power index values on the dimensionless frequency is shown. The obtained results decrease as power index values and electric voltages alter for both SSSS and CCCC BCs. A variation of non-dimensional frequencies versus various side-to-thickness ratios and electric voltages ($\alpha = 0.2$, g=5) is also displayed in Table 6. 9. It can be seen that nondimensional frequencies depend strongly on the thickness plate and electric voltages. Obtained values for thick and moderately thick FGP plates in accordance with increasing of ratios a/h are increased for all given BCs and electric voltages. However, when the thickness of the plate becomes thinner (a/h=150, 200, 250) the effect of the applied voltage is significant. It is found that with the augmentation of a valuable array of the side-to-thickness ratios, the negative value of applied voltage supplies the increasing of the natural frequency, while positive voltage makes the obtained results reduce.

Moreover, as $V_0 = 0$, the natural frequency of FGPMP plates is not much affected by higher values of side-to-thickness ratios. Furthermore, the first six mode shapes and respectively dimensionless frequencies for the CCCC FGPMP-I square plate with a complicated hole (a/h=50, V_0=0, g =5, $\alpha = 0.2$) are shown in Figure 6. 8.

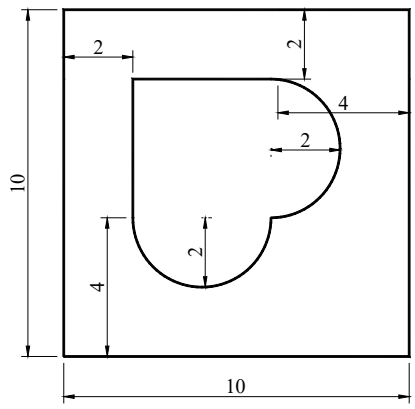

a)

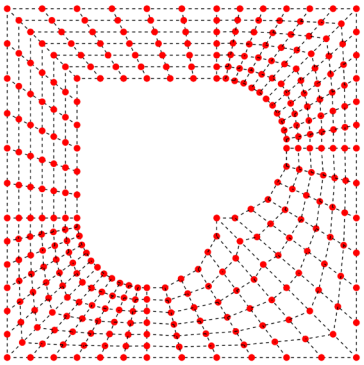

b)

Figure 6. 7. a) Geometry and b) A mesh of 336 control points with quadratic Bézier elements of a square plate with a complicated hole.

Table 6. 6: Comparisons of non-dimensional frequencies $\tilde{\omega} = \omega \frac{a^2}{h}\sqrt{\rho_c / E_c}$ of the FG square plate with a hole of complicated shape (a=b=10, a/h=20).

g	Method	Modes					
		1	2	3	4	5	6
a) SSSS BCs							
0	IGA-3D [168]	7.16	11.65	13.09	20.99	21.85	22.54
	Mesh-free [169]	7.1586	11.9392	13.3987	21.5109	22.4376	23.4263
	Present	7.1919	11.7590	13.2744	21.2602	21.8712	22.9182
1	IGA-3D [168]	6.58	10.73	12.06	19.35	20.77	20.92
	Mesh-free [169]	6.5853	11.0022	12.3439	19.8282	21.4529	21.6277
	Present	6.6167	10.8388	12.2331	19.6016	20.9152	21.1637
5	IGA-3D [168]	6.71	10.88	12.24	19.60	19.73	21.00
	Mesh-free [169]	6.7111	11.1480	12.5192	20.0718	20.2528	21.8177
	Present	6.7503	11.0220	12.4433	19.7416	19.9221	21.4607
20	IGA-3D [168]	6.46	10.48	11.79	18.89	19.05	20.25
	Mesh-free [169]	6.5590	10.9040	12.2431	19.5863	19.6350	21.3484

	Present	6.5932	10.7600	12.1486	19.0919	19.4476	20.9412
50	IGA-3D [168]	6.19	10.07	11.32	18.15	18.81	19.48
	Mesh-free [169]	6.3642	10.5978	11.8961	19.0892	19.4004	20.7723
	Present	6.3952	10.4463	11.7934	18.8836	18.9107	20.3444
100	IGA-3D [168]	6.15	10.00	11.25	18.04	18.78	19.36
	Mesh-free [169]	6.2664	10.4427	11.7206	18.8120	19.3328	20.4784
	Present	6.2964	10.2900	11.6165	18.6026	18.8448	20.0477
b) CCCC BCs							
0	IGA-3D [168]	15.8	27.28	27.45	33.22	34.28	41.21
	Mesh-free [169]	16.0324	27.2803	27.5366	33.8496	35.1963	43.1084
	Present	15.9791	27.4452	27.5505	33.5359	34.5845	41.9276
1	IGA-3D [168]	14.62	25.17	25.32	30.68	31.67	38.10
	Mesh-free [169]	14.7836	25.1888	25.4231	31.2910	32.5400	39.8986
	Present	14.7377	25.3346	25.4308	30.9969	31.9722	38.8082
5	IGA-3D [168]	14.79	25.38	25.54	30.83	31.80	38.16
	Mesh-free [169]	14.9499	25.3745	25.6213	31.4109	32.6465	39.8958
	Present	14.9715	25.6918	25.7906	31.3627	32.3396	39.1699
20	IGA-3D [168]	14.41	24.74	24.90	30.07	31.02	37.23
	Mesh-free [169]	14.6255	24.8309	25.0696	30.7487	31.9625	39.0741
	Present	14.6122	25.0712	25.1681	30.5945	31.5460	38.1960
50	IGA-3D [168]	13.8	23.79	23.93	28.95	29.87	35.90
	Mesh-free [169]	14.2233	24.1747	24.4041	29.9665	31.1547	38.1231
	Present	14.1904	24.3597	24.4535	29.7448	30.6726	37.1603
100	IGA-3D [168]	13.64	23.45	23.60	28.56	29.47	35.43
	Mesh-free [169]	14.0187	23.8394	24.0645	29.5646	30.7388	37.6306
	Present	13.9804	24.0057	24.0980	29.3229	30.2390	36.6471

Table 6. 7: The first dimensionless frequency $\tilde{\omega} = \omega b^2 / h\sqrt{\left(\rho / c_{11}\right)_{PZT-4}}$ of a FGPMP square plate with a complicated cutout ($\alpha = 0$) with different electric voltages (a=b=10, a/h=20).

V_0	BC	Perfect FGPM					
		g=0	g=1	g=5	g=20	g=50	g=100
-500	SSSS	5.8501	5.4275	5.2457	5.1149	5.0622	5.0409

	CCCC	15.0403	14.0986	13.6657	13.3776	13.2683	13.2248
0	SSSS	5.8497	5.4270	5.2453	5.1143	5.0617	5.0403
	CCCC	15.0400	14.0983	13.6655	13.3773	13.2680	13.2246
500	SSSS	5.8493	5.4265	5.2448	5.1138	5.0613	5.0399
	CCCC	15.0397	14.0980	13.6653	13.3770	13.2678	13.2244

Table 6. 8: The first dimensionless frequency $\tilde{\omega}$ of a square FGPMP plate with a complicated cutout ($\alpha = 0.2$) with different electric voltages (a=b=10, a/h=20).

V_0	BC	FGPMP-I			FGPMP-II		
		g=0	g=1	g=5	g=0	g=1	g=5
-500	SSSS	5.9470	5.4161	5.1898	6.0248	5.5644	5.3669
	CCCC	15.2538	14.0702	13.5298	15.4377	14.4097	13.9347
0	SSSS	5.9466	5.4156	5.1893	6.0244	5.5639	5.3664
	CCCC	15.2536	14.0700	13.5296	15.4375	14.4095	13.9345
500	SSSS	5.9462	5.4152	5.1889	6.0240	5.5635	5.3660
	CCCC	15.2534	14.0698	13.5294	15.4373	14.4094	13.9343

Table 6. 9: The first dimensionless frequency $\tilde{\omega}$ of a square FGPMP plate with a complicated cutout with various side-to-thickness ratios (a=b=10, $\alpha = 0.2$, g=5).

BC	a/h	FGPMP-I			FGPMP-II		
		V_0= -500	V_0= 0	V_0=500	V_0= -500	V_0= 0	V_0=500
SSSS	20	5.1898	5.1893	5.1889	5.3669	5.3665	5.3660
	50	5.3195	5.3122	5.3048	5.5039	5.4968	5.4897
	100	5.4438	5.3855	5.3265	5.6299	5.5737	5.5168
	150	5.6222	5.4296	5.2281	5.8048	5.6187	5.4247
	200	5.9141	5.4722	4.9818	6.0889	5.6612	5.1901
	250	6.3431	5.4997	4.5101	6.5071	5.6983	4.7426
CCCC	20	13.5298	13.5296	13.5294	13.9347	13.934	13.9343
	50	14.2322	14.2292	14.2263	14.6945	14.691	14.6888
	100	14.8413	14.5181	14.7948	15.3211	15.298	15.2763
	150	15.4552	14.8778	14.5998	15.9344	15.359	14.9844
	200	16.1832	14.9018	14.0176	16.6566	15.481	14.3038
	250	17.0282	14.9380	13.5174	17.4951	15.516	13.8091

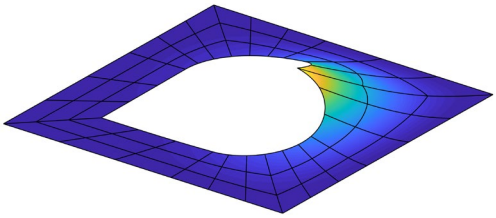

Mode 1: 14.2292

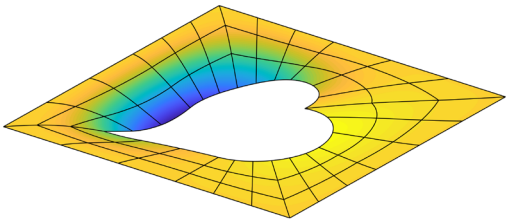

Mode 2: 25.1062

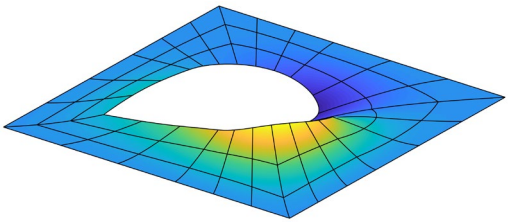

Mode 3: 25.7717

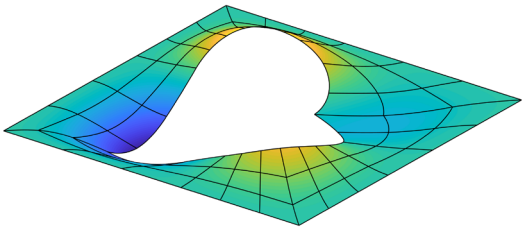

Mode 4: 30.6466

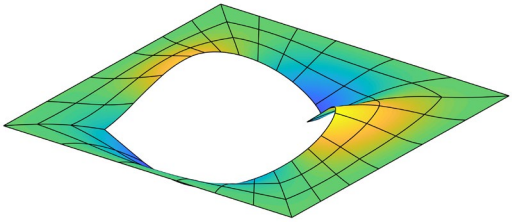

Mode 5: 30.9956

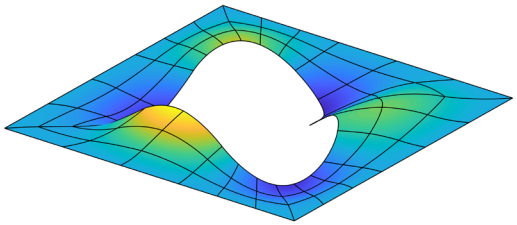

Mode 6: 39.0102

Figure 6. 8. The first six mode shapes of the fully clamped FGPMP-I square plate with a complicated hole (a/h=50, V_0=0, g =5, $\alpha = 0.2$).

6.3.2 Circular plates

6.3.2.1 Circular FGP plate

An isotropic circular plate with simply supported and fully clamped boundary conditions is considered, as shown in Figure 6. 9a. A mesh of 15×15 quadratic Bézier elements is shown in Figure 6. 9. For comparison purpose, firstly an isotropic circular plate is investigated. This plate has a unit radius (R = 1). Material parameters are taken as the modulus $E = 210$ GPa, Poisson's ratio $\nu = 0.3$ and density mass $\rho = 1$ kg/m^2. Considering two diameter-to-thickness ratios including 10 and 100 ($2R/h$ = 10, 100). The normalized frequencies are defined as $\tilde{\omega} = \omega R^2 (\rho h / D_m)^{1/2}$ in which $D_m = Eh^3 / 12\left(1-\nu^2\right)$. The obtained solutions are compared with those given by Irie et al. [170] based on the exact solution-FSDT and Nguyen-Xuan et al. [171]

based on the edge-based smoothed and discrete shear gap plate element (ES-DSG3)-FSDT. The first six non-dimensional frequencies are shown in Table 6. 10. As expected, the obtained results match well with other published solutions for two diameter-to-thickness ratios.

Next, an FGP circular plate is studied with initial parameters based on the isotropic circular plate. Material properties are adopted from [166] given in Table 6. 1. The non-dimensional frequencies are given by $\tilde{\omega} = 4\omega R^2 / h\sqrt{(\rho / c_{11})}_{PZT-4}$. The first dimensionless frequencies of a FGPMP circular plate with different electric voltages and power index parameters for two boundary conditions, SSSS and CCCC BCs, are summarized in Table 6. 11 and Table 6. 12.

Table 6. 13 displays variation of obtained results of first non-dimensional frequencies versus various side-to-thickness ratios and electric voltages. It is clear that the same behavior as the previous vibration problem for frequencies is confirmed. The first six mode shapes of a perfect FGPMP circular plate with R/h=5, g=1 are also illustrated in Figure 6. 10.

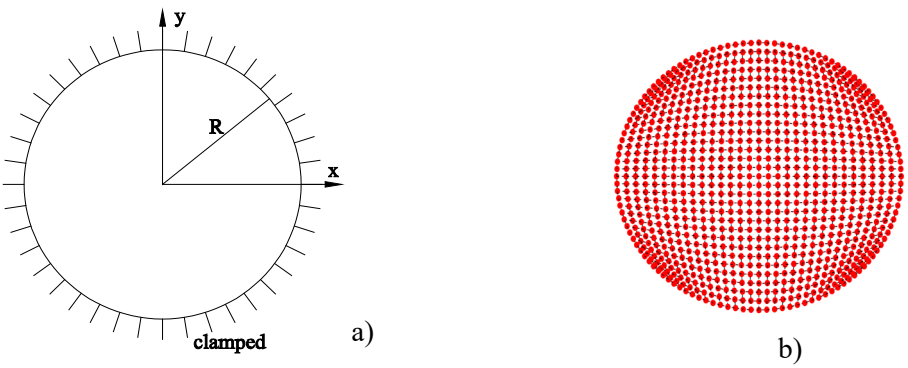

Figure 6. 9. a) Geometry and b) A mesh of 15×15 quadratic Bézier elements.

Table 6. 10: First six non-dimensional frequencies $\tilde{\omega} = \omega R^2(\rho h / D_m)^{1/2}$ of the fully clamped isotropic circular plate (R/h=5).

2R/h	Method	Modes					
		1	2	3	4	5	6
10	ES-DSG3 [171]	9.2527	17.8372	17.8428	27.2344	27.2391	30.5173

	Exact [170]	9.2277	17.8010	17.8010	26.6801	27.2246	29.8562
	Present	9.2398	17.8301	17.8396	27.2434	27.2210	30.5016
100	ES-DSG3 [171]	10.2402	21.3966	21.4096	35.3012	35.3277	40.3671
	Exact [170]	10.2160	21.2600	21.2600	34.8770	34.8770	39.7710
	Present	10.2388	21.5725	21.4001	35.2621	35.2961	40.2832

Table 6. 11: The first dimensionless frequency $\tilde{\omega} = 4\omega R^2 / h\sqrt{\left(\rho / c_{11}\right)_{PZT-4}}$ of a perfect FGPMP circular plate ($\alpha = 0$) with different electric voltages and power index parameters for SSSS and CCCC BCs (R/h=5).

V_0	BC	Perfect FGPM					
		g=0	g=1	g=5	g=20	g=50	g=100
-500	SSSS	5.4813	5.1700	5.0491	4.9671	4.9375	4.9259
	CCCC	10.4445	9.8270	9.5917	9.4342	9.3750	9.3515
0	SSSS	5.4812	5.1697	5.0487	4.9668	4.9371	4.9255
	CCCC	10.4444	9.8269	9.5915	9.4339	9.3748	9.3513
500	SSSS	5.4811	5.1694	5.0484	4.9664	4.9367	4.9251
	CCCC	10.4443	9.8268	9.5913	9.4337	9.3746	9.3510

Table 6. 12: The first dimensionless frequency $\tilde{\omega} = 4\omega R^2 / h\sqrt{\left(\rho / c_{11}\right)_{PZT-4}}$ of an imperfect FGPM circular plate ($\alpha = 0.5$) with different electric voltages and power index parameters for SSSS and CCCC BCs (R/h=5).

V_0	BC	FGPMP-I			FGPMP-II		
		g=0	g=10	g=20	g=0	g=10	g=20
-500	SSSS	6.0988	4.8457	4.7744	5.9657	5.3466	5.3018
	CCCC	11.6213	9.1864	9.0499	11.2864	10.0557	9.9707
0	SSSS	6.0987	4.8453	4.7739	5.9655	5.3463	5.3015
	CCCC	11.6212	9.1861	9.0497	11.2863	10.0554	9.9705
500	SSSS	6.0985	4.8448	4.7735	5.9653	5.3459	5.3011
	CCCC	11.6210	9.1859	9.0494	11.2862	10.0552	9.9703

Table 6. 13: The first dimensionless frequency $\tilde{\omega} = 4\omega R^2 / h\sqrt{(\rho / c_{11})}_{PZT-4}$ of a circular FGPMP plate with various side-to-thickness ratios ($\alpha = 0.2$, g=1).

BC	R/h	FGPMP-I			FGPMP-II		
		V_0 = -500	V_0 = 0	V_0=500	V_0 = -500	V_0 = 0	V_0=500
SSSS	5	5.1691	5.1690	5.1688	5.3017	5.3016	5.3014
	10	5.2489	5.2477	5.2465	5.3896	5.3884	5.3873
	20	5.2797	5.2702	5.2606	5.4228	5.4136	5.4043
	50	5.4274	5.2803	5.1291	5.5678	5.4248	5.2779
	80	5.8617	5.2830	4.6326	5.9918	5.4277	4.7978
	100	6.3651	5.2839	3.9144	6.4847	5.4287	4.1095
CCCC	5	9.8220	9.8219	9.8218	10.0456	10.0455	10.0454
	10	10.1915	10.1907	10.1900	10.4543	10.4536	10.4529
	20	10.3114	10.3056	10.2998	10.5893	10.5836	10.5780
	50	10.4555	10.3650	10.2736	10.7377	10.6497	10.5609
	80	10.7470	10.3818	10.0022	11.0234	10.6681	10.2996
	100	11.0882	10.3871	9.6309	11.3566	10.6740	9.9406

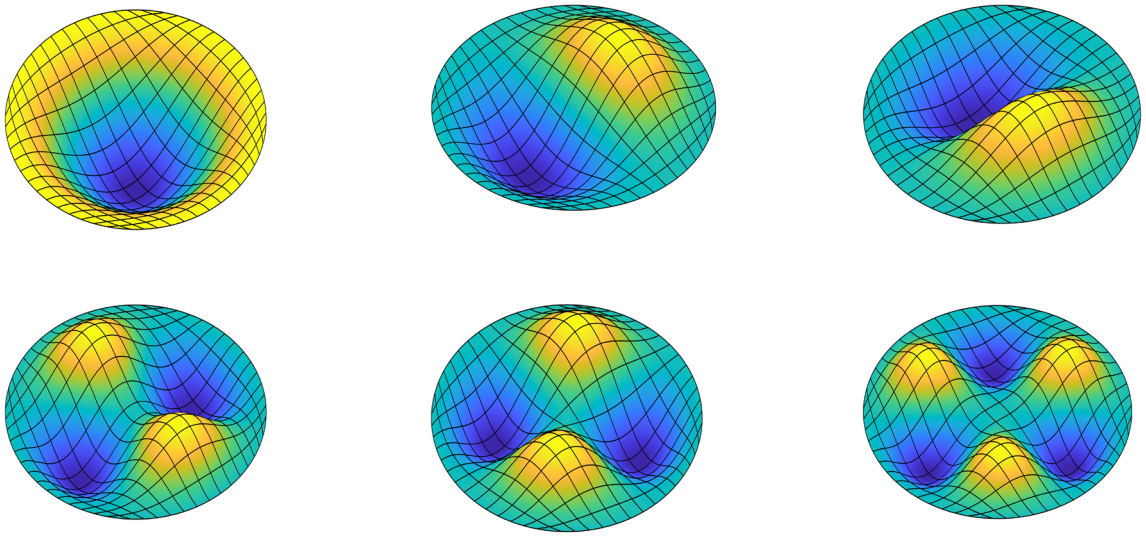

Figure 6. 10. Six mode shapes of a FGPMP circular plate ($\alpha = 0$) plate for CCCC boundary condition (R/h=5, g=1).

6.3.2.2 FGP annular plate

An FG annular plate made from aluminum (Al) and zirconia (ZrO_2-3) is considered, as illustrated in Figure 6. 11a. Material parameters are given as: $E_c = 168\text{GPa};\ \nu_c = 0.3;\ \rho_c = 5700\text{kg/m}^3$ and

$E_m = 70\text{GPa};\ \nu_m = 0.3;\ \rho_m = 2707\text{kg/m}^3$

Material properties are homogenized by the rule of mixture [172] as

$$\begin{gathered} E_e = \left(E_c - E_m\right)V(z) + E_m;\ \ \nu_e = \left(\nu_c - \nu_m\right)V(z) + \nu_m; \\ \rho_e = \left(\rho_c - \rho_m\right)V(z) + \rho_m; \\ V\left(z\right) = \left[1 - \frac{1}{2}\left(\frac{1}{2} + \frac{z}{h}\right)^2\right]^g \end{gathered} \tag{6.50}$$

The outer and inner radius are R = 2m and r = 0.5m, respectively. The FG plate subjected to the clamped around outer boundary is considered. The radius-to-thickness ratio is R/h=20. A set of 840 control points with quadratic Bézier elements is chosen to calculate the natural frequency, as shown in Figure 6. 11b. Numerical results of the first six natural frequencies (Hz) are compared to those reported by Tornabene [172] using a generalized differential quadrature (GDQ) solution based on FSDT, Nguyen and Nguyen-Xuan [168] using the IGA-3D solution and Thai et al. [173] using the IGA-Quasi-3D solution, as listed in Table 6. 14. It is seen that obtained results have good conformity with those results for different power index values. It is also observed that solutions derived from GDQ and IGA for mode 2 and 3, 4 and 5 are completely similar while our obtained results are anti-symmetry for mode 4 and 5 but the difference between two modes is small.

The FGPMP annular plate with porosities is continued investigating. Material properties given in ref. [166] are used. The influence of electric voltages and power index gradients on natural frequencies for both perfect and FGPMP plates as summarized in Table 6. 15. Numerical results with various electric voltages and porosity coefficients for the first six natural frequencies are given in Table 6. 16. Again, behavior of obtained solutions is completely similar to those found in the above numerical examples. Figure 6. 12 illustrates the first six mode shapes of a

porous FGPMP-II annular plate with R=2m; r=0.5m; R/h=50; g=1; $\alpha = 0.2$ and the natural frequencies, respectively. These mode shapes describe well the physical vibration of the plate.

Table 6. 14: Comparisons of the frequencies (Hz) of the FG annular plate (R/h=20).

		Mode			
g	Method	1	2,3	4,5	6
0	GDQ-FSDT [172]	70.13	127.5	212.58	296.99
	IGA-3D [168]	70.52	128.43	213.7	298.95
	IGA-Quasi3D [173]	72.1676	132.2599	217.8233	306.1282
	Present	70.1898	128.1321	213.3364	298.7625
				213.3496	
1	GDQ-FSDT [172]	68.71	124.95	208.35	291.13
	IGA-3D [168]	69.01	125.89	209.47	293.1
	IGA-Quasi3D [173]	70.7454	129.6654	213.6302	300.2181
	Present	68.7642	125.5741	209.0863	292.8719
				209.0995	
5	GDQ-FSDT [172]	66.36	120.75	201.35	281.41
	IGA-3D [168]	66.73	121.62	202.36	283.2
	IGA-Quasi3D [173]	68.4912	125.6639	207.3209	291.0517
	Present	66.4187	121.3562	202.0715	283.1232
				202.0846	
20	GDQ-FSDT [172]	68.84	125.11	208.58	291.33
	IGA-3D [168]	69.16	125.73	209.21	292.51
	IGA-Quasi3D [173]	71.0036	130.3345	214.9153	301.505
	Present	68.9046	125.7399	209.3388	293.0842
				209.3515	
50	GDQ-FSDT [172]	70.52	128.05	213.47	298.04
	IGA-3D [168]	69.16	125.73	209.21	292.51
	IGA-Quasi3D [173]	72.6279	133.2711	219.5564	308.0957
	Present	70.5863	128.6964	214.2403	299.8033
				214.2527	
100	GDQ-FSDT [172]	70.78	128.49	214.19	299.02

IGA-3D [168]	71.41	129.65	215.73	301.46
IGA-Quasi3D [173]	72.8398	133.6202	220.038	308.8717
Present	70.8443	129.1308	214.9585	300.7690
			214.9708	

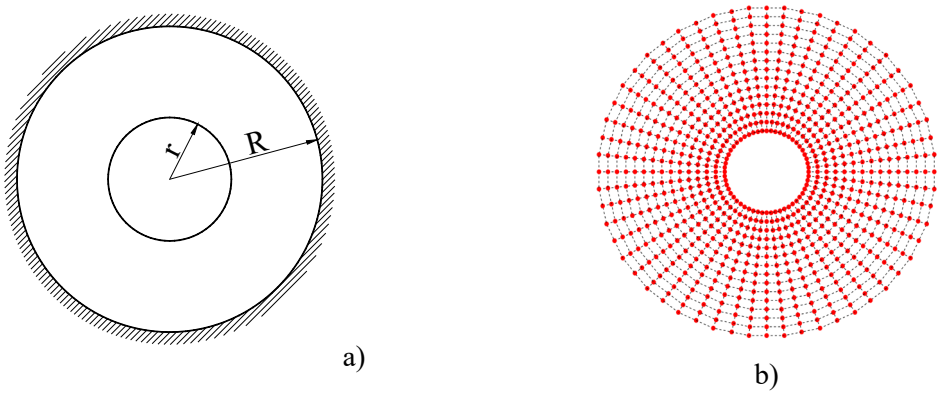

a) b)

Figure 6. 11. Geometry and a mesh of 840 control points with quadratic Bézier elements of the annular plate.

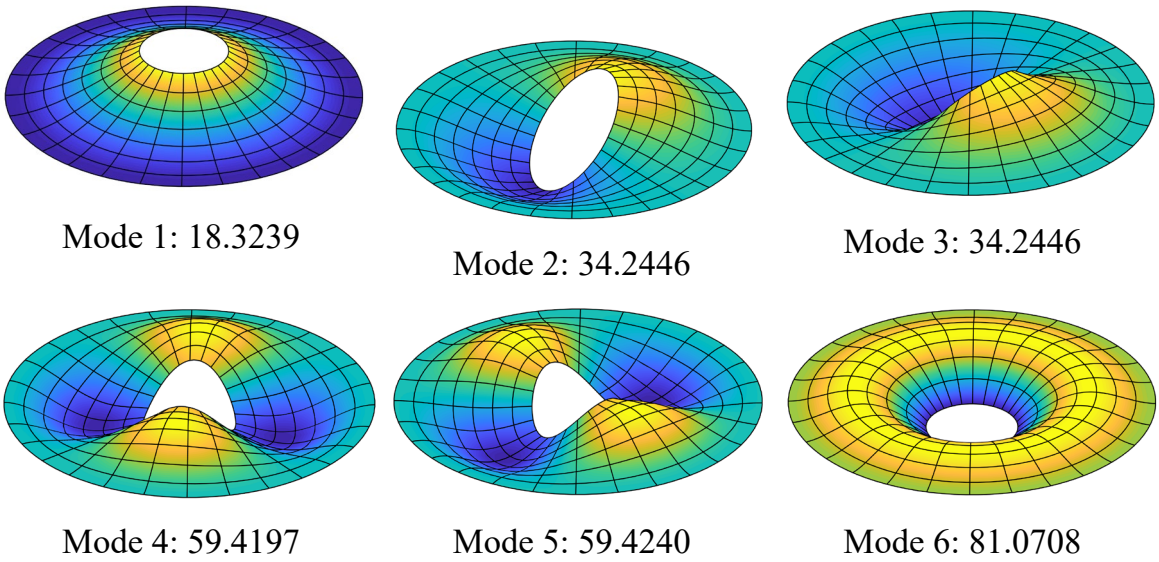

Mode 1: 18.3239 Mode 2: 34.2446 Mode 3: 34.2446

Mode 4: 59.4197 Mode 5: 59.4240 Mode 6: 81.0708

Figure 6. 12.. The first six mode shapes of a porous FGPMP-II annular plate with R=2; r=0.5; R/h=50; g=1; $\alpha = 0.2$.

Table 6. 15: The first natural frequency (Hz) of a FGPMP annular plate with different electric voltages and power index values (R=2m; r=0.5m; R/h=20).

	V_0	Type	Power index					
			g=0	g=1	g=5	g=20	g=50	g=100
$\alpha = 0$	-500		47.2239	44.4290	43.3147	42.4997	42.1819	42.0544
	0		47.2095	44.4094	43.2915	42.4748	42.1566	42.0289
	500		47.1951	44.3898	43.2682	42.4499	42.1312	42.0033
$\alpha = 0.5$	-500	FGPMP-I	51.2713	44.2238	42.0233	41.9682	39.8256	39.5602
	0		51.2612	44.2039	41.9958	40.4387	39.7932	39.5274
	500		51.2511	44.1839	41.9682	40.4075	39.7608	39.4945
	-500	FGPMP-II	51.4099	47.8447	46.4782	45.4882	45.0974	44.9399
	0		51.3978	47.8264	46.4555	45.4636	45.0722	44.9144
	500		51.3857	47.8082	46.4329	45.4390	45.0470	44.8890

Table 6. 16: The first six natural frequency (Hz) of a porous FGPMP annular plate with various electric voltages and porosity coefficients (R=2m; r=0.5m; R/h =10; g=1).

		FGPMP-I			FGPMP-II		
V_0	Mode	$\alpha = 0.1$	$\alpha = 0.2$	$\alpha = 0.3$	$\alpha = 0.1$	$\alpha = 0.2$	$\alpha = 0.3$
-500	1	87.8849	87.8404	87.7755	88.9889	90.1565	91.4321
	2,3	159.5446	159.466	159.353	161.369	163.278	165.342
	4	275.3469	275.254	275.120	278.353	281.507	284.895
	5	275.4049	275.312	275.178	278.418	281.580	284.973
	6	368.8354	368.673	368.437	372.679	376.659	380.901
0	1	87.8800	87.8355	87.7706	88.9841	90.1518	91.4275
	2,3	159.5411	159.463	159.349	161.366	163.275	165.338
	4	275.3431	275.250	275.116	278.349	281.504	284.886
	5	275.4011	275.309	275.174	278.414	281.577	284.969
	6	368.8294	368.667	368.431	372.673	376.654	380.896
500	1	87.8751	87.8306	87.7657	88.9793	90.1470	91.4228
	2,3	159.5376	159.459	159.346	161.362	163.272	165.335
	4	275.3393	275.247	275.112	278.345	281.500	284.883
	5	275.3973	275.302	275.170	278.410	281.573	284.966
	6	368.8234	368.663	368.425	372.667	376.648	380.890

6.4 Conclusions

An isogeometric Bézier finite element method in combination with C^0-type HSDT theory for electro-mechanical vibration analysis of functionally graded piezoelectric material porous plates is presented. Thanks to the Bézier extraction, the implementation of IGA becomes easily with Bernstein basis functions, which have a close resemblance to Lagrange shape functions as using C^0-continuous Bézier elements. Interestingly, obtained results matched well with extant studies or available solutions in the literature. Furthermore, numerical solutions for functionally graded piezoelectric porous plates were achieved, where analytical solutions have not been found yet. Throughout the free vibration analysis, it was observed that external electric voltages, power-law index, porosity coefficient, porosity distribution, geometrical aspect ratios and various boundary conditions significantly affect natural frequencies of structures. The combination of the best advantage of IGA in terms of the exact geometry and Bézier extraction which can integrate IGA into existing finite element codes along with a C^0-type HSDT theory showed the significant contribution in this paper. There are some remarkable conclusions as follows

a) the frequency parameter for FGP plate continuously decreases with the increasing of power-law index for both perfect and imperfect FGPM plates with all kinds of given boundary conditions and any porosity coefficients.
b) with the same porosity coefficient value, the frequency parameter of the FGPMP-I type is lower than the FGPMP-II type. In addition, as porosity coefficient increases, the obtained results reduce for FGPMP-I case but they increase for FGPMP-II case.
c) negative value of electric initial loading gives frequencies bigger than positive one for all examples with various boundary conditions and geometries. Of course, the plate has many constraints, natural frequencies will be increased.
d) the natural frequencies will be remarkably incremented as the thickness of the plate becomes thinner for thick and moderately plate. However, the obtained results are changed for much thin plate since the influence of external electric voltages. The plate thickness is smaller resulting in a bigger change in frequency parameters.

Chapter 7
CONCLUSIONS AND RECOMMENDATIONS

7.1 Conclusions

In this dissertation, the isogeometric analysis based on Bézier extraction to analyze and control the laminated plate structures has been developed. Four material models have been considered, namely, laminated composite plates, piezoelectric laminated composite plates, piezoelectric functionally graded porous plates with graphene platelets reinforcement and functionally graded piezoelectric material porous plates. The dissertation has two parts: a) Analysis and b) Control.

Isogeometric analysis (IGA) is proposed as the calculating tool for all problems in this dissertation. The main advantage of the IGA is using the same basis function, B-splines or the non-uniform rational B-splines (NURBS), to describe the geometry (CAD) and to approximate the problem unknowns. In IGA, NURBS allow us to define the curved geometry precisely such as conic by using only a few elements and yielding solutions with higher accuracy. It means that the exact geometry is preserved at the coarse level of discretization and the re-meshing is performed on this level without any further communication with initial CAD geometry. Thus, the computational cost will be significantly reduced. Furthermore, in comparison with basis functions obtained from Lagrange and Hermite interpolation widely used in FEM, the NURBS basis functions can achieve higher continuity of derivatives. However, the conventional IGA employs the recursive function for analysis. In addition, B-spline/NURBS basis functions spanning over the entire domain of structures do not possess a local domain as Lagrangian shape functions. The global structure requires complex implementation in the traditional finite element context. Additionally, the numerical computation of stiffness formulation needs to be further transformed into the parent element while basis functions are defined in the parametric space. By choosing Bernstein polynomials as the basis functions in Bézier extraction, IGA is done as easily as that in FEM. The Bernstein basis functions have

the C^0-continuity as Lagrangian shape functions do. By using the advantages of IGA which allow exact representation of various complex geometries, i.e., spheres, circles, ellipsoids, cylinders, etc., and Bézier extraction operator, it can be believed that this method gives many benefits. And this thing is verified through five numerical example chapters. A higher-order shear deformation theory with C^0-continuity is used for the unification of all chapters.

For smart plates bonded by piezoelectric layer on the top and bottom surfaces of plate, the electric potential is assumed to vary linearly through the thickness of each piezoelectric sublayer. A displacement and velocity feedback control algorithm is used for the active control of the static deflection and dynamic response of the plates through a closed-loop control with embedded distributed piezoelectric sensors and actuators. Both the linear and geometrically nonlinear responses are investigated. For the FGPMP plates, the material properties vary continuously in the thickness direction through a modified power-law formulation and an electric potential field in the form of a mixture of cosine and linear variation is adopted. Through several numerical results, some main conclusions can be stated as follows:

- The combination of IGA based on Bézier extraction with UHSDT and C^0-type HSDT for analyzing and controlling the static, free vibration and transient responses for four plate material models has been studied effectively. By using Bézier extraction operator, the implementation of IGA becomes significantly easier with Bernstein basis functions, which have a close resemblance to Lagrange shape functions as using C^0 continuous Bézier elements. This can be a reasonable choice due to the basis functions are given on localized form and the way of implementation in IGA is similar to that in FEM.
- By using the UHSDT and C^0-type HSDT, the proposed method relaxes the non-zero transverse shear stresses on the lower and upper surface of the plate and no shear correction factor is used. In addition, the HSDT and the CPT bear relation to derivation transverse displacement also called slope

components. In some complex geometries with symmetric boundary conditions, it is often difficult to enforce boundary conditions for slope components due to the unification of the approximated variables. So, the seven-dof shear deformation theory is applied in this dissertation.

- In static, free vibration and dynamic analysis, the predictions of the proposed approach agree well with analytical solutions and several available other approaches. Through the analysis, numerical results indicate that the proposed method achieves high reliability as compared with other published solutions and slightly better than the UTSDT using IGA based on Bézier extraction. Interestingly, obtained results match well with extant studies or available solutions in the literature. Furthermore, numerical solutions for PFGPM plates and piezoelectric FG porous reinforced by GPLs have been achieved. It is known that there have not yet been analytical solutions so far, so numerical solutions may be considered as reference solutions for future works.
- Both linear and nonlinear of FG porous reinforced by GPLs with piezoelectric sensors and actuators are investigated. The geometrically nonlinear equations are solved by the Newton-Raphson iterative procedure and the Newmark's time integration scheme. The influences of the porosity coefficients, weight fractions of GPLs as well as the external electrical voltage on the linear and geometrically nonlinear behaviors of the plates with different porosity distributions and GPL dispersion patterns are evidently investigated through numerical examples. The stiffness of the FG porous plate greatly decreases due to porosity coefficients. However, the stiffness of the plates remarkably increases as the FG porous plate is reinforced by GPLs. The obtained results in term of displacements and periods of motions for the FG porous plate without GPLs are smaller than those achieved for the FG porous plate with GPLs.

- For the first time, an isogeometric Bézier finite element method has been presented for electro-mechanical vibration analysis of functionally graded piezoelectric material porous plates. Through the free vibration analysis, it is observed that external electric voltages, power-law index, porosity coefficient, porosity distribution, geometrical aspect ratios and various boundary conditions significantly affect the natural frequencies of structures.
- The control algorithms based on the constant displacement and velocity feedbacks are applied to control linear and geometrically nonlinear static and dynamic responses of the plates, where the effect of the structural damping is considered, based on a closed-loop control with piezoelectric sensors and actuators. For geometrically nonlinear static response control of the FG porous plates, two effective algorithms are considered such as the input voltage control with opposite signs applied across the thickness of two piezoelectric layers and the displacement feedback control algorithm. In addition, the dynamic responses of the FG porous plate can be expectantly suppressed based on the effectiveness of the velocity feedback control algorithm.
- In this dissertation, in addition to some numerical examples with either square or circle/eclipse, there are various complex geometries which can be modeled easily with multi-patch approach. These complicated geometries can raise the IGA's advantages to the maximum.

7.2 Recommendations

Through the obtained results, it can be believed that the suggested approach with many new points may provide a reliable source of reference for calculating the behaviors of laminated plate structures. However, some restrictions should be mentioned as the suggestions for the potential extension of this work:

- Future research of this work should be done with the presence of shear traction parallel to the surfaces of the plate in the numerical examples (e.g., contact friction or boundary layer flow).
- It is possible to consider various boundary conditions rather than the homogeneous Dirichlet one which only used in this work.
- Another direction of research should be to expand these 2D theories to full-3D or quasi-3D ones.
- The proposed method should be applied to the microstructures using the theory of nonlocal elasticity and that of modified couple stress.
- The IGA can be used to compute for various problems such as incompressibility, phase-field analysis, large deformation with mesh distortion and shape optimization.
- This method should be applied in the industrial field or the practical problems, e.g. to machinery, automobiles, or offshore structures, etc.

REFERENCES

[1]. J. Argyris, S. Kelsey. *Energy Theorems and Structural Analysis*. Butterworths, London, 1960.

[2]. J. A. Cottrell, T. J. R. Hughes, Y. Bazilevs. *Isogeometric Analysis: Toward Integration of CAD and FEA.* Wiley, 2009.

[3]. R. Riesenfeld. *Applications of B-spline approximation to geometric problems of Computer-Aided Design*, 1972.

[4]. K. J. Versprille. *Computer-aided design applications of the rational B-spline approximation form*, 1975.

[5]. T. J. R. Hughes, J. A. Cottrell, Y. Bazilevs. Isogeometric analysis: CAD, finite elements, NURBS, exact geometry and mesh refinement. *Computer Methods in Applied Mechanics and Engineering,* 194, pp. 4135-4195, 2005.

[6]. D. Benson, Y. Bazilevs, M. Hsu, T. Hughes. Isogeometric shell analysis: The Reissner–Mindlin shell. *Computer Methods in Applied Mechanics and Engineering,* 199, pp. 276-289, 2010.

[7]. J. Cottrell, A. Reali, Y. Bazilevs, T. Hughes. Isogeometric analysis of structural vibrations. *Computer Methods in Applied Mechanics and Engineering,* 195, pp. 5257-5296, 2006.

[8]. T. Hughes, A. Reali, G. Sangalli. Duality and unified analysis of discrete approximations in structural dynamics and wave propagation: comparison of *p*-method finite elements with *k*-method NURBS. *Computer Methods in Applied Mechanics and Engineering,* 197, pp. 4104-4124, 2008.

[9]. Y. Bazilevs, V. Calo, T. Hughes,Y. Zhang. Isogeometric fluid-structure interaction: theory, algorithms, and computations. *Computational mechanics,* 43, 2008.

[10]. Y. Bazilevs, V. Calo, Y. Zhang, T. Hughes. Isogeometric Fluid structure Interaction Analysis with Applications to Arterial Blood Flow. *Computational Mechanics*, 38, no. 310-322, 2006.

[11]. A. Buffa, G. Sangalli, R. V´azquez. Isogeometric analysis in electromagnetics: B-splines approximation. *Computer Methods in Applied Mechanics and Engineering,* 199, pp. 1143-1152, 2010.

[12]. H. G´omez, V. Calo, Y. Bazilevs, T. Hughes. Isogeometric analysis of the Cahn-Hilliard phase-field model. *Computer Methods in Applied Mechanics and Engineering,* 197, pp. 4333-4352, 2008.

[13]. J.N. Reddy. *Mechanics of laminated composite plates and shells: theory and analysis*. CRC Press, New York, 2004.

[14]. J. Kiendl, K.U. Bletzinger, J. Linhard , R. Wüchner. Isogeometric shell analysis with Kirchhoff-Love element. *Computer Methods in Applied Mechanics and Engineering*, 198, pp. 3902–3914, 2009.

[15]. J. Kiendl, Y. Bazilevs, M.C. Hsu, R. Wüchner, K.U. Bletzinger. The bending strip method for isogeometric analysis of Kirchhoff–Love shell structures comprised of multiple patches. *Computer Methods in Applied Mechanics and Engineering*, 199, pp. 2403–2416, 2010.

[16]. H.C. Thai, H. Nguyen-Xuan, N. Nguyen-Thanh, T.H. Le, T. Nguyen- Thoi, T. Rabczuk. Static, free vibration, and buckling analysis of laminated composite Reissner-Mindlin plates using NURBS-based isogeometric approach. *International Journal for Numerical Methods in Engineering*, 91, pp. 571–603, 2012.

[17]. H. Kapoor, R.K. Kapania. Geometrically nonlinear NURBS isogeometric finite element analysis of laminated composite plates. *Composite Structures*, 94, pp. 3434–3447, 2012.

[18]. H.C. Thai, A.J.M. Ferreira, E. Carrera, H. Nguyen-Xuan. Isogeometric analysis of laminated composite and sandwich plates using a layerwise deformation theory. *Composite Structures*, 104, pp.196–214, 2013.

[19]. H. Nguyen-Xuan, H.C. Thai, T. Nguyen-Thoi. Isogeometric finite element analysis of composite sandwich plates using a new higher order shear deformation theory. *Composite Part B*, 55, pp. 558–574, 2013.

[20]. H.C. Thai, H. Nguyen-Xuan, S.P.A Bordas, N. Nguyen-Thanh, T. Rabczuk. Isogeometric analysis of laminated composite plates using the higher-order shear deformation theory. *Mechanics of Advanced Material and Structures*, 22, pp. 451–469, 2015.

[21]. V.L. Tran, A.J. Ferreira, H. Nguyen-Xuan. Isogeometric approach for analysis of functionally graded plates using higher- order shear deformation theory. *Composite Part B,* 51, pp. 368–383, 2013.

[22]. M. Lezgy-Nazargah, P. Vidal, O. Polit. NURBS-based isogeometric analysis of laminated composite beams using refined sinus model. *European Journal of Mechanics A/Solids*, 53, pp. 34–47, 2015.

[23]. N. Valizadeh, S.Sh. Ghorashi, H. Yousefi, T.Q. Bui, T. Rabczuk. Transient analysis of laminated composite plates using Isogeometric Analysis. The Eighth International Conference on Engineering Computational Technology, *Civil-Comp Press*, Stirlingshire, Scotland, 2012.

[24]. J.A. Mitchell, J.N. Reddy. A refined hybrid plate theory for composite laminates with piezoelectric laminae. *International Journal of Solids and Structures*, 32(16), pp. 2345-2367, 1995.

[25]. A. Suleman, V.B. Venkayya. A simply finite element formulation for a laminated composite plate with piezoelectric layers. *Journal of Intelligent Material Systems and Structures,*6, pp. 776-782, 1995.

[26]. M.F.C. Victor, A.A.G. Maria, S. Afzal, M.M.S Cristóvão, A.M.S. Carlos, C.V.M. Franco. Modelling and design of adaptive composite structures. *Computer Methods in Applied Mechanics and Engineering*,185, pp. 325-346, 2000.

[27]. K.M. Liew, J. Yang, S. Kittipornchai S. Postbuckling of piezoelectric FGM plates subjected to thermo-electro-mechanical loading. *International Journal of Solids and Structures*, 40, pp. 3869-3892, 2004.

[28]. G.R. Liu, K.Y. Dai, K.M. Lim. Static and vibration control of composite laminates integrated with piezoelectric sensors and actuators using the radial point interpolation method. *Smart Materials and Structures*, 13, pp. 1438-1447, 2014.

[29]. G.R. Liu, X.Q. Peng, K.Y. Lam, J. Tani. Vibration control simulation of laminated composite plates with integrated piezoelectrics. *Journal of Sound and Vibration*, 220, pp. 827–846, 1999.

[30]. W.C. Hwang, H.C. Park. Finite element modeling of piezoelectric sensors and actuators. *AIAA Journal*, 31, pp. 930-937, 1993.

[31]. D.A.F. Torres, Pd.T.R. Mendonca, C.Sd. Barcellos. Evalution and verification of an HSDT-layerwise generalized finite element formulation for adaptive piezoelectric laminated plates. *Computer Methods in Applied Mechanics and Engineerin*g, 200, pp. 675-691, 2011.

[32]. D.A. Saravanos, P.R. Heyliger, D.A. Hopkins. Layerwise mechanics and finite element for the dynamic analysis of piezoelectric composite plates. *International Journal of Solids and Structures,* 34, pp. 359-378, 1997.

[33]. J.N. Reddy. On laminated composite plates with integrated sensors and actuators. *Engineering Structures*, 21, pp. 568–593, 1999.

[34]. T. Bailey, J.E. Hubbard. Distributed piezoelectric-polymer active control of a cantilever beam. *Journal of Guidance Control and Dynamic*, 86, pp. 605–611, 1985.

[35]. I.S. Shen. Bending and torsional vibration control of composite beams through intelligent constrained-layer damping treatments. *Smart Materials and Structures*, 4, pp. 340–355, 1995.

[36]. H.S. Tzou, C.I. Tseng. Distributed piezoelectric sensor/actuation design for dynamic measurement/control of distributed systems: a piezoelectric finite element approach. *Journal of Sound and Vibration*, 138, pp. 17-34, 1990.

[37]. K.M. Liew, H.K. Lim, M.J. Tan, X.Q. He. Analysis of laminated composite beams and plate with piezoelectric patches using the element-free Galerkin method. *Computational Mechanics*, 294, pp. 86-497, 2002.

[38]. S.Y. Wang, S.T. Quek, K.K. Ang. Dynamic stability analysis of finite element modeling of piezoelectric composite plates. *International Journal of Solids and Structures*, 41, pp. 745-764, 2004.

[39]. X. He, T. Ng, S. Sivashanker, K. Liew. Active control of fgm plates with integrated piezoelectric sensors and actuators. *International journal of Solids and Structures*, 38, pp. 1641–1655, 2001.

[40]. B. Selim, L. Zhang, K. Liew. Active vibration control of FGM plates with piezoelectric layers based on Reddy's higher-order shear deformation theory. *Composite Structures*, 155, pp. 118–134, 2016.

[41]. P. Phung-Van, L. V. Tran, A. Ferreira, H. Nguyen-Xuan, M. Abdel-Wahab. Nonlinear transient isogeometric analysis of smart piezoelectric functionally graded material plates based on generalized shear deformation theory under thermo-electro-mechanical loads. *Nonlinear Dynamics*, 87, pp. 879–894, 2017.

[42]. A. Tampieri, G. Celotti, S. Sprio, A. Delcogliano, S. Franzese. Porosity-graded hydroxyapatite ceramics to replace natural bone. *Biomaterials*, 22 (11), pp. 1365–1370, 2001.

[43]. W. Pompe, H. Worch, M. Epple, W. Friess, M. Gelinsky, P. Greil, U. Hempel, D. Scharnweber, K. Schulte, Functionally graded materials for biomedical applications. *Materials Science and Engineering: A*, 362 (1-2), pp. 40–60, 2003.

[44]. L.P. Lefebvre, J. Banhart, D. C. Dunand. Porous metals and metallic foams: current status and recent developments. *Advanced Engineering Materials*, 10 (9), pp. 775–787, 2008.

[45]. C. Betts. Benefits of metal foams and developments in modelling techniques to assess their materials behaviour: a review. *Materials Science and Technology*, 28 (2), pp. 129–143, 2012.

[46]. B. Smith, S. Szyniszewski, J. Hajjar, B. Schafer, S. Arwade. Steel foam for structures: A review of applications, manufacturing and material properties. *Journal of Constructional Steel Research*, 71, pp. 1–10, 2012.

[47]. X. Xia, X. Chen, Z. Zhang, X. Chen, W. Zhao, B. Liao, B. Hur. Effects of porosity and pore size on the compressive properties of closed-cell mg alloy foam. *Journal of Magnesium and Alloys,* 1 (4), pp. 330–335, 2013.

[48]. S. Iijima. Helical microtubules of graphitic carbon. *Nature*, 354 (6348) 56, 1991.

[49]. K. Liew, Z. Lei, L. Zhang. Mechanical analysis of functionally graded carbon nanotube reinforced composites: a review. *Composite Structures,* 120, pp. 90–97, 2015.

[50]. T.Nguyen-Van, K.Nguyen-Dinh, T. Ngo-Duc, P.Tran, D.Nguyen-Dinh. Nonlinear dynamic response and vibration of functionally graded carbon nanotube-reinforced composite (FG-CNTRC) shear deformable plates with temperature-dependent material properties and surrounded on elastic foundations. *Journal of Thermal Stresses,* 40, pp. 1254-1274, 2017.

[51]. G. Mittal, V. Dhand, K. Y. Rhee, S.-J. Park, W. R. Lee. A review on carbon nanotubes and graphene as fillers in reinforced polymer nanocomposites. *Journal of Industrial and Engineering Chemistry*, 21, pp. 11–25, 2015.

[52]. D. G. Papageorgiou, I. A. Kinloch, R. J. Young. Mechanical properties of graphene and graphene-based nanocomposites. *Progress in Materials Science*, 90, pp. 75–127, 2017.

[53]. M. A. Rafiee, J. Rafiee, Z. Wang, H. Song, Z.-Z. Yu, N. Koratkar. Enhanced mechanical properties of nanocomposites at low graphene content. *ACS nano*, 3, pp. 3884–3890, 2009.

[54]. C. Betts. Benefits of metal foams and developments in modelling techniques to assess their materials behaviour: a review. *Materials Science and Technology*, 28, pp. 129–143, 2012.

[55]. L.P. Lefebvre, J. Banhart, and D. C. Dunand. Porous metals and metallic foams: current status and recent developments. *Advanced Engineering Materials*, 10, pp. 775–787, 2008.

[56]. H. N. Wadley, N. A. Fleck, A. G. Evans. Fa brication and structural performance of periodic cellular metal sandwich structures. *Composites Science and Technology*, 63, pp. 2331–2343, 2003.

[57]. J. Banhart. Manufacture, characterisation and application of cellular metals and metal foams. *Progress in Materials Science*, 46, pp. 559 – 632, 2001.

[58]. B. Smith, S. Szyniszewski, J. Hajjar, B. Schafer, S. Arwade. Steel foam for structures: A review of applications, manufacturing and material properties. *Journal of Constructional Steel Research*, 71, pp. 1 – 10, 2012.

[59]. L. J. Groven, J. A. Puszynski. Solution combustion synthesis of carbon nanotube loaded nickel foams. *Materials Letters*, 73, pp. 126–128, 2012.

[60]. I. Duarte, E. Ventura, S. Olhero, J. M. Ferreira. An effective approach to reinforced closed-cell al-alloy foams with multiwalled carbon nanotubes. *Carbon*, 95, pp. 589–600, 2015.

[61]. Y. Hangai, K. Saito, T. Utsunomiya, S. Kitahara, O. Kuwazuru, N. Yoshikawa,. Compression properties of Al/Al–Si–Cu alloy functionally graded aluminum foam fabricated by friction stir processing route. *Materials Transactions*, 54, pp. 405–408, 2013.

[62]. A. Hassani, A. Habibolahzadeh, H. Bafti. Production of graded aluminum foams via powder space holder technique. *Materials & Design*, 40, pp. 510–515, 2012.

[63]. S.Y. He, Y. Zhang, G. Dai, J.Q. Jiang. Preparation of density-graded aluminum foam. *Materials Science and Engineering: A*, 618, pp. 496–499, 2014.

[64]. S. Kitipornchai, D. Chen, J. Yang. Free vibration and elastic buckling of functionally graded porous beams reinforced by graphene platelets. *Materials & Design*, 116, pp. 656–665, 2017.

[65]. D. Chen, J. Yang, S. Kitipornchai. Nonlinear vibration and postbuckling of functionally graded graphene reinforced porous nanocomposite beams. *Composites Science and Technology*, 142, pp. 235–245, 2017.

[66]. J. Yang, D. Chen, S. Kitipornchai. Buckling and free vibration analyses of functionally graded graphene reinforced porous nanocomposite plates based on Chebyshev-Ritz method. *Composite Structures*, 193, pp. 281–294, 2018.

[67]. K. Li, D. Wu, X. Chen, J. Cheng, Z. Liu, W. Gao, M. Liu. Isogeometric analysis of functionally graded porous plates reinforced by graphene platelets. *Composite Structures*, 204, pp. 114–130, 2018.

[68]. D. Nguyen-Dinh. Nonlinear thermo-electro-mechanical dynamic response of shear deformable piezoelectric Sigmoid functionally graded sandwich circular cylindrical shells on elastic foundations, *Journal of Sandwich Structures & Materials*, 20, pp. 351-378, 2018.

[69]. D. Nguyen-Dinh, Q. Tran-Quoc, K. Nguyen-Dinh. New approach to investigate nonlinear dynamic response and vibration of imperfect functionally graded carbon nanotube reinforced composite double curved shallow shells, *Aerospace Science and Technology*, 71, pp. 360-372, 2017.

[70]. Q. Li, D. Wu, X. Chen, L. Liu, Y. Yu, W. Gao. Nonlinear vibration and dynamic buckling analyses of sandwich functionally graded porous plate with graphene platelet reinforcement resting on winkler-pasternak elastic foundation. *International Journal of Mechanical Sciences,* 148, pp. 596-610, 2018.

[71]. C.H. Thai, S. Kulasegaram, L.V. Tran, H. Nguyen-Xuan. Generalized shear deformation theory for functionally graded isotropic and sandwich plates based on isogeometric approach. *Computers & Structures*, 141, pp. 94-112, 2014.

[72]. M.A. Ansari, Ashrafi, T. Pourashraf, S. Sahmani. Vibration and buckling characteristics of functionally graded nanoplates subjected to thermal loading based on surface elasticity theory. *Acta Astronautica,* 109, pp. 42-51, 2015.

[73]. W. Zhang, J. Yang, Y.X. Hao. Chaotic vibrations of an orthotropic FGM rectangular plate based on third-order shear deformation theory. *Nonlinear Dynamics*, 59, pp. 619-60, 2010.

[74]. C.C.M. Wu, M. Kahn, W. Moy. Piezoelectric ceramics with functional gradients: a new application in material design. *Journal of the American Ceramic Society,*79, pp. 809–812, 1996.

[75]. Z. Zhong, E.T. Shang. Three-dimensional exact analysis of a simply supported functionally gradient piezoelectric plate. *International Journal of Solids and Structures,* 40, pp. 5335–5352, 2003.

[76]. P.A. Jadhav, K.M. Bajoria. Free and forced vibration control of piezoelectric FGM plate subjected to electro-mechanical loading. *Smart Materials and Structures*, 22(6), 2013.

[77]. Y. Kiani, M. Rezaei, S .Taheri, M.R. Eslami. Thermo-electrical buckling of piezoelectric functionally graded material Timoshenko beams. *International Journal of Mechanics and Materials in Design*, 7(3), pp. 185-97, 2011.

[78]. Sharma P, Parashar SK. Free vibration analysis of shear-induced flexural vibration of FGPM annular plate using Generalized Differential Quadrature method. *Composite Structures*, 155, pp. 213-22, 2016.

[79]. Y.S. Li, E. Pan. Static bending and free vibration of a functionally graded piezoelectric microplate based on the modified couple-stress theory. *International Journal of Engineering Science*,97, pp. 40–59, 2015.

[80]. B. Behjat, M.R. Khoshravan. Geometrically nonlinear for static and free vibration analysis of functionally graded piezoelectric plates. *Composite Structures*; 94, pp. 874–882, 2012.

[81]. Zhu Su, Guoyong Jin, Tiangui Ye. Electro-mechanical vibration characteristics of functionally graded piezoelectric plates with general boundary conditions. *International Journal of Mechanical Sciences*, 138-139, pp. 42-53, 2018.

[82]. M.R. Barati, H. Shahverdi, A.M. Zenkour. Electro-mechanical vibration of smart piezoelectric FG plates with porosities according to a refined four-variable theory. *Mechanics of Advanced Materials and Structures*, pp. 987-998, 2016.

[83]. M.R. Barati, M.H. Sadr, A.M. Zenkour. Buckling analysis of higher order graded smart piezoelectric plates with porosities resting on elastic foundation. *International Journal of Mechanical Sciences*, 117, pp. 309-320, 2016.

[84]. F. Ebrahimi, A. Jafari, M.R. Barati. Free Vibration Analysis of Smart Porous Plates Subjected to Various Physical Fields Considering Neutral Surface Position. *Arabian Journal for Science and Engineering,* 42, pp. 1865–1881, 2017.

[85]. Y.Q. Wang. Electro-mechanical vibration analysis of functionally graded piezoelectric porous plates in the translation state. *Acta Astro,* 143, pp. 263-271, 2018.

[86]. Y.Q. Wang, J.W. Zu. Porosity-dependent nonlinear forced vibration analysis of functionally graded piezoelectric smart material plates. *Smart materials and Structures,* 26(10), 2017.

[87]. S. Mann. A Blossoming Development of Splines. *Synthesis Lectures on Computer Graphics*, 1, pp. 1-108, 2006.

[88]. R. Bartels, J. Beatty, B. Barsky. *An Introduction to Splines for Use in Computer Graphics and Geometric Modeling.* Morgan Kaufmann, 1996.

[89]. C. d. Boor. *A Practical Guide to Splines*. Springer-Verlag New York, 1978.

[90]. M. J. Borden, M. A. Scott, J. A. Evans, T. J. R. Hughes. Isogeometric finite element data structures based on Bézier extraction of NURBS. *International Journal for Numerical Methods in Engineering*, 87, no. 1-5, 2011.

[91]. H. Prautzsch. Degree elevation of B-spline curves. *Computer Aided Geometric Design*, 1, pp. 193-198, 1984.

[92]. Piegl, W. Tiller. Software-engineering approach to degree elevation of B-spline curves. *Computer-Aided Design*, 26, pp. 17-28, 1994.

[93]. Liu. A simple, efficient degree raising algorithm for B-spline curves. *Computer Aided Geometric Design*, 14, pp. 693-698, 1997.

[94]. Q.X. Huang, S.M. Hu, R. R. Shi-Min. Fast degree elevation and knot insertion for B-spline curves. *Computer Aided Geometric Design*, 22, pp. 183-197, 2005.

[95]. J. Cottrell, T. Hughes, A. Reali. Studies of refinement and continuity in isogeometric structural analysis. *Computer Methods in Applied Mechanics and Engineering*, 196, pp. 4160-4183, 2007.

[96]. L. A. Piegl, W. Tiller. *The NURBS Book*. Springer, 1997.

[97]. M.J. Borden, M.A. Scott, J.A. Evans, T.J.R. Hughes. Isogeometric finite element data structures based on Bézier extraction of NURBS. *International Journal for Numerical Methods*, 86, pp. 15–47, 2011.

[98]. Lieu B. Nguyen, Chien H. Thai, H. Nguyen Xuan. A generalized unconstrained theory and isogeometric finite element analysis based on Bézier extraction for laminated composite plates. *Engineering with Computers*, 32, pp. 457–475, 2016.

[99]. N.J. Pagano. Exact solutions for rectangular bidirectional composites and sandwich plates. *Journal of Composite Materials*, 4, pp. 20–34, 1970.

[100]. A.K. Noor. Free vibration of multilayered composite plates. *American Institute of Aeronautics and Astronautic Journal*, 11, pp. 1038–1039, 1973.

[101]. A.K. Noor. Stability of multilayered composite plates. *Fibre Science and Technolog*, 8, pp. 81–89,1975.

[102]. A. Love. On the small free vibrations and deformations of elastic shells. *Philosophical Transactions of the Royal Society (London)*, 17, pp. 491–549, 1888.

[103]. R. Mindlin. Influence of rotatory inertia and shear on flexural motions of isotropic, elastic plates. *ASME Journal of Applied Mechanics*, 18, pp. 31–38, 1951.

[104]. N.Trung-Kien, V. Thuc P, T. Huu-Tai. Static and free vibration of axially loaded functionally graded beams based on the first-order shear deformation theory. *Composites Part B: Engineering*, 55, pp. 147-157, 2013.

[105]. T. Huu-Tai Thai, N. Trung-Kien, V. Thuc P, L. Jaehong. Analysis of functionally graded sandwich plates using a new first-order shear deformation theory. *European Journal of Mechanics-A/Solids*, 45, pp. 211-225, 2014.

[106]. N. Trung-Kien, S. Karam, B. Guy. First-order shear deformation plate models for functionally graded materials. *Composite Structures*, 83, pp. 25-36, 2008.

[107] . T. Nguyen-Thoi, P. Phung-Van, H. Luong-Van, H. Nguyen-Van, H. Nguyen-Xuan. A cell-based smoothed three-node Mindlin plate element (CS-MIN3) for static and free vibration analyses of plates. *Computational Mechanics*, 51, pp. 65-81, 2013.

[108]. L. Librescu. On the theory of anisotropic elastic shells and plates. *International Journal of Solids and Structure*, 3(1):53–68, 1967.

[109]. M. Levinson. An accurate, simple theory of the statics and dynamics of elastic plates. *Mechanics Research Communication*, 7(6):343–350, 1980.

[110]. A. Bhimaraddi, L.K. Stevens. A higher order theory for free vibration of orthotropic, homogeneous and laminated rectangular plates. Journal of Applied Mechanics, *Transactions ASME*, 51(1), pp. 195–198, 1984.

[111]. J.G. Ren. A new theory of laminated plate. *Composites Science and Technology*, 26, pp. 225–239,1986.

[112]. J.N. Reddy. A simple higher-order theory for laminated composite plates. *Journal of Applied Mechanics*, 51, pp. 745–752, 1984.

[113]. N. Van-Hau, N. Trung-Kien, T. Huu-Tai, V.Thuc P. A new inverse trigonometric shear deformation theory for isotropic and functionally graded sandwich plates. *Composites Part B: Engineering*, 66, pp. 233-246, 2014.

[114]. N. Trung-Kien, N. Ba-Duy. A new higher-order shear deformation theory for static, buckling and free vibration analysis of functionally graded sandwich beams. *Journal of Sandwich Structures & Materials*, 17, pp. 613-631, 2015.

[115]. H. Arya , R. P. Shimpi, N. K. Naik. A zig-zag model for laminated composite beams. *Composite Structures*, 56, pp. 21–24, 2002.

[116]. M.J. Karama, K. S. Afaq, S. Mistou. Mechanical behavior of laminated composite beam by new multi-layered laminated composite structures model with transverse shear stress continuity, *International Journal of Solids and Structures*, 40, pp. 1525–1546, 2003.

[117]. M. Touratier. An efficient standard plate theory. *International Journal of Engineering Science*, 29, pp. 745-752, 1991.

[118] . A.Y.T Leung. An unconstrained third-order plate theory. *Composite Structures*, 40(4), pp. 871–75, 1991.

[119]. H.C. Thai, A.J.M. Ferreira, T. Rabczuk,H. Nguyen-Xuan. A naturally stabilized nodal integration meshfree formulation for carbon nanotube-reinforced composite plate analysis. *Engineering Analysis with Boundary Elements*, 92, pp. 136-155, 2018.

[120]. P. Phung-Van, T. Nguyen-Thoi, T. Bui-Xuan, Q. Lieu-Xuan. A cell-based smoothed three-node Mindlin plate element (CS-FEM-MIN3) based on the C^0-type higher-order shear deformation for geometrically nonlinear analysis of laminated. *Computational Materials Science*, 96, pp. 549-558, 2015.

[121].T. Nguyen-Hoa, D. Nguyen-Dinh. The Composite Material-Mechanics and technology. *Science and Technical Publisher,* Hanoi, 2002.

[122]. Z. Wang, S. Chen, W. Han. The static shape control for intelligent structures, *Finite Elements in Analysis and Design*, 26, pp. 303-314, 1997.

[123]. L. Costa, I. Figueiredo, R. Leal, P. Oliveira, G. Stadler. Modeling and numerical study of actuator and sensor effects for a laminated piezoelectric plate. *Computers and Structures*, 85, pp. 385-403, 2007.

[124]. A. Mukherjee, S.P. Joshi, A. Ganguli. Active vibration control of piezolaminated stiffened plates. *Composite Structures*, 55(4), pp. 435-443, 2002.

[125]. S.Y. Wang, S.T. Quek, K.K. Ang. Vibration control of smart piezoelectric composite plates. *Smart Materials and Structures*,10, pp. 637-644, 2001.

[126]. H.F Tiersten. *Linear piezoelectric plate vibrations*. Plenum press, New York; 1969.

[127]. S. Kitipornchai, D. Chen, J. Yang. Free vibration and elastic buckling of functionally graded porous beams reinforced by graphene platelets. *Materials & Design*, 116, pp. 656–665, 2017.

[128]. A. P. Roberts, E. J. Garboczi. Elastic moduli of model random three-dimensional closed-cell cellular solids. *Acta materialia*, 49, pp. 189–197, 2001.

[129]. M. A. Rafiee, J. Rafiee, Z. Wang, H. Song, Z.-Z. Yu, N. Koratkar. Enhanced mechanical properties of nanocomposites at low graphene content. *ACS nano*, 3, pp. 3884–3890, 2009.

[130]. S. C. Tjong. Recent progress in the development and properties of novel metal matrix nanocomposites reinforced with carbon nanotubes and graphene nanosheets. *Materials Science and Engineering: R: Reports*, 74, pp. 281–350, 2013.

[131]. J. H. Affdl, J. Kardos. The Halpin-Tsai equations: a review. *Polymer Engineering & Science*, 16, pp. 344–352, 1976.

[132]. L.M.J.S.Dinis, R.M. Natal Jorge, J. Belinha. Static and dynamic analysis of laminated plates based on an unconstrained third-order theory and using a radial point interpolator meshless method. *Computer and Structures*, 89, pp. 1771–1784, 2011.

[133]. K.M. Liew, Y.Q. Huang, J.N. Reddy. Vibration analysis of symmetrically laminated plates based on FSDT using the moving least squares differential quadrature method. *Computer Methods in Applied Mechanics and Engineering*, 192, pp. 2203-2222, 2003.

[134]. H.C. Thai, A.J.M. Ferreira, S.P.A. Bordas, T. Rabczuk, H. Nguyen-Xuan. Isogeometric analysis of laminated composite and sandwich plates using a new inverse trigonometric shear deformation theory. *European Journal of Mechanics A/Solids,* 43, pp. 89-108, 2014.

[135]. J.Z. Luo, T.G. Liu, T.Zhang. Three-dimensional linear analysis for composite axially symmetrical circular plates. *International Journal of Solids and Structures*, 4, pp. 3689‑3706, 2004.

[136]. S. Kapuria, G.P. Dube, P.C. Dumir, S. Sengupta. Levy-type piezothermoelastic solution for hybrid plate by using first-order shear deformation theory. *Composite Part B*, 28B, pp. 535-546, 1997.

[137]. A.A. Khdeir, L. Librescu. Analysis of symmetric cross-ply elastic plates using a higher-order theory -part II: buckling and free vibration. *Composite Structures*, 9, pp. 259‑277, 1988.

[138]. N.J. Pagano. Exact solutions for rectangular bidirectional composites and sandwich plates. *Journal of Composite Materials,* 4, pp. 20‑34, 1970.

[139]. S.P. Timoshenko, J.N. Goodier. *Theory of Elasticity*. McGraw-Hill Book Company, Inc., New York, 1951.

[140]. K.M. Liew. Response of plates of arbitrary shape subject to static loading. *Journal of Applied Mechanics ASME*, 118, pp.1783‑1794, 1992.

[141]. K.M. Liew. Vibration of clamped circular symmetric laminates. *Journal of Vibration and Acoustics -ASME*, 116, pp. 141‑145, 1994.

[142]. A.J.M. Ferreira. A formulation of the multiquadric radial basis function method for the analysis of laminated composite plates. *Composite Structures*, 59, pp. 385‑392, 2003.

[143]. A.J.M. Ferreira, L.M.S. Castro, S. Bertoluzza. A high order collocation method for the static and vibration analysis ofcomposite plates using a first-order theory. *Composite Structures*, 89, pp. 424‑432, 2009.

[144]. W. Zhen, C. Wanji. Free vibration of laminated composite and sandwich plates using global-local higher-order theory. *Journal of Sound and Vibration.*, 298, pp. 333‑349, 2006.

[145]. K.N. Cho, C.W. Bert, A.G. Striz. Free vibration of laminated rectangular plates analyzed by higher-order individual-layer theory. *Journal of Sound and Vibration*, 145, pp. 429‑442, 1991.

[146]. H. Matsunaga. Vibration and stability of cross-ply laminated composite plates according to a global higher-order platetheory. *Composite Structures*, 48, pp. 231-244, 2000.

[147]. A.A. Khdeir, J.N. Reddy. Exact solution for the transient response of symmetric cross-ply laminates using a higher-order plate theory. *Composites Science and Technology*, 34, pp. 205‑224, 1989.

[148]. P.Phung-Van, L.B. Nguyen, L.V.Tran, T.D. Dinh, C.H.Thai, S.P.A.Bordas, M. Abdel-Wahab, H.Nguyen-Xuan. An efficient computational approach for control of nonlinear transient responses of smart piezoelectric composite plates. *International Journal of Non-Linear Mechanics,* 76*,* pp.190–202, 2015.

[149]. Y.Y. Wang, K.Y. Lam, G.R. Liu. A strip element method for the transient analysis of symmetric laminated plates. *International Journal of Solids and Structures*, 38, pp. 241‑259, 2001.

[150]. S.Y. Wang. A finite element model for the static and dynamic analysis of a piezoelectric bimorph. *International Journal of Solids and Structures*, 41, pp. 4075-4096, 2004.

[151]. P. Phung-Van, T. Nguyen-Thoi, T. Le-Dinh, H. Nguyen-Xuan. Static and free vibration analyses and dynamic control of composite plates integrated with piezoelectric sensors and actuators by the cell-based smoothed discrete shear gap method (CS-FEM-DSG3). *Smart Materials and Structures*, 22, 2013.

[152]. K.Y. Lam, X.Q. Peng, G.R. Liu, J.N. Reddy. A finite element model for piezoelectric composite laminates. *Smart Materials and Structures,* 6, pp. 583-591,1997.

[153]. L.B. Nguyen, N.V. Nguyen, C.H. Thai, A.M. J. Ferreira, H. Nguyen-Xuan. An isogeometric Bézier finite element analysis for piezoelectric FG porous plates reinforced by graphene platelets. *Composite Structure*, 214, pp. 227-245, 2019.

[154]. S. Kudus, Y Suzuki, M. Matsumura, K. Sugiura. Vibration-response due to thickness loss on steel plate excited by resonance frequency in *IOP Conerence Series*: *Earth and Environmental Science*, 140, no. 1. IOP Publishing, 2018.

[155]. T. Nakamura, T. Wang, S. Sampath. Determination of properties of graded materials by inverse analysis and instrumented indentation. *Acta Materialia*, 48, pp. 4293-4306, 2000.

[156]. K. Nguyen-Quang, H. Dang-Trung, V Ho-Huu, H. Luong-Van, T. Nguyen-Thoi. Analysis and control of FGM plates integrated with piezoelectric sensors and actuators using cell-based smoothed discrete shear gap method (CS-DSG3). *Composite Structures*, 165, pp. 115-129, 2017.

[157]. N. V. Nguyen, H. X. Nguyen, S. Lee, H. Nguyen-Xuan. Geometrically nonlinear finite element analysis of functionally graded porous plates. *Advances in Engineering Software*, 126, pp. 110 - 126, 2018.

[158]. J.N. Reddy. Analysis of functionally graded plates. *International Journal for Numerical methods in Engineering*, 47 (1-3), pp. 663–684, 2000.

[159]. J. N. Reddy. An Introduction to Nonlinear Finite Element Analysis: with applications to heat transfer, fluid mechanics, and solid mechanics. OUP Oxford, 2014.

[160]. S. Levy. Square plate with clamped edges under normal pressure producing large deflections. United States, 1942.

[161]. Y. Urthaler, J.N. Reddy. A mixed finite element for the nonlinear bending analysis of laminated composite plates based on FSDT. *Mechanics of Advanced Materials and structures*, 15 (5), pp. 335-354, 2008.

[162]. H. X. Nguyen, E. Atroshchenko, H. Nguyen-Xuan, T. P. Vo. Geometrically nonlinear isogeometric analysis of functionally graded microplates with the modified couple stress theory. *Computers & Structures*, 193, pp. 110-127, 2017.

[163]. J. Chen, D. Dawe, S. Wang. Nonlinear transient analysis of rectangular composite laminated plates. *Composite structures*, 49 (2), pp. 129-139, 2000.

[164]. T. Nakamura, T Wang, S. Sampath. Determination of properties of graded materials by inverse analysis and instrumented indentation. *Acta Materialia*, 48 (17), pp. 4293-4306, 2000.

[165]. F. Ramirez, P.R. Heyliger, E. Pan. Free vibration response of two-dimensional magneto-electro-elastic laminated plates. *Journal of Sound and Vibration.*, 292(3), pp. 626-644, 2006.

[166]. M. Bodaghi, M. Shakeri. An analytical approach for free vibration and transient response of functionally graded piezoelectric cylindrical panels subjected to impulsive loads. *Composite Structures*, 94, pp. 1721–1735, 2012.

[167]. Z. Su, G. Jin, T. Ye. Electro-mechanical vibration characteristics of functionally graded piezoelectric plates with general boundary conditions. *International Journal of Mechanical Sciences*, 138-139, pp. 42-53, 2018.

[168]. K.D. Nguyen, H. Nguyen-Xuan. An isogeometric finite element approach for three-dimensional static and dynamic analysis of functionally graded material plate structures. *Composite Structure*, 132, pp. 423–439, 2015.

[169]. H.C. Thai, A.J.M. Ferreira, M. Abdel Wahab, H. Nguyen-Xuan. A moving Kriging meshfree method with naturally stabilized nodal integration for analysis of functionally graded material sandwich plates. *Acta Mechanica*, 7, pp. 2997–3023, 2018.

[170]. T. Irie, G. Yamada, S. Aomura. Natural frequencies of Mindlin circular plates. *Journal of Applied Mechanics*, 47(3), pp. 652–655, 1980.

[171]. H. Nguyen-Xuan, G.R. Liu, C. Thai-Hoang, T. Nguyen-Thoi. An edge based smoothed finite element method (ES-FEM) with stabilized discrete shear gap

technique for analysis of Reissner–Mindlin plates. *Computer Methods in Applied Mechanics and Engineering*, 199, pp. 471–489, 2013.

[172]. F. Tornabene. Free vibration analysis of functionally graded conical, cylindrical shell and annular plate structures with a four-parameter power-law distribution. *Computer Methods in Applied Mechanics and Engineering*, 198, pp. 2911–2935, 2009.

[173]. H.C. Thai, A.M. Zenkour, M.A. Wahab, H. Nguyen-Xuan. A simple four unknown shear and normal deformations theory for functionally graded isotropic and sandwich plates based on isogeometric analysis. *Composite Structures,* 139, pp. 77–95, 2016.

[174]. L.B. Nguyen, H.C. Thai, A.M. Zenkour, H. Nguyen-Xuan. An isogeometric Bézier finite element method for vibration analysis of functionally graded piezoelectric material porous plates. *International Journal of Mechanical Sciences,* 157–158, pp. 165–183, 2019.

LIST OF PUBLICATIONS

Parts of this dissertation have been published in international journals, national journals or presented in conferences. These papers are:

- **Articles in ISI-covered journal**

1. **Lieu B. Nguyen**, Chien H. Thai and H. Nguyen-Xuan. A generalized unconstrained theory and isogeometric finite element analysis based on Bézier extraction for laminated composite plates. *Engineering with Computers,* 32(3), pp. 457-475, 2016. (SCIE, Q2).
2. P. Phung-Van, **Lieu B. Nguyen**, L.V. Tran, T.D. Dinh, Chien H. Thai, S.P.A. Bordas, M.A. Wahab, H Nguyen-Xuan. An efficient computational approach for control of nonlinear transient responses of smart piezoelectric composite plates. *International Journal of Non-Linear Mechanics*, 76, pp. 190-202, 2015. (SCI, Q1).
3. **Lieu B. Nguyen**, Nam V. Nguyen, Chien H. Thai, A.M. J. Ferreira, H. Nguyen-Xuan. An isogeometric Bézier finite element analysis for piezoelectric FG porous plates reinforced by graphene platelets. *Composite Structure*, 214, pp. 227-245, 2019. (SCIE, Q1).
4. **Lieu B. Nguyen**, Chien H. Thai, A.M. Zenkour, H. Nguyen-Xuan. An isogeometric Bézier finite element method for vibration analysis of functionally graded piezoelectric material porous plates. *International Journal of Mechanical Sciences*, 157–158, pp. 165–183, 2019. (SCI, Q1).
5. Nam V. Nguyen, **Lieu B. Nguyen**, Jaehong Lee, H. Nguyen-Xuan. Analysis and control of geometrically nonlinear responses of piezoelectric FG porous plates with graphene platelets einforcement using Bézier extraction. Submitted in *European Journal of Mechanics / A Solids*, reviewing (SCI, Q1).

- **Articles in national scientific journal**

1. **Lieu B. Nguyen**, Chien H. Thai, Ngon T. Dang, H. Nguyen Xuan. Transient Analysis of Laminated Composite Plates Using NURBS- Based Finite Elements. *Vietnam Journal of Mechanics*, 36, pp. 267-281, 2016.

- **International Conference**

1. **Lieu B. Nguyen**, Chien H. Thai, H. Nguyen-Xuan. Isogeometric analysis of laminated composite plates using a new unconstrained theory. *Proceedings of ICEMA-3, Ha Noi City, Viet Nam*, pp. 441-449, 2014.
2. **Lieu B. Nguyen**, Chien H. Thai, H. Nguyen-Xuan. Transient Analysis of Laminated Composite Plates Using Isogeometric Analysis. *Proceedings of GTSD'14, Ho Chi Minh City, Viet Nam*, pp. 73-82, 2014.

- **National Conference**

1. **Lieu B. Nguyen**, Chien H. Thai, H. Nguyen-Xuan. A novel four variable layerwise theory for laminated composite plates based on isogeometric analysis. *Proceedings of the National Conference on Mechanical Engineering, Da Nang City, Viet Nam*, pp. 758-768, 2015.
2. **Lieu B. Nguyen**, H. Nguyen-Xuan. Isogeometric approach for static analysis of laminated composite plates. *Proceedings of the National Conference on science and technology in mechanics IV, Ho Chi Minh City, Viet Nam*, pp. 177-187, 2015.